NASA/TM–20250006811

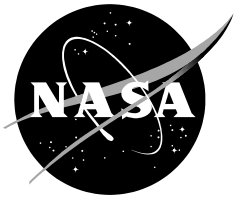

A Transportation and Habitation System Architecture Enabled by Multi-Modality Mobility Platforms

Larry A. Young
Ames Research Center, Moffett Field, California

August 2025

NASA STI Program ... in Profile

Since its founding, NASA has been dedicated to the advancement of aeronautics and space science. The NASA scientific and technical information (STI) program plays a key part in helping NASA maintain this important role.

The NASA STI program operates under the auspices of the Agency Chief Information Officer. It collects, organizes, provides for archiving, and disseminates NASA's STI. The NASA STI program provides access to the NTRS Registered and its public interface, the NASA Technical Reports Server, thus providing one of the largest collections of aeronautical and space science STI in the world. Results are published in both non-NASA channels and by NASA in the NASA STI Report Series, which includes the following report types:

- TECHNICAL PUBLICATION. Reports of completed research or a major significant phase of research that present the results of NASA Programs and include extensive data or theoretical analysis. Includes compilations of significant scientific and technical data and information deemed to be of continuing reference value. NASA counter-part of peer-reviewed formal professional studys but has less stringent limitations on manuscript length and extent of graphic presentations.

- TECHNICAL MEMORANDUM. Scientific and technical findings that are preliminary or of specialized interest, e.g., quick release reports, working studys, and bibliographies that contain minimal annotation. Does not contain extensive analysis.

- CONTRACTOR REPORT. Scientific and technical findings by NASA-sponsored contractors and grantees.

- CONFERENCE PUBLICATION. Collected studys from scientific and technical conferences, symposia, seminars, or other meetings sponsored or co-sponsored by NASA.

- SPECIAL PUBLICATION. Scientific, technical, or historical information from NASA programs, projects, and missions, often concerned with subjects having substantial public interest.

- TECHNICAL TRANSLATION. English-language translations of foreign scientific and technical material pertinent to NASA's mission.

Specialized services also include organizing and publishing research results, distributing specialized research announcements and feeds, providing information desk and personal search support, and enabling data exchange services.

For more information about the NASA STI program, see the following:

- Access the NASA STI program home page at http://www.sti.nasa.gov

- E-mail your question to help@sti.nasa.gov

- Phone the NASA STI Information Desk at 757-864-9658

- Write to:
  NASA STI Information Desk
  Mail Stop 148
  NASA Langley Research Center
  Hampton, VA 23681-2199

NASA/TM—20250006811

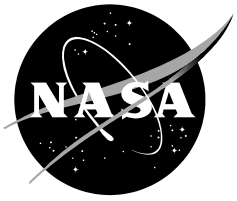

A Transportation and Habitation System Architecture Enabled by Multi-Modality Mobility Platforms

Larry A. Young
Ames Research Center, Moffett Field, California

National Aeronautics and
Space Administration

Ames Research Center
Moffett Field, CA 94035-1000

August 2025

A Transportation and Habitation System Architecture Enabled by Multi-Modality Mobility Platforms

Larry A. Young
Aeromechanics Office
NASA Ames Research Center
Moffett Field, CA 94035

Abstract

A novel urban/regional transportation and habitation architecture is proposed and explored in this study. This architecture uses rotorcraft and emerging eVTOL concepts and technologies as the underpinning for enabling surface/air mobility as well as the transport and staging of office/residential 'habitat modules.' These habitat modules would potentially entail camper or fifth-wheeler-like trailers with autonomous tugs for ground transportation – with maybe light-rail-type tie-in – and skycrane-like rotorcraft transportation as needed to help expedite their transport across an urban/regional landscape. This approach would be an alternate to various 'roadable' personal air vehicle and surface/ground "pod" transportation module concepts that have been previously proposed. The overall 'New Nomad' concept detailed in this study is unique in that goes beyond hybrid, or integrated, air and ground mobility concepts and makes the incorporation of habitat, or work/living environment, considerations an essential element of aerial vehicle design. Such a transportation and habitation system-of-systems architecture would have profound implications on the public's overall urban/regional 'livability' and the overall potential implications on community/urban planning. As a side note, the study also includes an examination of possible surface/air mobility solutions that incorporate modular, swappable propulsion options and cabin/chassis/fuselage common-core element. Ultimately, the study begins to try answering fundamental questions such as: can a novel transportation/habitation system architecture result in reduced commercial/residential habitation infrastructure costs, reduced mobility transportation costs, and increased social benefits such improved standard of living?

Table of Contents

Nomenclature

A	Rotor disk area, ft^2 or m^2
A_{Hab}	Nominal floor square footage of habitat
BEMT	Blade element momentum theory
BWB	Blended-wing-body aircraft configuration

BWBT	Blended-wing-body-tiltrotor configuration
C	Constant for livability index relating amount of recreation, entertainment, cultural activity enabled by habitat/transportation system, USD-day
C_{Com}	Cost (rental or mortgage) of commercial property per unit square footage per day
C_{Hab}	Cost (rental or mortgage) of habitat module per unit square footage per day
C_{Resid}	Cost (rental or mortgage) of residential property per unit square footage per day
$CL\alpha$	Lift curve slope, 1/Deg.
C_T	Rotor thrust coefficient, nondim.
CONOPS	Concept of Operations
d_A	Nominal distance covered by air for one habitat/transit movement, kilometers
d_G	Nominal distance covered by ground for one habitat/transit movement, kilometers
eVTOL	Electric- (propulsion-enabled) vertical takeoff and landing aircraft
$E_{Battery}$	Energy provided by the aerial vehicle's battery during a mission, KJ
E_{Total}	Total energy expended during a mission, KJ
f/A	Rotorcraft flat-plate area; f/A = Drag/(qA)
FM	Rotor hover figure of merit, nondim.
GPU	Graphics processing unit
HIGE	Hover in ground effect
HOGE	Hover out of ground effect
L_I	"Livability index" metric, nondim.
m_{GW}	'Gross weight' mass, kg
m_{EW}	'Empty weight' mass, kg
m_{EDTW}	(Electric) drive train mass, kg
m_{FW}	Fuselage mass, kg
m_{FEW}	Fixed equipment mass, kg
m_{RW}	Total rotor mass, kg
m_{WW}	Wing mass, kg
N_M	Number of average daily habitat/transit movements for commute or work-related
N_{MR}	Number of average daily habitat/transit movements for recreation, entertainment, and cultural activity
q	Freestream (forward flight) dynamic pressure, $q = 0.5\rho V^2$
QSMR	Quiet single main rotor
S_C	Daily cost savings for single occupant/passenger, USD/day
S_{CY}	Yearly cost savings for all occupants/passengers in a metropolitan area
S_t	Daily time savings for single occupant/passenger (as compared to ground travel during prime commute hours), hours
S_{wet}	Aerial vehicle wetted area, ft^2 or m^2, used for drag coefficient estimation
SMR	Single main rotor (with tail rotor) helicopter
SRS	Simple rotorcraft sizing analysis
USD	United States of America currency in dollars
UAM	Urban air mobility

V_A	Nominal aerial velocity, kilometers per hour
V_G	Nominal ground velocity from ground mobility option, kilometers per hour
V_{G0}	Nominal ground velocity from ground travel during prime commute hours, kilometers per hour
W	Average yearly wage/salary for residents of urban/regional area, USD
α	Angle of attack, Deg.
χ	Ratio of the share of cost savings for the occupant/passenger relative to the commercial/corporate entity, nondim.
κ	Time savings "circuity" correction, $\kappa \geq 1$, nondim.
ϕ	Ratio of the sum of residential and habitat daily costs (rental and mortgage) per unit square footage; $\Phi = (C_{Resid} + C_{Hab})/C_{Com}$
ε	Ratio of average daily habitat movements for recreation versus commute or work, $\varepsilon = N_{MR}/N_M$
ρ	Atmospheric density, slugs/ft^3 or kg/m^3
σ	Rotor solidity, blade area divided by rotor disk area

Introduction

In the twenty-first century, urban planning — including metropolitan transportation planning — is facing ever-increasing challenges. Aging infrastructure needs to be replaced and expanded. Residential and commercial buildings need to be expanded to reduce homeowner and rental costs while increasing capacity to accommodate the rapidly increasing city population sizes. Smaller or shrinking communities need to reinvent themselves to stem their population losses while maintaining and improving their living standards. Transportation systems need to be expanded and improved to combat street traffic congestion in larger cities. New modes of living and commercial property utilization must be accommodated to reflect expanding teleworking, telecommuting, and other inherent aspects of emerging knowledge/intellectual-based industries. Finally, coastal cities and/or 'sun belt' communities will need to proactively respond to climate change and evolving weather. Not all these urban planning problems are completely solvable by technological solutions, though many aspects might be partly addressed by technology. Of the subset of urban planning problems that are perhaps addressable by improved or innovative technology, it may appear at first that only some might be addressed by transportation technologies. Further, it seems even less likely that an aerospace-related set of technologies might come into play. And yet, it is a key proposition of this study that emerging aerospace/aviation technologies might profoundly influence the solution of some of the most pressing urban planning problems of the future. Such aerospace-related technologies and the underlying concepts inherent to them might radically redefine the American urban landscape — from the smallest rural towns to the largest cities. Adoption of these concepts not only could help reimagine transportation but also how people work and live. Some aspects of proposed ideas in this study are currently being explored by the rotorcraft research community such as urban aerial mobility and the use of electrical propulsion for aircraft. NASA Aeronautics Research Mission Directorate has been on the forefront of urban aerial mobility (UAM) and eVTOL (vertical takeoff and landing aerial

vehicles that use electric propulsion); e.g., Ref. 63. However, this study is unique in that it explores a seamless integration of the notions of transportation and habitation, the cross-pollination of multiple and linked modes of mobility, and even fundamental concepts regarding permanence versus the transitory nature of infrastructure and overall characteristics of cityscapes. The result might be a cultural shift towards twenty-first century 'New Nomads' (NN or N^2) enabled by radical new technologies. One such new technology might be the development of a short-range aerial vehicle, that could support the lifestyle of such New Nomads, is seen in Fig. 1a-c; in this example, a single-main-rotor (SMR) helicopter that is smaller than, but still reminiscent of, the Sikorsky (or now, Erickson) S-64 Skycrane heavy lift helicopters that would incorporate electric propulsion of some form.

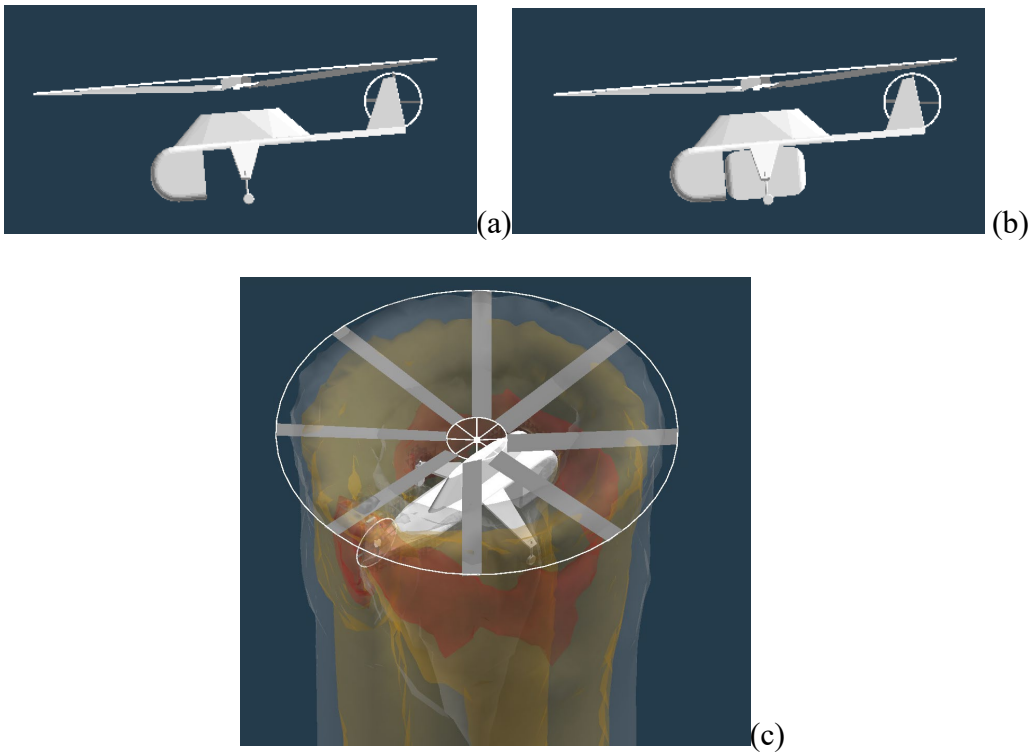
(a) (b) (c)

Figure 1. Aerial transport as a key element of a hybrid transportation/habitation system architecture: (a) SMR helicopter without habitat module, (b) with habitat module, and (c) hover CFD predictions of SMR helicopter without habitat module

Note that Fig. 1 represents just one possible conceptual design approach to providing both urban aerial – and habitation – mobility. A UAM-type aerial vehicle is employed for the aerial transport of 'campers' or referred to primarily in this report as 'habitat modules.' The habitat module might be imbued with its own ground mobility capability (such as a self-driving camper, of which some concepts are already being explored, e.g., Ref. 23). Or, alternatively, the habitat module might be towed by other self-driving ground vehicles,

possibly even including small special-purposed automated 'tugs'. The habitat modules might range in size and interior capabilities from small portable offices to larger recreational vehicles (RV) primarily intended as short-term residences. The size and weight of the habitat modules will have significant implications for the autonomous aerial cargo-carrying vehicles that might be rented from a commercial, or public, entity to complete the aerial legs of the habitat module transit(s). There can be either a tight or loose integration between mobility modes for multi-modality platforms, refer to Fig. 2. The vehicle presented in Fig. 1, given the Fig. 2 classification, represents a moderate coupling of mobility modality modes – in this case air and ground transport – for an UAM-type NN short-range aerial vehicle capable of carrying a camper-type habitat module. In Fig. 1, the habitat module would be notionally towed by an automated tug when moving on roadways, before and/or after each flight; in flight, the habitat module would be directly mounted/supported underneath the aerial vehicle in a partially aerodynamically conforming manner.

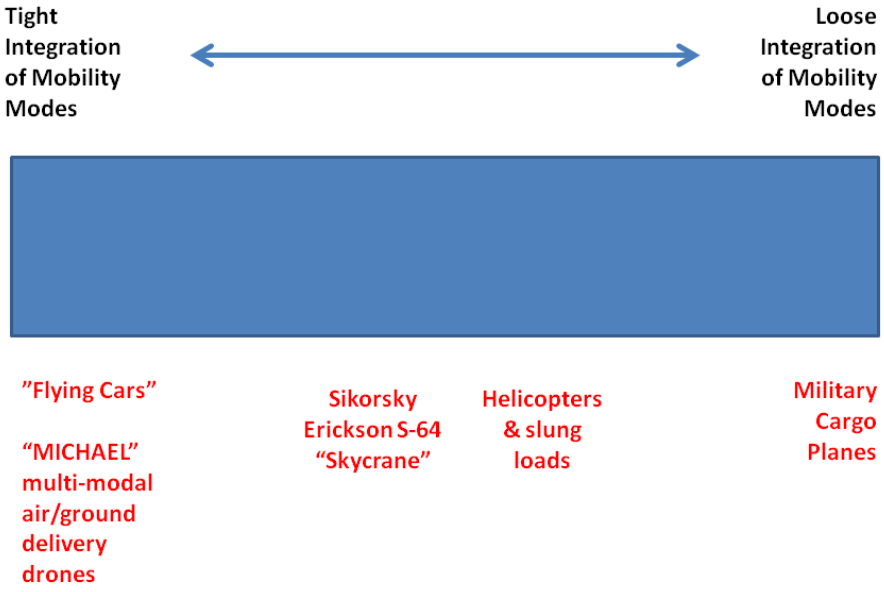

Figure 2. Tight versus Loose Integration of Mobility Modes[1]

Potential Societal Futures with respect to Mobility and Habitability

There are multiple possible societal future states that could benefit from the New Nomad multimodality mobility concept. Table 1 summarizes some of these possible future states. The New Nomad concept is not just about a class of aircraft/rotorcraft design; it is not just another possible metro/regional aerial transportation systems design (comparing it

[1] See Ref. 22, for introduction to the 'MICHAEL' air/ground delivery drone concept.

to the emerging field on air taxi, on-demand aircraft, and urban air mobility concepts being currently explored). And, though it derives insights from and draws its heritage from early studies such as Refs. 9-13, it stands apart from those other metro/regional aerial transportation system concepts. The New Nomad concept does not just seek to address the future commercial and public transportation challenges of the urban environment it instead proposes a possible approach to address a number of urban challenges: improving transportation speed and efficiency, accommodating urban expansion by opening up new boundaries, providing for affordable and readily available housing, expanding -- but reducing the cost of -- commercial properties but not at the expense of housing, providing for more urban green space and more public space, and finally potentially even redefining the whole world-view of urban, suburban, and rural communities. This is a very bold vision, and clearly it is not solely a question as to aerial transportation expertise and analysis that would be necessary to realize such a vision. Urban planners, public transportation experts, experts in robotics and telepresence, architects and automotive designers, self-driving car experts, and electric propulsion experts would all be necessary to work together to help realize this vision. But, at the same time, it is not totally implausible that something like what is envisioned is possible. Astounding semi-independent concurrent advancements are occurring in all these fields at this moment in time. Our cities need help. Our suburbs need help. Our rural communities need help. If they don't receive help, then the significant infrastructure challenges we face today could be so much worse in the not-too-distant future. Some of the future states summarized in Table 1 and discussed further below are potentially well worth exploring and perhaps one day realizing.

Table 1. Some Potential Futures Enabled by Novel Rotorcraft Concepts

#	Description
A	Improved multimodal public transportation incorporating aerial mobility
B	Evolving urban landscapes and sustainable growth
C	'Unity' networks: aerial vehicle networks that link rural communities with urban centers
D	Evolving suburbs and improved regional/urban balance of resources and costs
E	'Pogo' networks: high-speed rail or bus network analog
F	Enabling techno-nomadic communities
G	Symbiotic robotic ecosystems existing to support humanity

Note the above future states are almost divided equally between the evolution or development of aerial mobility infrastructure capabilities (i.e., systems and networks) and novel utility or usage of that infrastructure to affect some sort of population lifestyle change or evolutions. I.e., the above list is almost equally divided between 'capability' and 'utility.'

Improved multimodal public transportation incorporating aerial mobility. Many researchers and aircraft developers are considering and, in some cases, actively working towards developing the capability of metro/regional aerial transportations systems. Such efforts are currently oftentimes described as eVTOL, urban air mobility, or advanced air mobility. The novelty of the New Nomad concept with respect to this other body of work: the New Nomad concept not only allows for the transport of passengers and small cargo, but it is integral to the concept to transport 'habitat modules' to change not only *where* people work and live but *how* they work and live. Considering both short- and long-range aerial mobility options should be part of the considerations of potentially realizing this future capability. But equally important to realizing this future capability is considering a complete set of multimodal mobility options and their interplay with each other. Advanced ground transportation is just as important to realizing this future capability as aerial transportation systems. New approaches in the form of architectural and urban planning advances – how to use habitat modules and integrate into residential and commercial properties – will also be essential to be defined.

Evolving urban landscapes and sustainable growth. What if urban landscapes could be transformed over the periods of months, weeks, or even days to address evolving community needs? What if this were made possible by the development of new forms of multimodal mobility systems, especially aerial transportation networks. This kind of future state could be enabled by an expansion in capability of metro/regional aerial transportation systems and multimodal mobility networks – including advances in self-driving cars – that are being pursued currently. That expansion consists of including 'habitat modules' as a part of the cargo being anticipated as being transported by means of the proposed autonomous multimodal mobility systems. Short- and long-range aerial mobility options are a key part of the considerations of realizing this future utility.

'Unity' networks: aerial vehicle networks that link rural communities with urban centers. Such networks, through a combination of CTOL, VSTOL, and VTOL electric-propulsion vehicles encompassing moderate-sized passenger-carrying or cargo-carrying vehicles and small aerial robots, would increase regional economic strength as well as improving connectivity with nearby urban centers. An example of the criticality of this need is emergency hospital services for rural communities who no longer have local hospitals. The unity network concept is a natural follow-on to metro/regional aerial transportation network concepts being explored in this work and other parallel ongoing research efforts.

Evolving suburbs and improved regional/urban balance of resources and costs. The potential evolution of the suburban and near-rural community is the possible consequence of developing New Nomad urban and Unity suburban/rural networks. It is not possible to have healthy (in terms of economic strength and adequacy and efficiency of distribution of public services) cities and unhealthy suburbs or unhealthy adjacent rural communities, or vice versa. It is a united we stand or united we fall situation with regards of improved regional/urban balances of resources and costs. Accordingly, one of the key fallouts of the development of notional New Nomad and Unity networks is the potential achievement of

such an improved economic and stand-of-living balance throughout a regional area. The end goal should be to improve the livability of cities and communities.

Architecting our coastal waters: the implications of aviation to enable coastal water infrastructure including possible 'floating cities' accessed and supported by amphibious aircraft and vertical lift vehicles. For example, if the waters do rise significantly because of climate change, then what are our coastal cities of the future going to look like? Alternatively, population pressures may force the expansion of large urban city boundaries by expanding into the near-adjacent waters of their waterfront boundaries.

'Pogo' networks: high-speed rail or bus network analog ('Pony Express' for all-electric VTOL/VSTOL vehicles). Overlay a linear network of vertiport charging stations for all-electric VTOL/VSTOL vehicles over rail and freeways. This would balance vehicle per-charge range with a modest number of large rail-station-like vertiports/charging stations. Developing regional electric-propulsion vehicles is worthy of research but, likely, such longer-range vehicles will be hybrid-electric in nature. This will reduce their carbon-footprint by some modest amount but will not have the payoff of all-electric vehicles. The only way to have longer-range all-electric vehicles is to string together pogo-like hops (conceptually not literally) with moderately frequent recharging. This is a larger research goal that is partly addressed in a small way as the third key focus of this report as a consideration of longer-range aerial mobility options.

Enabling techno-nomadic communities for the mid-twenty-first century through new modes of societal mobility, including vertical lift aerial vehicles. The creation and evolution of techno-nomadic communities may be the consequence of developing New Nomad, Unity, and Pogo aerial transportation networks. And, obviously, this notional future state is the focus of this report.

Symbiotic robotic ecosystems existing to support humanity. Harmonious intersections between aerial transport directly supporting humankind augmented by aerial (and other modalities) robotics supporting a sustainable world. Advances in small and large autonomous aerial vehicles – whether small delivery, or cargo-carrying, or passenger-transporting – will all have to coexist in an aerial transportation ecosystem that will be driven by advances in artificial intelligence, machine learning, advanced avionics and electric propulsions systems, and robotic technologies and systems. Our world is under considerable strain right now. Climate change, coupled with a continuing loss of biodiversity, the environmental and personal losses of human overpopulation, the substantial increases seen in natural and human-created disasters are all potentially addressable through a rethinking of the role of aviation in addressing such problems.

Some past work has already begun to consider symbiotic aerial robotic ecosystems (e.g., Refs. 1-8, 21-22). And there has been precursor work looking into metro/regional aerial transportation systems (e.g., Refs. 9-11, 20). There has even been some early work directed towards coastal/littoral water hybrid aerial and water mobility transportation systems (Ref. 12-13). However, here are still many of the above future world scenarios – and the aerial transportation systems that might enable those future scenarios that are well

beyond the scope of the current study. This includes the above noted 'Unity' and 'Pogo' network concepts; these will need to be explored in future work.

There are already many (beneficial and not-so-beneficial) analogs to many of these potential future states. For example, recreational vehicles (RV) and (automotive towed or transported) campers have existed for decades. "Tiny houses" are relative recent phenomena; in many, cases these 'tiny houses' are also frequently towed/transported by automobiles. RV, campers, and mobile parks have existed as well for decades though arguably they are at a nadir currently. Parking structures have become ubiquitous in recent years (it doesn't take a great leap of imagination to see parking structures evolve towards supporting 'habitat modules' supporting office work or being used as housing as described in this report). Unfortunately, a negative analog that has appeared over the past couple of decades has been the appearance of homeless encampments. The fundamental challenge, other than the technological ones, is to ensure that the overall consequences of the New Nomad concept, if one day realized in some form, are positive ones for society. At its core, the New Nomad concept is partly motivated by the observation that modern urban and suburban landscapes are dominated by a considerable amount of wasted real estate space. Too many unused commercial parking structures and parking lots during noncommercial hours of operation. Too much roadway that never really addresses ground traffic congestion. Single use infrastructure contributes to the problem; multi-purpose use infrastructure may be part of the solution. The New Nomad concept, or some similar approach, might well address these urban planning problems through a multimodal transportation solution, with a significant urban aerial transportation component.

A Spectrum of Notional Mission Scenarios

The essential propositions of the New Nomad network concept are twofold: first, advanced transportation system networks – in addition to passengers and general commercial cargo – might also transport 'habitat modules' that, in turn, might redefine how people work, commute, and otherwise live in urban areas in the future; second, by potentially merging mobility/transportation and habitation concepts in one system-of-systems architecture for metropolitan regions could possibly enable urban planning initiatives that reduce housing costs, increase green space and public space, and improve the distribution of services and lifestyle benefits of citizens and visitors. To help rotorcraft and aerospace engineers and technologists better appreciate the scope of the engineering challenges inherent in developing short- and long-range aerial mobility options for cargo-carrying aircraft to transport one or more habitat modules in the range of thousands of pounds of weight, while emphasizing vehicle automation/autonomy and all- or hybrid-electric-propulsion in the vehicle designs. Some of these notional mission scenarios are summarized in Table 2. Further, these Table 2 notional mission scenarios are intended to be traceable from the Table 1 potential future states in which metro/regional aerial transportation system networks might support their realization.

Table 2. Notional Mission Scenario Descriptions

Scenario #	Name	Description
1	Commuting	Habitat is relocatable office space. Aerial transport could be an element of habitat transport, but other transportation modalities could be more predominant. Habitat moved to the work site and then back once a day.
2	Weekending	Habitat module is primarily as a temporary habitation or living space for recreation or vacationing. Habitat module would need to be potentially transportable either by short- or long-range aerial mobility vehicles and/or other multimodal ground/water mobility options.
3	Event-driven relocation	Habitat module is primarily as a temporary habitation or living space for short-stay durations to support attendance at events. Habitat module would need to be potentially transportable either by short- or long-range aerial mobility vehicles and/or other multimodal ground/water mobility options.
4	Temporary/short-term (days-long stays) relocation	Habitat modules support business and/or recreational activities that span several days. Habitat module would likely not be considered a primary residence. Habitat modules would have to be transportable short and long ranges by multimodal mobility platforms, including possibly aerial transport.
5	Moderate-duration (weeks-long stays) relocation	Habitat modules support business and/or recreational activities that span several weeks. Habitat module might then singularly, or an aggregate sense if multiple modules were employed/owned, be considered a primary residence. Habitat modules would have to be transportable short and long ranges by multimodal mobility platforms, including possibly aerial transport.
6	"Seasonal"/lifestyle-change (months-long stays) relocation	Habitat modules would likely be de facto residences, singularly or in aggregate sense. Habitat modules would have to be transportable short and long ranges by multimodal mobility platforms, including possibly aerial transport.
7	Nomadic (frequent, impromptu, variable duration stays and departures)	Habitat modules would likely be de facto residences, singularly or in aggregate sense. Stays would likely be of variable duration with great frequency. Entire communities might form and dissolve because ephemeral dictates. Habitat modules would have to be transportable short and long ranges by multimodal mobility platforms, including possibly aerial transport.

The Table 2 notional mission scenarios represent a spectrum of evolving mission capabilities. In each progressive scenario the capabilities of the vehicles and network increase and become more complex. Ultimately, the mission scenarios begin to expand beyond the urban environment, to the regional, and then potential to become national in scope. In all these mission scenarios, the viewpoint of aerial vehicles as merely part of some overall transportation system evolves to one in which the population's day-to-day living patterns and social behavior have been transformed by such vehicles.

Table 3. Anticipated Mobility/Habitability Requirements

Scenario #	Automotive	Rail	Water (mobile)	Water (stationary)	Air Short/range	Air Long-range	Office	Domicile habitation
1	X				X		X	X
2	X	X	X	X		X		X
3	X	X				X		X
4	X	X	X	X	X	X	X	X
5	X	X	X	X	X	X	X	X
6	X	X	X	X	X	X	X	X
7	X	X	X	X	X	X	X	X

Note: In the above table, these are not exhaustive scenarios and, further, may not exhaustively identify all possible mobility modality options or habitation options. Further, building-in both office and domicile habitation capabilities into a given habitat module potentially allows for the expansion of off-hours (especially late evening/early morning) commuting, especially by self-driving automotive tugs. 'Sleep-to-work' might be a viable approach to reduce roadway congestion – and/or reduce evening/morning aerial vehicle overflights and attendant noise.

A Variety of Mobility/Habitat Concepts

The concept of a "camper" or, rather, a 'habitat module' and its multimodal transportation considerations and implications will be discussed in the next section of the report. The habitat module is essentially at the core of the New Nomad network concept.

The following as a list of possible "New Nomad" (NN) scenarios/storyboards and associated graphics that will be introduced later in this report:

1. "Camper" (aka 'habitat module') being towed by an autonomous tug/ground-vehicle.
2. Camper parked at or integrated/grafted onto a residential home.
3. Camper parked at or integrated/grafted onto a commercial property/office-building.
4. Camper being aerially transported by a "skycrane" like rotorcraft for short urban environment hops.
5. Camper being transported by a specialized cargo plane for long distances.
6. Camper being placed/transported on rail service transporters.
7. Large-scale semi-organized landscape of campers for temporary communities.
8. Temporary "houseboat" lake and/or ocean communities.

Mobility/Vehicle-System Concepts

Several approaches will now be discussed as to ground- and/or surface-mobility of habitat modules in relation to being operated independently of the air-mobility capability of the utility carrier-platform flight vehicle. Automotive/ground mobility options will be discussed, followed by a brief discussion of water-surface mobility options. Additionally, some of the aerial mobility considerations of the utility carrier-platform flight vehicle will be discussed, primarily in terms of short-range and long-range aerial mobility.

Automotive/Ground Mobility

Of the possible automotive/ground mobility options that might be considered, those options include: towing of the habitat by a ground vehicle acting as a 'tug;' a palletized approach to lifting up and placing on a large flatbed of a ground transport vehicle; self-driving/self-propelled habitats.

Towed:

An example illustration of a towed habitat module behind a small notional autonomous 'tug' ground vehicle is shown in Fig. 3. The configuration shown in Fig. 3 is not the only approach for such a towed vehicle but is merely presented as one notional approach.

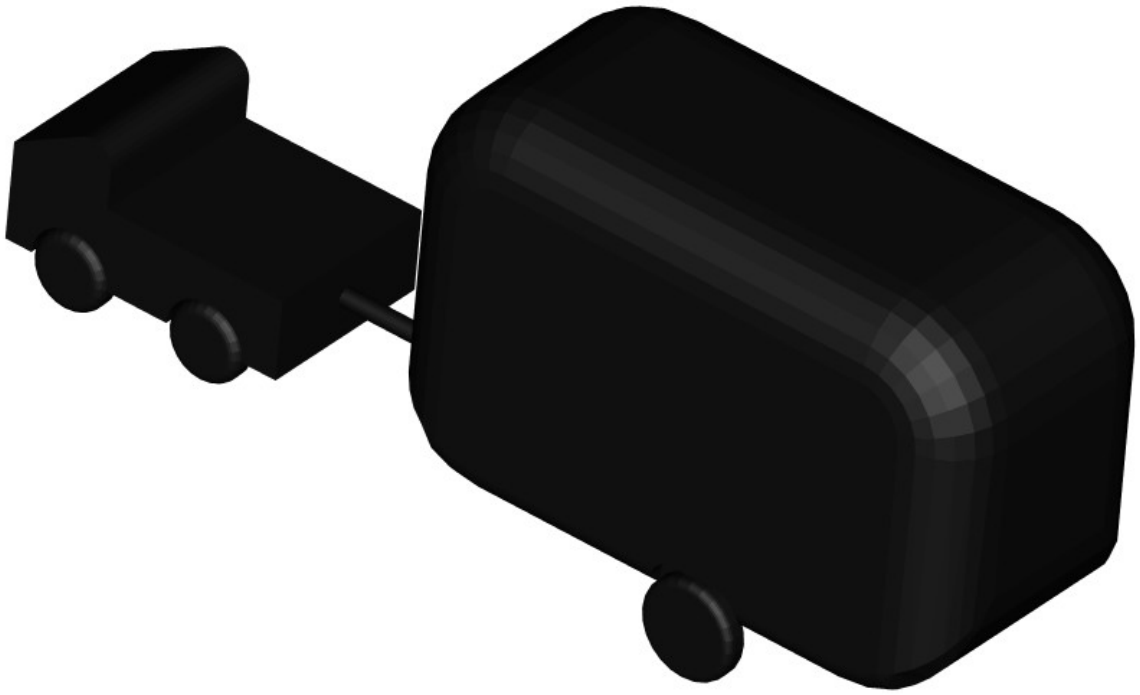

Figure 3. Autonomous automotive tug for a towed habitat

Note from an energy consumption perspective, for a towed camper-like habitat, it is advantageous to make the habitat as lightweight as possible. This is especially true if an NN aerial vehicle transport component of habitat conveyance is to be realized. This means that the proposed habitats might only be a fraction of the weight of current (solely automotive towed) campers. The difficulty of making such camper-like habitats very lightweight is that the habitats might then suffer from tendencies to roll-over under high crosswinds while being towed. Creative application of aerodynamic subsystems such as spoilers, strakes, and other concepts to mitigate roll-over aerodynamic moments will need to be devised to allow the transport of very lightweight habitat structures. Similarly, in areas of the country plagued by high-winds and other severe atmospheric events, even stationary vehicles might be subject to large aerodynamic roll-over moment and, this too, needs to be carefully considered in the development of such habitats.

Ideally, such vehicles must be capable of being autonomously towed/transported by the various transport modalities while being occupied. This, of course, raises several crucial safety considerations that will have to be addressed in the overall system architecture design as well as the individual safety systems onboard the habitats. This will in turn require reexamining governmental transportation system regulations. For example, a habitat might be transported in the early morning, or evening, (during off-commuter hours) with the habitat occupant(s) potentially asleep to arrive at the business work site (and with the habitat interior subsequently converting in a semi-automated fashion into a workspace versus its prior living-space configuration. Off-hour transport, while not inconveniencing the sleep patterns of the occupant/commuter, could lead to reduced trip time, commute hour freeway/roadway congestion, and overall commute energy expenditure. Note that currently the automotive transport of people in towed trailers/campers is not legal in many states; it is plausible, though, that this might be reconsidered in the future if adequate safety provisions could be provided for occupants of such trailers/campers while being towed.

Another nontrivial automation challenge to consider is the loading and unloading of habitat modules onto/into the New Nomad aerial vehicles while on the ground prior to flight. For example, automated winches and automated clamps or fasteners might be required to transport and attach habitat modules the final small but non-negligible between the module and the aerial vehicle. The design of such automated loading and unloading – and stowing/docking – mechanisms would clearly be impacted by tradeoffs of speed and ease of process versus safety and reliability of that same automated process.

This hybrid transportation/habitat concept places future commuting for work into a potentially emergent area of work-life nestled between long commute hours in highly congested metropolitan regions versus work solely by telework. It also tackles critical questions about providing for affordable living spaces in urban areas (especially those costs associated with housing).

There clearly is a trade between transporting one's living- and/or working-spaces everywhere in the above noted manner versus just renting transportation (rental cars/vans)

and living spaces (such as hotels, timeshare condos, or internet-enabled housing rental services).

Palletized Module on Trailer and Towed:

Habitat module weight could be kept to a bare minimum if such modules were palletized and stacked on separate trailers and towed. In this manner, module weight would not need to include reinforced lower/floor structures, nor would they need to include axles, wheels, brakes, and other such hardware. The downside of this approach is that auxiliary equipment needs to be in place at both the departure and arrival sites to load/unload the habitat modules from the trailers.

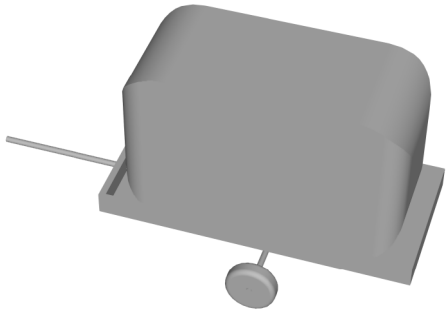

Figure 4. Palletized Module loaded/unloaded on Trailer and Towed

Figure 4 illustrates a notional shipping-container-like palletized habitat module. This palletized module could be lifted by a crane or, alternatively, lifted by a fork-lift and placed onto a flatbed trailer to be towed to a destination or intermediate waypoint/waystation. The obvious downside of this approach is the labor/effort of transferring the module on and off the flatbed trailer and the requirement of having external equipment in place to do the transfer/lifting.

Integral (Self-Mobile and Self-Controlled):

This self-mobile and self-controlled 'habitat module' is analogous to automotive-like "pod" hybrid air/ground (two-component or two-element composite systems) vehicles (e.g., Refs. 23, 55). The key difference is that the "pod" ground-mobile element has an (small) automobile-like interior whereas a self-mobile, self-controlled habitat module has an office-like interior layout or a recreational vehicle (RV) like living-space interior. Figure 5 is an illustration of such a notional self-mobile and self-controlled habitat module.

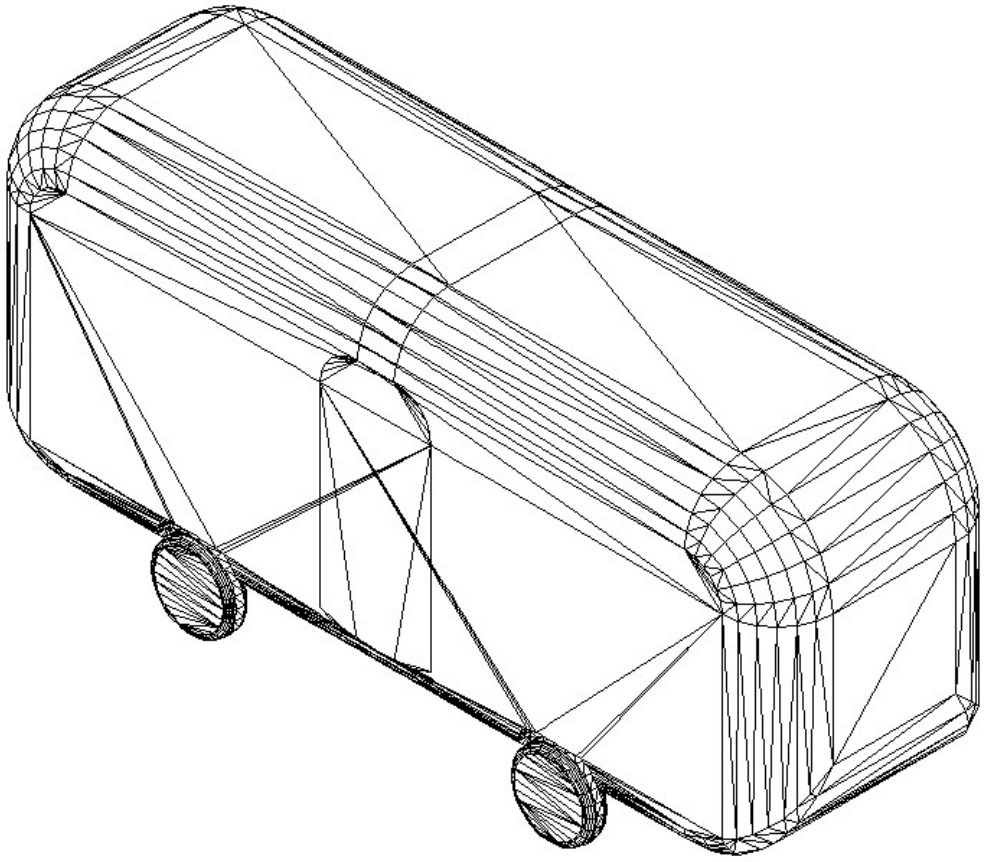

Figure 5. Self-mobile and self-controlled 'habitat module' with integral ground mobility

Networked (Physically Attached or Loosely Coordinated Convoys):

Advances in autonomous, self-driving automobiles, coupled with distributed control applications might make both physically coupled and/or very closely spaced vehicles act in concert, rather than individual modules. Figure 6 is an illustration of such a notional (physically attached) convoy (i.e., train on a freeway).

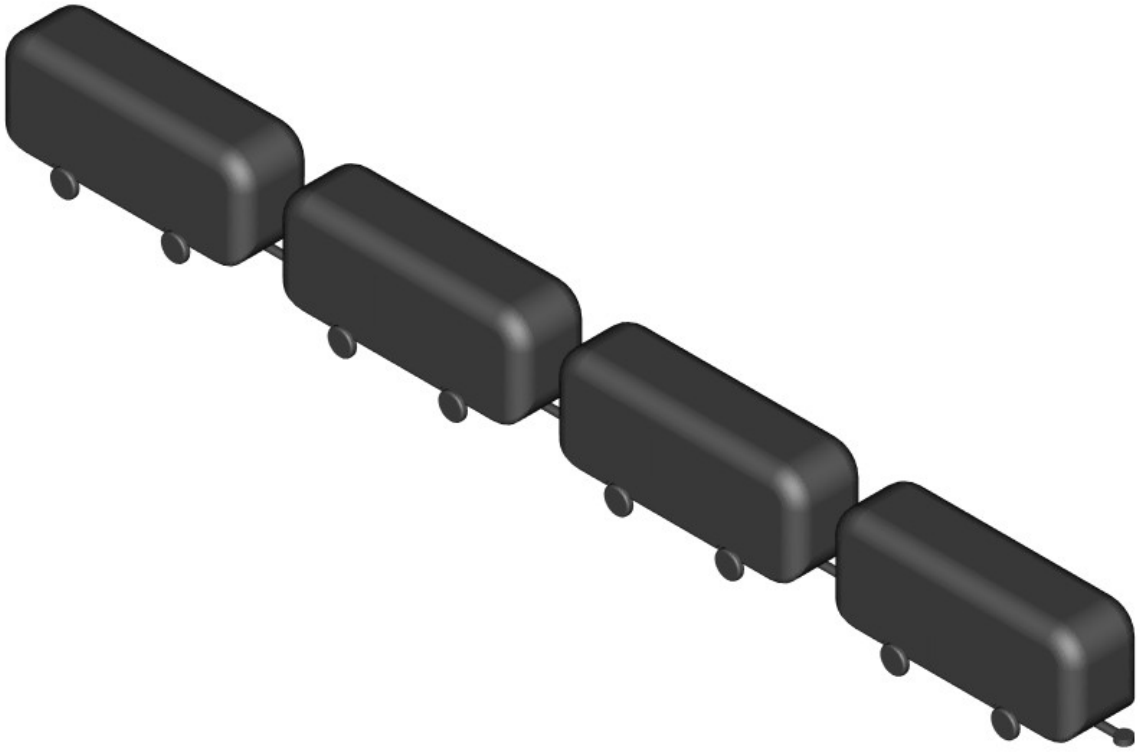

Figure 6. 'Networked' habitat modules that are physically linked together or closely coordinated (i.e., tightly spaced 'convoy')

Rail/Light Rail Mobility

Transport of cargo by railway has long been a feature of industrialized society, literally dating all the way to the invention of the steam-engine trains of the early nineteenth century. Building in the capacity to load/unload and transport large numbers of habitat modules on railway systems would potentially further enhance (efficient) ground mobility for these modules and passengers. From a total systems energy perspective, it is hard to beat the energy efficiency of rail transport. However, from a time savings perspective, roadway/automotive-like ground mobility will inevitably result in greater time savings than rail. And, of course, nothing can match the time savings inherent with aerial mobility. Figure 7 is an illustration of notional flatbed transport of habitat modules on rail cars.

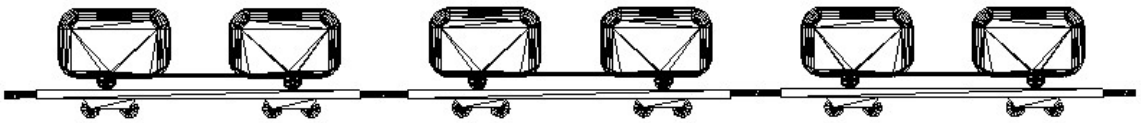

Figure 7. Habitat modules on flat-car railways

Water (stationary or mobile)

The transport of goods/cargo by watercraft dates all the way to the earliest antiquities. The use of palletized/crane-transported 'cargo containers' dates to the 1950's at least. Except for a few notable cities located on major waterways (rivers and or littoral bays/sounds), scheduled and/or demand transport of passengers to/from one urban location to another is relatively infrequent. Figure 8 is an illustration of the notional transport of habitat modules on watercraft, or a marine ferry.

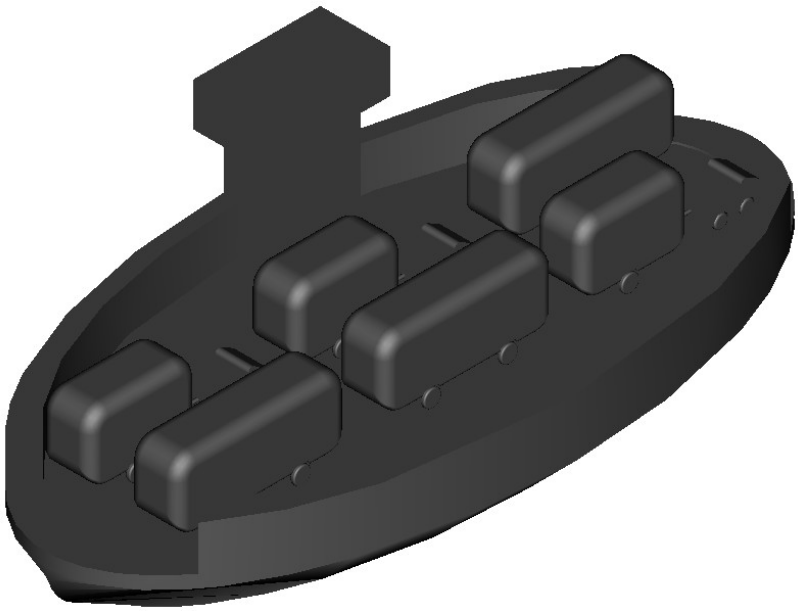

Figure 8. Water ferry transport of habitat modules

Aerial Urban/Short-Range Mobility

Rotary-wing aerial transport of cargo (either in the interior of the vehicle or by external slung loads) has been a regular application since the development of 'heavy lift' helicopters in the 1950's. This study, though, seeks to focus in on the novel and/or unique challenges of transport of office/residential habitat modules, which arguably quite different in nature than other payloads considered to date. But, on the other hand, there are also in-kind common challenges to New Nomad aerial vehicle design that are also faced by the emerging class of urban aerial mobility (UAM), aka eVTOL, aerial vehicles. Two different reference design examples for a New Nomad short-range mobility aerial vehicle will be presented, discussed, and analyzed in this study. Generic, simple CAD outer mold line (OML) drawings of the first New Nomad short-range aerial vehicle reference design, is shown in Fig. 9a-b (with and without habitat module attached to the vehicle airframe/fuselage).

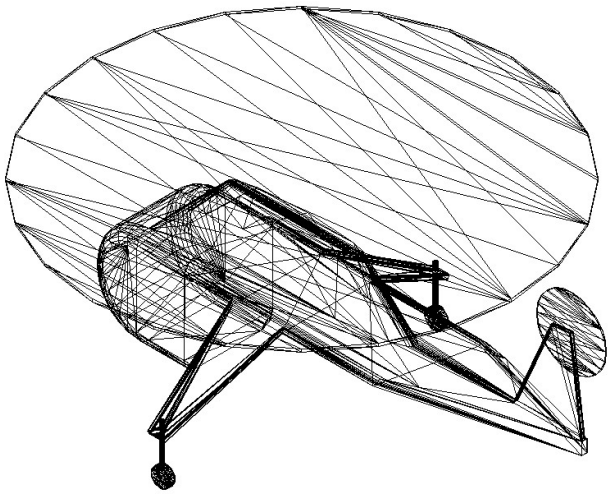

(a)

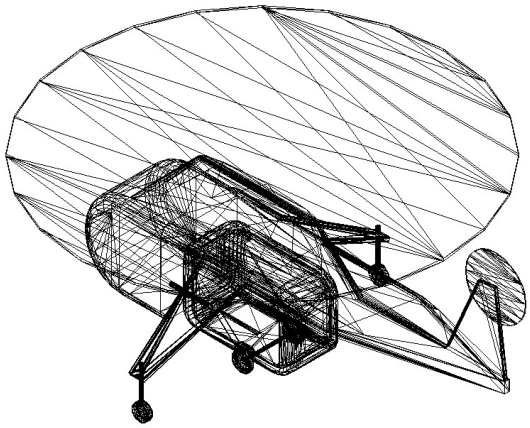

(b)

Figure 9. Aerial transporter (a) without a stowed habitat and (b) with a stowed habitat

A second short-range aerial mobility reference design will be presented later in the report. Figure 9a-b represents a more conventional single-main-rotor and tail-rotor helicopter design, where the second reference design will be a multirotor configuration more representative of some of the recent UAM and eVTOL designs being developed by industry.

The New Nomad aerial vehicle reference designs and their design/technology challenges are likely of the greatest interest to the rotorcraft research community. But, as will be seen through the discussion in this study, the aerial vehicle design challenges are intrinsically linked to the associated ground mobility, network, and habitation urban planning challenges.

The ultimate solution with respect to the transport of passengers, cargo, and habitat modules will likely consist of more than one of the above ground/air/water mobility capabilities for the urban and metropolitan regional environments. This key point is emphasized several times throughout this report.

Aerial Long-Range Mobility

The merging of transportation and habitation architectures is not just limited to short-range trips such as inter-city commuting but will also equally focus on long-range trips such as regional (city-to-city or city-to-rural-location) events or occurrences (such as for recreation or vacation travel and camping/temporary-residence.

In the case of long-range mobility, more efficient aerial transportation/conveyance will be required as compared to helicopter/vertical-lift operations. In this case, large cargo transport using conventional fixed-wing aircraft or hybrid tiltrotor/tiltwing aircraft will likely be required. Such aircraft configuration designs will be heavily influenced by the automated loading and unloading of multiple habitat modules for any given flight. Though large cargo transport aircraft are a well-explored design problem for military aircraft, developing such transport aircraft for carrying habitat modules will have their own set of design challenges.

If hybrid tiltrotor/tiltwing aircraft were developed for multiple habitat modules transportation, instead of using conventional fixed-wing cargo aircraft, then the VTOL capabilities of these vehicles would likely reduce the infrastructure and logistics footprints required to transport such habitat modules – as well as also support cargo transport – thereby enabling conveyance of these habitats to some truly remote areas on-demand.

Figure 10 depicts a notional habitat loading and unloading sequence of habitats onto a notional blended-wing-body-like (BWB) tiltrotor configuration where the central portion of the hull can slide accordion-like laterally to allow for unimpeded access to deployable ramps and a carrier floor-platform to load the habitats.

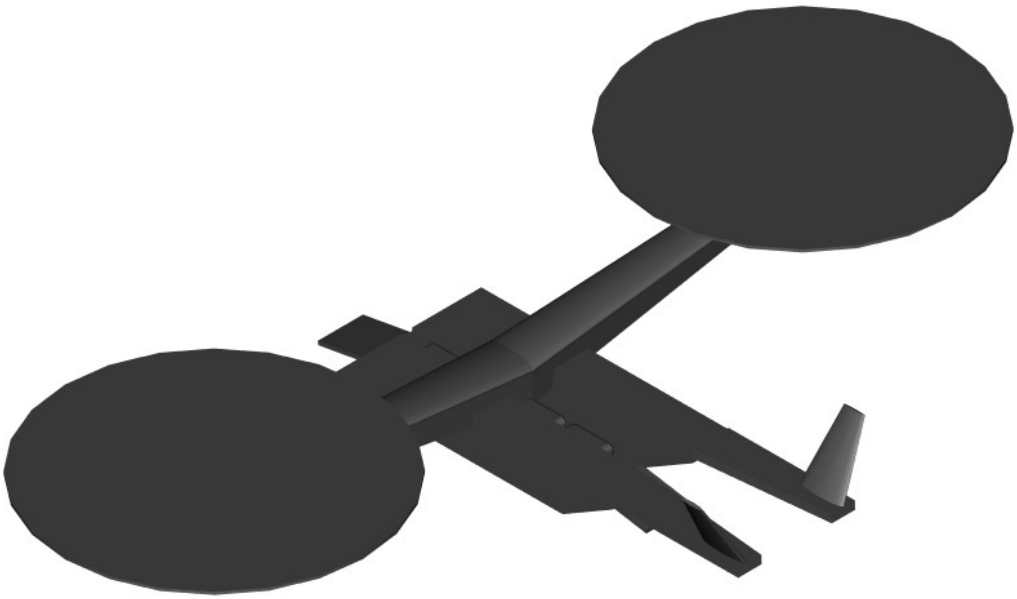

(a)

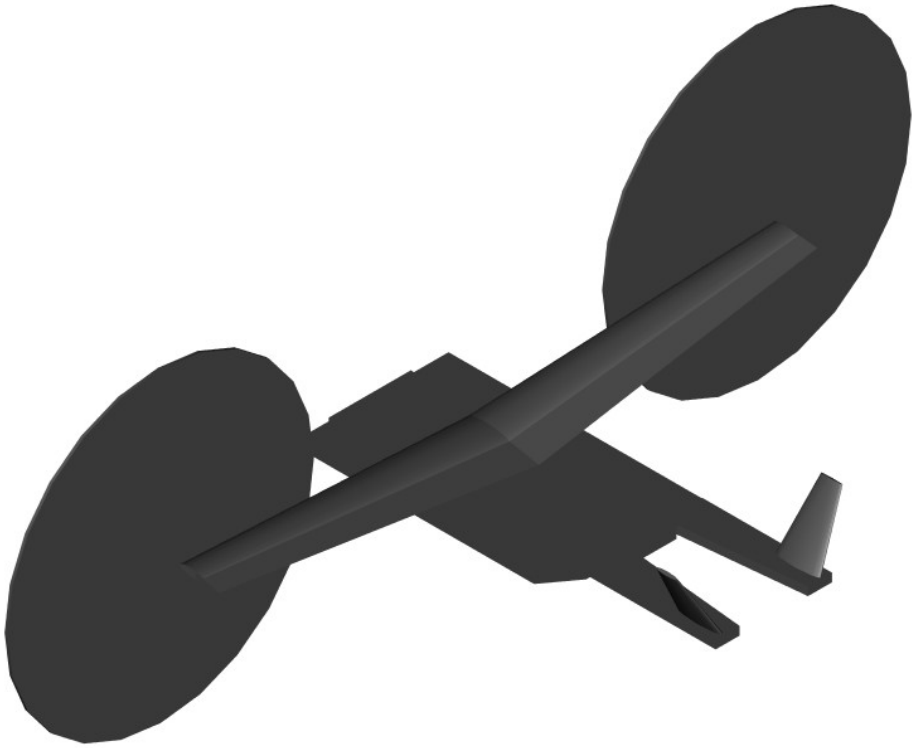

(b)

Figure 10. Long range transport of habitats: (a) loading habitat convoy onto fore- and aft-ramps on notional long-range aerial transport and (b) stowed and inflight

A BWB-tiltrotor configuration is largely unexplored to date in the literature. Although it may have advantages from a cargo-stowing perspective, there are several aerodynamic challenges that need to be faced to arrive at an aerodynamic performance efficient design. Chief among these aerodynamic challenges is the likely increase hover download of a BWB-tiltrotor versus a conventional tube-and-wing tiltrotor. An additional challenge is arriving at satisfactory lift-over-drag ratios for the vehicle in highspeed cruise, which will likely be more challenging to achieve than that for tube-and-wing conventional tiltrotor configurations. Nonetheless, this study uses the BWB-tiltrotor configuration as a baseline reference design for all the discussion in this report related to long-range aerial mobility to support regional New Nomad transport to and from the urban centers to outlying areas. Other, alternate, long range NN aerial vehicle configurations could be explored in future work; the BWB configuration explored in this report should not be considered the 'best' configuration for this mission application.

Habitat/Habitability Concepts

There is nothing new about automotive transport of habitats in the form of truck camper shells, towed campers and/or 'tiny houses, vans with built-in living spaces, or large bus-style recreational vehicles (RV's). What is perhaps new is to suggest that: (1) aerial transportation might be an important component of such habitat conveyance; (2) such habitats could be tailored to be not only occasional recreational assets but essential contributors to residential and commercial office architectures for both daily commutes and providing simultaneously for business work- and living-space needs for the metropolitan regions of the future; (3) finally, autonomous system technologies in the form of automated automotive and other transport-modes could provide for the efficient, safe, timely, and low-energy transport of these notional habitat modules (autonomous automotive tugs so to speak).

Stand-alone "Camper" like Habitat

The habitat modules discussed in this report can all claim some heritage with respect to automobile-towed campers, trailers, and (RV) recreational vehicles. And, yet, despite that heritage, there are unique challenges to arrive at lightweight but structurally robust (for both air and ground mobility) module as well as the additional unique design challenges of trying to not have standalone/independent modules but to seek to integrate these modules cohesively in a synergistic fashion with other habitat modules and fixed/semipermanent

architectural structures. It is only in this manner that a true transportation and habitation architecture can be achieved that potentially leads to new paradigms for urban planning and living. Figure 11 illustrates a notional stand-alone (not being integrated with other residential/commercial architectural structures) habitat module.

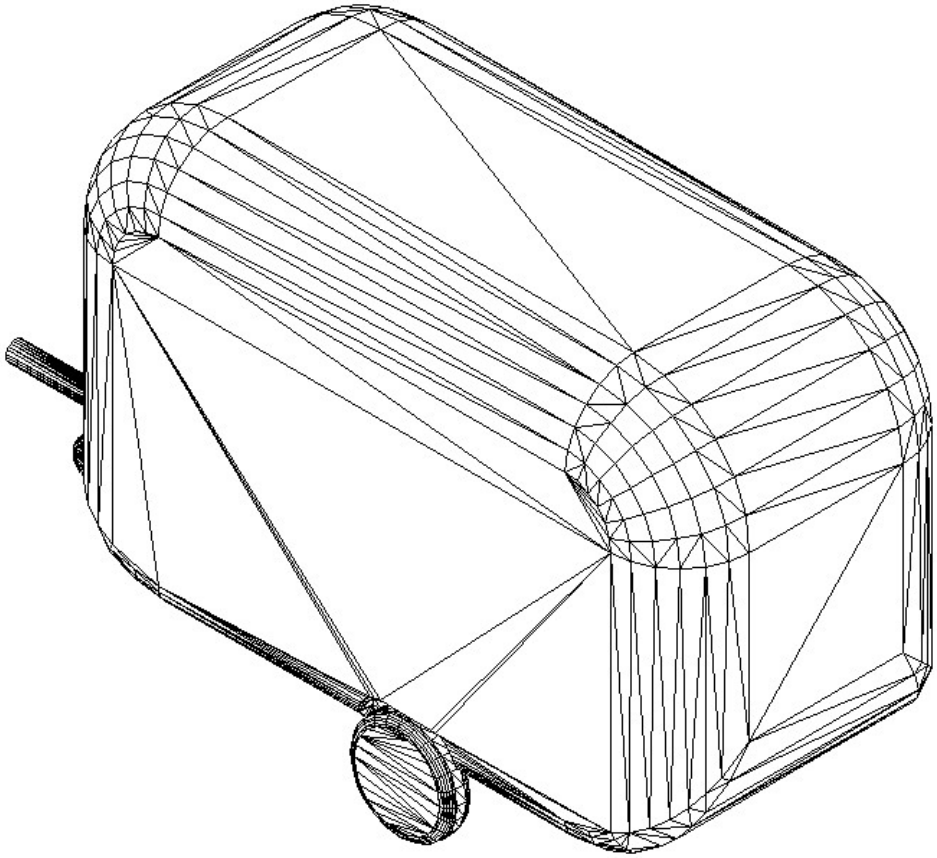

Figure 11. Stand-alone Camper-like Habitat Module

Plug-n-play Habitat Modules

As briefly mentioned earlier, one cannot merely consider the standalone design features of a given habitat module design, but rather one must also consider how to integrate such modules into fixed/semipermanent architectural structures. The next couple of subsections of the report will discuss this module/architectural integration in more detail. Figure 12 notionally reflects several different module/architecture integration approaches.

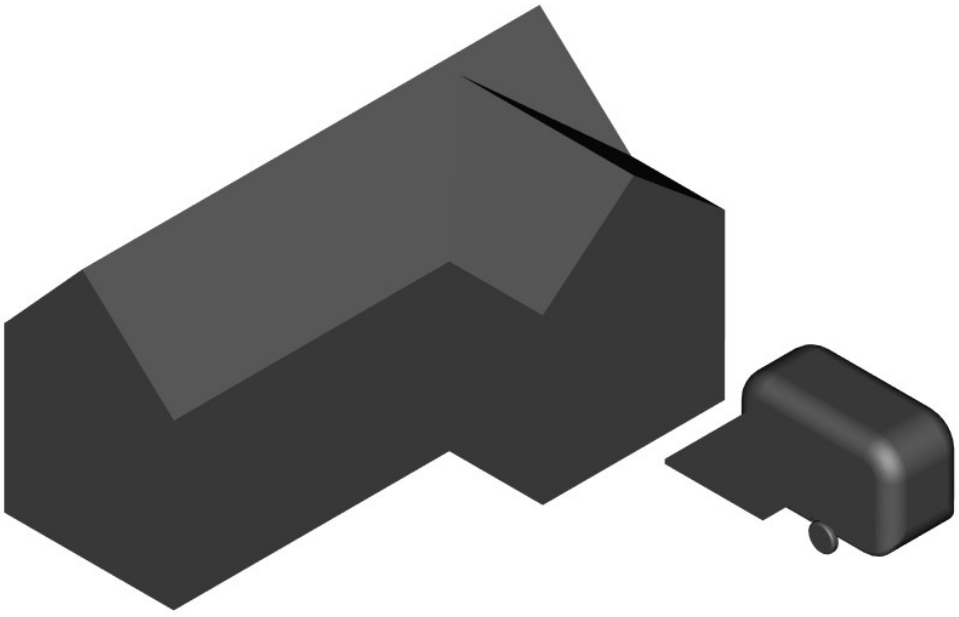

(a)

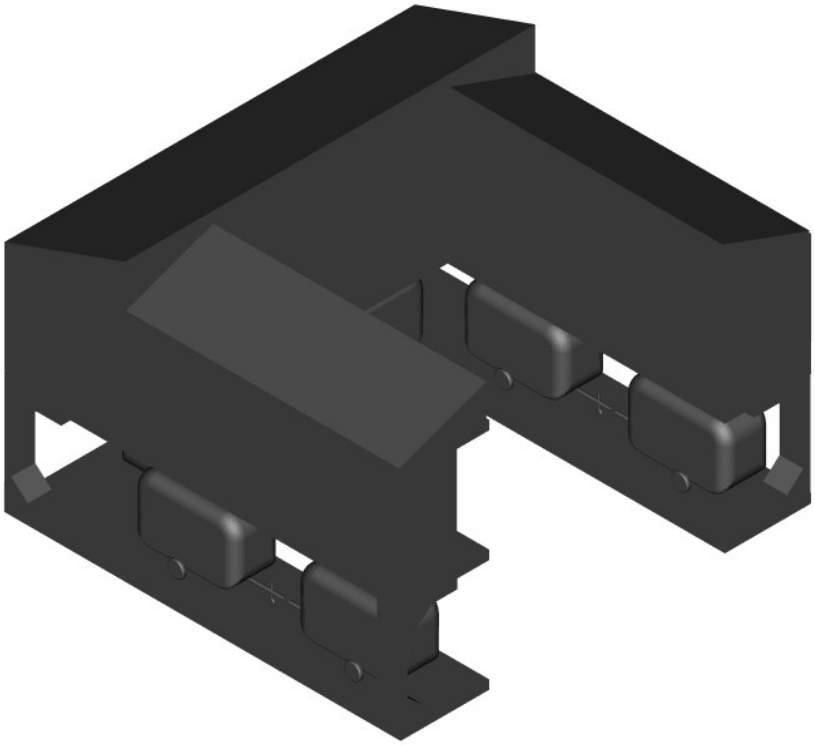

(b)

Figure 12. Habitat Modules: (a) simple integration with conventional residence ('parking strip') and (b) full plug-and-play reconfigurable (multiple) habitat modules ('carports')

More challenging perhaps would be achieving module/architectural integration for commercial buildings (where the modules serve as physically transportable offices). Figure 13 presents one notional concept for such habitat module integration into commercial buildings.

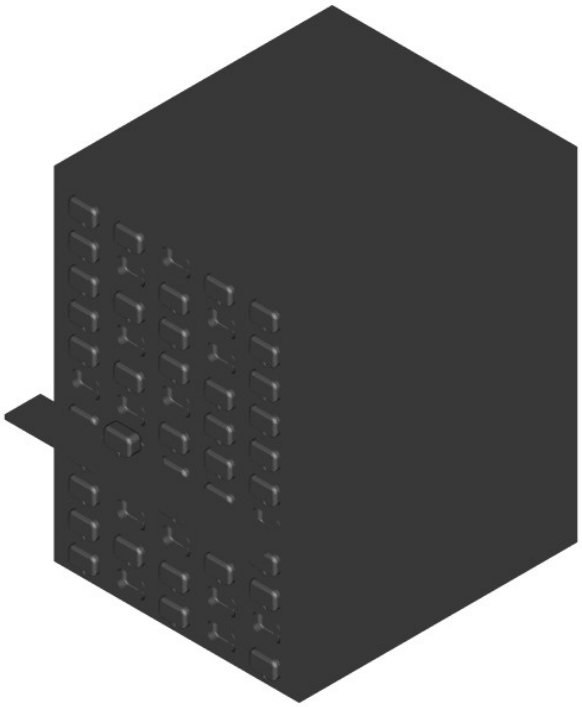

(a)

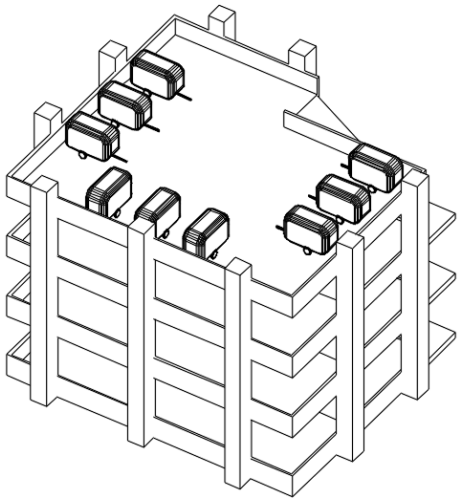

(b)

Figure 13. Habitat modules: redesigning (a) office complexes or (b) commercial parking structures

There is the potential to use modified parking structures, as shown in Fig. 13b, as places to load and unload habitat modules for adaptive housing and or commercial office complexes.

Networked/Community Habitats

The proposed transportation and habitation architectural enabled by rotary-wing aerial vehicles could also potentially enable a renaissance of networked communities. Many motorhome and mobile-home parks have been lost over the years to more conventional apartment complexes and single-family residences, but proposed transportation and habitation architecture could catalyze a renewal of such networked communities. This also possibly holds true for marinas and houseboat communities as well. Figures 14a-c and 15a-b notionally illustrate some of these renewed/reimagined networked communities that could be enabled by habitat modules transported by ground/air/water mobility systems.

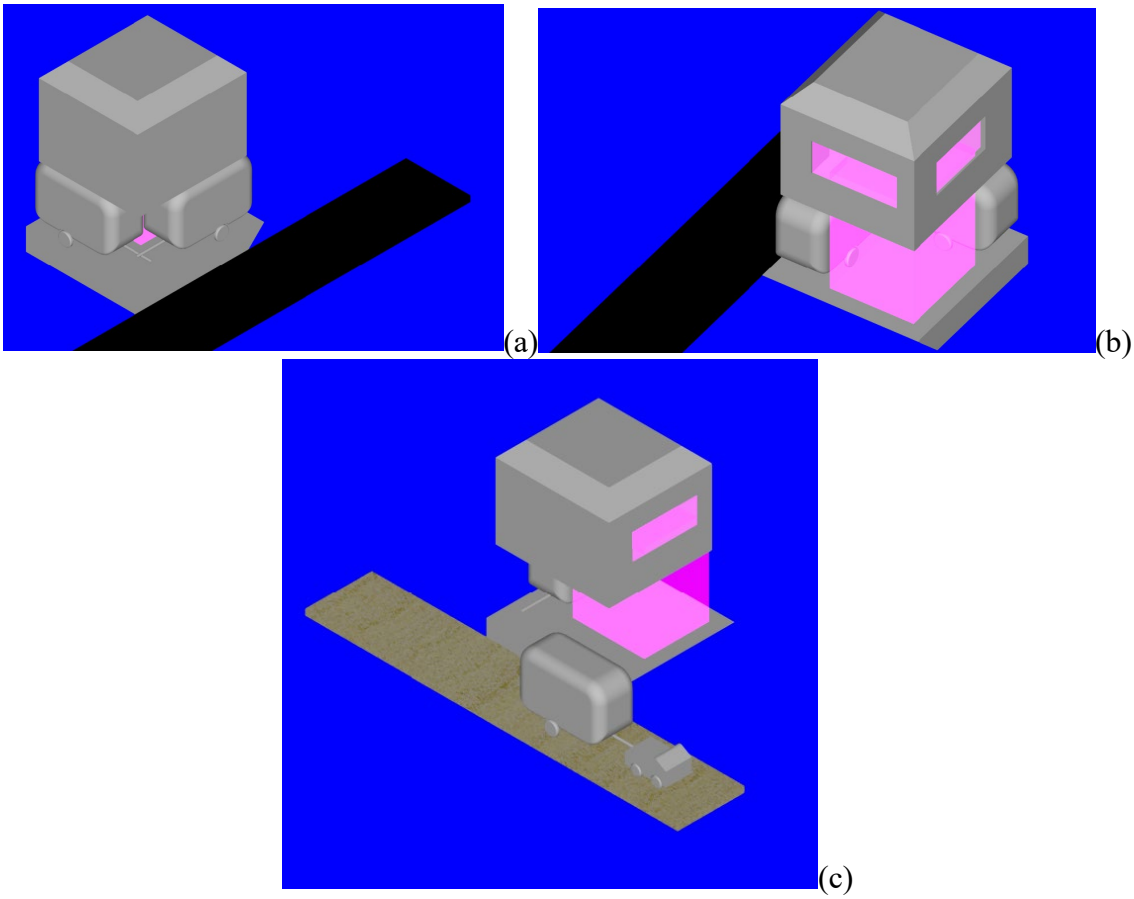

(a) (b) (c)

Figure 14. Marina/Houseboat Communities: (a-c) different isometric views of a houseboat' and an adjacent dock incorporating NN habitat modules as well as showing modules being towed by automated tugs

Figure 15a-b are illustrations of a residential-neighborhood-style networked community employing, in part, NN habitat modules.

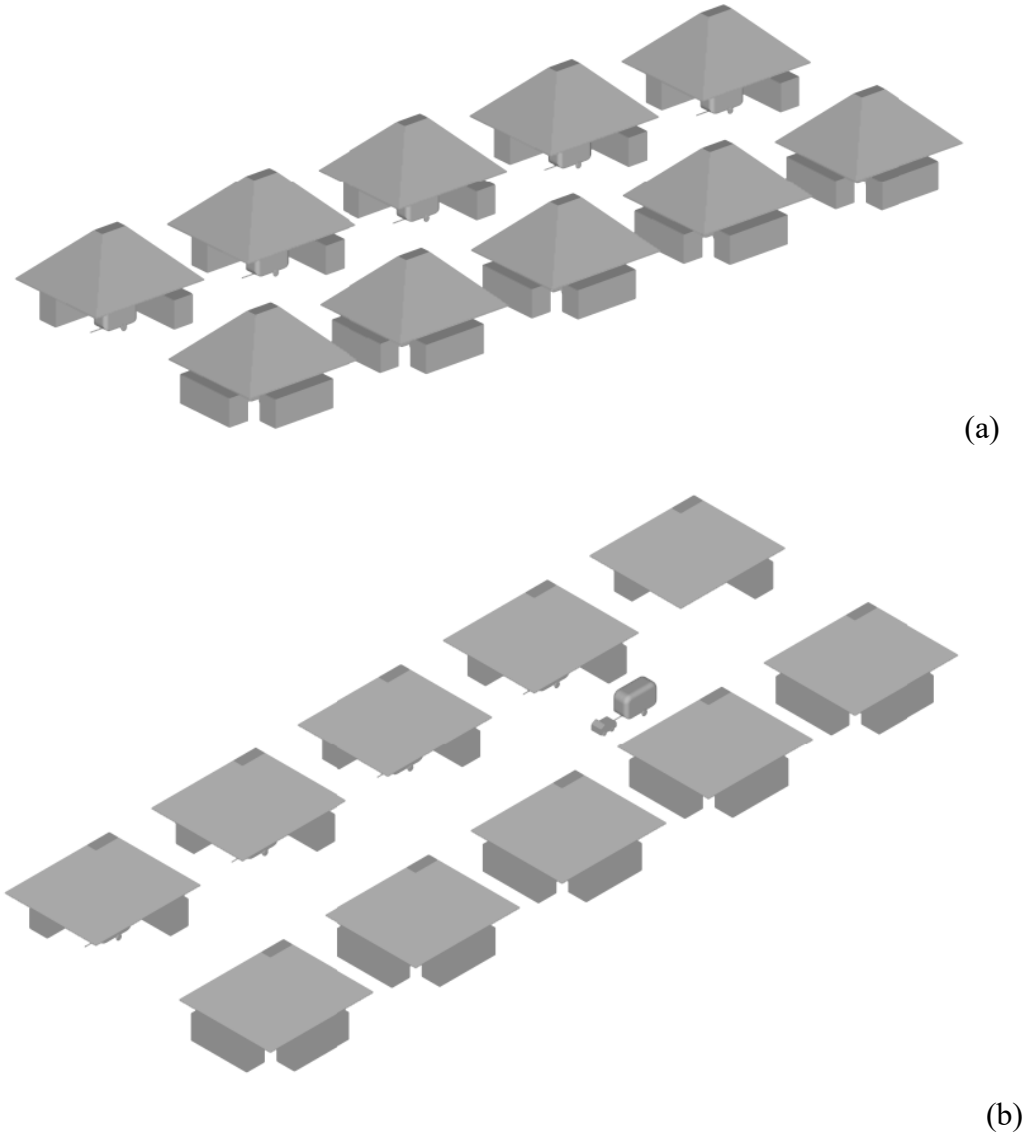

(a)

(b)

Figure 15. Small networks of temporary or adaptive communities through use of habitat modules transported by ground/air/water mobility: (a) isometric view of residential homes incorporating NN habitat modules and (b) residential homes and NN habitat module on the 'street' being towed by an automated tug

Aerial Urban/Short-Range Mobility Aerodynamic Performance Analysis

Figure 16a-b represent two distinctly different short-range aerial vehicle mission profiles. Figure 16a assumes that the habitat module is transported via ground mobility (such as by an automated tug) to a vertiport for loading onto an aerial vehicle and then the subsequent aerial mobility transport to a second vertiport for unloading and follow-on ground transport to the destination. This vertiport-to-vertiport mission profile is more consistent with mission profiles supporting scheduled multi-modal public-transportation-like networks. Figure 16b, however, represents a more on-demand and (near) anywhere aerial transportation of habitat modules and passengers. In this notional mission profile, a more on-demand and from (near) anywhere short-range aerial transport mission is assumed. This short-range mission profile will be used later in the study to perform some first-order single-main-rotor rotorcraft sizing analysis; this sizing analysis will be performed to give an initial assessment of the dependency of aerial vehicle size and gross weight on the habitat model size/weight.

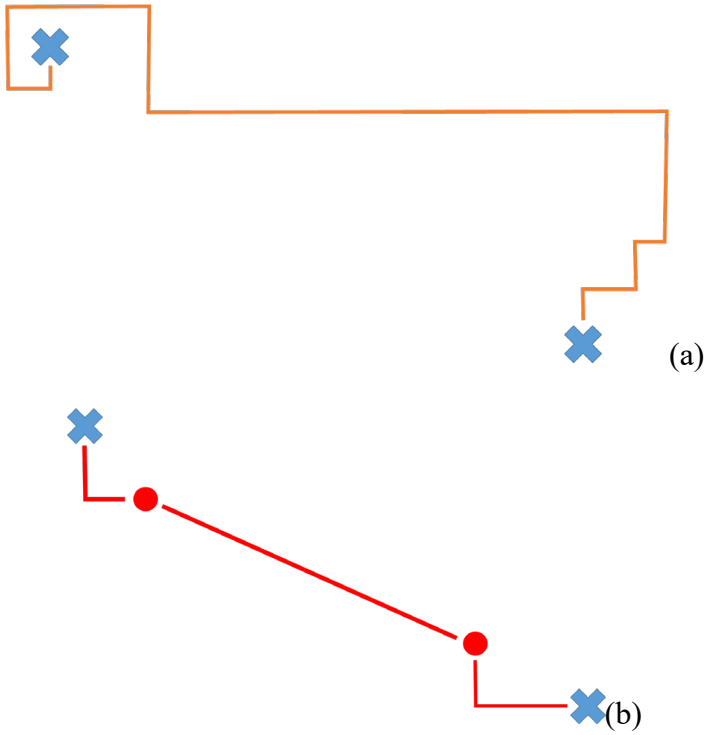

Figure 16. Competing Mission Profiles: (a) ground mobility only and (b) short-range aerial and ground mobility

A key system-of-systems design challenge for any type of urban air mobility network/system (including a New Nomad type system) is providing for a spectrum of vertiports (in terms of capability) for the rotary-wing aerial vehicles to vertically takeoff and land from. These vertiports can range from a simple cleared pavement space to more elaborate transportation centers/hubs. Figures 17 and 18 illustrate some of the more elaborate transportation center/hub vertiports that might be employed; additionally, Figs. 17 and 18 illustrate that there will inevitably be design challenges associated with safely taking off and landing of such vehicles while protecting structures, property, and people from high noise and high rotor outwash velocities. In the end, it doesn't matter how well designed and efficient the aerial vehicles are if they cannot take off and land where the demand is.

A considerable amount of the discussion that follows in this report focuses on the challenges of vertiport siting and New Nomad aerial vehicle operation in the urban environment (both in the air and on the (near-) ground).

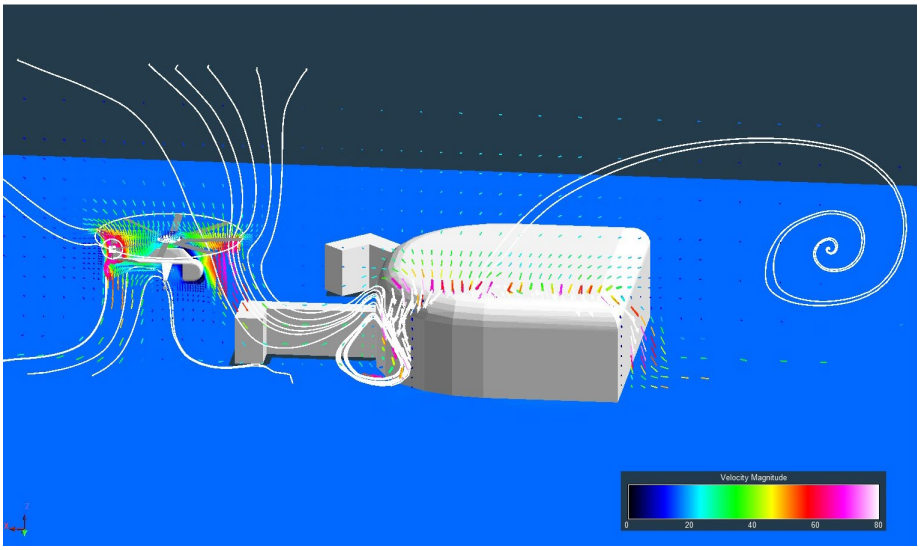

Figure 17. Short-range aerial vehicle hovering near vertiport (vertiport representative of that studied in Ref. 40)

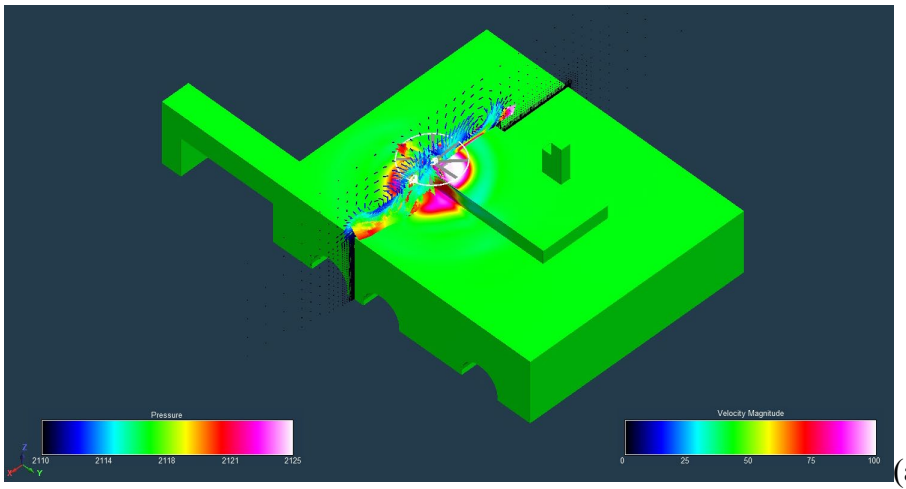

(a)

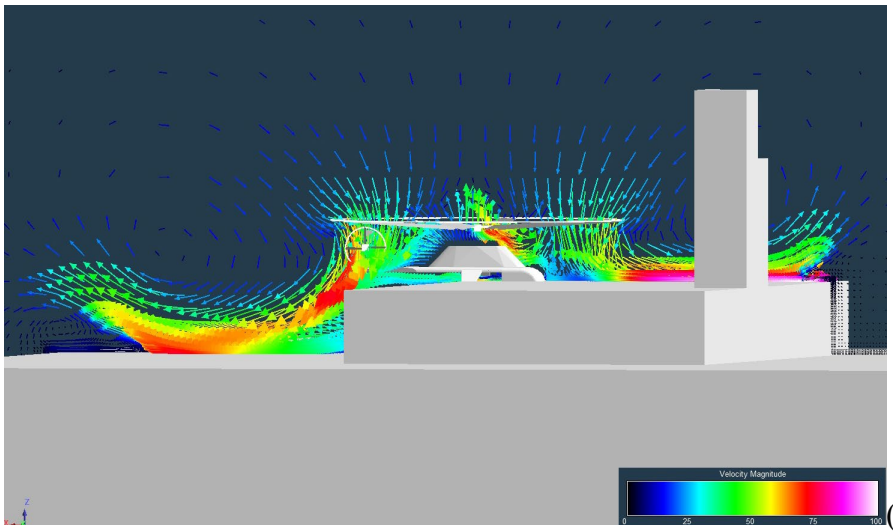

(b)

Figure 18. Short-range aerial vehicle hovering (CFD predictions of rotor wakes) near alternate vertiport (vertiport representative of that studied in Ref. 9): (a) top view and (b) side view

In addition to considering the rotor outwash implications at vertiports, it is also important to consider outwash effects stemming from low-level flight over, and takeoff and landing near non-vertiport buildings, vehicles, and other ground-based property. Figure 19a-c presents velocity magnitude isosurfaces of the rotor wake propagating downwards towards a passenger ferry from the single-main-rotor NN short-range aerial mobility vehicle reference design flying low alongside the water vessel. Many urban environments are close to waterways (the San Francisco Bay and the Pacific Northwest Puget Sound are just two examples); amphibious operations of UAM/eVTOL vehicles operating overwater are to be expected, Ref. 13.

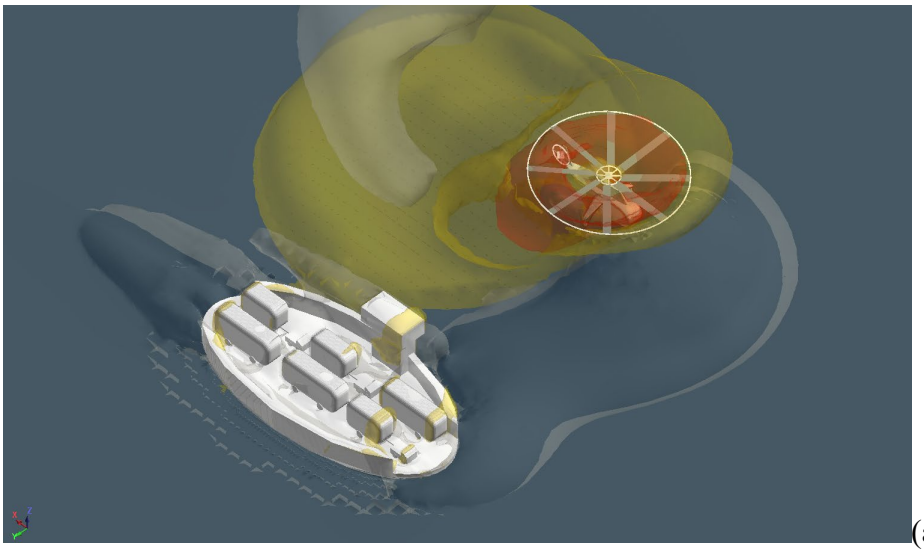
(a)

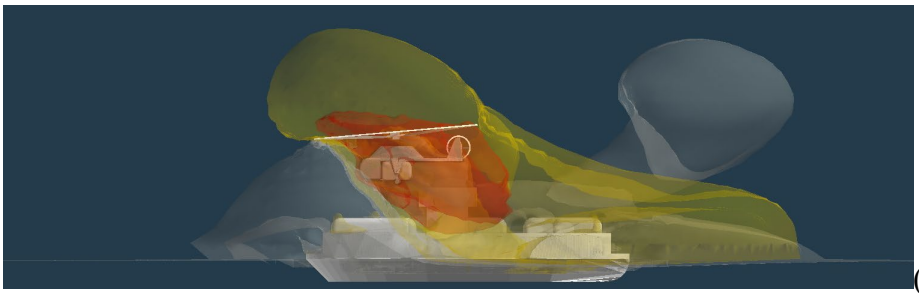
(b)

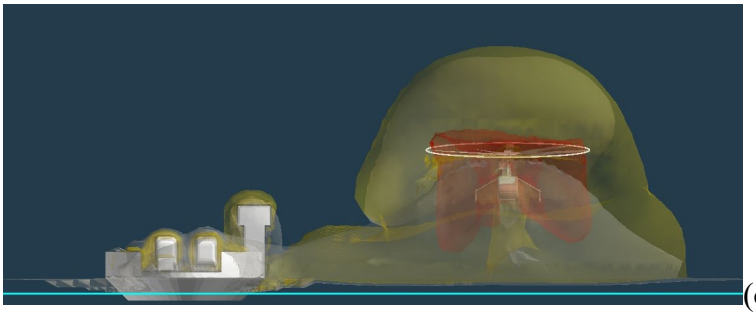
(c)

Figure 19. Rotorcraft wake interactions during over-water and near shore operations near piers and marinas for urban areas near waterways (in this particular case, wake interactions with a water ferry transporting cars/passengers): (a) top view, (b) side view, and (c) front view

Figure 20 presents velocity vector maps, streamlines, and velocity magnitude isosurfaces of rotor wake outwash of the single-main-rotor NN aerial vehicle hovering near a single dwelling residence. More rotor outwash work will be presented later in the report. This additional work will also consider the induced surface pressures on buildings stemming from the rotor outwash velocities. Such rotor outwash work will be instrumental

in defining CONOPS and other operational restrictions for New Nomad and other UAM/eVTOL vehicles close to the ground, in the urban environment. These initial results also emphasize the need for the widespread use of mid-fidelity or higher CFD being applied to consider rotor outwash in complex environments. The CFD predictions presented throughout this report are based on the use of the mid-fidelity CFD software tool, RotCFD, Refs. 56-57. RotCFD has been used for several related problems prior to its application to the New Nomad study, e.g., Refs. 39-40. Figure 21 illustrates the single-main-rotor NN aerial vehicle with and without a habitat module mounted directly to the vehicle airframe.

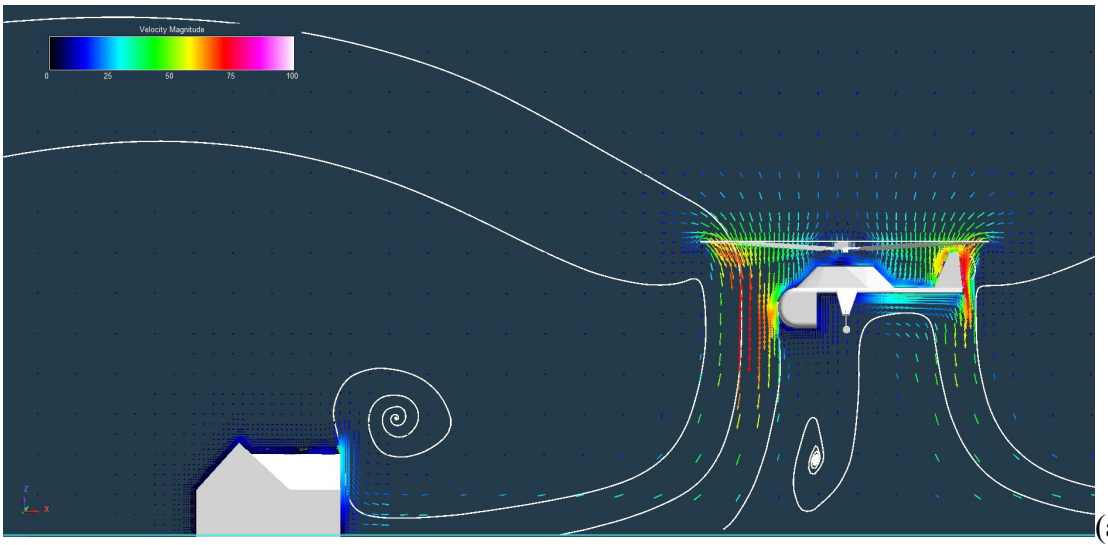

(a)

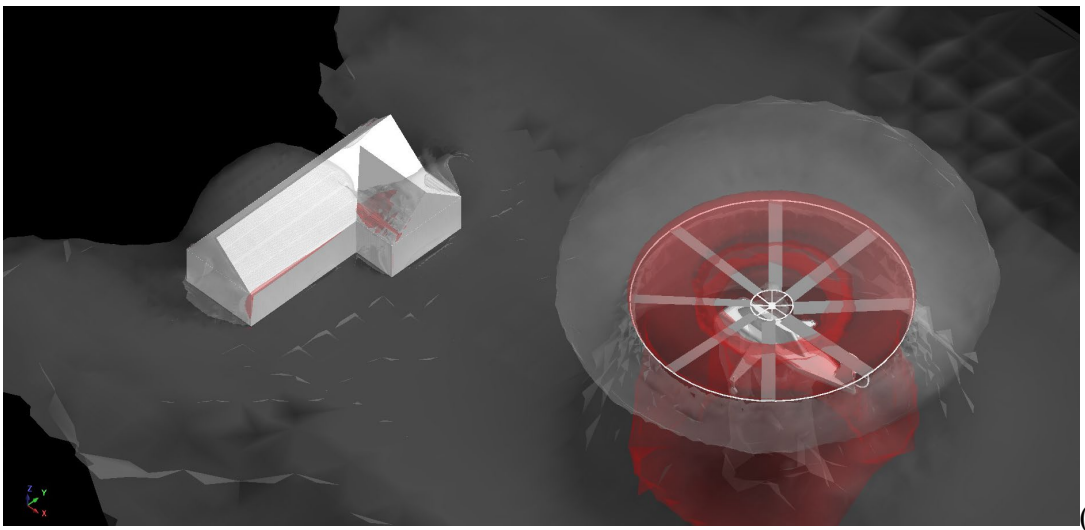
(b)

Figure 20. Rotor Wake Interactions in HIGE with single residence house: (a) side view of rotor outwash streamlines and velocity vector map; (b) rotor wake velocity magnitude isosurfaces

Anyone who has lived under the flight path of helicopters can attest to the impact of the sound and low-frequency vibrations induced in homes from those aircraft. Gaining as much technical insight as possible into such issues to address community acceptance is crucial.

Other aerial vehicle types could be explored as compared to the single-main-rotor (SMR) helicopter originally presented in Fig. 1 or shown again, below, in Fig. 21. A wide array of multirotor, tiltrotor, and tiltwing configurations are currently being studied in the complementary urban aerial mobility (UAM) trade space. These novel vehicle configurations are argued as being potentially low-cost, more easily manufactured and maintained, more amenable to supporting electric propulsion, safer, and quieter than conventional helicopters. These vehicles are at most still at the prototype stage, though, and further have primarily focused on a small number of passengers or relatively light cargo/payloads. However, SMR helicopters have been extensively studied and fielded for heavy-lift missions and/or external cargo slung load applications.

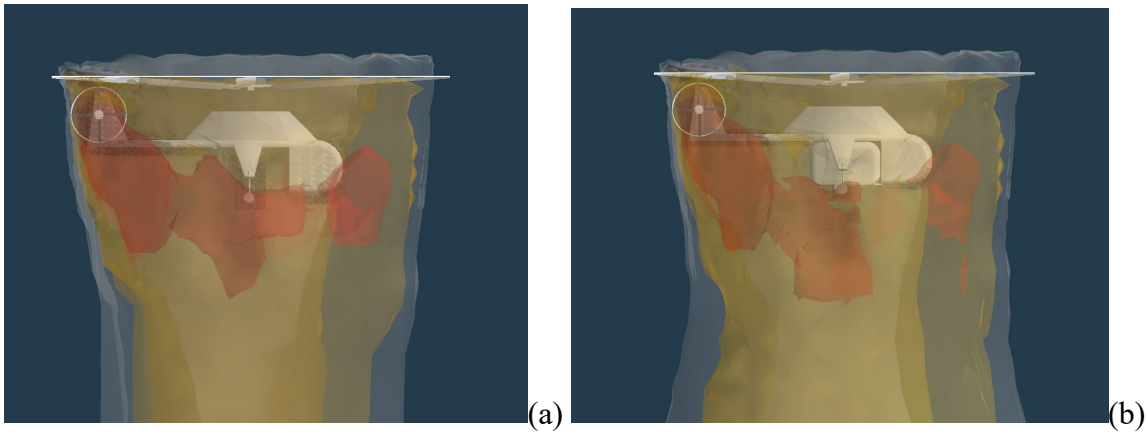

Figure 21. Flow field predictions of New Nomad single-main-rotor vehicle in hover: (a) without habitat and (b) with habitat (suspended under the cabin)

Efficiently Lifting Large Things in Hover

Figure 22 illustrates RotCFD results for a single rotor in hover, with a rectangular prism representing a variety of different habitat module sizes. The resulting predicted aerial vehicle with habitat module download ratios (DL/T) are also presented for several rotor disk loadings in Fig. 23. The hover aerodynamic performance, aka aeroperformance, influence of vehicle span length is studied by inserting rectilinear fuselage 'plugs' into the forward and aft sections of the vehicle. Similar extension 'plugs' are inserted into the

habitat module carried underneath the vehicle. This approach to modify the vehicle and habitat module longitudinal length spans is shown in Fig. 22a-l respectively. Figure 22a-l illustrates hover RotCFD results for the general single-main-rotor vehicle first noted in Fig. 1. Figure 23a-b present hover performance and vehicle fuselage download results for several different rotor disk loadings (different rotor collectives for the same rotor configuration) for a range of vehicle longitudinal length spans.

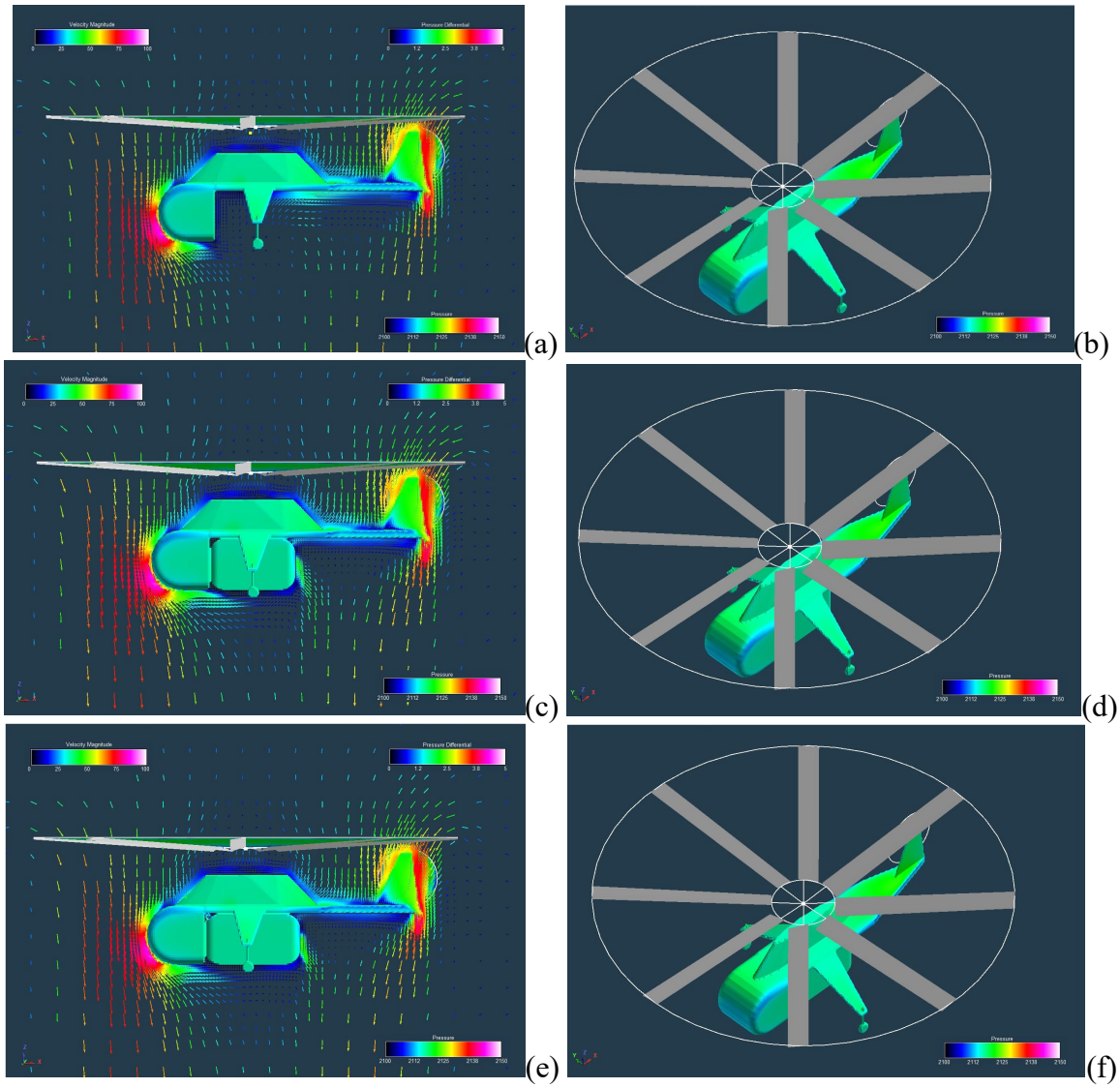

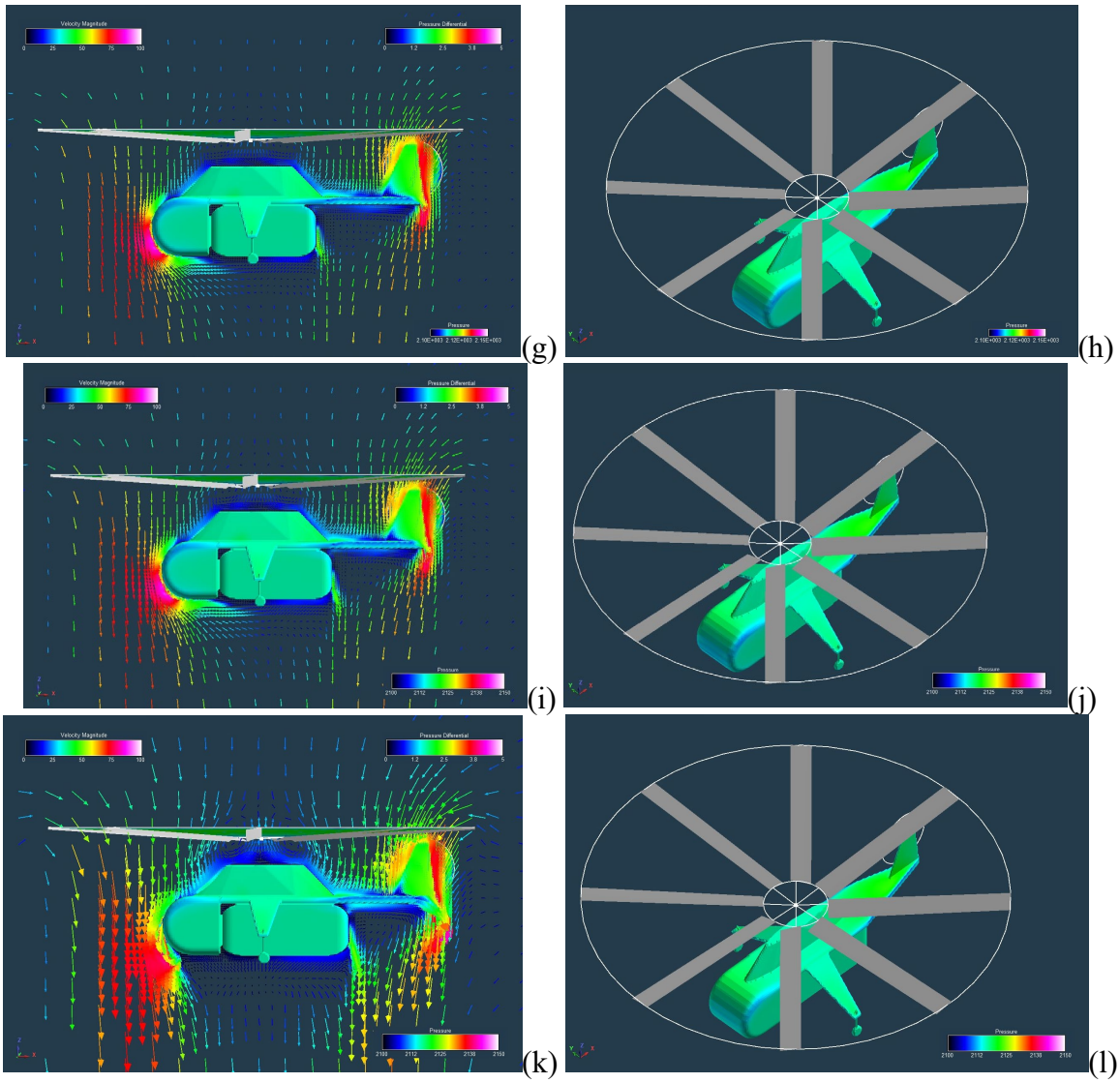

Figure 22. Hover flow field predictions of fuselage and habitat modules of various different sizes (i.e., different longitudinal spans): (a-b) no habitat module (zero 'stretch'); (c-d) baseline 'non-stretched' habitat module; (e-f) 1.125 times the longitudinal span of baseline module; (g-h) 1.25 times the longitudinal span; (i-j) 1.375 times the longitudinal span; (k-l) 1.5 times the longitudinal span of baseline module

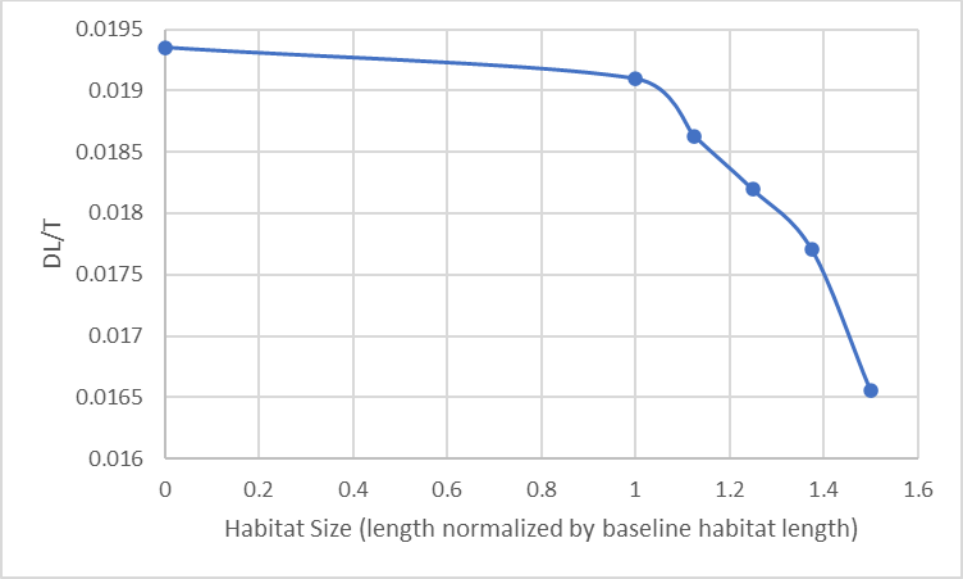

Figure 23. Overall vehicle (with habitat module) download ratio (DL/T) as influenced by vehicle having various different habitat sizes

All results in Figs. 24-25 are presented for a forward flight condition of a prescribed vehicle pitch altitude of -5Deg. (nose down) and forward flight velocity of 50 m/s (165ft/s). The rotor collective and cyclic are not set to trim the vehicle; the rotor collective is set to 10Deg. There are aircraft- and mechanical-design challenges anticipated for allowing for the large center of gravity shifts that would result from flying without a habitat module installed and flying with a module installed. Further, if a large range of habitat module sizes need to be provided for, then this further exacerbates the center of gravity problem.

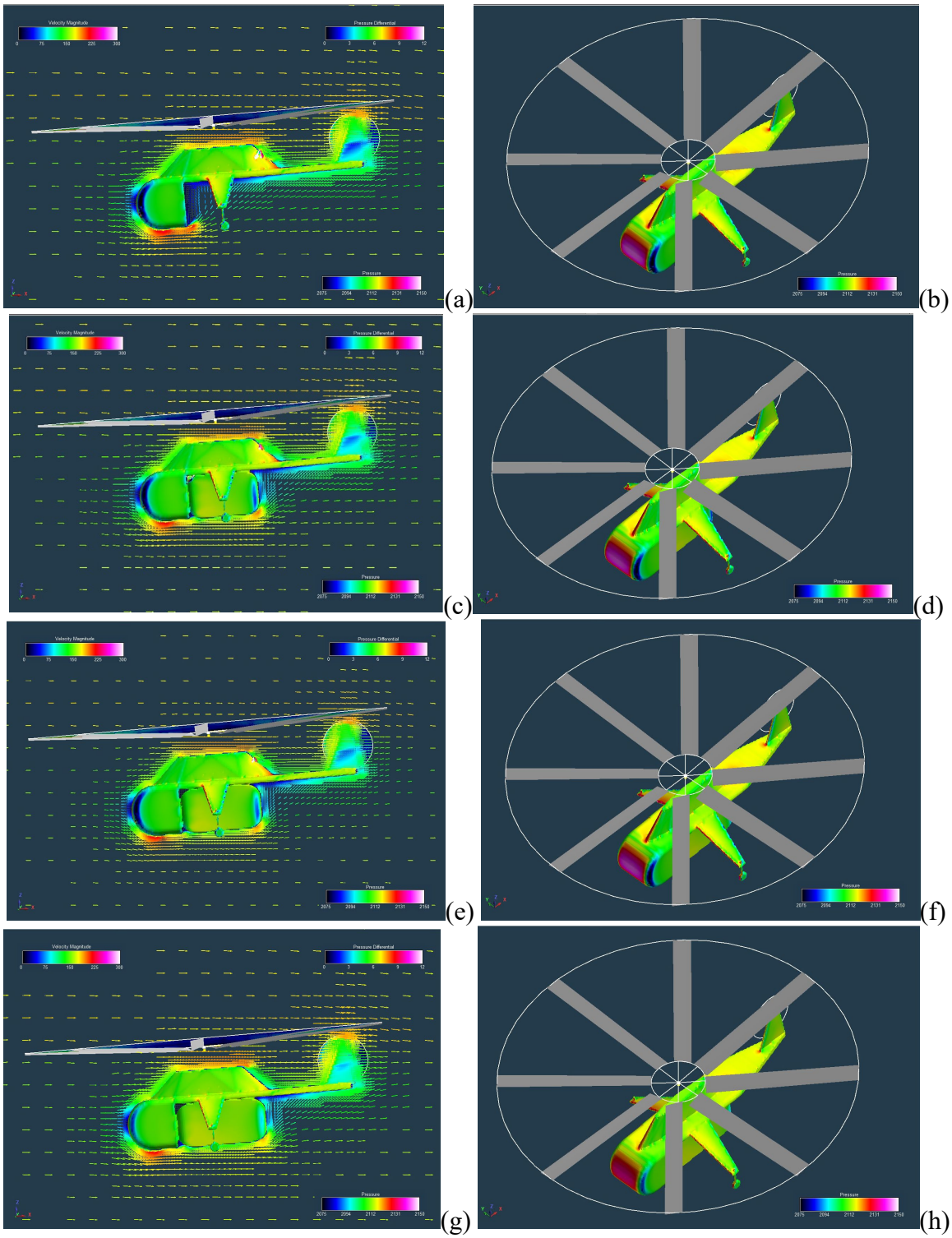
(a)
(b)
(c)
(d)
(e)
(f)
(g)
(h)

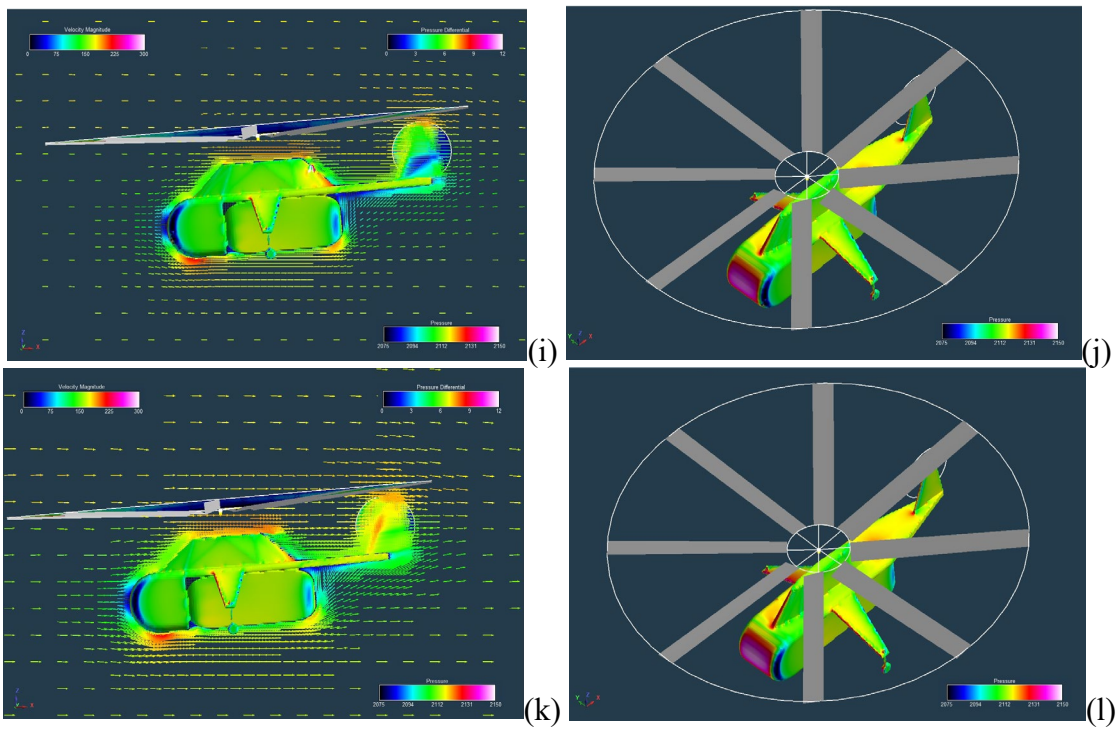

Figure 24. Forward flight flow field predictions of fuselage and habitat modules of various sizes (i.e., different longitudinal spans): (a-b) no habitat module (zero 'stretch'); (c-d) baseline 'non-stretched' habitat module; (e-f) 1.125 times the longitudinal span of baseline module; (g-h) 1.25 times the longitudinal span; (i-j) 1.375 times the longitudinal span; (k-l) 1.5 times the longitudinal span of baseline module

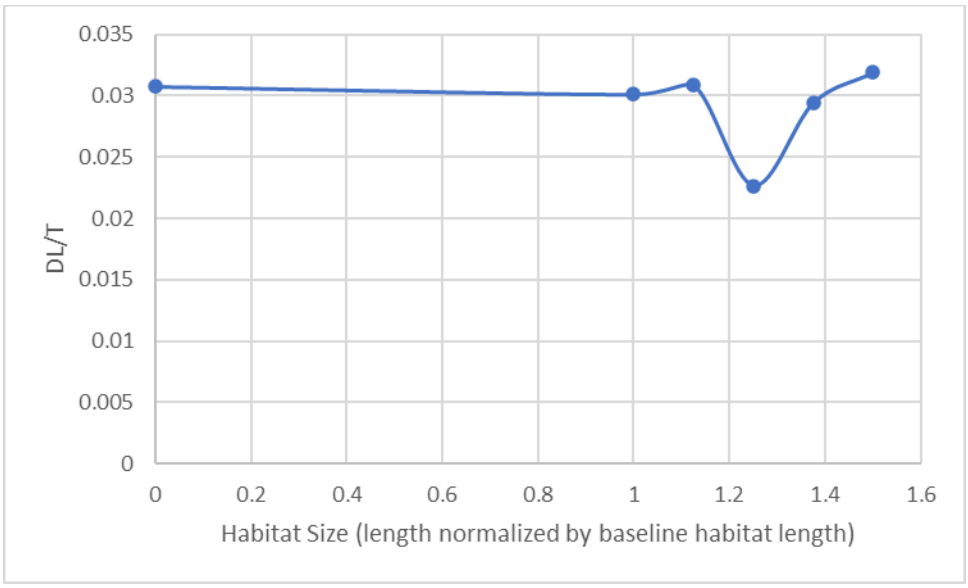

(a)

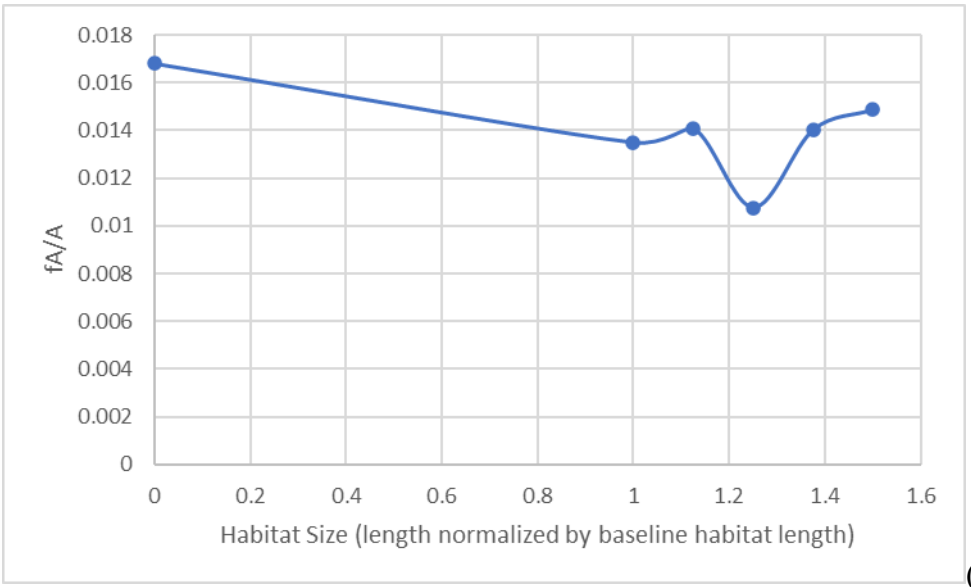

(b)

Figure 25. Vehicle airframe forward flight performance as influenced by vehicle having various habitat sizes: (a) vehicle download (DL/T) and (b) drag (f/A = (D/q)/(πR²) flat-plate area divided by rotor disk area

Figure 26 presents flow field predictions of slung loads suspended beneath the SMR NN aerial vehicle.[2] The RotCFD run cases shown in Fig. 26 were performed to consider the impact on aggregate vehicle and habitat module download ratio as a function of the habitat module being carried notionally as a 'slung load' rather than directly mounted to,

[2] It should be noted that given the thinness of the modeled tether(s) that occasional 'breaks' in the resulting automated-gridding representation of the tether, for longer tether lengths. This is an issue that will have to be addressed in future work.

or integrated into, the vehicle structure. Slung, or sling, loads are the conventional way military helicopters carry heavy external loads. There is typically a tradeoff of a reduction in vehicle speed versus the convenience of carrying an external load by a sling or tethers. The two limitations in vehicle speed while carrying a slung load are (1) the resulting overall drag of the vehicle and external load and (2) the stability (lack of pendulum motion and/or load spinning) of the external load. There is an extensive body of research, e.g., Refs. 64-65, typically by US Army rotorcraft researchers or sponsored academics, examining the minutia of slung load transport by rotorcraft.

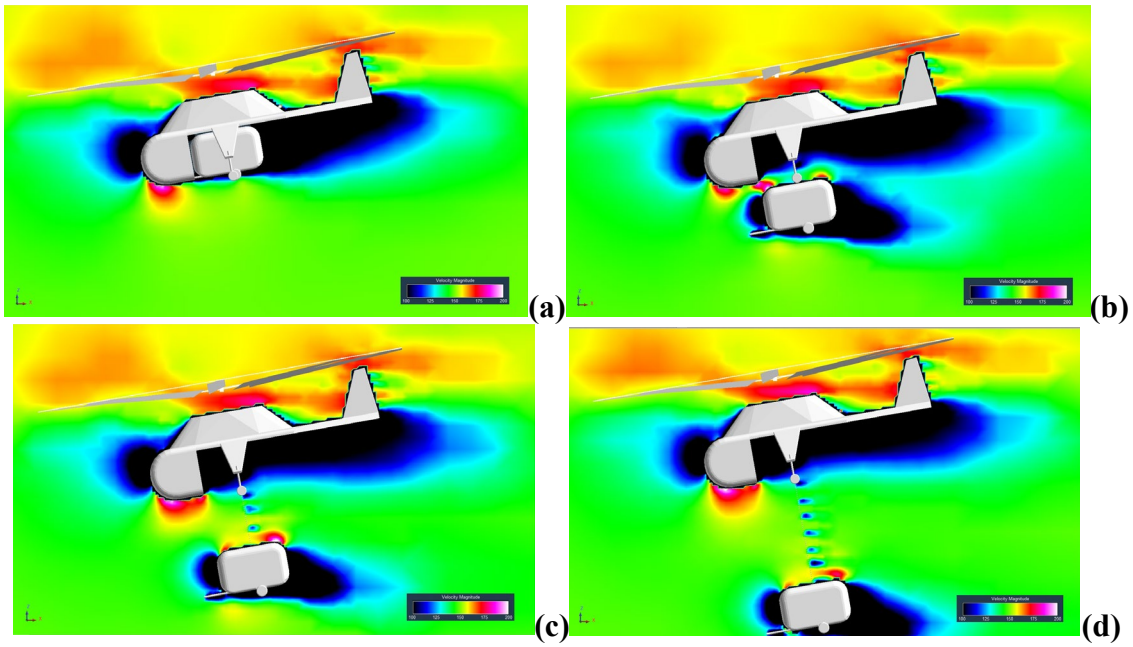

Figure 26. Simple RotCFD model showing the flow field (velocity magnitudes) of the vehicle carrying the habitat module as a slung load: (a) tether length y/R= 0; (b) y/R=0.28; (c) y/R=0.56; (d) y/R=0.83

Referring to Fig. 27a-b, it appears that there is a trade between reducing aggregate download versus reducing overall drag through using a slung load versus a conformal (tether length zero) stowing of the habitat module. I.E., a short tether might reduce overall download, but the drag is at its lowest when no tether is used. Further, the required tether length to reduce download might be too short to be safely implemented in forward flight.

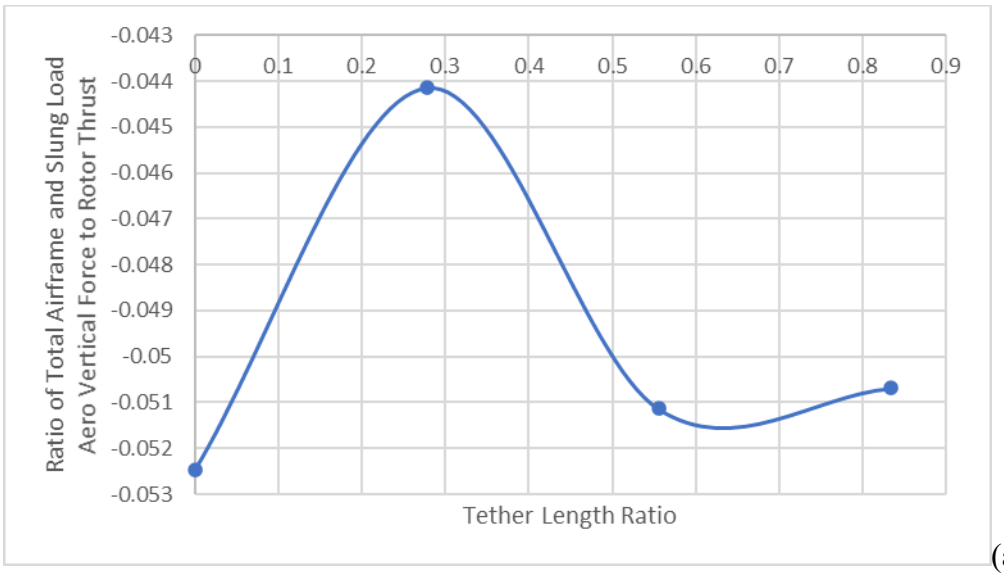

(a)

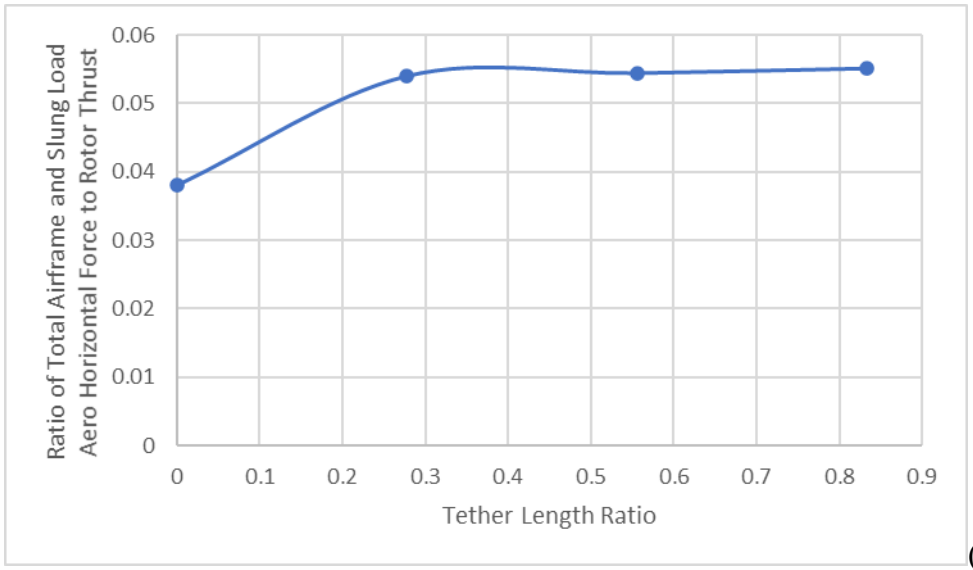

(b)

Figure 27. Drag and download trends of the aggregate baseline single-main-rotor and tail-rotor vehicle and suspended habitat module as a function of slung load tether length (nondimensionalized by main rotor radius; forward velocity of 150ft/s and a minus ten deg. nose down pitch attitude): (a) vertical force (download); (b) drag

Accordingly, it is an important open design question as to whether habitat modules should be carried via slung load or somehow captured/integrated into the airframe of the NN aerial vehicles. Overall vehicle/system drag will be impacted by the outcome of this design decision. Further, the relative size and weight of the transported habitat modules will also have important implications as to the NN vehicle design.

The work in the following subsection begins to consider the aerodynamic implications of the single-main-rotor vehicle reference design whereby the habitat module is integrated directly into the airframe of the vehicle.

Efficiently Commuting by Air

Figure 28 presents forward-flight total power estimates of the (Fig. 1) single-main-rotor (SMR) vehicle with the integrated – or, rather, the directly structurally mounted to the vehicle – habitat module. Such estimates were made by a simple rotorcraft sizing analysis of the SMR baseline reference design vehicle based on first-order rotor blade element momentum theory (BEMT) estimates. BEMT equations and methodology are well-known and can be found in textbook references such as Ref. 66.

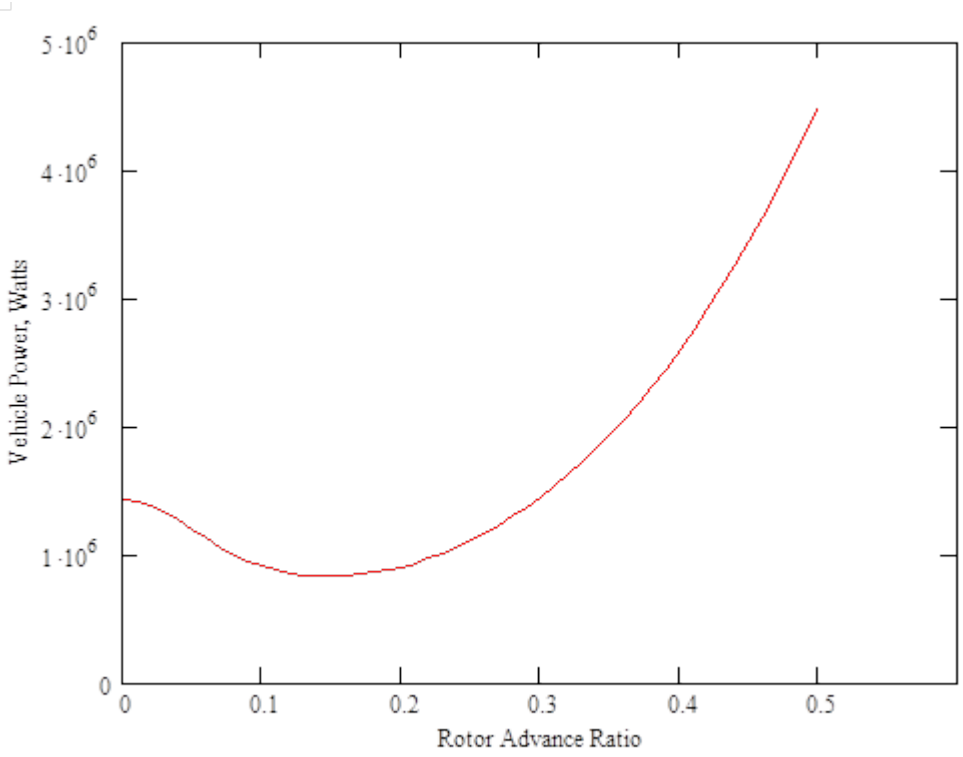

(a)

Figure 28. Forward flight vehicle (SMR baseline with 3000lbf (1364kg) payload) performance; power as a function of forward velocity: simple momentum theory vehicle performance estimates used in the sizing analysis

The target figure of merit used in the sizing analysis was a conservative value of 0.65. Even so, with the use of a NACA 0012 airfoil decks in RotCFD (used for convenience), reaching this target figure of merit was still challenging to achieve (while at the same time keeping the rotor solidity and, therefore, rotor blade weight down). Initially a linear twist rate of -10Deg. was used but was found to result in premature stalling of the airfoils before

the target thrust coefficient and figure of merit was reached. A small study of different twist rates, including nonlinear (or rather bi-linear) twist rates, was performed to reach the target figure of merit for the target thrust coefficient; refer to Figs. 29-30.

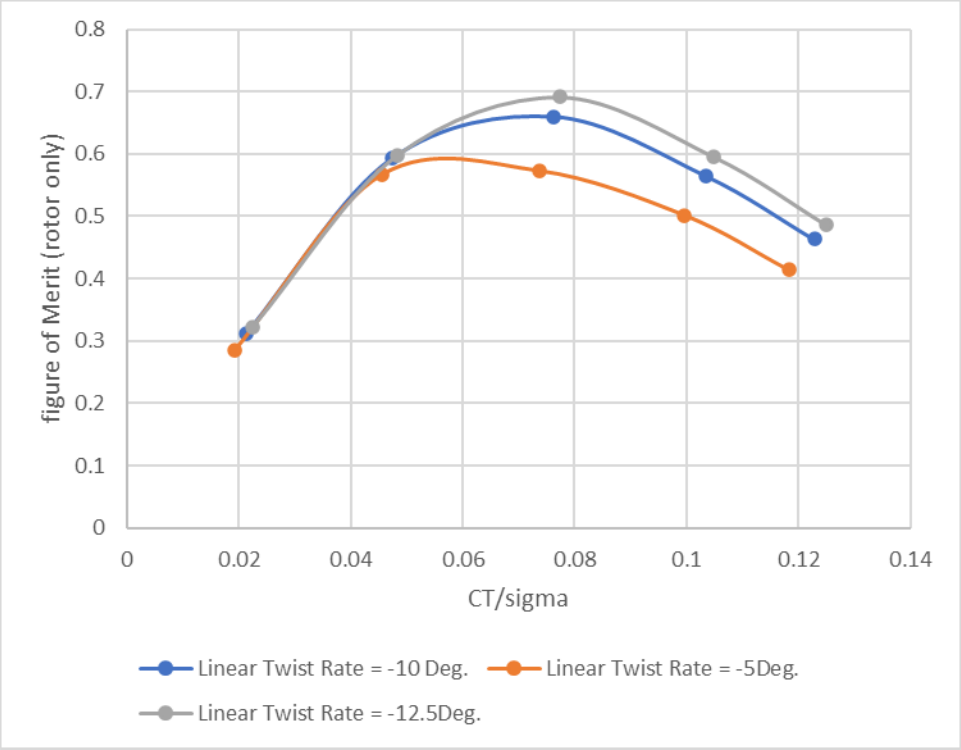

Figure 29. Baseline SMR vehicle main rotor figure of merit trends for various linear twist rates

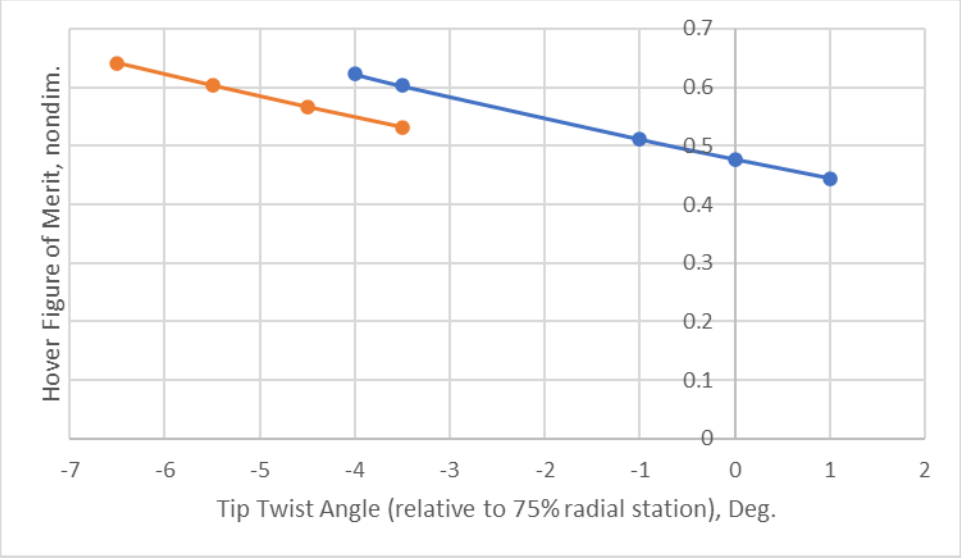

Figure 30. Baseline SMR vehicle main rotor figure of merit trends for various nonlinear twist rates (the outer 25% of rotor is at a steeper twist rate than the inboard 75% of the rotor)

The resulting 'best' nonlinear (bi-linear) twist rate found from the simple RotCFD BEMT analysis summarized in Figs. 29-30 has a tip twist angle is set to -6.5Deg. This 'best' rotor blade twist distribution is shown in in Fig. 31.

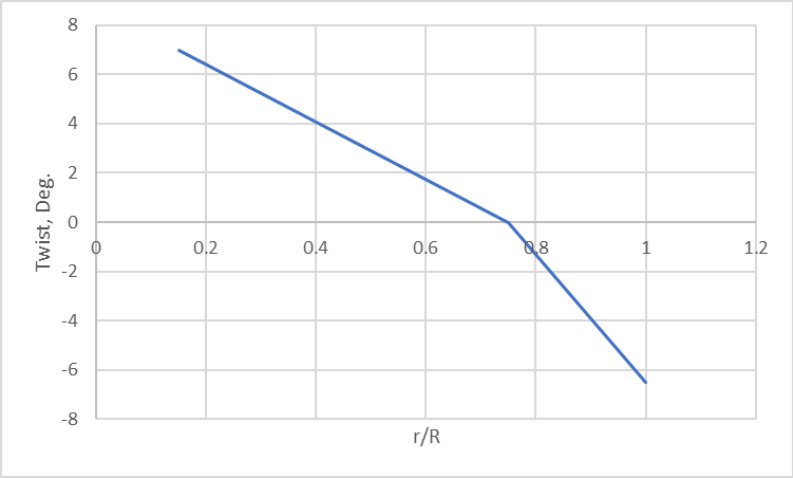

Figure 31. The final 'best' nonlinear twist rate for baseline New Nomad vehicle

Figure 32 presents vehicle power versus speed curve based on both RotCFD and the simple momentum theory results used in the sizing analysis. The agreement between the two sets of results is relatively good for hover and low speed flight because of incorporation of bi-linear twist in the rotors. At higher speeds, though, the disagreement grows larger.

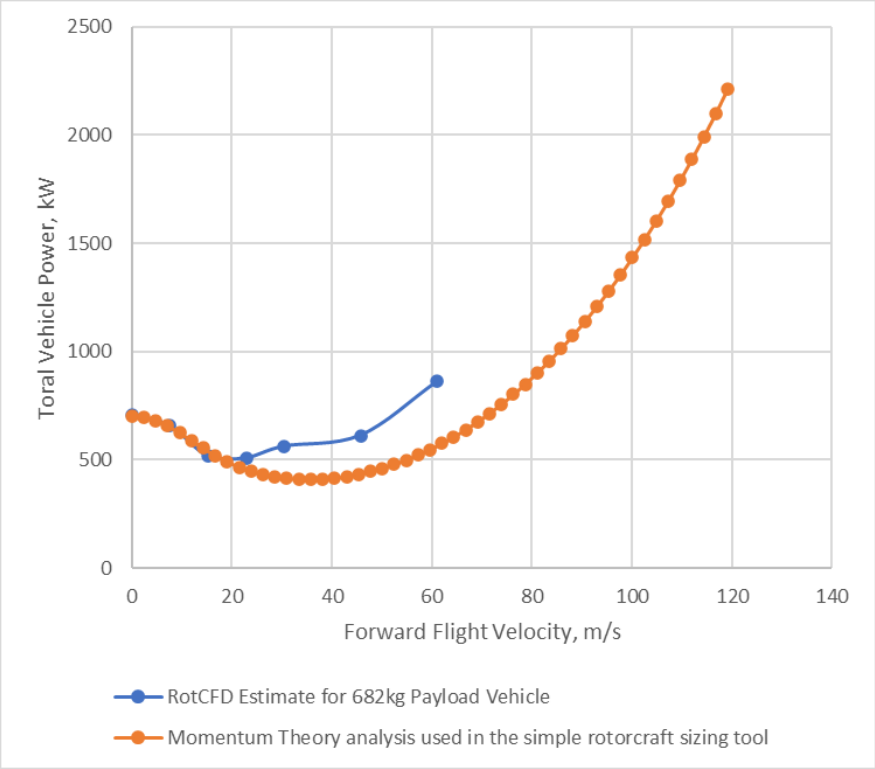

Figure 32. Simple momentum theory and RotCFD predictions of forward flight vehicle (SMR baseline with 1500lbf (682kg) payload) performance (Fig. 31 twist)

In the above comparison of the simple momentum theory analysis results used for sizing analysis to RotCFD, RotCFD is clearly predicting higher total rotor power (single main rotor plus the tail rotor power) than that used in the simple analysis. A flat-plate area value of f/A=0.015 was used for the simple momentum theory analysis; the RotCFD predictions for the fuselage flat-plate drag are comparable in magnitude. For example, refer to the Fig. 25 flat-plate area f/A estimates. The Fig. 25 RotCFD results were run non-rotor-trimmed at a vehicle nose down attitude of -5Deg.; the Fig. 32 RotCFD results were run rotor-trimmed (with cyclic and collective inputs) at a prescribed vehicle attitude at 50m/s of -10Deg. (more nose down than the comparable Fig. 25 results) or, more, precisely the prescribed vehicle attitude angles were AOA = $-0.3911V + 0.0061V^2 - 0.00001V^3$; this appears to have been too conservative (too much nose down attitude) by as much as approximately -6Deg. (In retrospect, the vehicle attitude would have been better prescribed by AOA = $-\text{asin}(0.00003177V^2)$.[3]) The trimmed versus non-trimmed run cases appear to have a big influence on the total rotor power discrepancies observed. Future work will have to do a better job of harmonizing the run cases for improved comparison. An additional preliminary look at the predictive capability of RotCFD for bluff-bodies is presented in Appendix A. Appendix A presents RotCFD drag results for a range of

[3] Note: $D = (f/A)Aq \approx -Tsin(AOA)$ which yields the approximate relationship for vehicle attitude of $AOA = -asin((f/A)Aq/T)$. Using a value of f/A=0.015, a rotor radius of 5.9m, assuming standard sea level atmospheric densities, and a vehicle gross weight of 3250kg, the AOA prescribed attitude expression in the main body of the report is derived.

Reynolds numbers is for a series of reference textbook bluff body drag curve trends, e.g., Ref. 51.

A key message, though, from Fig. 32 is that NN aerial vehicle drag will be an important consideration for arriving at satisfactory aircraft designs for even the relatively low cruise speeds of NN and other UAM and eVTOL vehicles. This will be a continuing aeroperformance challenge as 'heavy lift' helicopters have typically worse drag characteristics as compared to rotorcraft.

In addition to full vehicle power estimates provided by RotCFD, there are shown in Fig. 33a-b fuselage/airframe download and drag trends with forward flight speed (the vehicle nose down attitude as a function of speed and its influence on fuselage aero loads) is partly accounted for in the RotCFD estimates. The mid-range forward flight speed results yield a f/A=0.015 which is consistent with the Simple Rotorcraft Sizing (SRS) analysis employed in this report. These drag flat-plate area estimates are preliminary, though, and more work is required for future definition of reference designs for NN aerial vehicles.

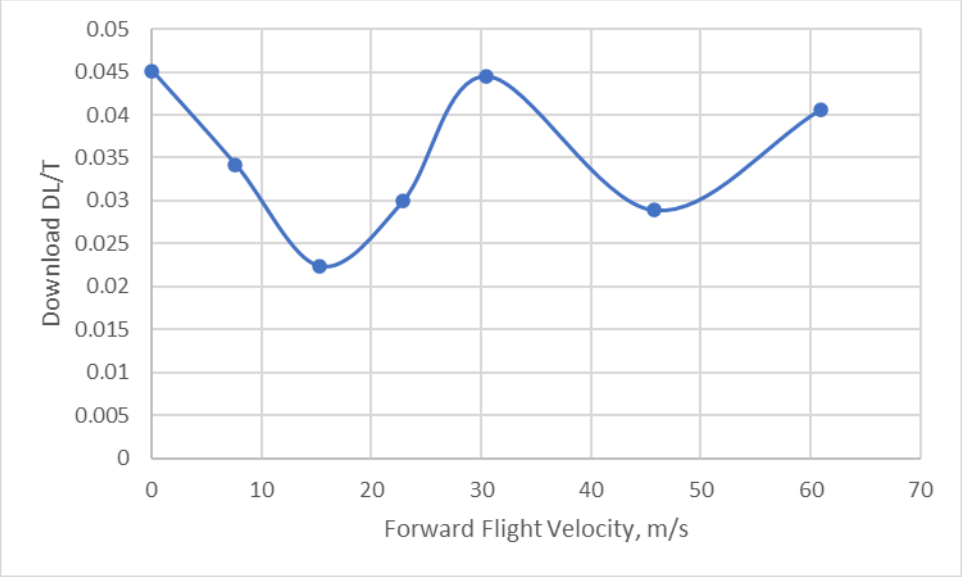

(a)

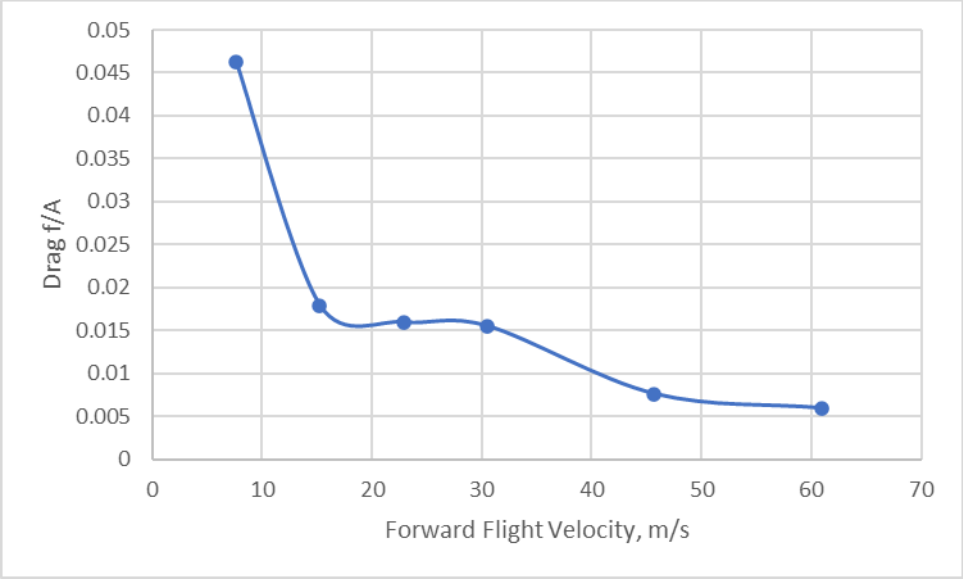

(b)

Figure 33. RotCFD predictions of fuselage and integrated habitat module (a) ratio of download to thrust and (b) drag flat-plate area f/A as a function of forward flight speed

Figure 34 present similar forward flight performance predictions as Fig. 33a-b but for the case of the vehicle transporting the habitat module as a slung load. Note that the slung load forward flight performance numbers are for the original main rotor (linear) twist rate of -10Deg. and not the bi-linear 'best' twist rate performance numbers shown in Fig. 31 and, therefore, somewhat higher vehicle total power trends are shown in Fig. 32.

As can be seen in Figs. 34-35, the total power and drag (for the vehicle plus tethers plus habitat module) are shown for the integrated vehicle and the habitat module carried as a slung load. The results are presented for a fixed 10Deg. collective and an untrimmed (with respect to cyclic pitch) single-main rotor. The total power includes both the power for the SMR and the tail rotor (the tail rotor is also at a fixed 10Deg. collective and not fully trimmed for antitorque in these preliminary results). Figures 34-35 are presented for a forward flight speed of 45.7m/s (150fps) and a vehicle attitude of -10Deg. Note that tether length ratio is defined as tether length divided by main rotor radius. As these results are still preliminary, it is still an open question for the NN short-range aerial mobility mission as to whether slung load transport is truly less efficient that directly integrating/mounting/supporting the habitat modules to the vehicle fuselage.

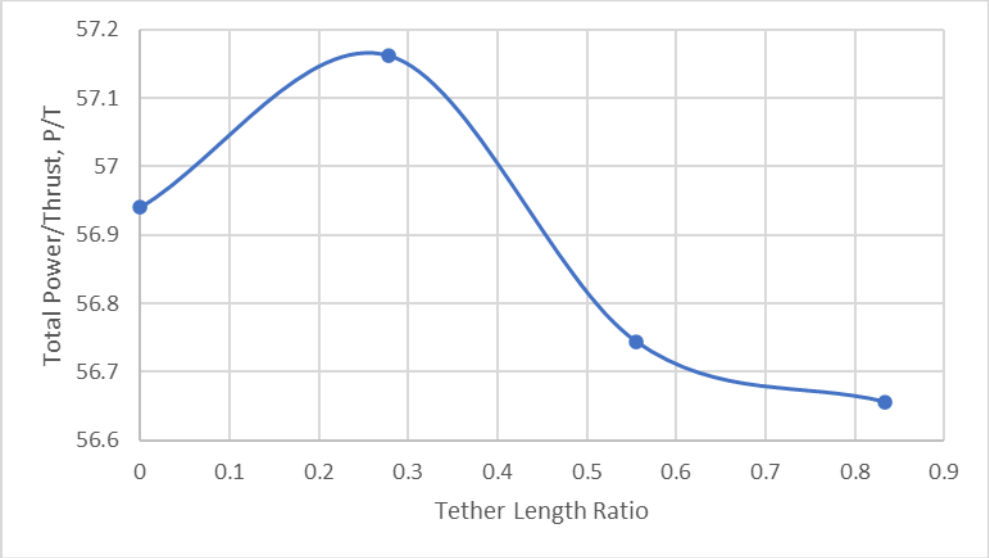

Figure 34. Forward flight performance for the vehicle carrying the habitat module as a slung load (cruise speed of 46 m/s or 150 ft/s): ratio of total power to thrust (untrimmed SMR rotor cyclic/collective) as a function of tether length ratio

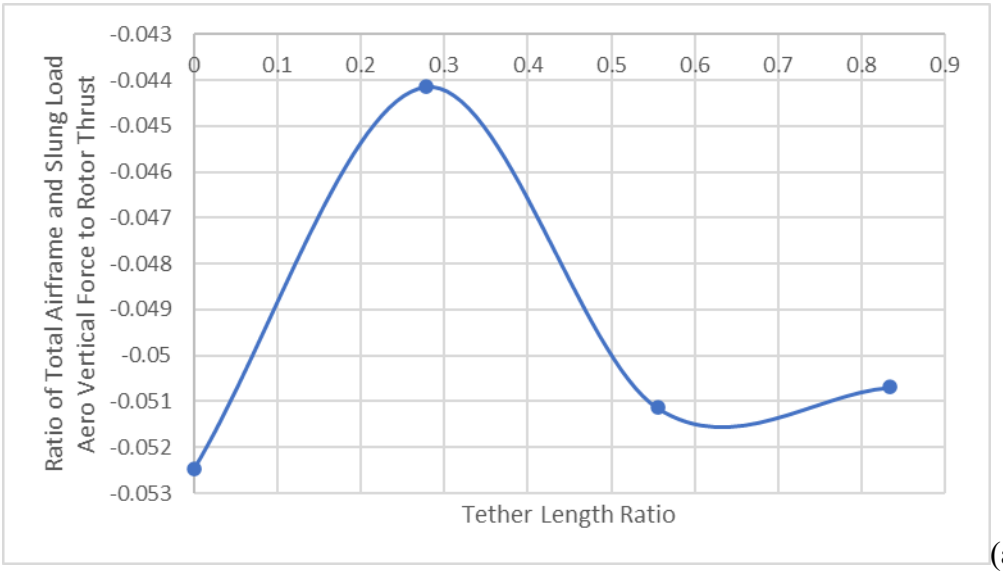

(a)

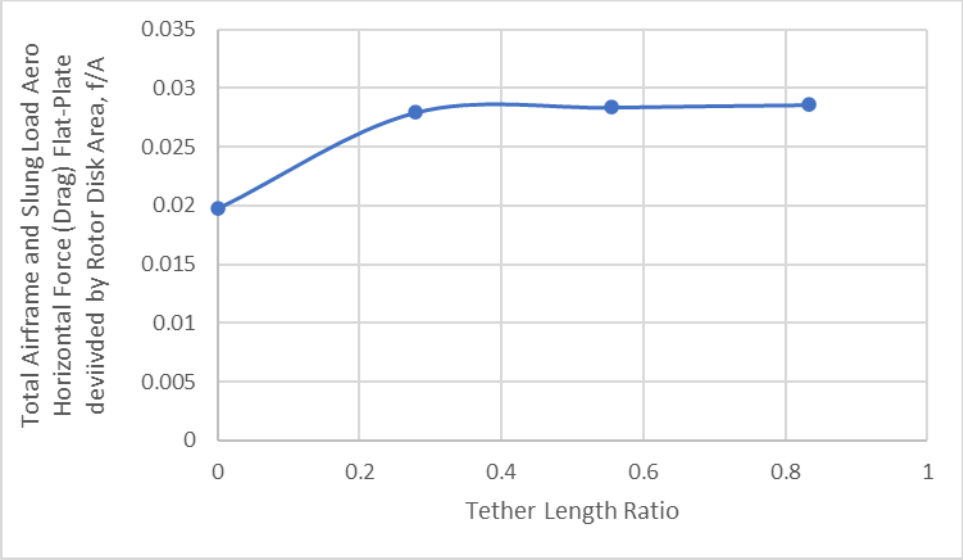

(b)

Figure 35. Fuselage and the habitat module as a slung load (cruise speed of 46 m/s or 150 ft/s): (a) ratio of download to thrust and (b) drag f/A flat-plate area as a function of tether length ratio

Safely Taking Off and Landing in Communities: hover rotor wake interactions in proximity to buildings and other property

Figures 36-37 represent an initial study of the (Fig. 1) baseline short-range SMR vehicle's hover rotor wake interactions in proximity to buildings and other property. Some of the generic buildings and property modeled includes single residences, parked automobiles, parked trains/light rail, piers and sailboats/ships, parking structures, or office buildings, etc. This rotor wake interaction with buildings/property can be considered an extension of past work documented in Refs. 9 and 40.

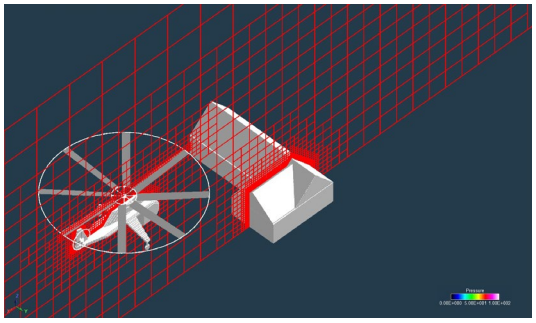
(a)
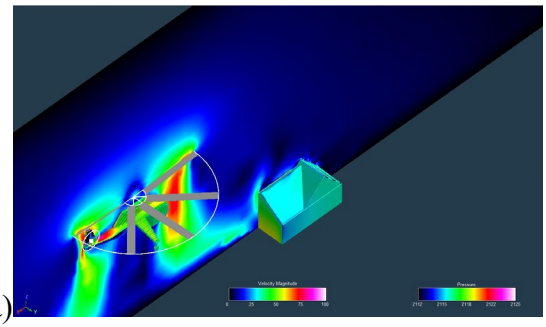
(b)

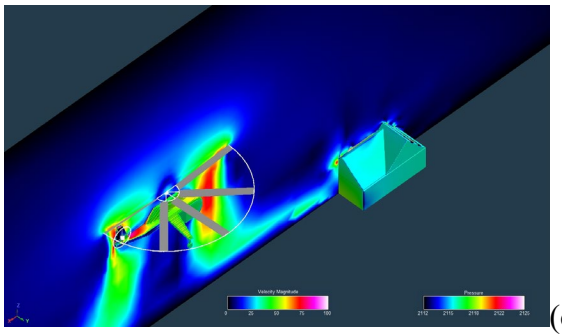
(c)
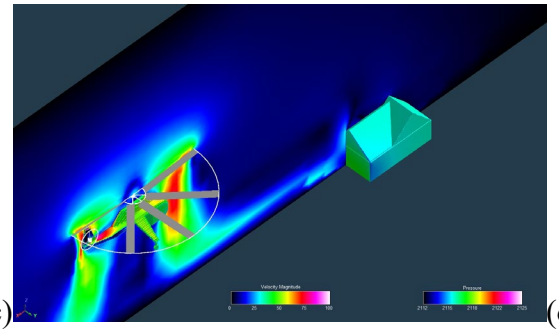
(d)
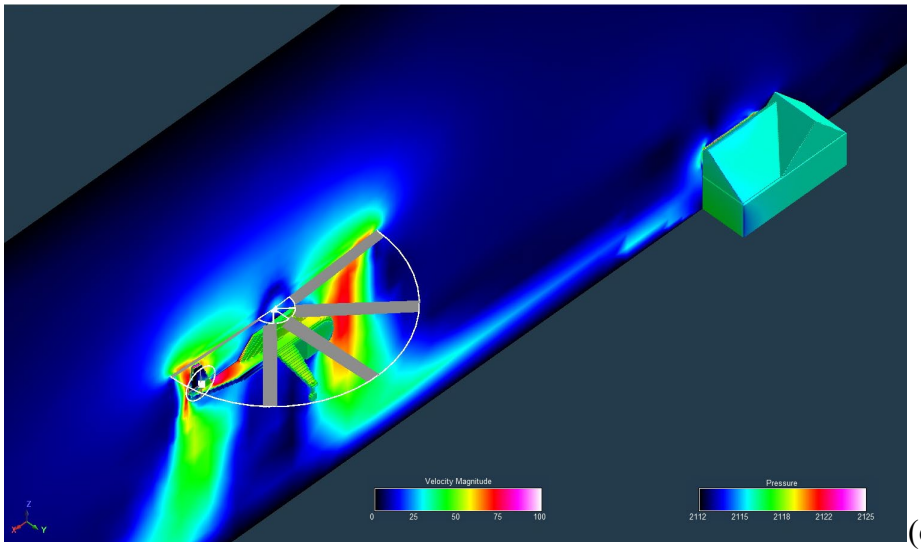

(e)

Figure 36. RotCFD rotor wake flow outwash (velocity magnitude contours) near a single residence building (h/R= 1.97): (a) gridding example at x/R = 2.08, (b) longitudinal distance of vehicle from single residence x/R = 2.08, (c) x/R = 2.78, (d) x/R = 3.5, (e) x/R = 4.17

Some early proponents of eVTOL 'air taxis' conjectured that such vehicles could be fully on-demand, door-to-doorstep, transport. In recent years, more of an on-demand, or even scheduled service, vertiport-to-vertiport model is being adopted as the CONOPS of choice. Nonetheless, the Figs. 36-37 are preliminary analysis related to housing structural airloads suffered because of NN aerial vehicles hovering and takeoff and landing nearby. Figure presents outwash velocities (velocity magnitude contours) from those vehicles as well as surface pressures induced by those velocities. Figure 37 integrates those surface pressures and presents trends of normalized horizontal and vertical forces as a function of the inverse of the NN vehicle distance (normalized by rotor radius) from a notional single residence building (for two different heights from which the vehicle is hovering above the ground). As anticipated these outwash-induced building airloads can be quite high and this issue of how close can vehicle takeoff and landing operations occur next to residential areas will continue to be of great importance and consequence.

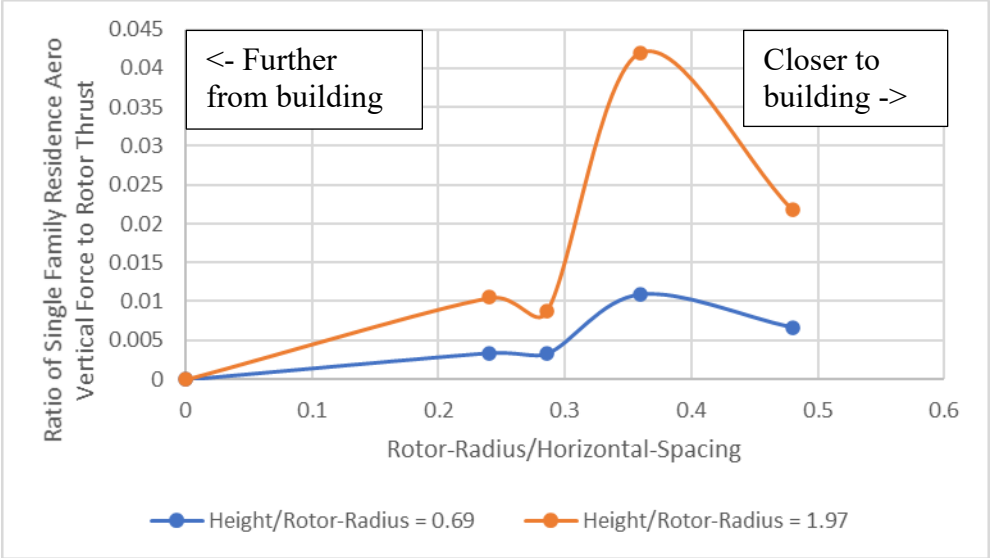
Ratio of Single Family Residence Aero Vertical Force to Rotor Thrust
0.045
0.04
0.035
0.03
0.025
0.02
0.015
0.01
0.005
0
<- Further from building
Closer to building ->
0
0.1
0.2
0.3
0.4
0.5
0.6
Rotor-Radius/Horizontal-Spacing
Height/Rotor-Radius = 0.69
Height/Rotor-Radius = 1.97

(a)

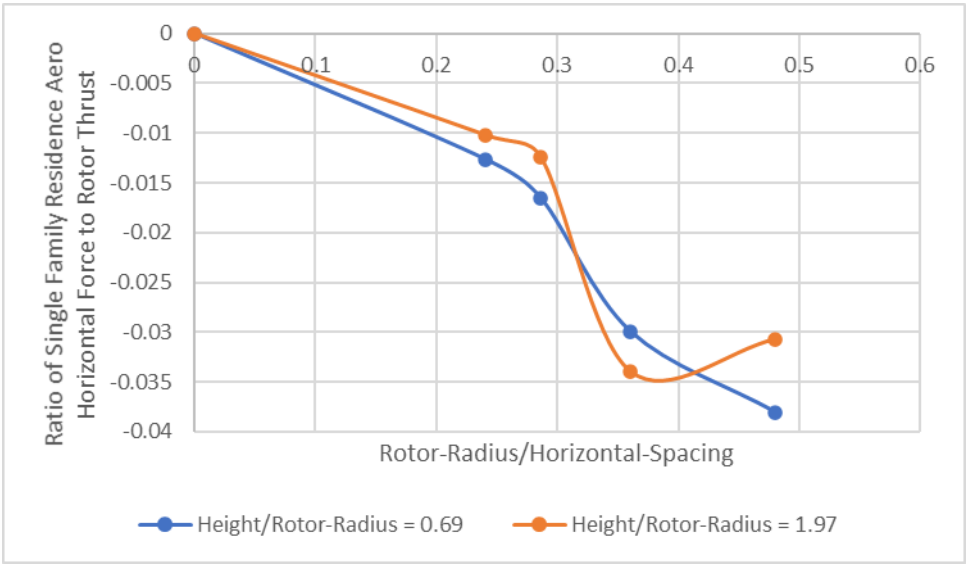
Ratio of Single Family Residence Aero Horizontal Force to Rotor Thrust
0
-0.005
-0.01
-0.015
-0.02
-0.025
-0.03
-0.035
-0.04
0
0.1
0.2
0.3
0.4
0.5
0.6
Rotor-Radius/Horizontal-Spacing
Height/Rotor-Radius = 0.69
Height/Rotor-Radius = 1.97

(b)

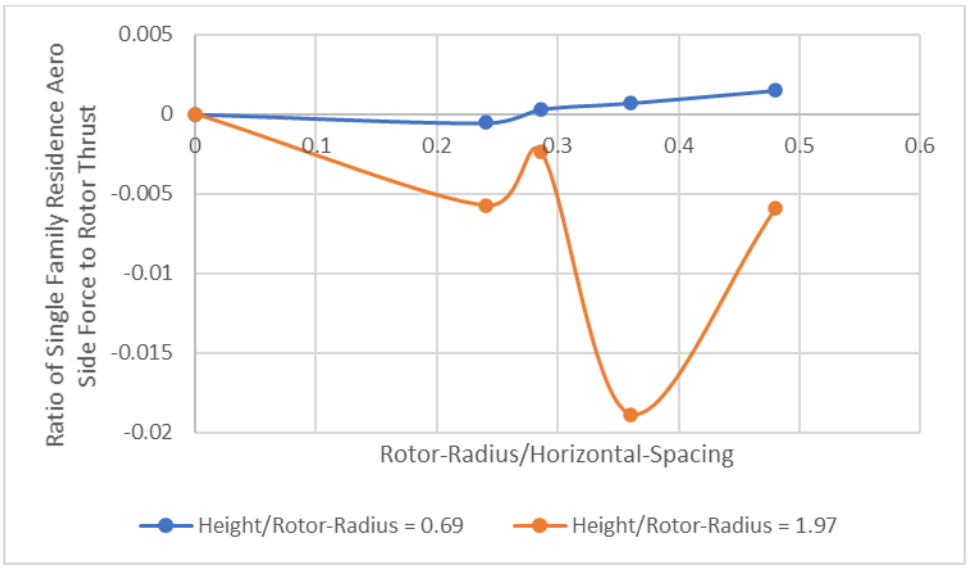

(c)

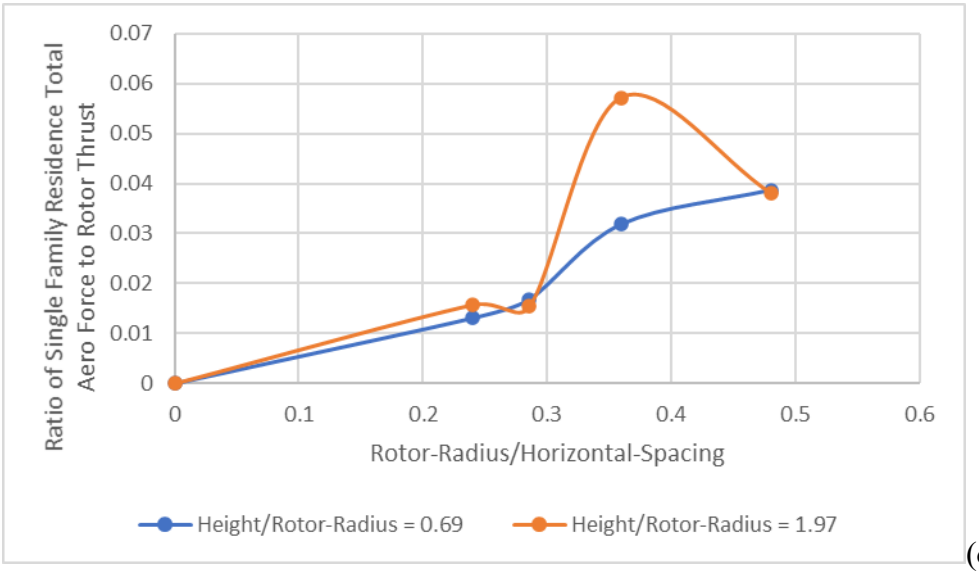

(d)

Figure 37. Incremental forces (nondimensionalized by rotor thrust) observed on single residence due to rotor outwash as a function of the inverse of longitudinal (horizontal) distance (nondimensionalized by main rotor radius) from a hovering vehicle: (a) aero vertical force; (b) aero longitudinal/horizontal force; (c) lateral/side-force aero force; (d) total aero force

The RotCFD predictions in Figs. 36-37 demonstrate the expected behavior of building aero loads (due to rotor outwash impingement) increasing as the NN aerial vehicle hovers closer and closer to the building. But not all rotor/building wake interactions happen in hover or near the ground with residential buildings. Instead, there are numerous issues that might crop up when low-flying rotorcraft, including NN, UAM, and eVTOL aerial vehicles, fly in an 'urban canyon' environment, especially under windy conditions. This issue will be examined in the next subsection of the report. New Nomad network

simulation analysis will be required to determine the most optimal approach to operating NN aerial vehicles. Are they on-demand, all-point-to-to-point operating vehicles, or will they have fixed-vertiport locations with regular scheduling, or will it be some combination of the two options? This network operations discussion will follow later in this report. Meanwhile, some additional urban canyon discussion and preliminary results will be presented in the next section.

Safely Flying in Communities: urban canyon wake interactions in conjunction with winds and no winds

Urban canyon rotor/building/wind CFD predictions are an emerging area of study given the significant potential safety implications for UAM and eVTOL (and NN) aerial vehicles. Some early work in this area, using RotCFD, was presented in Ref. 12. Analogously, this problem continues to be extensively studied for naval applications for shipboard operations of rotorcraft, e.g., Ref. 53.

Figures 38-39 show a canonical-type problem with regards to urban canyon flying. It builds upon earlier work discussed in Refs. 12 and 39. In this case, a head-on wind is blowing (represented by a uniform upstream flow field) past a tall skyscraper-like building. Further, the baseline single-main-rotor NN reference design vehicle is descending towards the building rooftop for a hover and a subsequent landing.

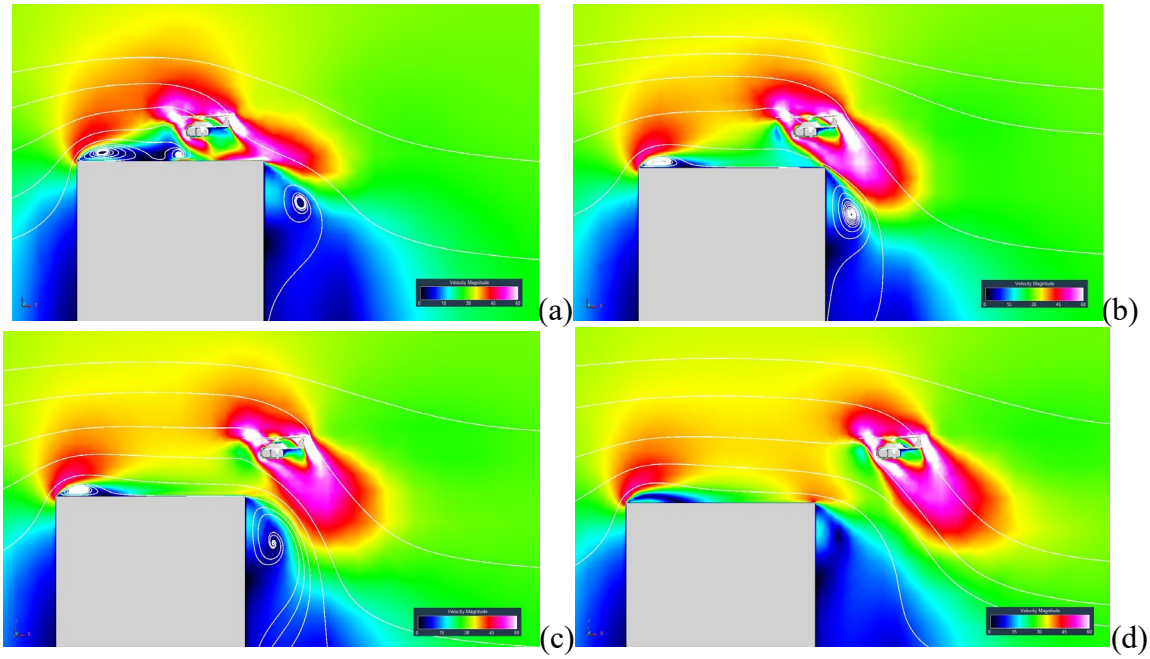

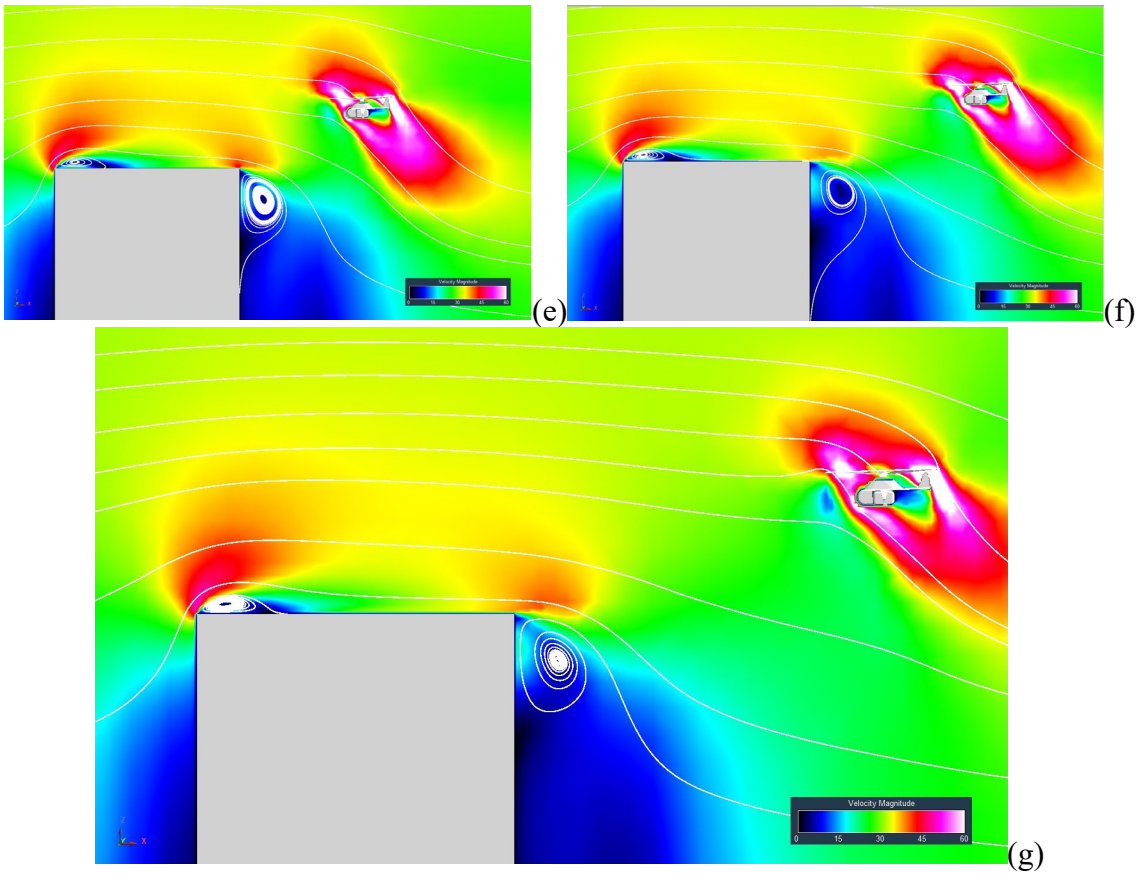

Figure 38. RotCFD model of urban canyon problem for baseline single main rotor (SMR) vehicle configuration (wind 9.1 m/s (30 ft/s) blowing left to right; vehicle on a six-degree descending glide slope to hover waypoint): (a) x/R=0; (b) x/R=1.39; (c) x/R=2.78; (d) x/R=4.17; (e) x/R=5.56; (f) x/R=6.94; (g) x/R=8.33

In addition to the general flow field predictions presented above, Fig. 39 presents quasi-steady predictions of the vehicle and rotor forces and moments as a function of approaching a rooftop landing zone from above and behind a high-rise building in wind. The main rotor is untrimmed (the collective and cyclic pitch settings are fixed/unchanged among the run cases performed) in this longitudinal traverse study. The delta pitching moment is assumed to be zero at $x/R \rightarrow \infty$. This traverse is a simulated quasi-steady descent/approach to a hover point above a building in a longitudinal cross wind at a descent glide slope of ten degrees. Therefore, as the vehicle longitudinally approaches the building it vertically drops lower. There are two major shed vortices being generated by the building in the cross wind: a shed vortex on the forward-facing rooftop, that influences the vehicle as it is nearly over the building, and a second vortex of the aft-facing side of the building, on the side of the building nearest the vehicle as it approaches the building. These shed building vortices can be clearly seen in the Fig. 38 velocity magnitude contours and the streamline plots. It is the complexity of the building and vehicle flow field interaction that makes the vehicle delta pitching moment trend with longitudinal traverse distance challenging. It is clear,

though, that as the vehicle approaches and crosses over the building rooftop that there is a sharp change in vehicle pitching moment.

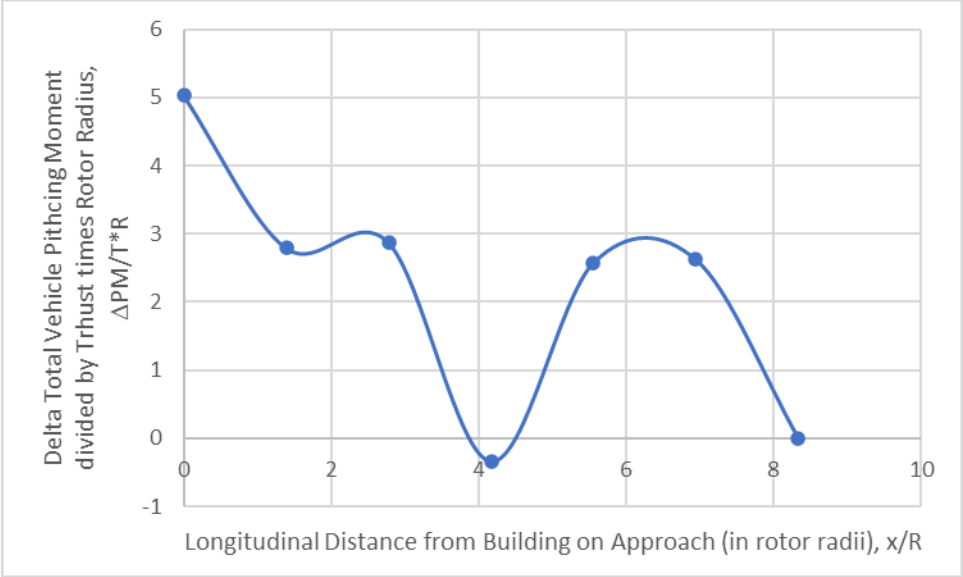

Figure 39. SMR baseline vehicle delta total pitching moment ratio (PM/(T*R)) as function of traverses behind a building in a constant wind of 9.1 m/s (30 ft/s)

Alternate Aerial Urban/Short-Range Mobility Approach/Analysis

Some might be disappointed that the discussion so far has focused on a conventional single-main-rotor and tail-rotor helicopter configuration for effecting aerial short-range mobility. Many researchers and vehicle developers are currently focused instead on alternate vehicle configurations such as multirotor configurations. There are pros and cons for both approaches and, ultimately, the aviation marketplace will be the decider as to which is the better approach: more conventional helicopters and rotorcraft or somewhat more exotic platforms such as multirotor vehicles. For completeness, one alternate vehicle configuration is presented and discussed in a similar manner as that done for the skycrane-like single-main-rotor helicopter discussed for aerial urban/short-range mobility.

A ten-rotor (eight lifting rotors and two propulsor rotors/propellers) multirotor configuration is introduced in Fig. 40. The vehicle conceptual design retains the same general fuselage as the single-main-rotor helicopter design discussed earlier. In addition to the larger numbers of rotors and incorporating a heterogeneous mix of rotor sizes and disk loadings, a canard, main wing, and tail horizontal wing are included in the conceptual design to act primarily as structural supports for the rotors. The incorporation of the tractor propulsor propellers into the landing gear support also allows this vehicle to fly at near-zero fuselage angle-of-attack in level forward-flight. The rotor count and overall sizing is

somewhat arbitrary – with emphasis on higher rotor counts and a greater mix of rotor sizes than is currently being explored by most eVTOL, UAM, or air-taxi developers. This alternate configuration is presented solely to discuss the vehicle and habitat integration issues and the resulting aeroperformance implications of different implementation approaches.

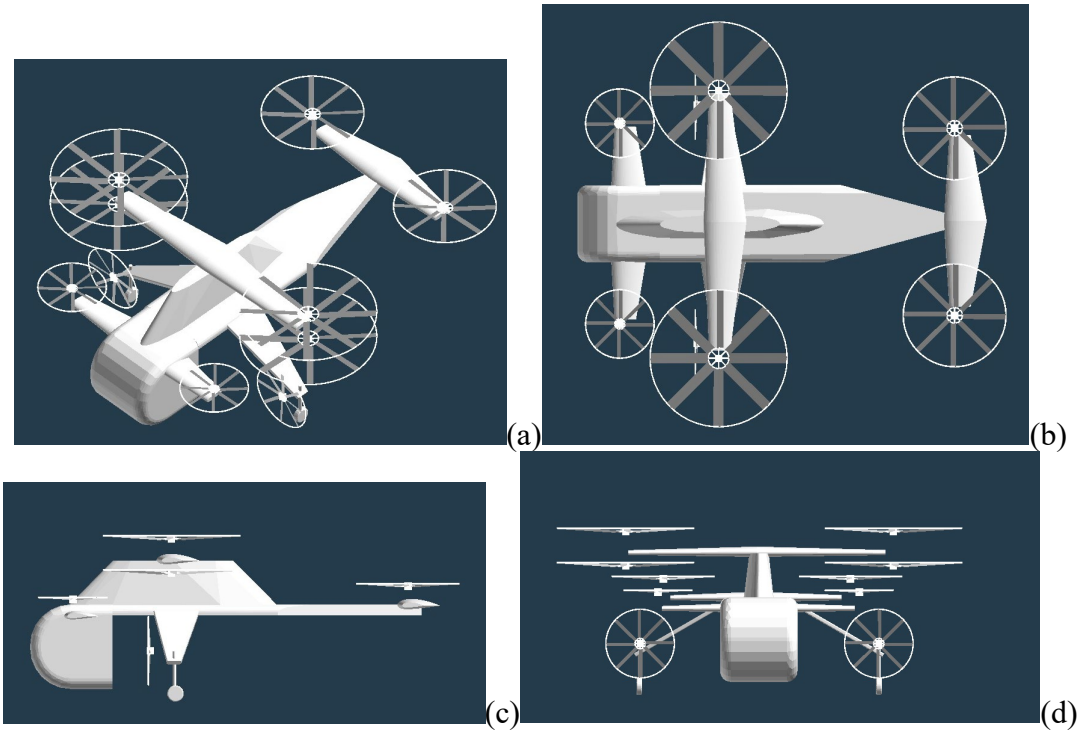

Figure 40. Layout of Notional Multirotor Configuration

Some preliminary mid-fidelity CFD predictions in hover are presented in Fig. 41; isosurfaces of velocity magnitude are shown to illustrate the (multiple) rotor wakes of such a multirotor vehicle.

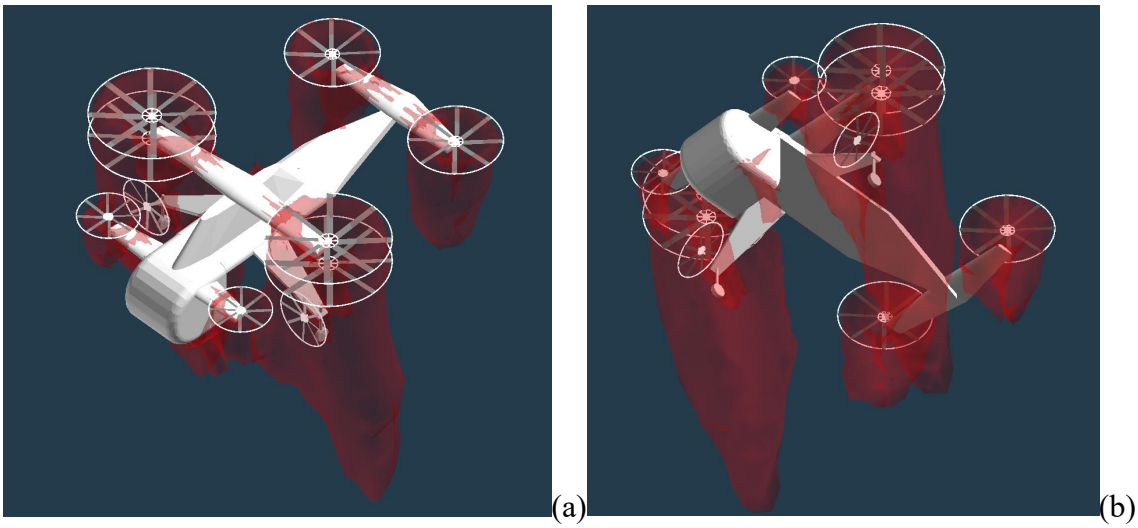

(a) (b)

Figure 41. Preliminary CFD Flow Field Predictions in HOGE (isosurfaces of velocity magnitude to capture rotor wake boundaries)

Some preliminary CFD predictions in edgewise forward-flight for the multirotor vehicle configuration are presented in Fig. 42. Because propulsive propellers are used in this alternate multirotor NN aerial vehicle configuration, the vehicle can be trimmed such that vehicle nose is always level for all forward flight speeds. The rotor wakes are again primarily visualized by showing isosurfaces of nondimensional Q-criterion (versus velocity magnitude as shown for the hover predictions). Additionally, the individual rotors differential pressures are shown as color contours across the rotor disks.

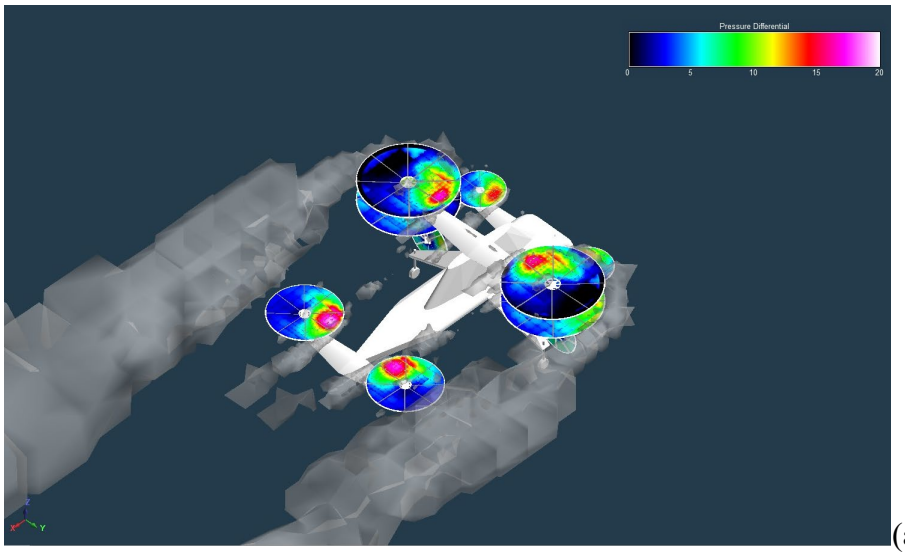

(a)

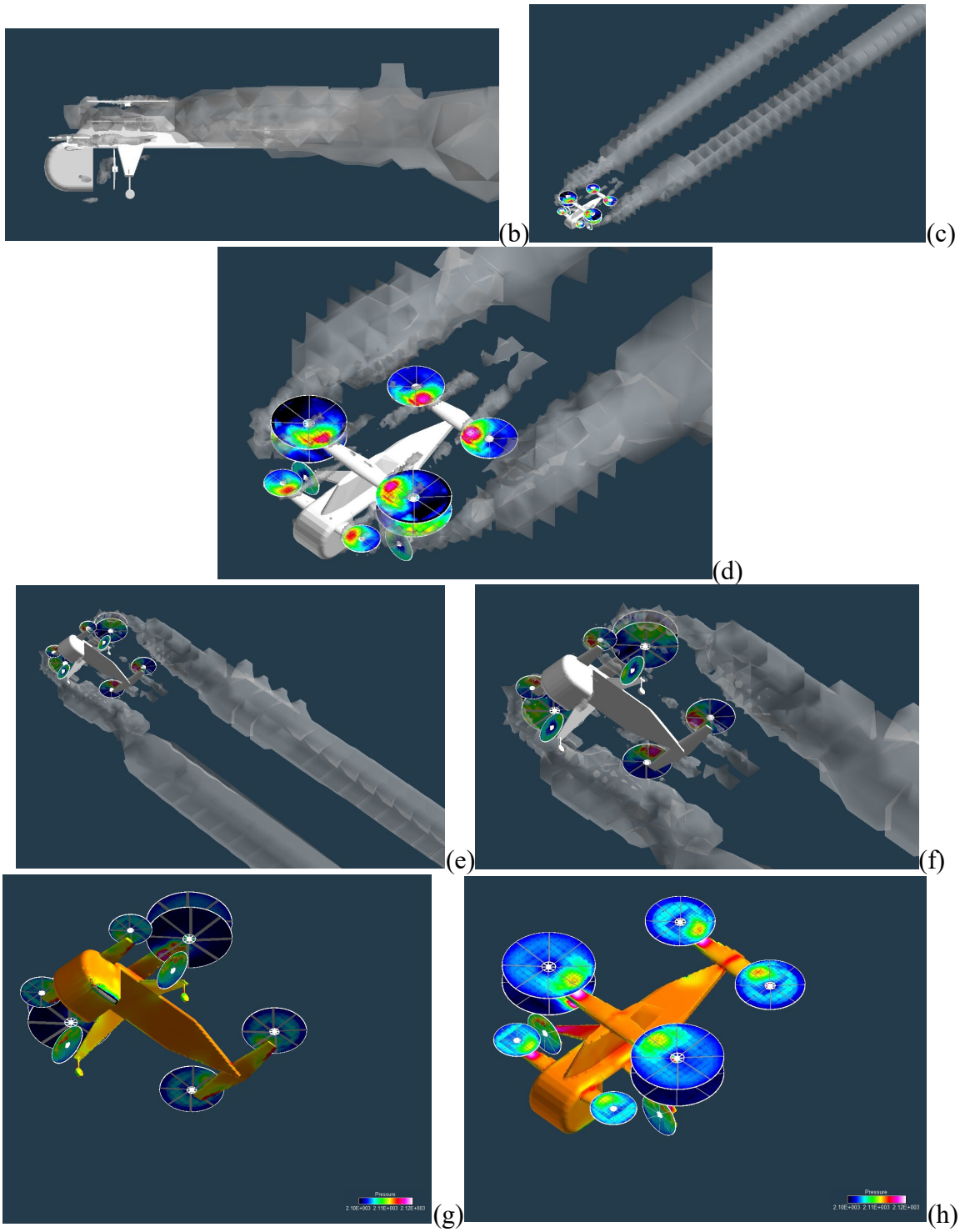

Figure 42. Preliminary CFD Flow Field Predictions in Edgewise Forward-Flight (cruise speed of 150 ft/s; isosurfaces of nondimensional Q-criterion to capture rotor wake vorticity)

Figure 43 illustrates representative vehicle performance as a function of advance ratio for the alternate multirotor configuration carrying a 3000lbf (1360kg) payload and has a fore and aft lifting rotor lift fraction of 0.25 and a main-wing-mounted disk loading ratio of 0.5. Figure 43 presents vehicle performance estimates based on the simple blade element and momentum theory estimates used in the vehicle first-order sizing analysis. The alternate multirotor vehicle configuration is predicted to have significantly less power required for the complete vehicle forward flight speed range, as compared to the baseline SMR vehicle Fig. 28 results. This possibility of improved aerodynamic efficiency of the multirotor versus the single main rotor vehicle is obviously of great interest and needs to be further explored in future work.

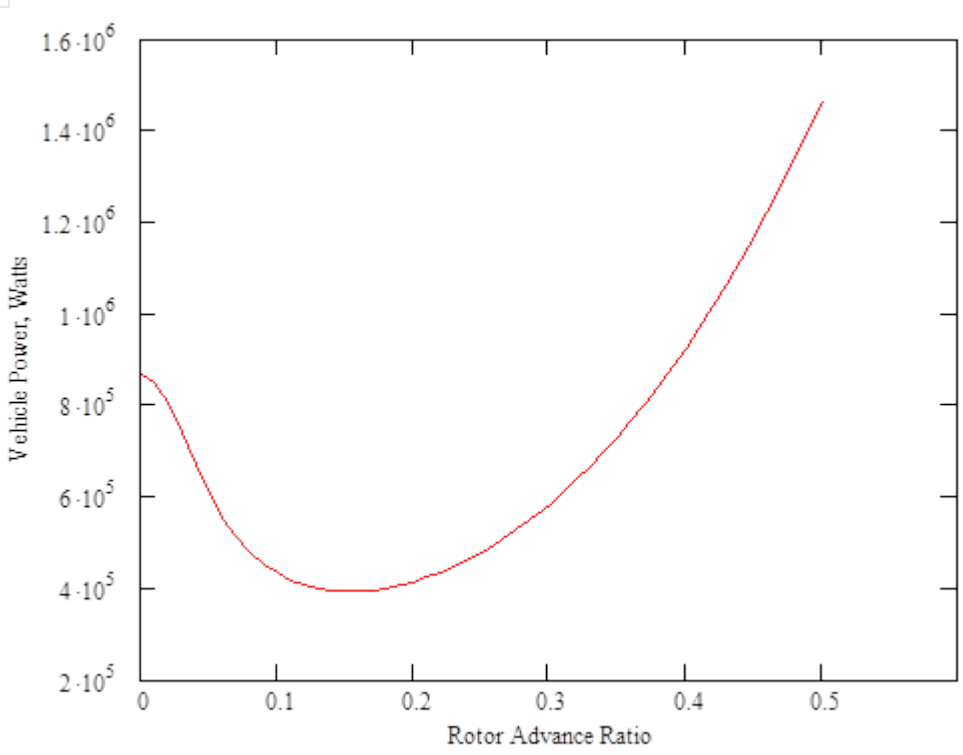

Figure 43. Forward flight vehicle performance: power as a function of forward velocity based on simple momentum theory vehicle performance estimates as used in sizing analysis (3000 lbf (1360 kg) payload)

The rotor/building wake aerodynamic interactions of the alternate short-range multirotor vehicle is now briefly discussed. This type of urban canyon analysis can only, because of the sheer magnitude of the overall problem, be considered a proof-of-concept test case.

Figures 44-45 show the influences of the short-range multirotor vehicle in a representative urban canyon environment. As was shown earlier for the baseline SMR short-range vehicle the multirotor vehicle approaching and descending to a landing pad atop a building under a head-on wind (entertaining shed vorticity from the building rooftop)

is presented in the form of delta rotor/fuselage forces and moments. The longitudinal traverse distance from the vehicle to the building is now scaled against a different reference rotor radius than the baseline SMR scaling shown in Fig. 39. The alternate multirotor vehicle approaches the building edge approximately $x/R_{Max}=22$, Figs. 44-45, instead of the crossing at the crossing occurring approximately $x/R=4$ for the Figs. 38-39 results for the baseline SMR vehicle. However, in both Fig. 39 and Fig. 45, the influence of the approaching and crossing over the building edge (and consequentially encountering the shed vortex on the aft side of the building) does result in a sudden change in the vehicle pitching moments (in both sets of results the rotor(s) are not trimmed and have fixed pitch angles). The two different vehicles, though, do have two different global pitching moment trends: the baseline SMR vehicle has a nose-up pitching moment as the building crosses over the building rooftop and the alternate multirotor vehicle has a next nose-down pitching moment. Further, the alternate multirotor configuration might be more sensitive to building/vehicle wake interactions due to its distributed rotors; this is evidenced by the sudden change in pitching moment occurring further away than comparable absolute longitudinal traverse distance as seen for the baseline SMR vehicle.

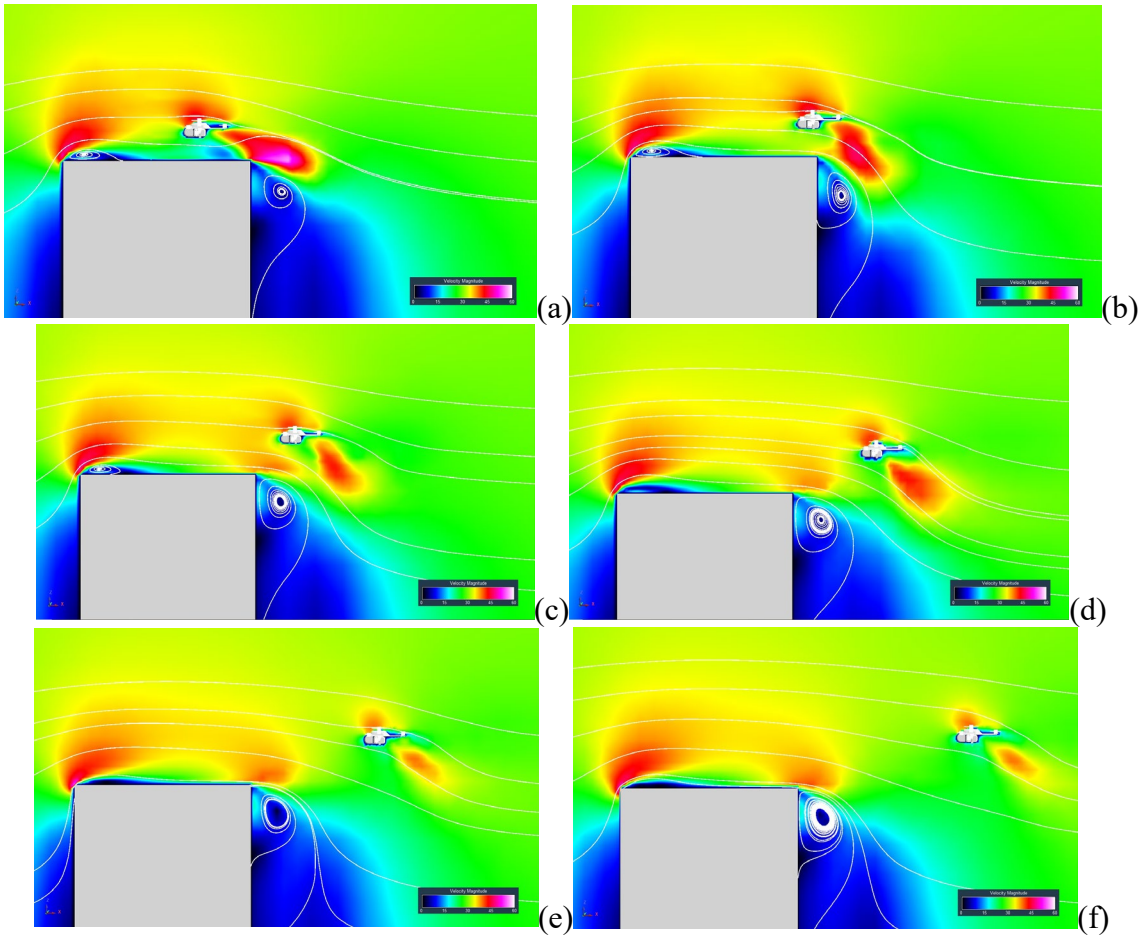

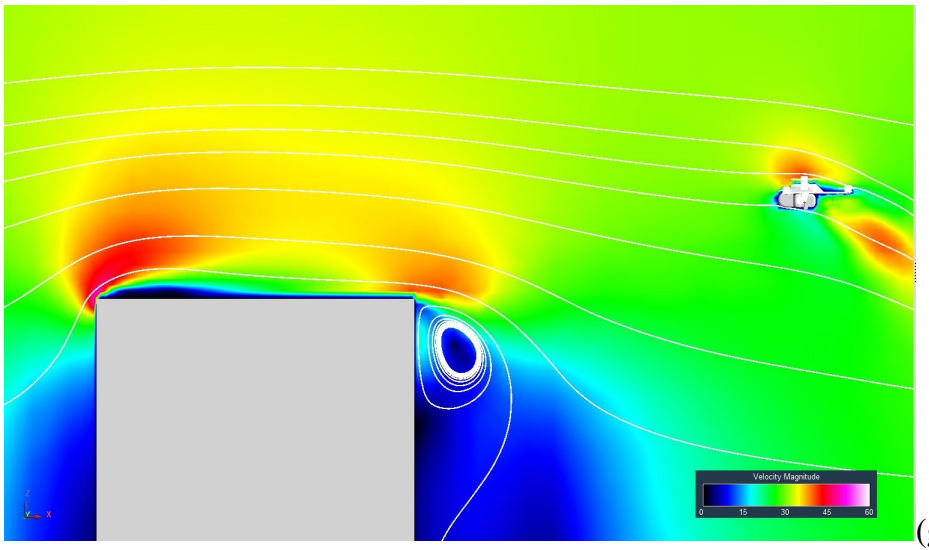

(g)

Figure 44. RotCFD model of urban canyon problem for alternate multirotor vehicle configuration (wind 30 ft/s blowing left to right; vehicle on a six-degree descending glide slope to hover waypoint): (a) $x/R_{max}=0$; (b) $x/R_{max}=6.25$; (c) $x/R_{max}=12.5$; (d) $x/R_{max}=18.75$; (e) $x/R_{max}=25.0$; (f) $x/R_{max}=31.25$; (g) $x/R_{max}=37.5$

The urban canyon problem will be of continuing long-term interest for urban planners, building architects, vertiport developers, as well as urban air mobility, or aka eVTOL, vehicle developers. In this regard, this is not a problem unique to New Nomad vehicles. The habitation aspect of the NN concept, though, might dictate different categories of vertiport and takeoff and landing sites than as compared to other UAM/eVTOL vehicles/networks.

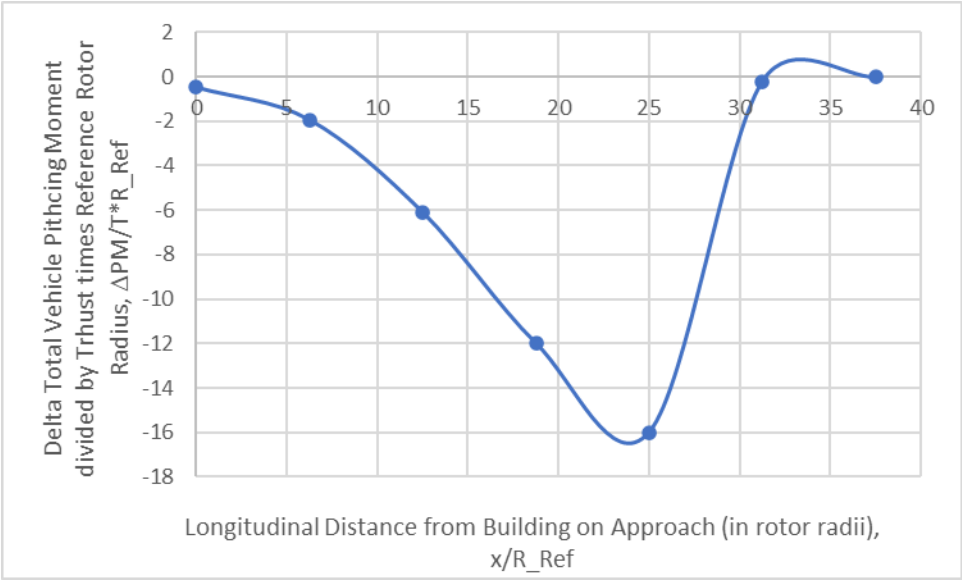

Figure 45. Alternate multirotor vehicle and rotor(s) forces and moments as function of traverses behind a building in a constant wind of 9.1 m/s (30 ft/s)

Similarly, Fig. 46 presents slung-load predictions for the short-range multirotor vehicle. These overall forces are quasi-steady. The slung load problem though is influence by tether movement over time. Ideally, the tether length should be zero to minimize drag, but to deploy the module, with a tether, there be some back-and-forth pendulum-like motion, influenced by wind and vehicle speed/acceleration changes? It is a question for future work as to how loads would change at different points in this back-and-forth motion (if the tether angle is increased between the helicopter and the module).

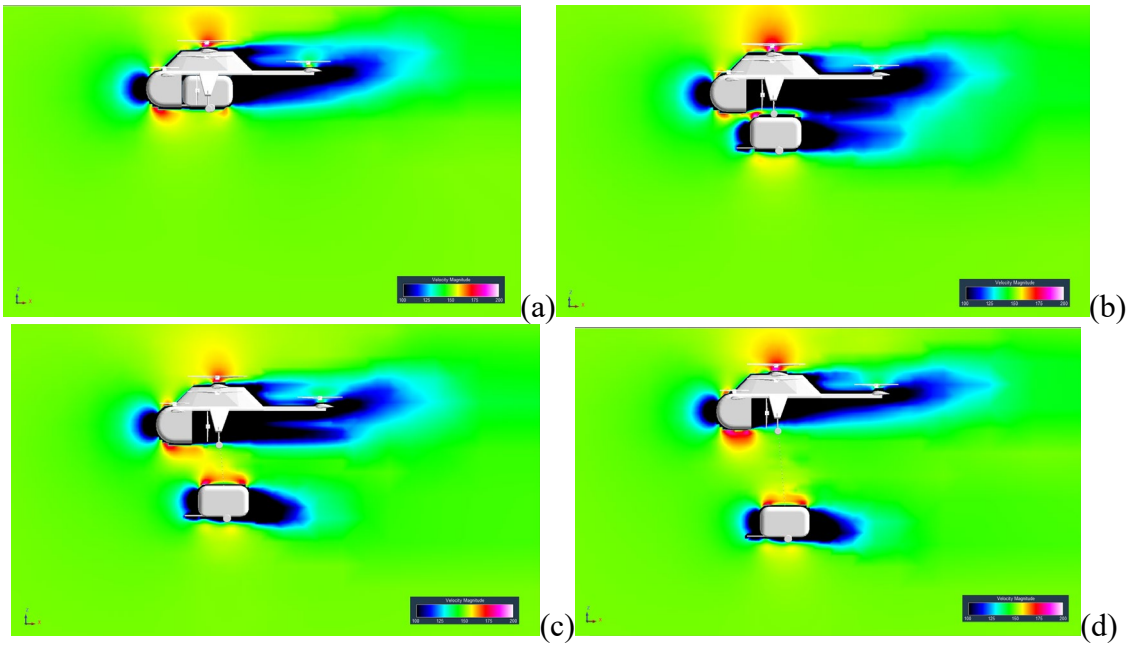

Figure 46. Simple RotCFD model of the alternative multirotor vehicle carrying the habitat module as a slung load: (a) tether length $y/R_{max}= 0$; (b) $y/R_{max}=1.25$; (c) $y/R_{max}=2.5$; (d) $y/R_{max}=3.75$

The slung load tether length trend for the alternate multirotor configuration was like the trend for the baseline single-main-rotor and tail-rotor configuration. The aggregate quasi-steady vehicle vertical force (download) might benefit from using short tethers during slung load transport of the habitat module, but the drag results would suggest that a conformal (zero tether length) stowing of the habitat module is best for overall lowest drag.

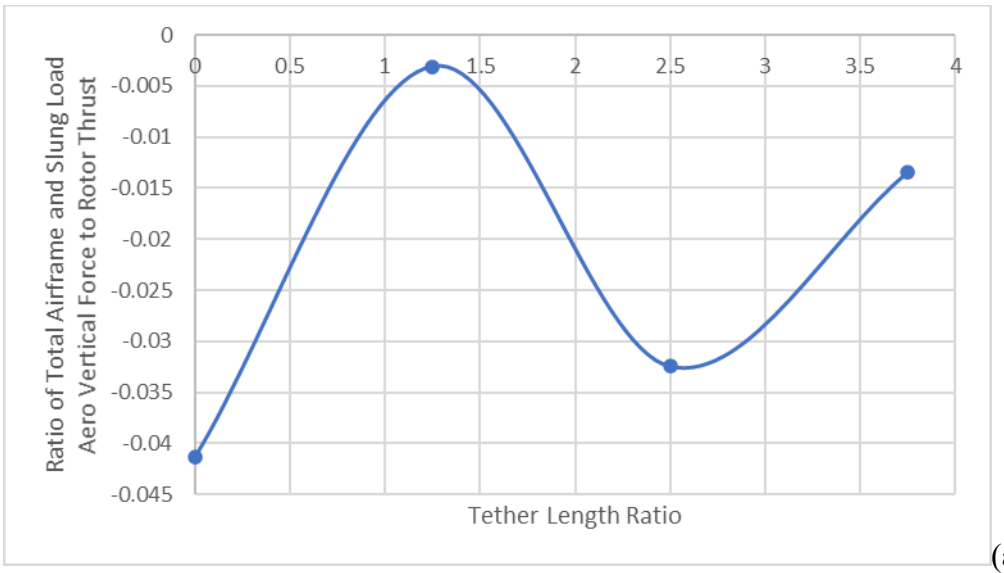

(a)

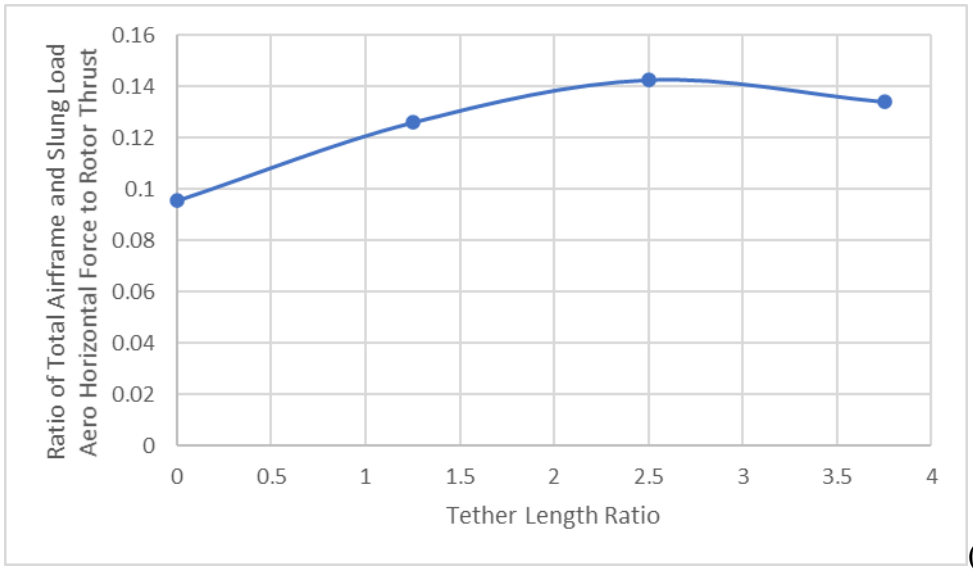

(b)

Figure 47. Drag and download trends of the aggregate alternate multirotor vehicle and suspended habitat module as a function of slung load tether length (nondimensionalized by maximum rotor radii; forward velocity of 150ft/s and a zero-deg. nose down pitch attitude (a) vertical force (download); (b) drag

Aerial Regional/Long-Range Mobility Aeroperformance Analysis

Though there is a considerable amount of attention within the rotorcraft community as to urban air mobility vehicle research (eVTOL, air taxis, etc.), there are still key opportunities to consider regional and therefore longer-range hybrid-electric vehicles. This section of the report will consider these longer-range vehicles in the context of the transport of habitat modules and mid- and large-payload-weight cargo delivery services.

Mission Profile and Design Considerations

In addition to short-range UAM, or eVTOL, vehicles tailored to provide New Nomad habitat module transport capability, longer range vehicles could be contemplated for providing New Nomad transport capabilities to regional (and not just urban) networks. Figure 48b illustrates one notional missional profile for the development of longer-range New Nomad transport aerial vehicle. Figure 48a illustrates a competing (rail) ground mobility option. The yellow shaded area in Fig. 48a-b is intended to reflect two distance metropolitan areas separated by a large distance.

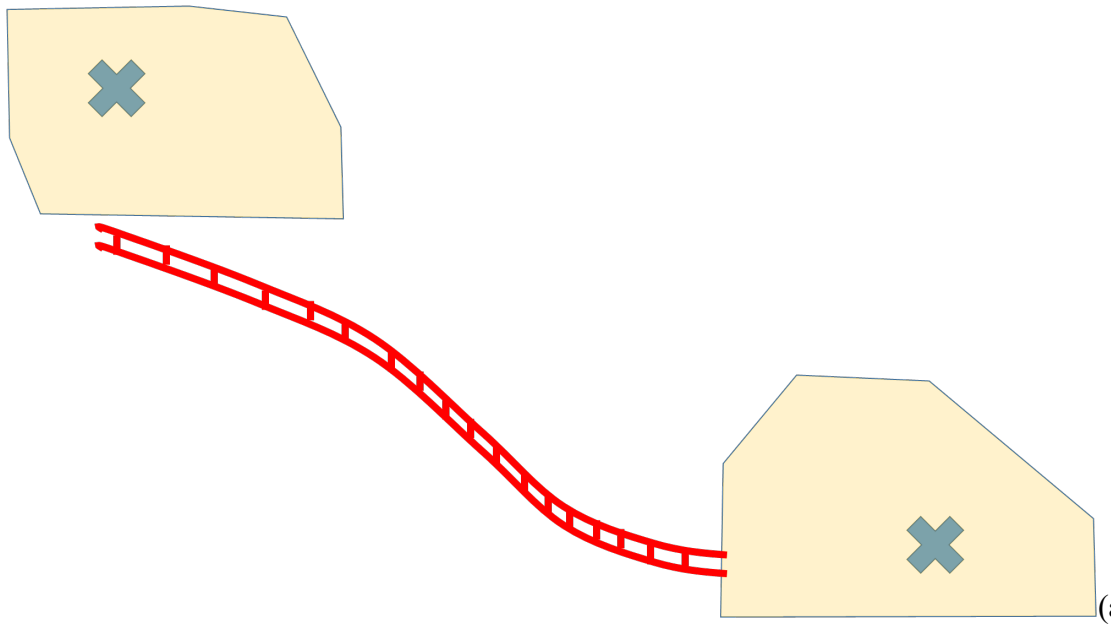

(a)

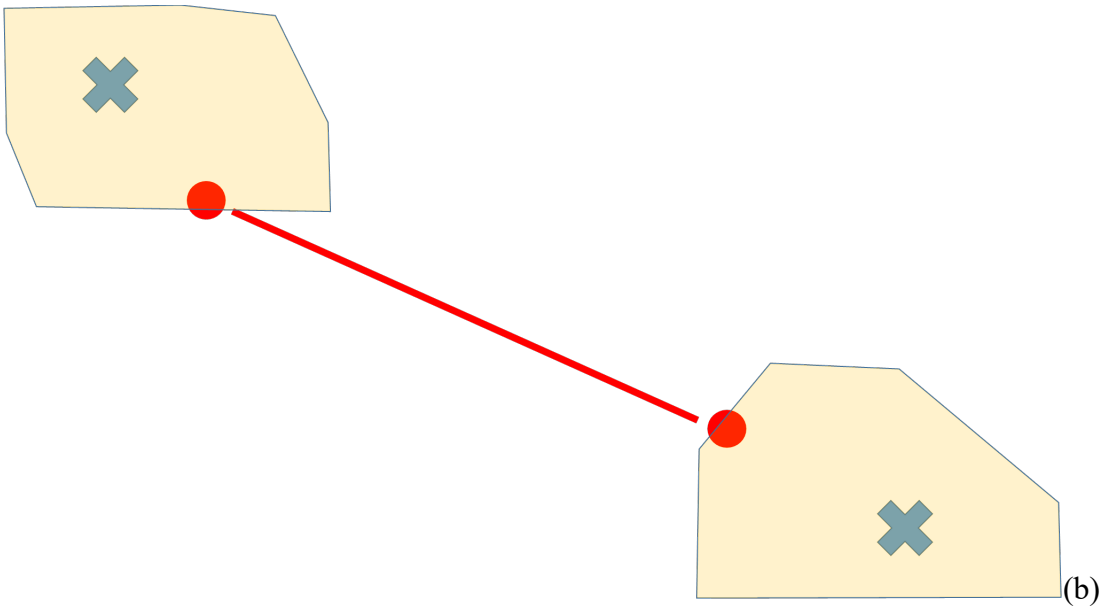

(b)

Figure 48. Competing mobility options: (a) long-range ground mobility only and (b) combination(s) of long-range aerial and ground mobility

The vehicle configuration adopted in this study to examine the New Nomad long-range aerial mobility mission profile is a novel tiltrotor aircraft in which the novelty is primarily manifested in the wide hull (two to three times wider than conventional tiltrotors) used for the aircraft. This wide hull for the tiltrotor aircraft configuration enables easy loading and unloading of multiple habitation modules onboard the aircraft. This aircraft configuration can be notionally thought of as blended-wing-body tiltrotor configuration (BWBT)

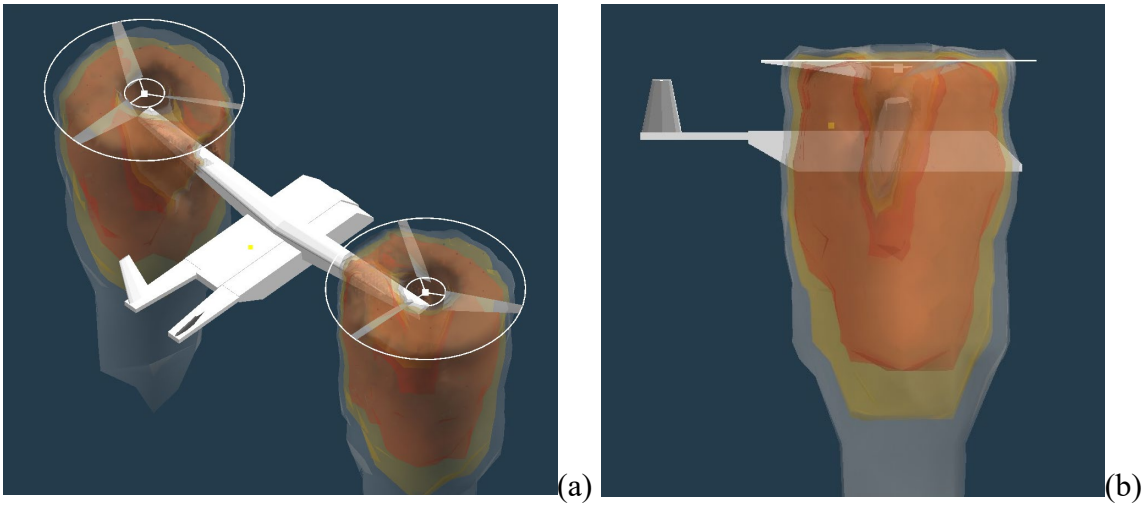

(a) (b)

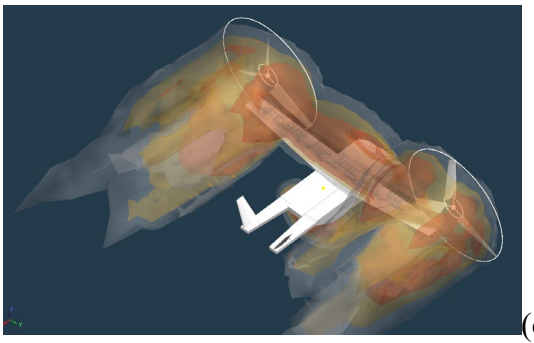
(c)
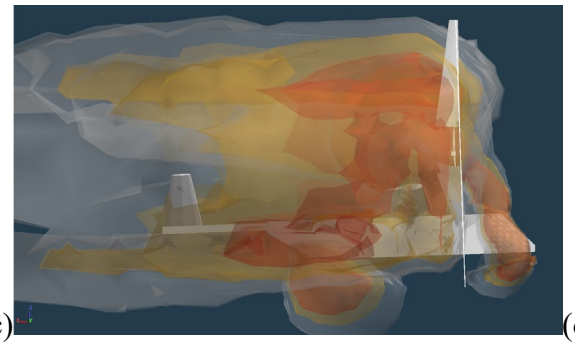
(d)

Figure 49. CFD flow field predictions of the New Nomad tiltrotor aircraft configuration: (a) and (b) hover; (c) and (d) forward-flight cruise

There are downsides with this type of wide hull tiltrotor aircraft configuration: first, the fuselage weight fraction is higher than a conventional 'tube' type fuselage and, second, the parasite drag of the wider fuselage will also be higher than 'tube' type fuselages. The wetted area, S_{wet}, estimates for configuration 1, the fuselage-only and the complete airframe (fuselage and wing) are respectively 3519 and 6510 ft^2. The aspect ratio for the wing is 10.6 and the wing taper is 0.58. The configuration 1 wing planform area is 1327 ft^2. Some initial mid-fidelity RotCFD lift and drag predictions are made for the fuselage-only and the complete airframe (with wings); refer to Figs. 50-51. As can be clearly seen in these figures, the complete airframe lift-to-drag ratios are relatively low and future work is still needed to see if a wide-hull design can be developed that has significantly improved airframe aerodynamic performance. Configuration 1 is quite 'boxy' looking with sharp corners/edges that as a minimum could be more rounded to try arriving at a more streamlined shape. Further, the wing/fuselage joint could probably be significantly improved to reduce high levels of parasite drag. Additionally, both the CAD and CFD models reflect coarse geometries and gridding. This further compound the higher drag predictions resulting from RotCFD.

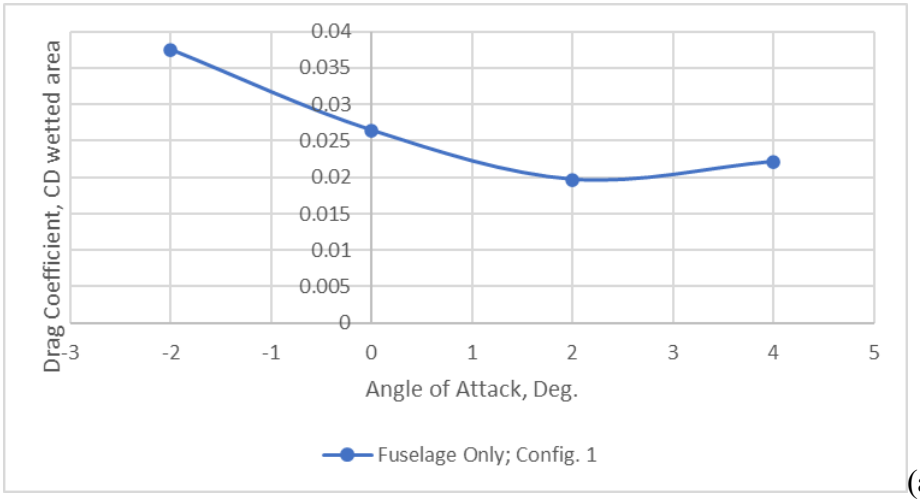

(a)

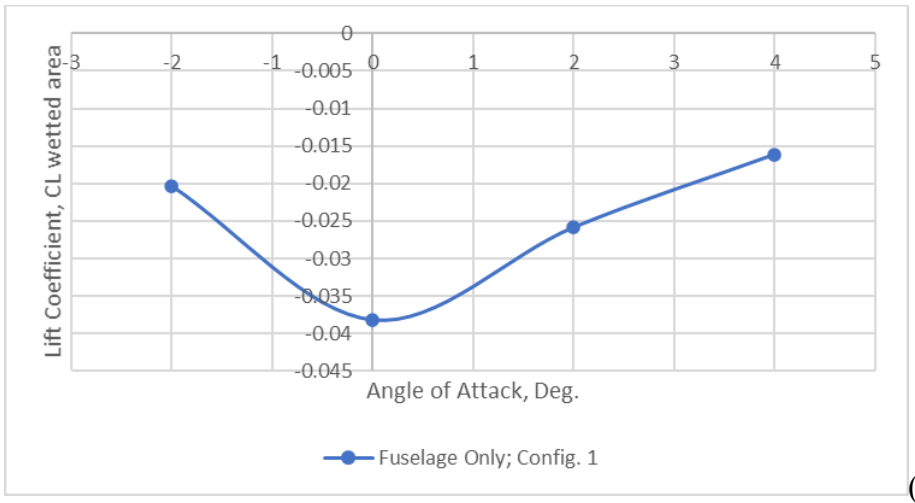

(b)

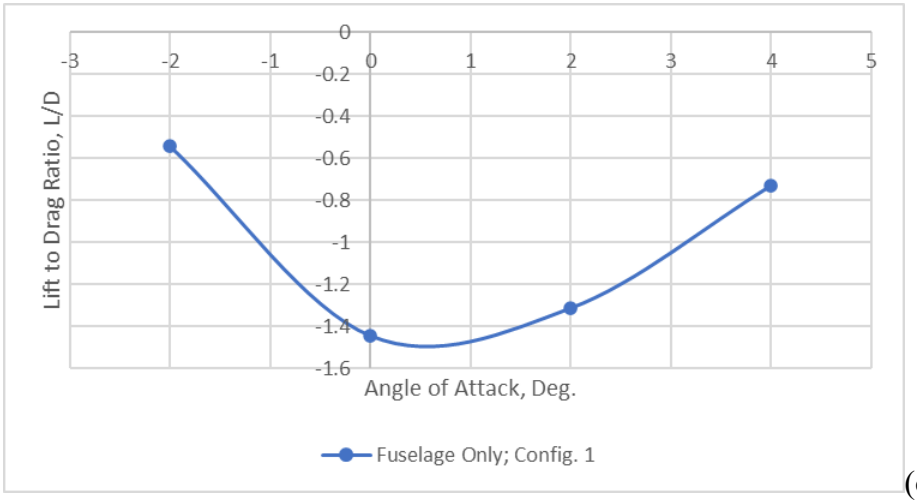

(c)

Figure 50. Fuselage Only Aerodynamics (coefficients based on fuselage wetted area): (a) drag coefficient; (b) lift coefficient; and (c) lift-to-drag ratio versus angle of attack (Configuration 1; coarse grid and low-fidelity CAD model)

Figure 51 presents the RotCFD results for the complete airframe (with wings and proprotor-induced interactional aero effects included). The maximum L/D predicted is only ~3.5 whereas for a good tiltrotor configuration the L/D should be greater than ~7. More work obviously is required to arrive at a cleaner design.

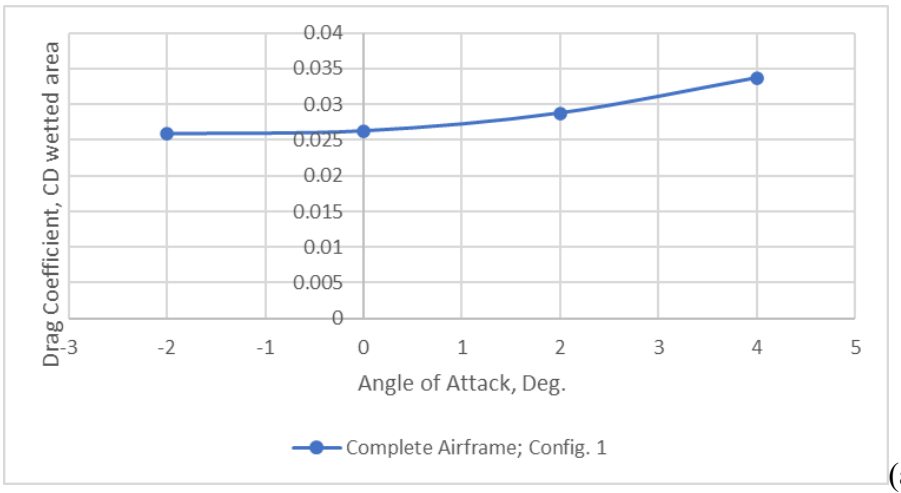

(a)

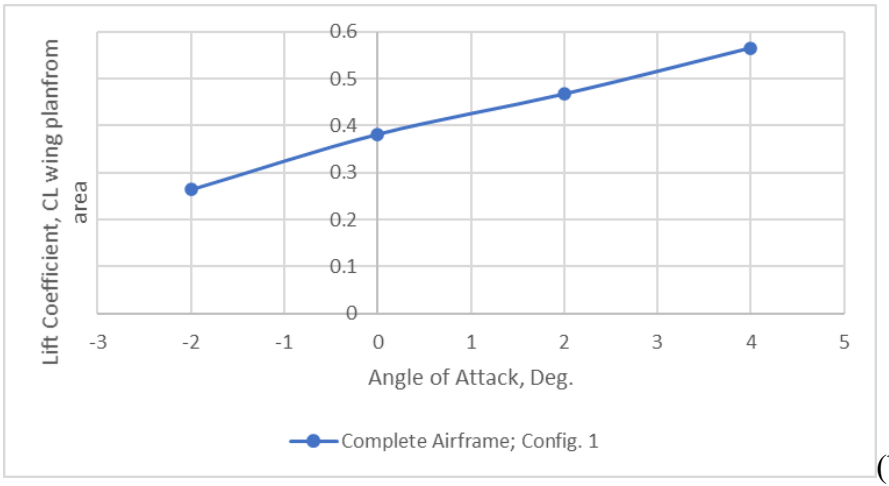

(b)

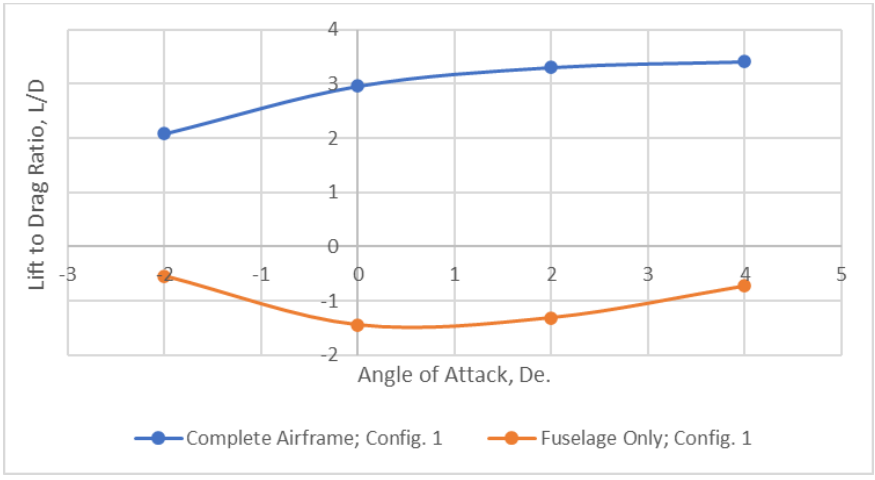

(c)

Figure 51. Complete Airframe (with rotor interactions) Aerodynamics (coefficients based on fuselage wetted area): (a) drag coefficient; (b) lift coefficient; and (c) lift-to-drag ratio versus angle of attack (Configuration 1; coarse grid and low-fidelity CAD model)

The complete airframe $C_{L\alpha}$ is 0.049 Deg^{-1} as approximately derived from the predicted lift to angle of attack results presented in Fig. 51. This is a low estimate of lift curve slope for the wing aspect ratio used in this initial vehicle design. In this initial modeling effort, the coarseness of the gridding yielded only lower accuracy estimates of the complete airframe aeroperformance characteristics. The use of analytic wall-laws to model boundary layer effects on the wings also possibly contributed to lower accuracy. (Additionally, as can be seen in the correlation studies summarized in the appendices, double-precision vs. single-precision GPU operations might need to be performed to arrive at improved drag results. All predictions for the long-range aerial mobility tiltrotor configuration(s) were run with single-precision GPU operations.) Though improved gridding might help with the mid-fidelity CFD results, higher fidelity tools might need to be employed to arrive at more accurate lift and drag estimates and, consequently, better guide improved vehicle airframe configuration designs.

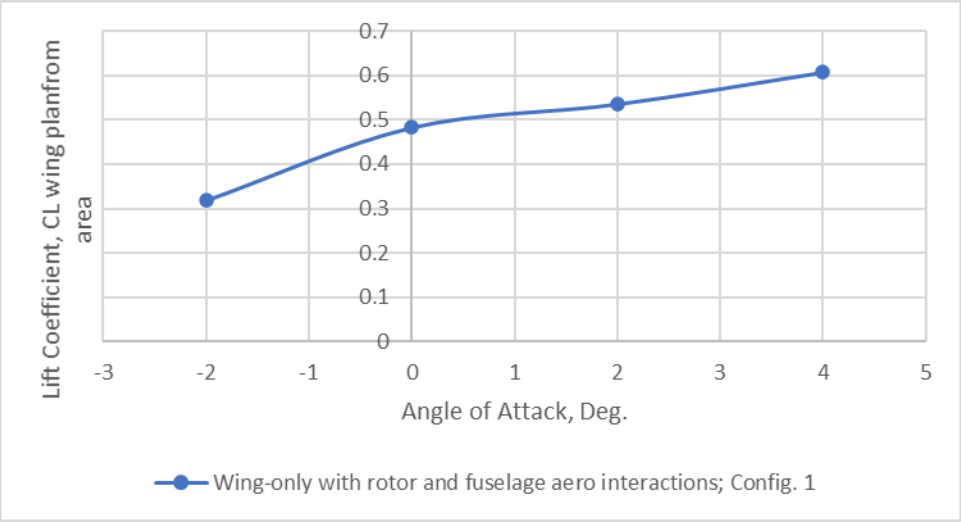

Figure 52. Wing Only (but still with fuselage and rotor aerodynamic interference effects) Aerodynamics; lift coefficient versus angle of attack

Figure 52 presents the lift-curve for configuration 1 for the wing-only (but still with fuselage and rotor-induced aerodynamic interference effects); the estimated $C_{L\alpha}$ is 0.046 Deg^{-1}. Accordingly, there is only a relatively small difference between the predictions of the airframe lift-curve-slope and the wing-only slope.

To better understand some of the implications of the vehicle modeling and CFD gridding on the performance estimates a slightly modified "configuration 2" model was subsequently studied, in addition to the original "configuration 1" airframe. The wetted area, S_{wet}, estimates for configuration 2, the fuselage-only and the complete airframe (fuselage and wing) are respectively 3519 and 6037 ft^2. The aspect ratio for the wing is 12.8 and the wing taper is 0.87. Configuration 2 wing planform area is 1117 ft^2. Configuration 2 only differs from configuration 1 because of the smaller chord wing – and

the higher fidelity CAD and finer CFD gridding employed as compared to the earlier work. (Even with the finer gridding, the trailing edge of the wing is still a bit jagged; this is a consequence of the limitations of the automated gridding of the RotCFD tool for wing-like surfaces with sharp trailing edges.)

The wing uses sectional coordinates for a four-digit NACA 4424 airfoil. The predicted wing-only (with and without interactional interference effects from the rotors and the fuselage) lift curves as a function of angle of attack are reasonably linear as anticipated, but the lift curve slopes still seem to be significantly below their theoretical values (~0.068 deg.$^{-1}$ versus ~0.1 deg.$^{-1}$). This is an area for future study for RotCFD predictions of wing/tail-surfaces.

Figure 53a-c presents the fuselage-only predicted aerodynamics of Configuration 2 of the long-range aerial vehicle; a combination blended-wing-body and tiltrotor or (BWBT).

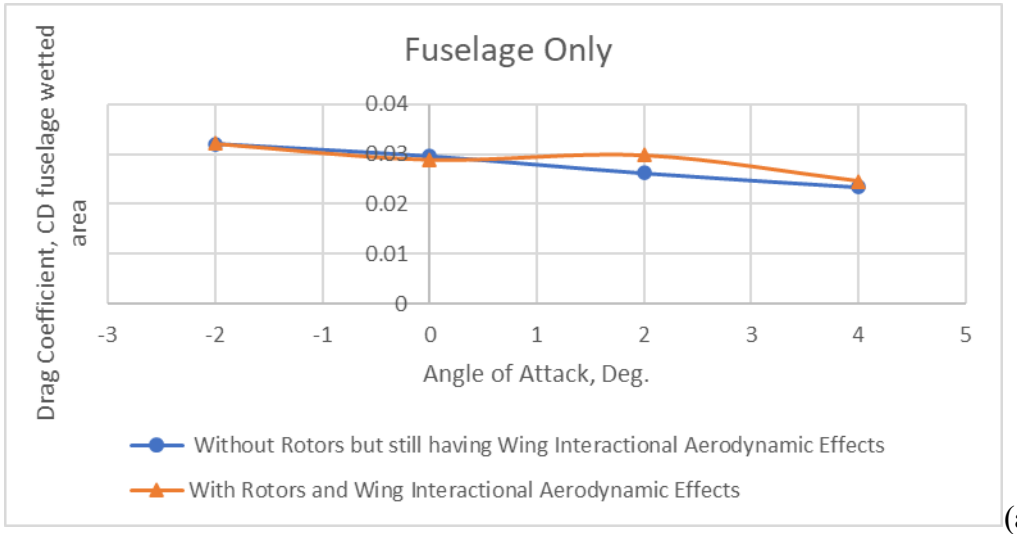

(a)

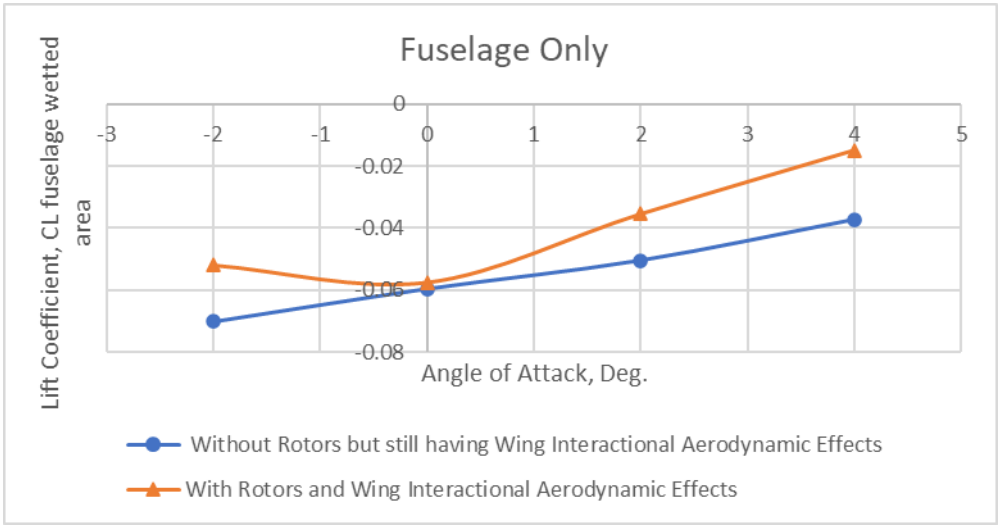

(b)

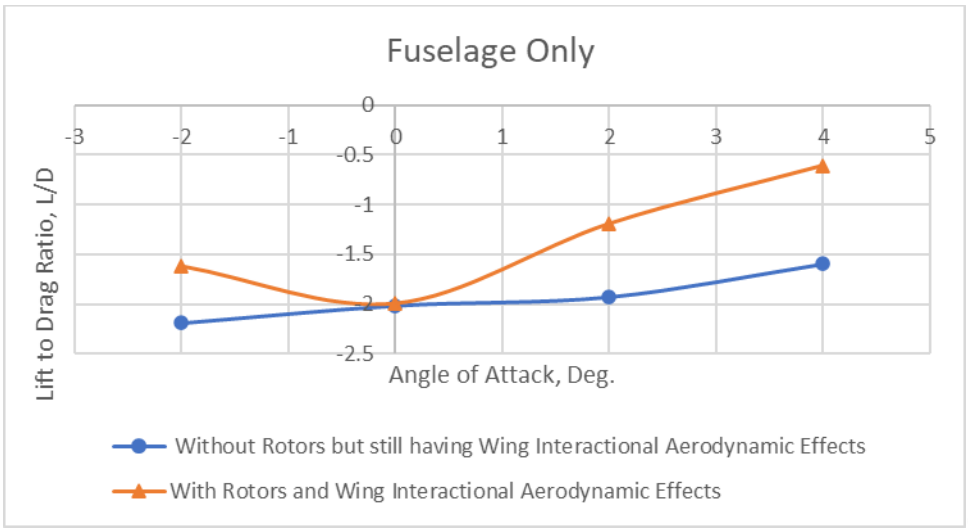

(c)

Figure 53. Fuselage-Only (with wing and with and without rotor aerodynamic interference effects) Aerodynamics of Configuration 2: (a) drag coefficient versus angle of attack; (b) lift coefficient versus angle of attack; (c) lift-to-drag ratio versus angle of attack. (Fine grid and higher-fidelity CAD model of the wing.)

Figure 54a-c presents the complete airframe aerodynamics of the Configuration 2 BWB-tiltrotor (BWBT).

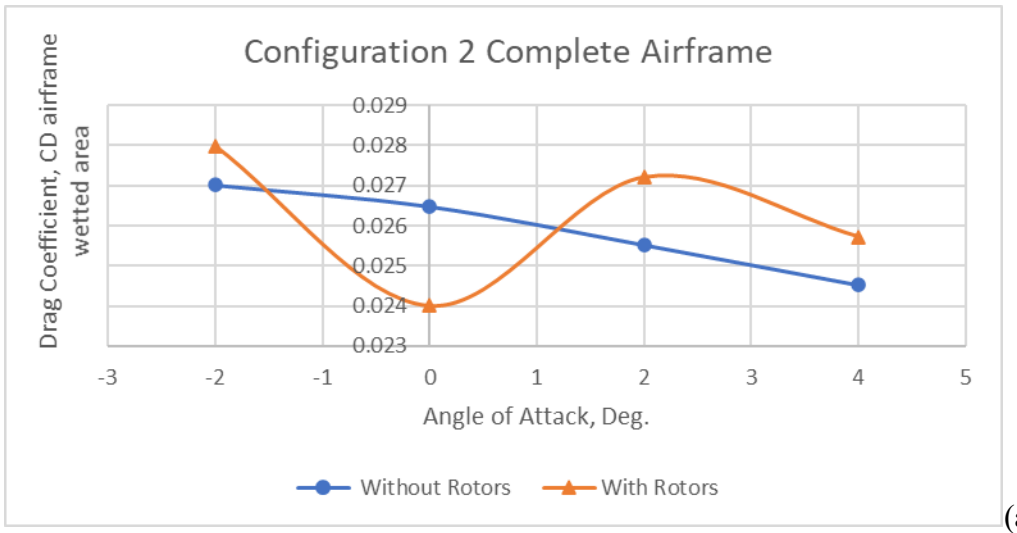

(a)

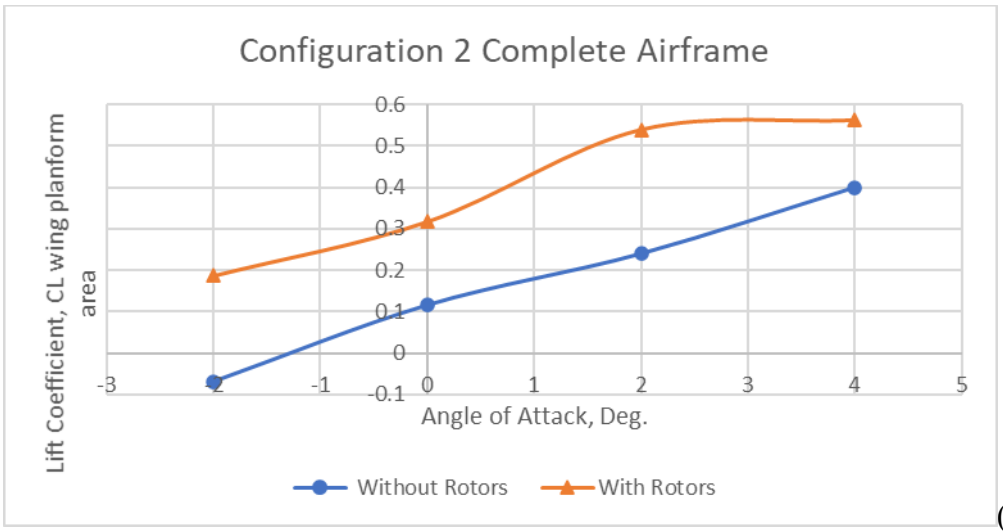

(b)

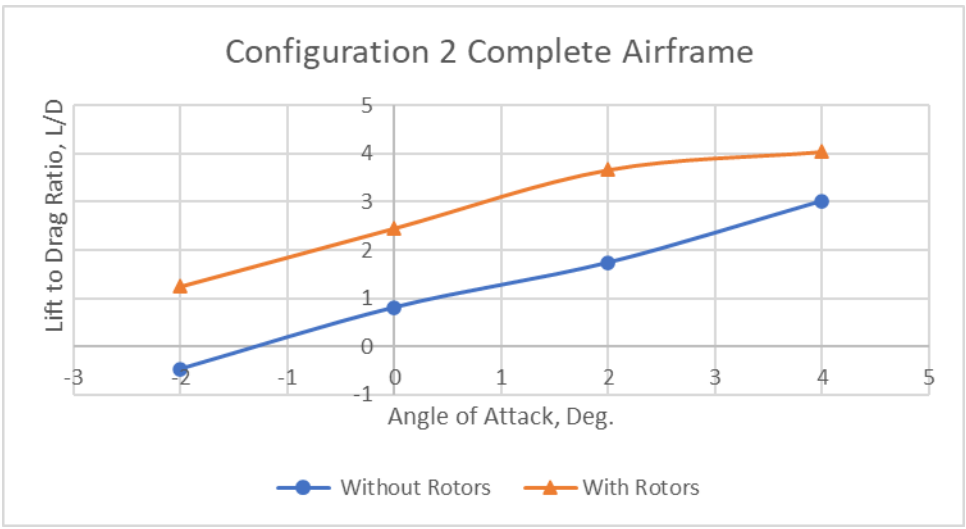

(c)

Figure 54. Complete Airframe Aerodynamics of Configuration 2: (a) drag coefficient versus angle of attack; (b) lift coefficient versus angle of attack; (c) lift-to-drag ratio versus angle of attack. (Fine grid and higher-fidelity CAD model of wing)

Figure 55a-c is the wing-only (but still with rotor and fuselage interference effects included) predicted aerodynamics of Configuration 2 BWB-tiltrotor. With the higher fidelity CAD of the wing and the increased fineness of the gridding, the wing-only L/D's begin to increase to more reasonable values.

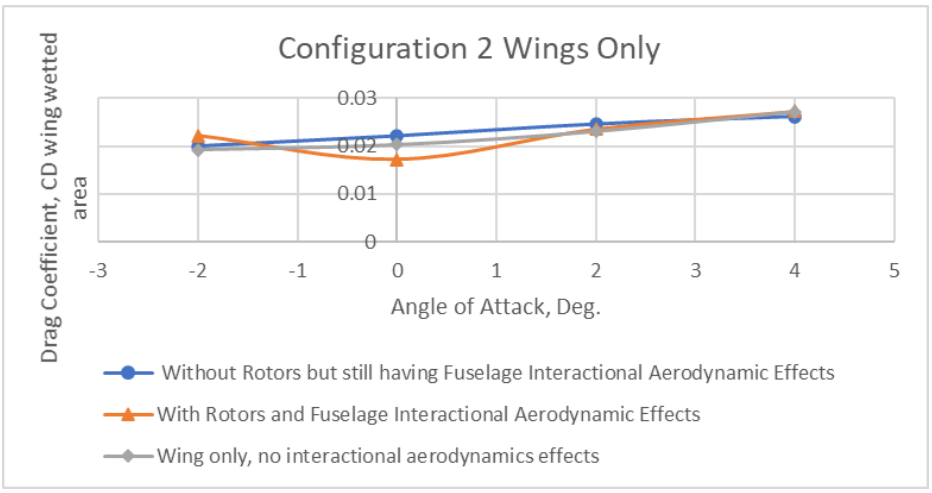

(a)

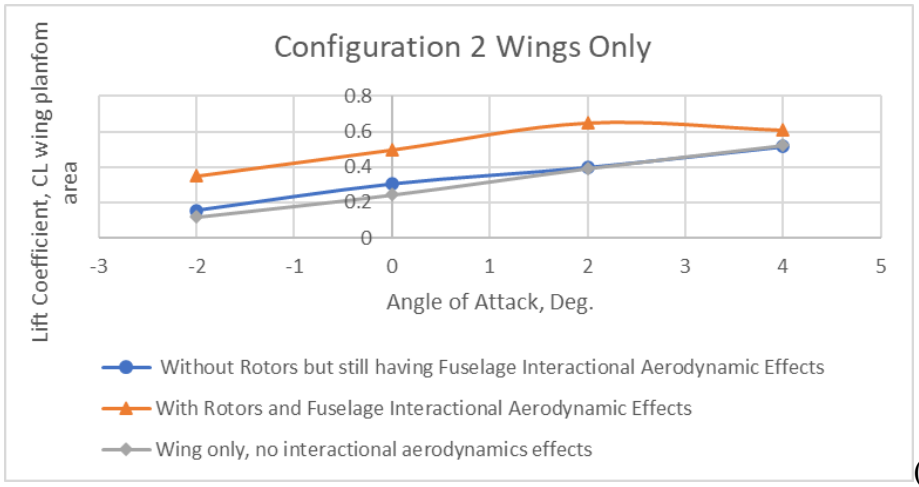

(b)

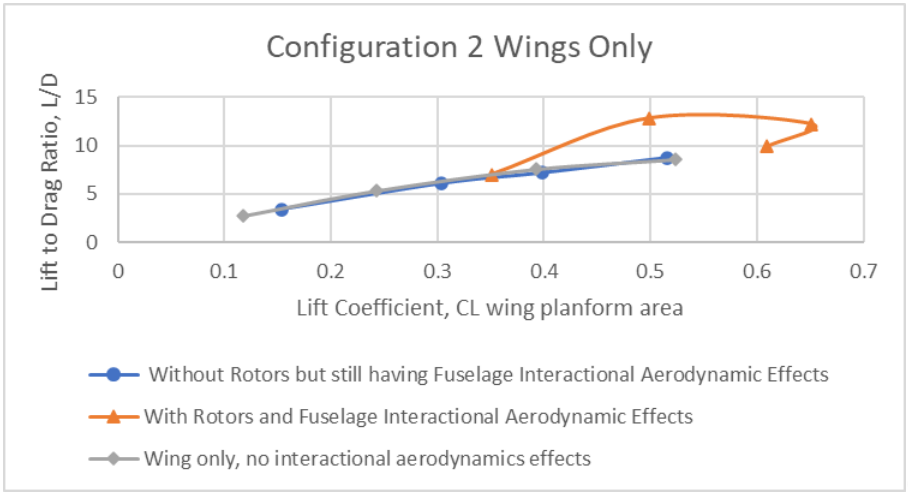

(c)

Figure 55. Wing-only Aerodynamics of Configuration 2: (a) drag coefficient versus angle of attack; (b) lift coefficient versus angle of attack; (c) lift-to-drag ratio versus angle of attack. (Fine grid and higher-fidelity CAD model of the wing)

Habitat Module Design Considerations

Figures 56-58 present some notional interiors of various habitat module types. A high degree of automation and furniture and appliances reconfigurability is assumed for all types of modules. Reference 50 touches on some of the same transformation of transportation to office/living space. In the case of Ref. 50, it discusses the speculation of self-driving cars being transformed, or transitioned, to office spaces. The habitat modules proposed in this work take this paradigm even further into the aviation sector and not just the automotive sector.

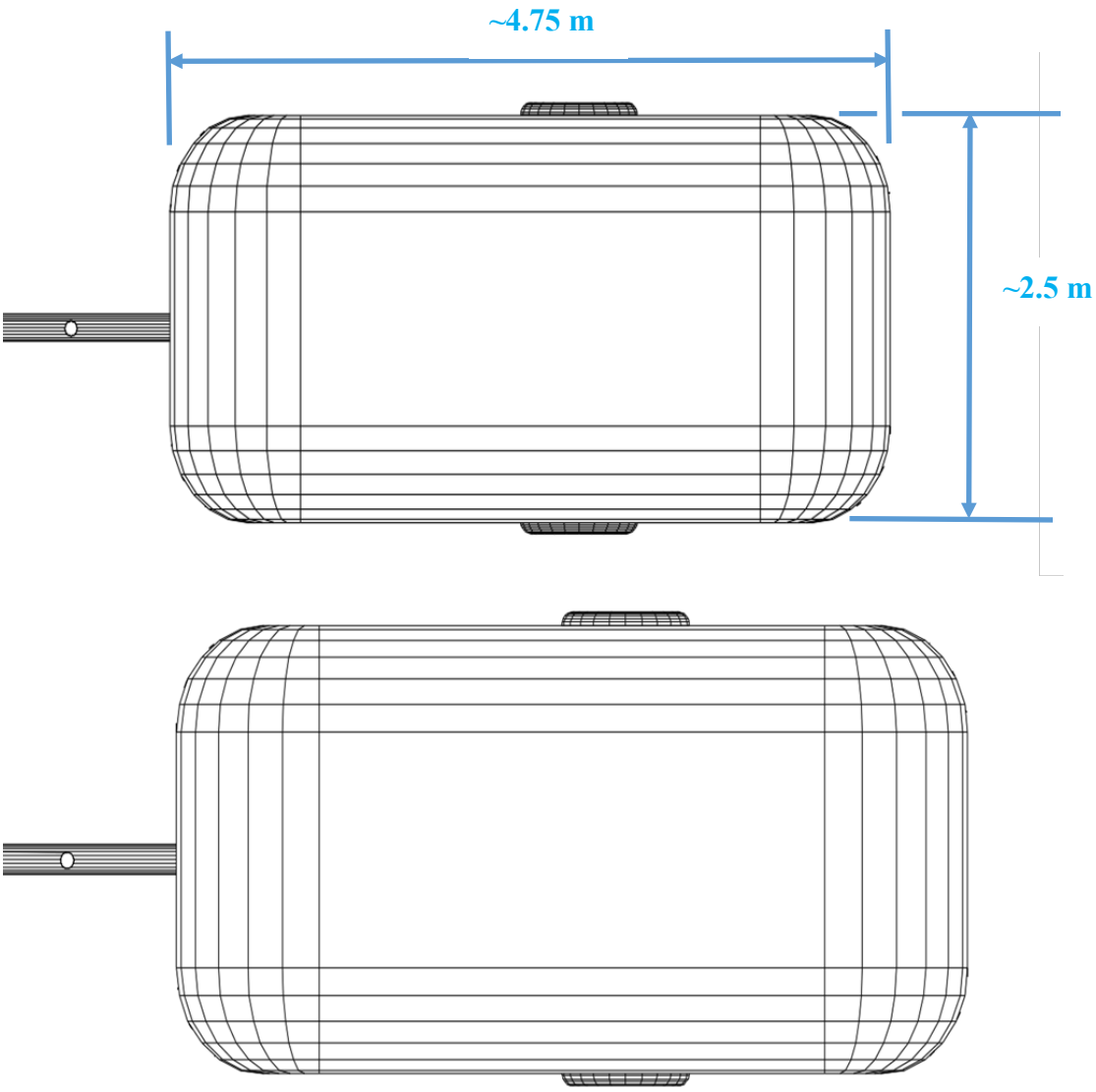

Figure 56. Habitat Modules of Different 'Stretched' Sizes and Functions

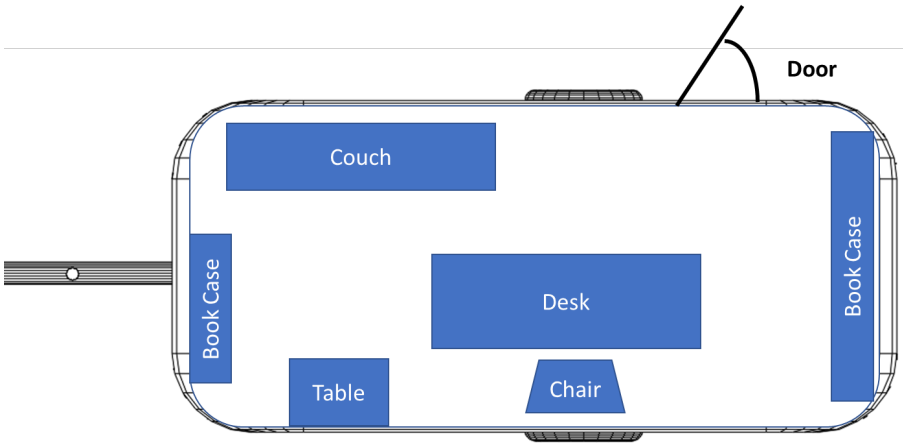

Figure 57. Small Habitat Module, Office Configuration

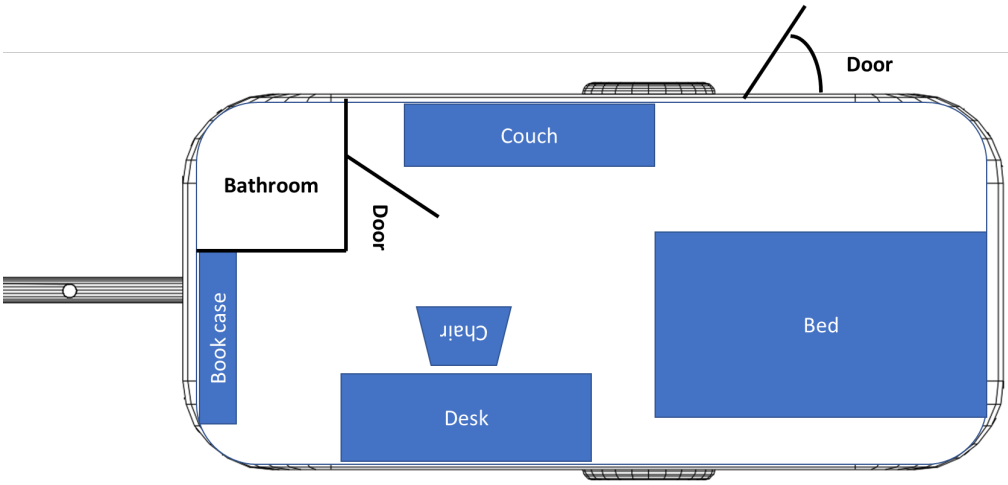

Figure 58. Stretched Habitat Module, Living Space Configuration

Advances in mechanical design as influencing lightweight, compact, and perhaps stowable furniture design (partly influenced by the 'tiny home' movement), coupled with advances in "intelligent furniture" (e.g., Refs. 34-36) and "smart home" technologies offer key opportunities to develop habitat modules for office and living spaces. A key interior design challenge for the habitat module is the ability to efficiently and speedily 'stow' furniture and other contents in the module in a suitable manner to allow for ground and

aerial transport of the module. Finally, large LED wall display panels and the availability of low-cost and high-resolution cameras allow for an alternate interior display arrangements as compared to conventional windows. Using such display panels could result in lighter-weight, more rigid, and structurally more sound habitat modules than if, instead, windows had to be incorporated.

Swappable Propulsion Energy Systems Module Design Considerations

Most of the focus of urban air mobility system studies have focused on all-electric systems, most of which are battery-based with the remainder investigating fuel-cell systems. Hybrid-electric systems are also being explored but are mostly focused on regional type transportation systems. Largely unexplored is the possibility of swappable (swap-out-able) propulsion energy system modules that can be replaced, on a per flight basis, so that the vehicle can be flown either as an all-electric or, alternatively, a hybrid-electric system. Such per flight mission flexibility has potentially tremendous advantages. (This approach has potential if the hybrid-electric concepts proposed convert all combustion-based energy to electric energy in the process of going from energy storage to power supplied to the rotors.) The only known previous discussion of this swappable propulsion energy system concept was Ref. 9.

Figure 59 illustrates some high-level graphics of this notional swappable propulsion energy system concept.

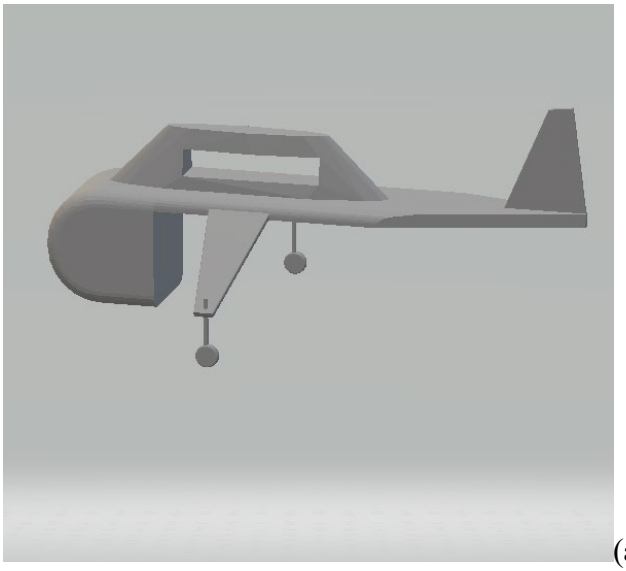

(a)

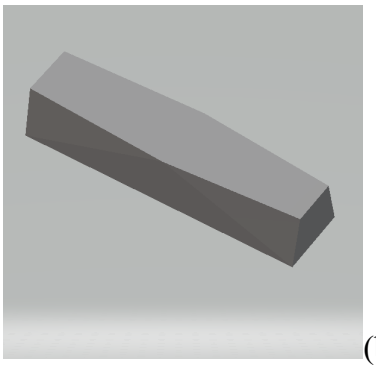
(b)
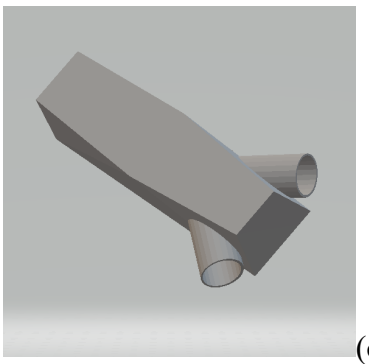
(c)

Figure 59. Swappable propulsion energy system concepts schematics: (a) propulsion-module 'cut-out' in vehicle pylon; (b) all-electric battery-pack propulsion-module; (c) hybrid-electric turboshaft-generator propulsion-module

Simple Rotorcraft Sizing (SRS) of Baseline Short-Range Vehicles as a function of habitat module size/weight

A spreadsheet-style, first-order rotorcraft sizing analysis (custom-built in the MathCAD commercial software tool, Ref. 54) was developed and exercised to conceptually design a short-range single-main rotor heavy-lift helicopter for carrying habitat modules for various notional sizes and weights. All designs considered only vehicles with all-electric propulsion with batteries. The rotorcraft sizing analysis weight equations and methodology are primarily drawn from Refs. 37-38. The vehicle aerodynamic performance draws on simple blade element momentum theory models, augmented in part by RotCFD performance estimates. Overall, this methodology is referred to in this report as Simple Rotorcraft Sizing (SRS).

A first-order validation of the simple rotorcraft sizing analysis used in this report was performed by considering the small single-main-rotor (with NOTAR – versus tail rotor – and twin (two) turboshaft engines) UAM design reported in Ref. 33 using the NASA NDARC sizing tool, Ref. 31; this Ref. 33 conceptual design is referred to as the QSMR (quiet single main rotor). The resulting agreement is reasonable for the purposes of this report.

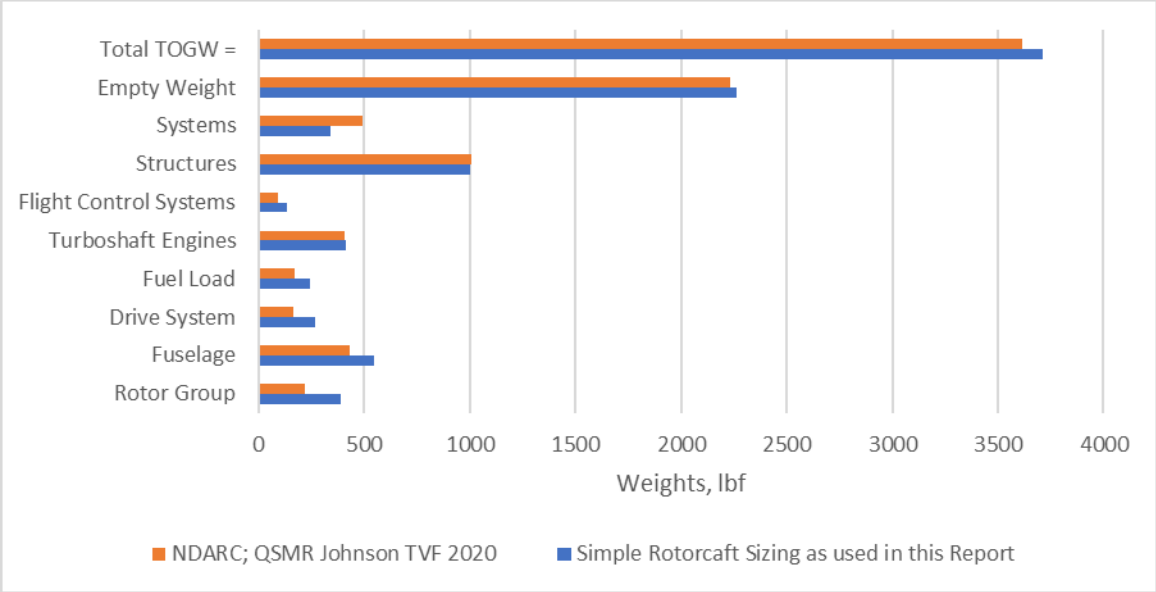

Figure 60. Cross-validation of this work's Simple Rotorcraft Sizing (SRS) versus the NDARC sizing analysis (Ref. 31) for Ref. 33 QSMR single main helicopter reference design

First-order sizing is performed for habitat module sizes (or rather longitudinal length spans; the module cross-sectional area is assumed constant): 50% span, 75% span, 100% span, 125%, and 150% span. The weight for each differently sized habitat module is estimated on the basis of assuming a constant effective 'structural density,' which acknowledging the constant cross-sectional area assumption, yields the linear relationship of $W_{Habitat} = W_{100\%spanHabitat} \cdot (Span\%/100\%)$. Based on a brief perusal of existent automotive-towed campers, a value of$W_{100\%spanHabitat} = 3000lbf = 1364kg$ is used. Correspondingly, the physical longitudinal length span of the various habitat modules is $Span = \ell_{100\%span} \cdot (Span\%/100\%)$. The baseline module 100% span is assumed to be 20ft or 6.1m. In addition to the habitat module weight is also assumed that two passengers and a small amount of luggage (but no crew/pilot, as the vehicle is assumed autonomous in operation) are carried in the vehicle's forward (permanent) cabin, this would give a passenger weight of $W_{Passengers} = 500lbf = 227kg$. The mission profile, used for all vehicle sizing performed, is comprised of three primary phases. Additionally, some of the key assumptions for the mission profile are: (a) the vehicle will be deployed from a depot site to the initial passenger/habitat pick-up site; (b) recharging is not feasible at the passenger destination site (where the passengers and the habitat are dropped off); (c) the vehicle has to return to, or fly to an alternate, depot site for recharging and future deployments. The mission profile is shown in Fig. 61. Note that the ranges used in the mission profile are all relatively short range, reflecting the emphasis of transportation in an urban or metropolitan regional area (as well as the emphasis on all- or hybrid-electric propulsion for the vehicles considered in this report). Greater distances would have to draw on multi-modal transportation services for the passengers and habitat modules or rely on longer-range aerial mobility options as discussed earlier in the study.

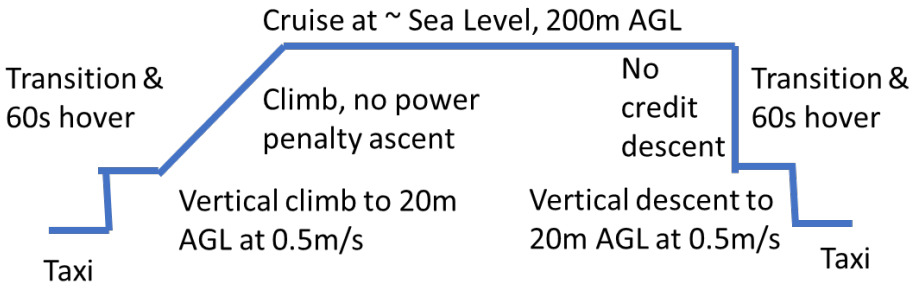

Figure 61. Baseline simple mission profile for New Nomad SRS sizing exercise

Tables 4-9 present some initial all-electric sizing results for the baseline SMR New Nomad short-range aerial mobility vehicles for different habitat module payload weights.

Table 4 – Baseline Single Main Rotor and Tail Rotor Configuration, All-Electric Battery Propulsion, 455 kg (1000 lbf) Payload

Main Rotor Disk Loading	324.4	N/m^2
Main Rotor Radius	4.82	m
Number of Blades	4	nondim.
Main Rotor Solidity	0.04	nondim.
Main Rotor Tip Speed	238.21	m/s
Number of Motors/Engines per Rotor	1	nondim.
Hover Power	450.28	kW
Advance Ratio	0.21	nondim.
Nominal Forward Flight Power	312.1	kW
Tail Rotor Radius	1.07	m
Payload (Passenger(s) and Habitat Module)	454.5	kg
Weight of Rotor Blades	80.7	kg
Main Hub and Hinges	47.3	kg
Fuselage	205.7	kg
(Skid Type) Landing Gear	36.3	kg
Drive System	150.8	kg
Batteries	672.1	kg
Auxiliary Power Systems	134.4	kg
Electric Motors	292.4	kg
Propulsion Subsystems	64.3	kg
Flight Control Systems	63.9	kg
Total TOGW =	2202.5	kg

Table 5 – Baseline Single Main Rotor and Tail Rotor Configuration, All-Electric Battery Propulsion, 682 kg (1500 lbf) Payload

Main Rotor Disk Loading	324	N/m^2
Main Rotor Radius	5.9	m
Number of Blades	4	nondim.
Main Rotor Solidity	0.04	nondim.
Main Rotor Tip Speed	238	m/s
Number of Motors/Engines per Rotor	1	nondim.
Hover Power	665.2	kW
Advance Ratio	0.21	nondim.
Nominal Forward Flight Power	461	kW
Tail Rotor Radius	1.3	m
Payload (Passenger(s) and Habitat Module)	682	kg
Weight of Rotor Blades	127.5	kg
Main Hub and Hinges	69.8	kg
Fuselage	329.9	kg
(Skid Type) Landing Gear	53.6	kg
Drive System	224.0	kg
Batteries	992.8	kg
Auxiliary Power Systems	198.6	kg
Electric Motors	396.4	kg
Propulsion Subsystems	87.2	kg
Flight Control Systems	90.1	kg
Total TOGW =	3251.8	kg

Table 6 – Baseline Single Main Rotor and Tail Rotor Configuration, All-Electric Battery Propulsion, 909 kg (2000 lbf) Payload

Main Rotor Disk Loading	324.4	N/m^2
Main Rotor Radius	6.83	m
Number of Blades	4	nondim.
Main Rotor Solidity	0.04	nondim.
Main Rotor Tip Speed	238.2	m/s
Number of Motors/Engines per Rotor	1	nondim.
Hover Power	900.6	kW
Advance Ratio	0.21	nondim.
Nominal Forward Flight Power	624.1	kW
Tail Rotor Radius	1.52	m

Payload (Passenger(s) and Habitat Module)	909.1	kg
Weight of Rotor Blades	181.9	kg
Main Hub and Hinges	93.7	kg
Fuselage	475.9	kg
(Skid Type) Landing Gear	72.6	kg
Drive System	324.9	kg
Batteries	1344.1	kg
Auxiliary Power Systems	268.8	kg
Electric Motors	502.1	kg
Propulsion Subsystems	110.5	kg
Flight Control Systems	117.6	kg
Total TOGW =	4401.3	kg

Table 7 – Baseline Single Main Rotor and Tail Rotor Configuration, All-Electric Battery Propulsion, 1136 kg (2500 lbf) Payload

Main Rotor Disk Loading	324.4	N/m^2
Main Rotor Radius	7.63	m
Number of Blades	4	nondim.
Main Rotor Solidity	0.04	nondim.
Main Rotor Tip Speed	238.2	m/s
Number of Motors/Engines per Rotor	1	nondim.
Hover Power	1125.7	kW
Advance Ratio	0.21	nondim.
Nominal Forward Flight Power	780.1	kW
Tail Rotor Radius	1.70	m
Payload (Passenger(s) and Habitat Module)	1136.4	kg
Weight of Rotor Blades	236.4	kg
Main Hub and Hinges	117.1	kg
Fuselage	623.5	kg
(Skid Type) Landing Gear	90.8	kg
Drive System	407.4	kg
Batteries	1680.1	kg
Auxiliary Power Systems	336.0	kg
Electric Motors	597.6	kg
Propulsion Subsystems	131.5	kg
Flight Control Systems	143.2	kg
Total TOGW =	5499.9	kg

Table 8 – Baseline Single Main Rotor and Tail Rotor Configuration, All-Electric Battery Propulsion, 1364 kg (3000 lbf) Payload

Main Rotor Disk Loading	324.4	N/m^2
Main Rotor Radius	8.36	m
Number of Blades	4	nondim.
Main Rotor Solidity	0.04	nondim.
Main Rotor Tip Speed	238.2	m/s
Number of Motors/Engines per Rotor	1	nondim.
Hover Power	1350.8	kW
Advance Ratio	0.21	nondim.
Nominal Forward Flight Power	936.2	kW
Tail Rotor Radius	1.86	m
Payload (Passenger(s) and Habitat Module)	1363.6	kg
Weight of Rotor Blades	292.7	kg
Main Hub and Hinges	141.9	kg
Fuselage	777.3	kg
(Skid Type) Landing Gear	108.9	kg
Drive System	490.3	kg
Batteries	2016.2	kg
Auxiliary Power Systems	403.2	kg
Electric Motors	688.9	kg
Propulsion Subsystems	151.6	kg
Flight Control Systems	168.2	kg
Total TOGW =	6602.9	kg

Table 9 – Baseline Single Main Rotor and Tail Rotor Configuration, All-Electric Battery Propulsion, 1591 kg (3500 lbf) Payload

Main Rotor Disk Loading	324.4	N/m2
Main Rotor Radius	9.06	m
Number of Blades	4	nondim.
Main Rotor Solidity	0.04	nondim.
Main Rotor Tip Speed	238.2	m/s
Number of Motors/Engines per Rotor	1	nondim.
Hover Power	1586.2	kW
Advance Ratio	0.21	nondim.
Nominal Forward Flight Power	1099.3	kW
Tail Rotor Radius	2.01	m
Payload (Passenger(s) and Habitat Module)	1590.9	kg

Weight of Rotor Blades	353.4	kg
Main Hub and Hinges	170.1	kg
Fuselage	944.1	kg
(Skid Type) Landing Gear	127.9	kg
Drive System	577.1	kg
Batteries	2367.5	kg
Auxiliary Power Systems	473.5	kg
Electric Motors	780.8	kg
Propulsion Subsystems	171.8	kg
Flight Control Systems	193.9	kg
Total TOGW =	7751.0	kg

Figures 62-63 summarize some of the sizing results presented in Tables 4-9. Figure 62 is the SMR vehicle takeoff gross weight and battery weight as a function of habitat module weight. Figure 63 illustrates the baseline New Nomad main rotor and tail rotor sizes (radii) as a function of habitat module weight.

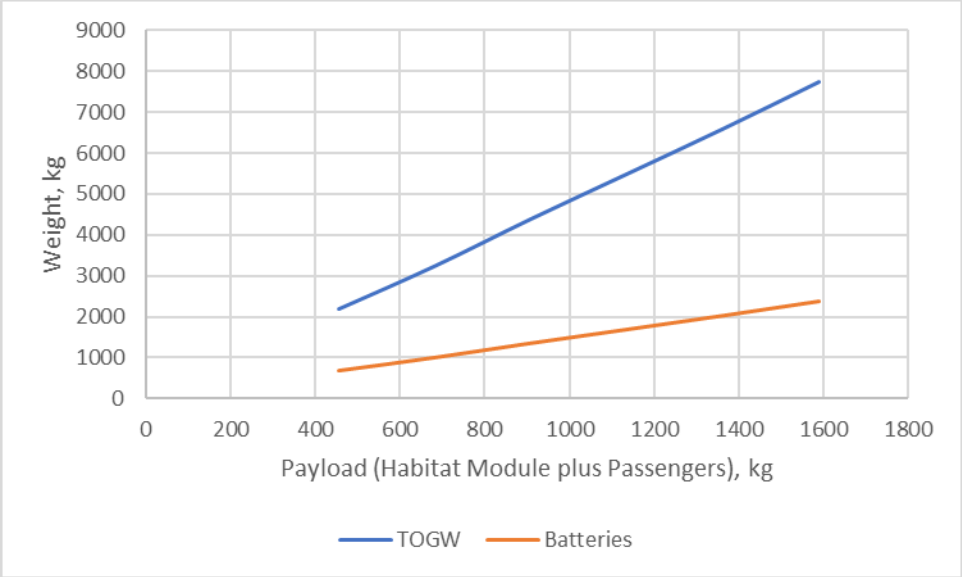

Figure 62. Baseline SMR vehicle take-off gross weight estimates as a function of habitat module (payload) size and weight

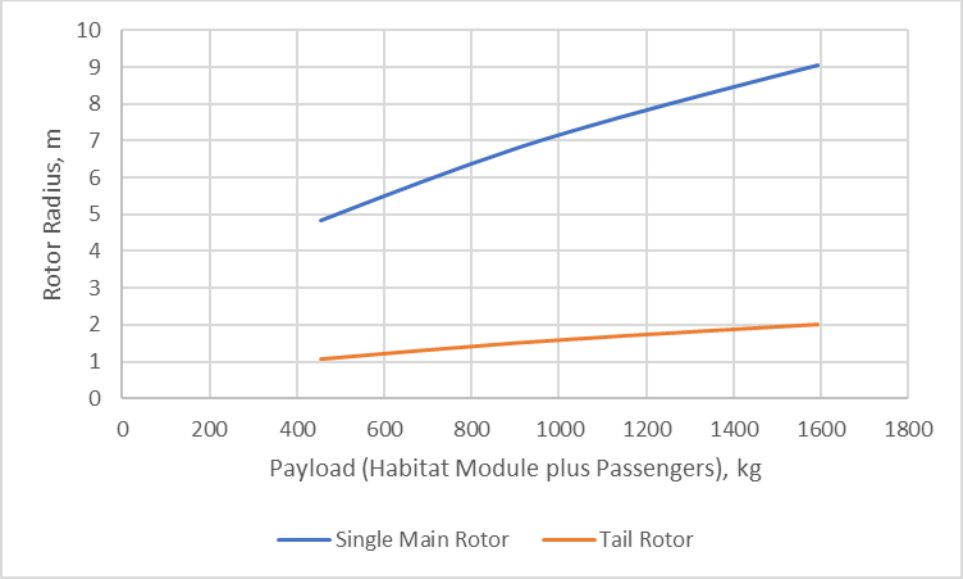

Figure 63. Baseline Single Main Rotor and Tail Rotor Radii estimates as a function of habitat module (payload) weight

Figure 64 represents a more ambitious short-range vehicle mission profile for future work beyond the scope of the current, i.e., than the Fig. 61 simple mission profile presented earlier (and to which all single-main-rotor and tail rotor configurations were sized to in this initial sizing as well as subsequent sizing of an alternate multirotor configuration).

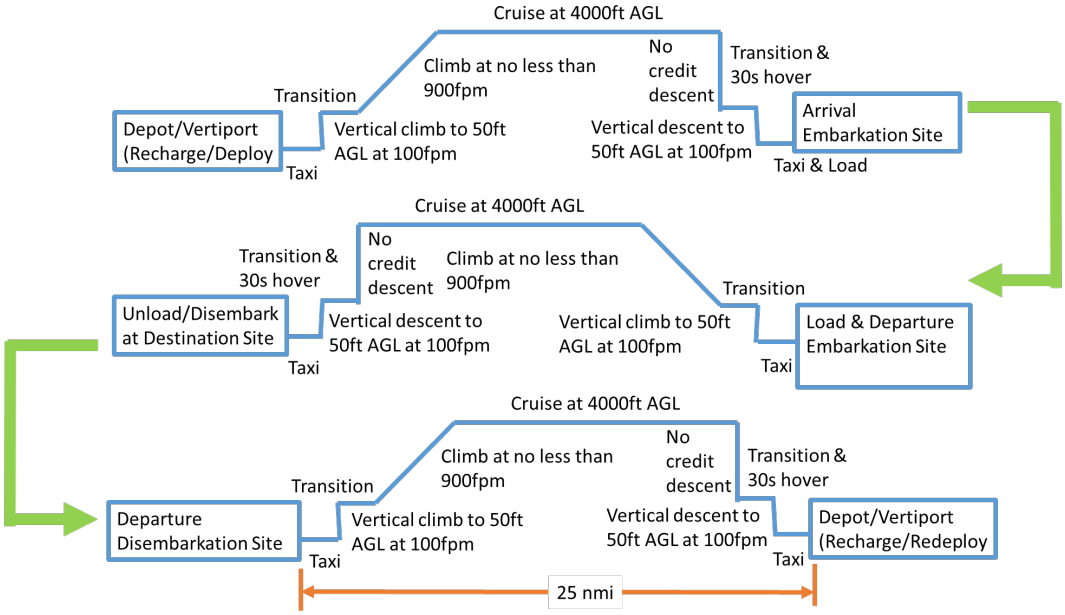

Figure 64. More detailed mission profile for future sizing work

Simple Rotorcraft Sizing of Alternate (Multirotor) Short-Range Vehicle as a function of habitat module size/weight

A spreadsheet-style, first-order, simple rotorcraft sizing (SRS) analysis was developed and exercised to conceptually design the alternate short-range multirotor vehicle for carrying habitat modules for various notional sizes and weights. The alternate multirotor vehicles were also sized assuming all-electric propulsion with batteries.

A high-level validation effort for the simple rotorcraft sizing tool for multirotor configurations was performed against the six passenger Quadrotor UAM design sized using NDARC in Refs. 18 and 32. This weight breakdown comparison is less detailed than the earlier validation study performed for single main rotor configurations earlier in this report primarily because Refs. 32-33 provided a less detailed breakdown. A novel wing (cross-arm) estimate was included in the structures weight estimates; this cross-arm estimation was based on a reinterpretation through analogy of the Ref. 38 blade weight estimation formula. Additionally, unlike the earlier single main rotor configuration validation performed, the material of the rotor blades was assumed to be fully composite versus the metallic spar assumed in the SMR study. Generally, the reasonable agreement between the two sets of results is sufficient to proceed with a sizing study of the alternate multirotor configuration for this New Nomad study.

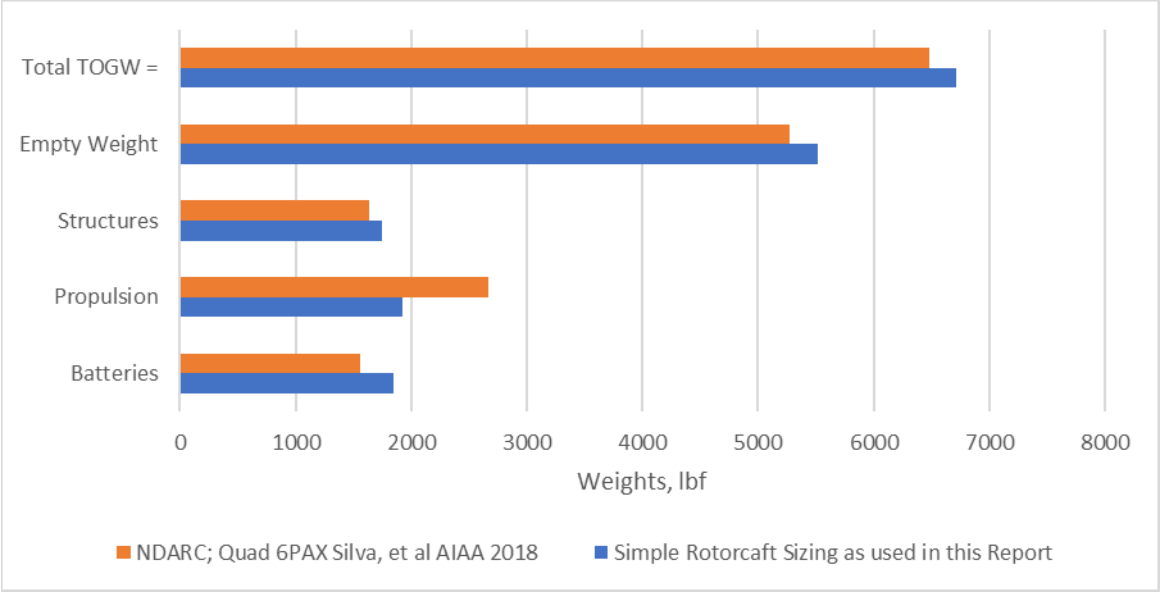

Figure 65. Weight breakdown comparison between the simple rotorcraft sizing analysis used in this report and the NASA NDARC tool, as applied to the Refs. 18 and 32 Quadrotor 6PAX UAM conceptual reference design

The specific multirotor configuration sized in this study was a ten-rotor configuration (four fore and aft lifting rotors and four main-wing-mounted lifting rotors (two pairs of coaxial rotors) and two propulsive-only propellers). The simple primary mission for the multirotor vehicle was the same as Fig. 61 and the same primary mission used to size the SMR and tail rotor baseline helicopter configuration.

The weight estimate methodology is still primarily based on the analysis of Stepnewski and Shinn (Ref. 37) and Tischenko (Ref. 38), as appropriate, but with modifications and extensions as needed. The weight model results should be considered of lower confidence in their accuracy as applied to multirotor configurations versus that of the SMR and tail-rotor baseline configuration.

The four fore and aft lifting rotors are assumed to be identical to each other (except for rotation direction); similarly, the four wing-tip-mounted lifting rotors, as a group, are also assumed to be identical with respect to each other. This prescribed design constraint, then, yields two key nondimensional design parameters to consider in the sizing study of the alternate multirotor vehicles: (1) the relative fraction of vehicle lift carried by the fore and aft lifting rotors as compared to the total vehicle weight and (2) the relative fraction of rotor disk loading for the main-wing-mounted lifting rotors relative to the disk loading of the fore and aft lifting rotors. (This latter fraction is assumed less than or equal to unity. The expectation is that these main-wing-mounted rotors are assumed to be more efficient, lower disk loading, larger rotors that carry more of the vehicle weight than the fore and aft lifting rotors.)

Tables 10-22 summarize the sizing analysis results for the alternative multirotor New Nomad short-range aerial mobility vehicle for various habitat payload weights and various fore and aft rotor lift fractions, and various main-wing-mounted rotor disk loading fractions.

Table 10 – Alternate Multirotor (ten rotors) Configuration, All-Electric Battery Propulsion, 455 kg (1000 lbf) Payload, fore and aft rotors lift fraction of 0.25 and the main-wing mounted rotors disk loading fraction of 0.5

(Two) Fore and (Two) Aft Rotors Disk Loading	243.3	N/m^2
(Two) Fore and (Two) Aft Rotors Radii	1.45	m
(Two) Fore and (Two) Aft Rotors Number of Blades	4	nondim.
(Two) Fore and (Two) Aft Rotors Tip Mach Number	0.7	nondim.
Main-Wing-Mounted (Two Pairs of Coaxial) Rotors Disk Loading	243.3	N/m^2
Main-Wing-Mounted (Two Pairs of Coaxial) Rotors Radii	3.48	m
Number of Blades for Main-wing-Mounted Coaxial Rotors	4	nondim.
Propeller Cruise Disk Loading	805.5	N/m^2
Propeller Radii	0.35	m

Propeller Number of Blades	2	nondim.
Number of Motors/Engines per Rotor	1	nondim.
Hover Power	386.7	kW
Advance Ratio	0.21	nondim.
Nominal Forward Flight Power	215.4	kW
Payload (Passenger(s) and Habitat Module)	454.5	kg
Weight of Rotor Blades	68.5	kg
Main Hub and Hinges	31.1	kg
Fuselage	192.7	kg
Multirotor Support/Cross-Arms (or 'Wings')	38.2	kg
(Skid Type) Landing Gear	38.3	kg
Drive System	172.6	kg
Batteries	577.2	kg
Auxiliary Power Systems	346.3	kg
Electric Motors	454.9	kg
Propulsion Subsystems	97.1	kg
Flight Control Systems	85.2	kg
Total TOGW =	2556.7	kg

Table 11 – Alternate Multirotor (ten rotors) Configuration, All-Electric Battery Propulsion, 682 kg (1500 lbf) Payload, fore and aft rotors lift fraction of 0.25 and the main-wing mounted rotors disk loading fraction of 0.5

(Two) Fore and (Two) Aft Rotors Disk Loading	243.3	N/m^2
(Two) Fore and (Two) Aft Rotors Radii	2.37	m
(Two) Fore and (Two) Aft Rotors Number of Blades	4	nondim.
(Two) Fore and (Two) Aft Rotors Tip Mach Number	0.7	nondim.
Main-Wing-Mounted (Two Pairs of Coaxial) Rotors Disk Loading	121.6	N/m^2
Main-Wing-Mounted (Two Pairs of Coaxial) Rotors Radii	4.22	m
Number of Blades for Main-wing-Mounted Coaxial Rotors	4	nondim.
Propeller Cruise Disk Loading	805.5	N/m^2
Propeller Radii	0.35	m
Propeller Number of Blades	2	nondim.
Number of Motors/Engines per Rotor	1	nondim.
Hover Power	449.3	kW
Advance Ratio	0.21	nondim.
Nominal Forward Flight Power	252.4	kW
Payload (Passenger(s) and Habitat Module)	681.8	kg

Weight of Rotor Blades	152.2	kg
Main Hub and Hinges	68.7	kg
Fuselage	219.3	kg
Multirotor Support/Cross-Arms (or 'Wings')	95.2	kg
(Skid Type) Landing Gear	51.4	kg
Drive System	238.1	kg
Batteries	670.5	kg
Auxiliary Power Systems	402.3	kg
Electric Motors	516.2	kg
Propulsion Subsystems	168.3	kg
Flight Control Systems	159.0	kg
Total TOGW =	3423.0	kg

Table 12 – Alternate Multirotor (ten rotors) Configuration, All-Electric Battery Propulsion, 909 kg (2000 lbf) Payload, fore and aft rotors lift fraction of 0.25 and the main-wing mounted rotors disk loading fraction of 0.5

(Two) Fore and (Two) Aft Rotors Disk Loading	243.3	N/m^2
(Two) Fore and (Two) Aft Rotors Radii	2.71	m
(Two) Fore and (Two) Aft Rotors Number of Blades	4	nondim.
(Two) Fore and (Two) Aft Rotors Tip Mach Number	0.7	nondim.
Main-Wing-Mounted (Two Pairs of Coaxial) Rotors Disk Loading	121.6	N/m^2
Main-Wing-Mounted (Two Pairs of Coaxial) Rotors Radii	4.85	m
Number of Blades for Main-wing-Mounted Coaxial Rotors	4	nondim.
Propeller Cruise Disk Loading	805.5	N/m^2
Propeller Radii	0.35	m
Propeller Number of Blades	2	nondim.
Number of Motors/Engines per Rotor	1	nondim.
Hover Power	587.6	kW
Advance Ratio	0.21	nondim.
Nominal Forward Flight Power	318.1	kW
Payload (Passenger(s) and Habitat Module)	909.1	kg
Weight of Rotor Blades	208.5	kg
Main Hub and Hinges	93.2	kg
Fuselage	303.5	kg
Multirotor Support/Cross-Arms (or 'Wings')	136.8	kg
(Skid Type) Landing Gear	67.2	kg
Drive System	319.9	kg

Batteries	877.1	kg
Auxiliary Power Systems	526.2	kg
Electric Motors	629.3	kg
Propulsion Subsystems	207.1	kg
Flight Control Systems	201.9	kg
Total TOGW =	4479.8	kg

Table 13 – Alternate Multirotor (ten rotors) Configuration, All-Electric Battery Propulsion, 1136 kg (2500 lbf) Payload, fore and aft rotors lift fraction of 0.25 and the main-wing mounted rotors disk loading fraction of 0.5

(Two) Fore and (Two) Aft Rotors Disk Loading	243.3	N/m^2
(Two) Fore and (Two) Aft Rotors Radii	2.37	m
(Two) Fore and (Two) Aft Rotors Number of Blades	4	nondim.
(Two) Fore and (Two) Aft Rotors Tip Mach Number	0.7	nondim.
Main-Wing-Mounted (Two Pairs of Coaxial) Rotors Disk Loading	243.3	N/m^2
Main-Wing-Mounted (Two Pairs of Coaxial) Rotors Radii	5.41	m
Number of Blades for Main-wing-Mounted Coaxial Rotors	4	nondim.
Propeller Cruise Disk Loading	805.5	N/m^2
Propeller Radii	0.35	m
Propeller Number of Blades	2	nondim.
Number of Motors/Engines per Rotor	1	nondim.
Hover Power	1041.3	kW
Advance Ratio	0.21	nondim.
Nominal Forward Flight Power	513.9	kW
Payload (Passenger(s) and Habitat Module)	1363.6	kg
Weight of Rotor Blades	218.1	kg
Main Hub and Hinges	96.5	kg
Fuselage	639.0	kg
Multirotor Support/Cross-Arms (or 'Wings')	145.0	kg
(Skid Type) Landing Gear	103.2	kg
Drive System	466.0	kg
Batteries	1554.2	kg
Auxiliary Power Systems	932.5	kg
Electric Motors	948.9	kg
Propulsion Subsystems	208.5	kg
Flight Control Systems	205.2	kg

Total TOGW =	6880.8	kg

Table 14 – Alternate Multirotor (ten rotors) Configuration, All-Electric Battery Propulsion, 1364 kg (3000 lbf) Payload, fore and aft rotors lift fraction of 0.25 and the main-wing mounted rotors disk loading fraction of 0.5

(Two) Fore and (Two) Aft Rotors Disk Loading	243.3	N/m^2
(Two) Fore and (Two) Aft Rotors Radii	2.59	m
(Two) Fore and (Two) Aft Rotors Number of Blades	4	nondim.
(Two) Fore and (Two) Aft Rotors Tip Mach Number	0.7	nondim.
Main-Wing-Mounted (Two Pairs of Coaxial) Rotors Disk Loading	121.6	N/m^2
Main-Wing-Mounted (Two Pairs of Coaxial) Rotors Radii	5.94	m
Number of Blades for Main-wing-Mounted Coaxial Rotors	4	nondim.
Propeller Cruise Disk Loading	805.5	N/m^2
Propeller Radii	0.35	m
Propeller Number of Blades	2	nondim.
Number of Motors/Engines per Rotor	1	nondim.
Hover Power	972.2	kW
Advance Ratio	0.21	nondim.
Nominal Forward Flight Power	491.4	kW
Payload (Passenger(s) and Habitat Module)	1590.9	kg
Weight of Rotor Blades	533.3	kg
Main Hub and Hinges	211.6	kg
Fuselage	790.8	kg
Multirotor Support/Cross-Arms (or 'Wings')	436.4	kg
(Skid Type) Landing Gear	123.1	kg
Drive System	537.3	kg
Batteries	1451.0	kg
Auxiliary Power Systems	870.6	kg
Electric Motors	910.8	kg
Propulsion Subsystems	359.3	kg
Flight Control Systems	391.7	kg
Total TOGW =	8206.9	kg

Table 15 – Alternate Multirotor (ten rotors) Configuration, All-Electric Battery Propulsion, 1591 kg (3500 lbf) Payload, fore and aft rotors lift fraction of 0.25 and the main-wing mounted rotors disk loading fraction of 0.5

(Two) Fore and (Two) Aft Rotors Disk Loading	243.3	N/m^2
(Two) Fore and (Two) Aft Rotors Radii	3.53	m
(Two) Fore and (Two) Aft Rotors Number of Blades	4	nondim.
(Two) Fore and (Two) Aft Rotors Tip Mach Number	0.7	nondim.
Main-Wing-Mounted (Two Pairs of Coaxial) Rotors Disk Loading	121.6	N/m^2
Main-Wing-Mounted (Two Pairs of Coaxial) Rotors Radii	6.44	m
Number of Blades for Main-wing-Mounted Coaxial Rotors	4	nondim.
Propeller Cruise Disk Loading	805.5	N/m^2
Propeller Radii	0.35	m
Propeller Number of Blades	2	nondim.
Number of Motors/Engines per Rotor	1	nondim.
Hover Power	1000.2	kW
Advance Ratio	0.21	nondim.
Nominal Forward Flight Power	514.01	kW
Payload (Passenger(s) and Habitat Module)	1590.9	kg
Weight of Rotor Blades	388.7	kg
Main Hub and Hinges	167.0	kg
Fuselage	577.7	kg
Multirotor Support/Cross-Arms (or 'Wings')	287.9	kg
(Skid Type) Landing Gear	114.4	kg
Drive System	537.3	kg
Batteries	1492.8	kg
Auxiliary Power Systems	895.7	kg
Electric Motors	936.8	kg
Propulsion Subsystems	312.8	kg
Flight Control Systems	324.7	kg
Total TOGW =	7626.7	kg

Table 16 – Alternate Multirotor (ten rotors) Configuration, All-Electric Battery Propulsion, 455 kg (1000 lbf) Payload, fore and aft rotors lift fraction of 0.5 and the main-wing-mounted-rotors disk loading fraction of 0.5

(Two) Fore and (Two) Aft Rotors Disk Loading	243.3	N/m^2
(Two) Fore and (Two) Aft Rotors Radii	1.98	m
(Two) Fore and (Two) Aft Rotors Number of Blades	4	nondim.
(Two) Fore and (Two) Aft Rotors Tip Mach Number	0.7	nondim.
Main-Wing-Mounted (Two Pairs of Coaxial) Rotors Disk Loading	121.6	N/m^2
Main-Wing-Mounted (Two Pairs of Coaxial) Rotors Radii	2.84	m
Number of Blades for Main-wing-Mounted Coaxial Rotors	4	nondim.
Propeller Cruise Disk Loading	805.5	N/m^2
Propeller Radii	0.35	m
Propeller Number of Blades	2	nondim.
Number of Motors/Engines per Rotor	1	nondim.
Hover Power	314.8	kW
Advance Ratio	0.21	nondim.
Nominal Forward Flight Power	188.5	kW
Payload (Passenger(s) and Habitat Module)	454.5	kg
Weight of Rotor Blades	100.4	kg
Main Hub and Hinges	45.5	kg
Fuselage	142.6	kg
Multirotor Support/Cross-Arms (or 'Wings')	59.6	kg
(Skid Type) Landing Gear	36	kg
Drive System	168.8	kg
Batteries	469.9	kg
Auxiliary Power Systems	281.9	kg
Electric Motors	398.7	kg
Propulsion Subsystems	127.9	kg
Flight Control Systems	115.9	kg
Total TOGW =	2401.8	kg

Table 17 – Alternate Multirotor (ten rotors) Configuration, All-Electric Battery Propulsion, 682 kg (1500 lbf) Payload, fore and aft rotors lift fraction of 0.5 and the main-wing mounted rotors disk loading fraction of 0.5

(Two) Fore and (Two) Aft Rotors Disk Loading	243.3	N/m^2
(Two) Fore and (Two) Aft Rotors Radii	2.37	m
(Two) Fore and (Two) Aft Rotors Number of Blades	4	nondim.
(Two) Fore and (Two) Aft Rotors Tip Mach Number	0.7	nondim.
Main-Wing-Mounted (Two Pairs of Coaxial) Rotors Disk Loading	121.6	N/m^2
Main-Wing-Mounted (Two Pairs of Coaxial) Rotors Radii	3.40	m
Number of Blades for Main-wing-Mounted Coaxial Rotors	4	nondim.
Propeller Cruise Disk Loading	805.5	N/m^2
Propeller Radii	0.35	m
Propeller Number of Blades	2	nondim.
Number of Motors/Engines per Rotor	1	nondim.
Hover Power	449.3	kW
Advance Ratio	0.21	nondim.
Nominal Forward Flight Power	252.4	kW
Payload (Passenger(s) and Habitat Module)	681.8	kg
Weight of Rotor Blades	152.2	kg
Main Hub and Hinges	68.7	kg
Fuselage	219.3	kg
Multirotor Support/Cross-Arms (or 'Wings')	95.2	kg
(Skid Type) Landing Gear	51.4	kg
Drive System	238.1	kg
Batteries	670.5	kg
Auxiliary Power Systems	402.3	kg
Electric Motors	516.2	kg
Propulsion Subsystems	168.3	kg
Flight Control Systems	159.0	kg
Total TOGW =	3423.0	kg

Table 18 – Alternate Multirotor (ten rotors) Configuration, All-Electric Battery Propulsion, 909 kg (2000 lbf) Payload, fore and aft rotors lift fraction of 0.5 and the main-wing mounted rotors disk loading fraction of 0.5

(Two) Fore and (Two) Aft Rotors Disk Loading	243.3	N/m^2
(Two) Fore and (Two) Aft Rotors Radii	2.71	m
(Two) Fore and (Two) Aft Rotors Number of Blades	4	nondim.
(Two) Fore and (Two) Aft Rotors Tip Mach Number	0.7	nondim.
Main-Wing-Mounted (Two Pairs of Coaxial) Rotors Disk Loading	121.6	N/m^2
Main-Wing-Mounted (Two Pairs of Coaxial) Rotors Radii	3.89	m
Number of Blades for Main-wing-Mounted Coaxial Rotors	4	nondim.
Propeller Cruise Disk Loading	805.5	N/m^2
Propeller Radii	0.35	m
Propeller Number of Blades	2	nondim.
Number of Motors/Engines per Rotor	1	nondim.
Hover Power	587.6	kW
Advance Ratio	0.21	nondim.
Nominal Forward Flight Power	318.1	kW
Payload (Passenger(s) and Habitat Module)	909.1	kg
Weight of Rotor Blades	208.5	kg
Main Hub and Hinges	93.2	kg
Fuselage	303.5	kg
Multirotor Support/Cross-Arms (or 'Wings')	136.8	kg
(Skid Type) Landing Gear	67.2	kg
Drive System	319.9	kg
Batteries	877.0	kg
Auxiliary Power Systems	526.2	kg
Electric Motors	629.3	kg
Propulsion Subsystems	207.1	kg
Flight Control Systems	201.9	kg
Total TOGW =	4479.8	kg

Table 19 – Alternate Multirotor (ten rotors) Configuration, All-Electric Battery Propulsion, 1136 kg (2500 lbf) Payload, fore and aft rotors lift fraction of 0.5 and the main-wing-mounted-rotors disk loading fraction of 0.5

(Two) Fore and (Two) Aft Rotors Disk Loading	243.3	N/m^2
(Two) Fore and (Two) Aft Rotors Radii	3.00	m
(Two) Fore and (Two) Aft Rotors Number of Blades	4	nondim.
(Two) Fore and (Two) Aft Rotors Tip Mach Number	0.7	nondim.
Main-Wing-Mounted (Two Pairs of Coaxial) Rotors Disk Loading	121.6	N/m^2
Main-Wing-Mounted (Two Pairs of Coaxial) Rotors Radii	4.31	m
Number of Blades for Main-wing-Mounted Coaxial Rotors	4	nondim.
Propeller Cruise Disk Loading	805.5	N/m^2
Propeller Radii	0.35	m
Propeller Number of Blades	2	nondim.
Number of Motors/Engines per Rotor	1	nondim.
Hover Power	722.7	kW
Advance Ratio	0.21	nondim.
Nominal Forward Flight Power	382.2	kW
Payload (Passenger(s) and Habitat Module)	1136.4	kg
Weight of Rotor Blades	265.7	kg
Main Hub and Hinges	117.4	kg
Fuselage	389.9	kg
Multirotor Support/Cross-Arms (or 'Wings')	182.0	kg
(Skid Type) Landing Gear	82.7	kg
Drive System	391.3	kg
Batteries	1078.7	kg
Auxiliary Power Systems	647.2	kg
Electric Motors	734.1	kg
Propulsion Subsystems	243.1	kg
Flight Control Systems	242.9	kg
Total TOGW =	5511.2	kg

Table 20 – Alternate Multirotor (ten rotors) Configuration, All-Electric Battery Propulsion, 1364 kg (3000 lbf) Payload, fore and aft rotors lift fraction of 0.5 and the main-wing-mounted-rotors disk loading fraction of 0.5

(Two) Fore and (Two) Aft Rotors Disk Loading	243.3	N/m^2
(Two) Fore and (Two) Aft Rotors Radii	3.28	m
(Two) Fore and (Two) Aft Rotors Number of Blades	4	nondim.
(Two) Fore and (Two) Aft Rotors Tip Mach Number	0.7	nondim.
Main-Wing-Mounted (Two Pairs of Coaxial) Rotors Disk Loading	121.6	N/m^2
Main-Wing-Mounted (Two Pairs of Coaxial) Rotors Radii	4.70	m
Number of Blades for Main-wing-Mounted Coaxial Rotors	4	nondim.
Propeller Cruise Disk Loading	805.5	N/m^2
Propeller Radii	0.35	m
Propeller Number of Blades	2	nondim.
Number of Motors/Engines per Rotor	1	nondim.
Hover Power	859.8	kW
Advance Ratio	0.21	nondim.
Nominal Forward Flight Power	447.3	kW
Payload (Passenger(s) and Habitat Module)	1363.6	kg
Weight of Rotor Blades	325.6	kg
Main Hub and Hinges	141.9	kg
Fuselage	481.1	kg
Multirotor Support/Cross-Arms (or 'Wings')	232.3	kg
(Skid Type) Landing Gear	98.3	kg
Drive System	463.5	kg
Batteries	1283.3	kg
Auxiliary Power Systems	770.0	kg
Electric Motors	836.0	kg
Propulsion Subsystems	278.2	kg
Flight Control Systems	283.7	kg
Total TOGW =	6557.5	kg

Table 21 – Alternate Multirotor (ten rotors) Configuration, All-Electric Battery Propulsion, 1591 kg (3500 lbf) Payload, fore and aft rotors lift fraction of 0.5 and the main-wing-mounted-rotors disk loading fraction of 0.5

(Two) Fore and (Two) Aft Rotors Disk Loading	243.3	N/m^2
(Two) Fore and (Two) Aft Rotors Radii	3.53	m
(Two) Fore and (Two) Aft Rotors Number of Blades	4	nondim.
(Two) Fore and (Two) Aft Rotors Tip Mach Number	0.7	nondim.
Main-Wing-Mounted (Two Pairs of Coaxial) Rotors Disk Loading	121.6	N/m^2
Main-Wing-Mounted (Two Pairs of Coaxial) Rotors Radii	5.07	m
Number of Blades for Main-wing-Mounted Coaxial Rotors	4	nondim.
Propeller Cruise Disk Loading	805.5	N/m^2
Propeller Radii	0.35	m
Propeller Number of Blades	2	nondim.
Number of Motors/Engines per Rotor	1	nondim.
Hover Power	1000.2	kW
Advance Ratio	0.21	nondim.
Nominal Forward Flight Power	514.0	kW
Payload (Passenger(s) and Habitat Module)	1590.9	kg
Weight of Rotor Blades	388.7	kg
Main Hub and Hinges	167.0	kg
Fuselage	577.7	kg
Multirotor Support/Cross-Arms (or 'Wings')	287.9	kg
(Skid Type) Landing Gear	114.4	kg
Drive System	537.3	kg
Batteries	1492.8	kg
Auxiliary Power Systems	895.7	kg
Electric Motors	936.8	kg
Propulsion Subsystems	312.8	kg
Flight Control Systems	324.7	kg
Total TOGW =	7626.7	kg

Tables 22-29 examine the influence of main-wing-mounted lifting rotors disk loading ratio with respect to the fore and aft lifting rotors disk loading for two different payloads: (a) 455 kg (1000 lbf) and (b) 1364 kg (3000 lbf).

Table 22 – Alternate Multirotor (ten rotors) Configuration, All-Electric Battery Propulsion, 455 kg (1000 lbf) Payload, fore and aft rotors lift fraction of 0.25 and the main-wing mounted rotors disk loading fraction of 0.625

(Two) Fore and (Two) Aft Rotors Disk Loading	243.3	N/m^2
(Two) Fore and (Two) Aft Rotors Radii	1.38	m
(Two) Fore and (Two) Aft Rotors Number of Blades	4	nondim.
(Two) Fore and (Two) Aft Rotors Tip Mach Number	0.7	nondim.
Main-Wing-Mounted (Two Pairs of Coaxial) Rotors Disk Loading	152.1	N/m^2
Main-Wing-Mounted (Two Pairs of Coaxial) Rotors Radii	3.06	m
Number of Blades for Main-wing-Mounted Coaxial Rotors	4	nondim.
Propeller Cruise Disk Loading	805.5	N/m^2
Propeller Radii	0.35	m
Propeller Number of Blades	2	nondim.
Number of Motors/Engines per Rotor	1	nondim.
Hover Power	296.6	kW
Advance Ratio	0.21	nondim.
Nominal Forward Flight Power	174.3	kW
Payload (Passenger(s) and Habitat Module)	454.5	kg
Weight of Rotor Blades	96.5	kg
Main Hub and Hinges	43.7	kg
Fuselage	171.5	kg
Multirotor Support/Cross-Arms (or 'Wings')	55.6	kg
(Skid Type) Landing Gear	34.8	kg
Drive System	152.7	kg
Batteries	442.7	kg
Auxiliary Power Systems	265.6	kg
Electric Motors	378.5	kg
Propulsion Subsystems	117.9	kg
Flight Control Systems	107.8	kg
Total TOGW =	2321.9	kg

Table 23 – Alternate Multirotor (ten rotors) Configuration, All-Electric Battery Propulsion, 455 kg (1000 lbf) Payload, fore and aft rotors lift fraction of 0.25 and the main-wing-mounted-rotors disk loading fraction of 0.75

(Two) Fore and (Two) Aft Rotors Disk Loading	243.3	N/m^2
(Two) Fore and (Two) Aft Rotors Radii	1.39	m
(Two) Fore and (Two) Aft Rotors Number of Blades	4	nondim.
(Two) Fore and (Two) Aft Rotors Tip Mach Number	0.7	nondim.
Main-Wing-Mounted (Two Pairs of Coaxial) Rotors Disk Loading	182.5	N/m^2
Main-Wing-Mounted (Two Pairs of Coaxial) Rotors Radii	2.81	m
Number of Blades for Main-wing-Mounted Coaxial Rotors	4	nondim.
Propeller Cruise Disk Loading	805.5	N/m^2
Propeller Radii	0.35	m
Propeller Number of Blades	2	nondim.
Number of Motors/Engines per Rotor	1	nondim.
Hover Power	320.4	kW
Advance Ratio	0.21	nondim.
Nominal Forward Flight Power	184.3	kW
Payload (Passenger(s) and Habitat Module)	454.5	kg
Weight of Rotor Blades	81.7	kg
Main Hub and Hinges	37.0	kg
Fuselage	174.2	kg
Multirotor Support/Cross-Arms (or 'Wings')	46.0	kg
(Skid Type) Landing Gear	35.3	kg
Drive System	156.2	kg
Batteries	478.1	kg
Auxiliary Power Systems	286.9	kg
Electric Motors	398.9	kg
Propulsion Subsystems	107.0	kg
Flight Control Systems	95.9	kg
Total TOGW =	2351.7	kg

Table 24 – Alternate Multirotor (ten rotors) Configuration, All-Electric Battery Propulsion, 455 kg (1000 lbf) Payload, fore and aft rotors lift fraction of 0.25 and the main-wing-mounted-rotors disk loading fraction of 0.875

(Two) Fore and (Two) Aft Rotors Disk Loading	243.3	N/m^2
(Two) Fore and (Two) Aft Rotors Radii	1.41	m
(Two) Fore and (Two) Aft Rotors Number of Blades	4	nondim.
(Two) Fore and (Two) Aft Rotors Tip Mach Number	0.7	nondim.
Main-Wing-Mounted (Two Pairs of Coaxial) Rotors Disk Loading	212.9	N/m^2
Main-Wing-Mounted (Two Pairs of Coaxial) Rotors Radii	2.66	m
Number of Blades for Main-wing-Mounted Coaxial Rotors	4	nondim.
Propeller Cruise Disk Loading	805.5	N/m^2
Propeller Radii	0.35	m
Propeller Number of Blades	2	nondim.
Number of Motors/Engines per Rotor	1	nondim.
Hover Power	351.6	kW
Advance Ratio	0.21	nondim.
Nominal Forward Flight Power	198.6	kW
Payload (Passenger(s) and Habitat Module)	454.5	kg
Weight of Rotor Blades	73.5	kg
Main Hub and Hinges	33.4	kg
Fuselage	182.3	kg
Multirotor Support/Cross-Arms (or 'Wings')	41.1	kg
(Skid Type) Landing Gear	36.6	kg
Drive System	163.5	kg
Batteries	524.8	kg
Auxiliary Power Systems	314.9	kg
Electric Motors	425.6	kg
Propulsion Subsystems	100.9	kg
Flight Control Systems	89.3	kg
Total TOGW =	2440.4	kg

Table 25 – Alternate Multirotor (ten rotors) Configuration, All-Electric Battery Propulsion, 455 kg (1000 lbf) Payload, fore and aft rotors lift fraction of 0.25 and the main-wing-mounted-rotors disk loading fraction of 1.0

(Two) Fore and (Two) Aft Rotors Disk Loading	243.3	N/m^2
(Two) Fore and (Two) Aft Rotors Radii	1.45	m
(Two) Fore and (Two) Aft Rotors Number of Blades	4	nondim.
(Two) Fore and (Two) Aft Rotors Tip Mach Number	0.7	nondim.
Main-Wing-Mounted (Two Pairs of Coaxial) Rotors Disk Loading	243.3	N/m^2
Main-Wing-Mounted (Two Pairs of Coaxial) Rotors Radii	2.54	m
Number of Blades for Main-wing-Mounted Coaxial Rotors	4	nondim.
Propeller Cruise Disk Loading	805.5	N/m^2
Propeller Radii	0.35	m
Propeller Number of Blades	2	nondim.
Number of Motors/Engines per Rotor	1	nondim.
Hover Power	386.7	kW
Advance Ratio	0.21	nondim.
Nominal Forward Flight Power	215.4	kW
Payload (Passenger(s) and Habitat Module)	454.5	kg
Weight of Rotor Blades	68.5	kg
Main Hub and Hinges	31.1	kg
Fuselage	192.7	kg
Multirotor Support/Cross-Arms (or 'Wings')	38.2	kg
(Skid Type) Landing Gear	38.3	kg
Drive System	172.6	kg
Batteries	577.2	kg
Auxiliary Power Systems	346.3	kg
Electric Motors	454.9	kg
Propulsion Subsystems	97.1	kg
Flight Control Systems	85.2	kg
Total TOGW =	2556.7	kg

Table 26 – Alternate Multirotor (ten rotors) Configuration, All-Electric Battery Propulsion, 1364 kg (3000 lbf) Payload, fore and aft rotors lift fraction of 0.25 and the main-wing-mounted-rotors disk loading fraction of 0.625

(Two) Fore and (Two) Aft Rotors Disk Loading	243.3	N/m^2
(Two) Fore and (Two) Aft Rotors Radii	2.31	m
(Two) Fore and (Two) Aft Rotors Number of Blades	4	nondim.
(Two) Fore and (Two) Aft Rotors Tip Mach Number	0.7	nondim.
Main-Wing-Mounted (Two Pairs of Coaxial) Rotors Disk Loading	152.2	N/m^2
Main-Wing-Mounted (Two Pairs of Coaxial) Rotors Radii	5.14	m
Number of Blades for Main-wing-Mounted Coaxial Rotors	4	nondim.
Propeller Cruise Disk Loading	805.5	N/m^2
Propeller Radii	0.35	m
Propeller Number of Blades	2	nondim.
Number of Motors/Engines per Rotor	1	nondim.
Hover Power	834.9	kW
Advance Ratio	0.21	nondim.
Nominal Forward Flight Power	419.8	kW
Payload (Passenger(s) and Habitat Module)	1363.6	kg
Weight of Rotor Blades	324.1	kg
Main Hub and Hinges	137.6	kg
Fuselage	599.9	kg
Multirotor Support/Cross-Arms (or 'Wings')	235.8	kg
(Skid Type) Landing Gear	98.0	kg
Drive System	432.6	kg
Batteries	1246.1	kg
Auxiliary Power Systems	747.6	kg
Electric Motors	809.8	kg
Propulsion Subsystems	262.4	kg
Flight Control Systems	270.9	kg
Total TOGW =	6528.4	kg

Table 27 – Alternate Multirotor (ten rotors) Configuration, All-Electric Battery Propulsion, 1364 kg (3000 lbf) Payload, fore and aft rotors lift fraction of 0.25 and the main-wing-mounted-rotors disk loading fraction of 0.75

(Two) Fore and (Two) Aft Rotors Disk Loading	243.3	N/m^2
(Two) Fore and (Two) Aft Rotors Radii	2.30	m
(Two) Fore and (Two) Aft Rotors Number of Blades	4	nondim.
(Two) Fore and (Two) Aft Rotors Tip Mach Number	0.7	nondim.
Main-Wing-Mounted (Two Pairs of Coaxial) Rotors Disk Loading	182.5	N/m^2
Main-Wing-Mounted (Two Pairs of Coaxial) Rotors Radii	4.67	m
Number of Blades for Main-wing-Mounted Coaxial Rotors	4	nondim.
Propeller Cruise Disk Loading	805.5	N/m^2
Propeller Radii	0.35	m
Propeller Number of Blades	2	nondim.
Number of Motors/Engines per Rotor	1	nondim.
Hover Power	883.4	kW
Advance Ratio	0.21	nondim.
Nominal Forward Flight Power	439.4	kW
Payload (Passenger(s) and Habitat Module)	1363.6	kg
Weight of Rotor Blades	267.7	kg
Main Hub and Hinges	116.2	kg
Fuselage	594.3	kg
Multirotor Support/Cross-Arms (or 'Wings')	186.3	kg
(Skid Type) Landing Gear	97.2	kg
Drive System	432.6	kg
Batteries	1318.4	kg
Auxiliary Power Systems	791.1	kg
Electric Motors	842.4	kg
Propulsion Subsystems	234.2	kg
Flight Control Systems	236.4	kg
Total TOGW =	6480.4	kg

Table 28 – Alternate Multirotor (ten rotors) Configuration, All-Electric Battery Propulsion, 1364 kg (3000 lbf) Payload, fore and aft rotors lift fraction of 0.25 and the main-wing-mounted-rotors disk loading fraction of 0.875

(Two) Fore and (Two) Aft Rotors Disk Loading	243.3	N/m^2
(Two) Fore and (Two) Aft Rotors Radii	2.33	m
(Two) Fore and (Two) Aft Rotors Number of Blades	4	nondim.
(Two) Fore and (Two) Aft Rotors Tip Mach Number	0.7	nondim.
Main-Wing-Mounted (Two Pairs of Coaxial) Rotors Disk Loading	212.9	N/m^2
Main-Wing-Mounted (Two Pairs of Coaxial) Rotors Radii	4.37	m
Number of Blades for Main-wing-Mounted Coaxial Rotors	4	nondim.
Propeller Cruise Disk Loading	805.5	N/m^2
Propeller Radii	0.35	m
Propeller Number of Blades	2	nondim.
Number of Motors/Engines per Rotor	1	nondim.
Hover Power	954.0	kW
Advance Ratio	0.21	nondim.
Nominal Forward Flight Power	471.9	kW
Payload (Passenger(s) and Habitat Module)	1363.6	kg
Weight of Rotor Blades	236.3	kg
Main Hub and Hinges	103.9	kg
Fuselage	609.9	kg
Multirotor Support/Cross-Arms (or 'Wings')	160.0	kg
(Skid Type) Landing Gear	99.3	kg
Drive System	445.2	kg
Batteries	1423.9	kg
Auxiliary Power Systems	854.3	kg
Electric Motors	890.3	kg
Propulsion Subsystems	217.9	kg
Flight Control Systems	216.7	kg
Total TOGW =	6621.4	kg

Table 29 – Alternate Multirotor (ten rotors) Configuration, All-Electric Battery Propulsion, 1364 kg (3000 lbf) Payload, fore and aft rotors lift fraction of 0.25 and the main-wing-mounted-rotors disk loading fraction of 1.0

(Two) Fore and (Two) Aft Rotors Disk Loading	243.3	N/m^2
(Two) Fore and (Two) Aft Rotors Radii	2.37	m
(Two) Fore and (Two) Aft Rotors Number of Blades	4	nondim.
(Two) Fore and (Two) Aft Rotors Tip Mach Number	0.7	nondim.
Main-Wing-Mounted (Two Pairs of Coaxial) Rotors Disk Loading	243.3	N/m^2
Main-Wing-Mounted (Two Pairs of Coaxial) Rotors Radii	4.17	m
Number of Blades for Main-wing-Mounted Coaxial Rotors	4	nondim.
Propeller Cruise Disk Loading	805.5	N/m^2
Propeller Radii	0.35	m
Propeller Number of Blades	2	nondim.
Number of Motors/Engines per Rotor	1	nondim.
Hover Power	1041.3	kW
Advance Ratio	0.21	nondim.
Nominal Forward Flight Power	513.9	kW
Payload (Passenger(s) and Habitat Module)	1363.6	kg
Weight of Rotor Blades	218.1	kg
Main Hub and Hinges	96.5	kg
Fuselage	639.0	kg
Multirotor Support/Cross-Arms (or 'Wings')	145.0	kg
(Skid Type) Landing Gear	103.2	kg
Drive System	466.0	kg
Batteries	1554.2	kg
Auxiliary Power Systems	932.5	kg
Electric Motors	948.9	kg
Propulsion Subsystems	208.5	kg
Flight Control Systems	205.2	kg
Total TOGW =	6880.8	kg

Figures 66-67 summarize some of the sizing result trends embodied in Tables 10-29 for the alternate multirotor (ten rotor/propeller) New Nomad vehicle. As expected, as payload increases (payload being comprised of habitat module and passenger weight), the vehicle aggregate rotor sizes increase. The relative lift fraction and the main wing mounted disk loading multiplier factor (the two parameters how the relative disk loading of the multiple rotors has been defined in this report) had small nontrivial impacts on the vehicle gross weight.

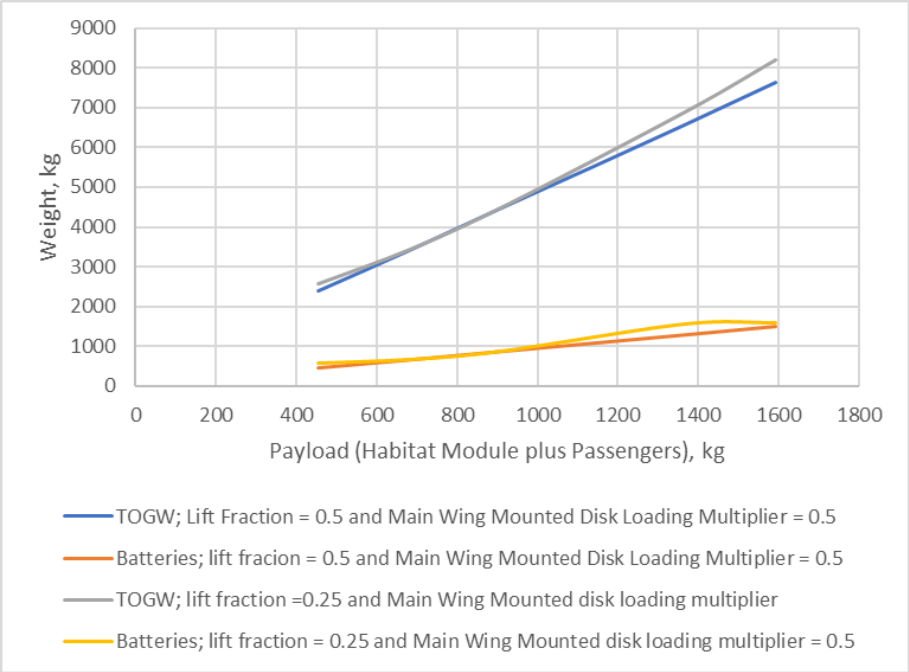

Figure 66. Alternate Multirotor Weights as a function of Payload Weight and (fore and aft rotor sets) lift fraction (relative to main-wing-mounted set of lifting rotors)

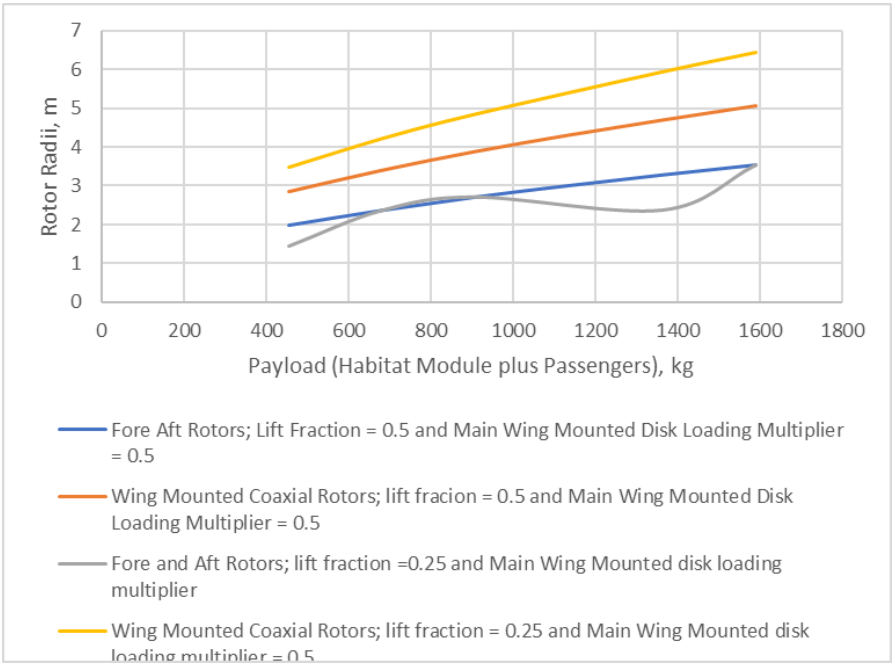

Figure 67. Rotor Sizes for Alternate Multirotor Vehicle as a function of Payload Weight and (fore and aft rotor sets) lift fraction (relative to main-wing-mounted set of lifting rotors)

There does appear to be a main-wing-mounted rotor disk loading fraction (relative to the fore and aft lift rotors disk loading) whereby there is a minimum gross weight for the ten-rotor, alternate, New Nomad vehicle. This minimum gross weight seems to require a main-wing-mounted rotor disk loading fraction of approximately 0.625 to 0.75, given the results presented in Fig. 68 for the two payloads examined.

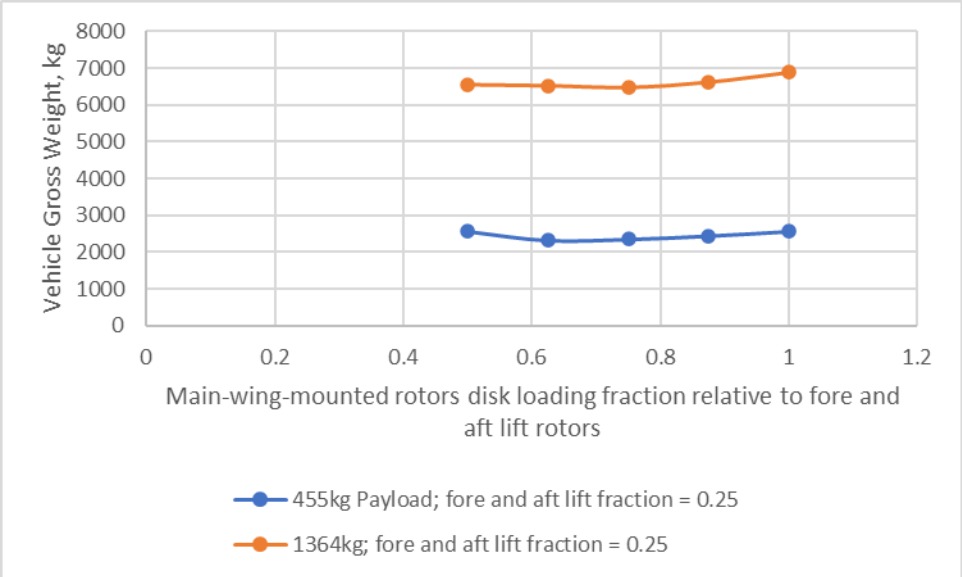

Figure 68. Alternate multirotor vehicle take-off gross weight estimates as a function of main-wing-mounted rotors disk loading fraction relative to fore and aft lift rotors; fore and aft lift fraction is equal to 0.25

Simple Rotorcraft Sizing of Baseline Long-Range Vehicle

References 19 and 26-29 were the primary data sources for the development of a Mathcad-based (Ref. 54) spreadsheet-style sizing analysis for a multiple habitat module cargo transport tiltrotor configuration employing hybrid turboelectric propulsion. Specifically, this was a blended-wing-body-tiltrotor cargo transport. A simple regression analysis set of equations were custom developed for this sizing analysis based on the earlier tiltrotor conceptual design work and diverse sizing analyses performed in Refs. 26-29. This approach is consistent with the first-order analysis nature of this study. Future work beyond this study can draw on more sophisticated rotorcraft sizing analyses available to the rotorcraft research community. But for the purposes of this study, the simple weight trends and equation summarized below will be sufficient.

Figures 69-74 illustrate the simple scaled weight trends and regression equations used in the current sizing analysis.

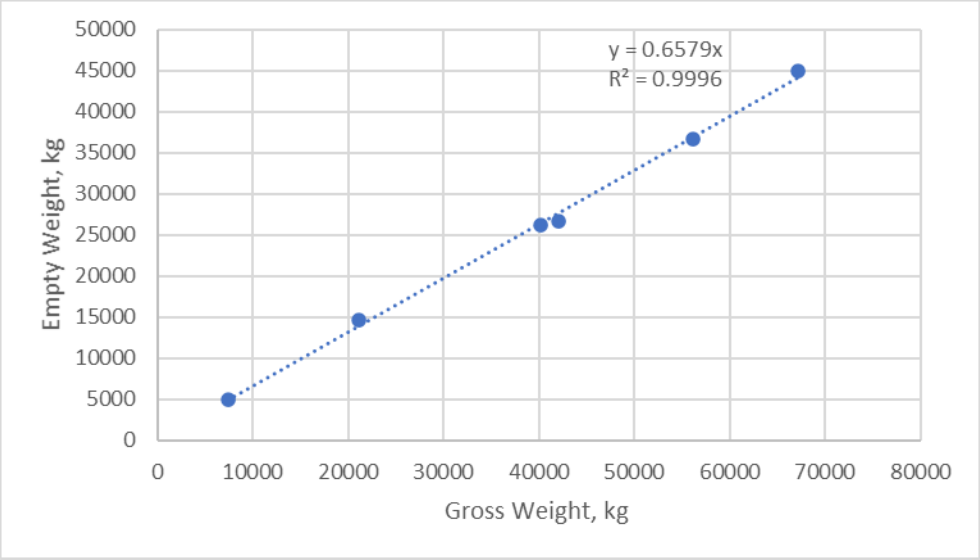

Figure 69. Tiltrotor (tube and wing fuselage) empty weight as a function of gross weight

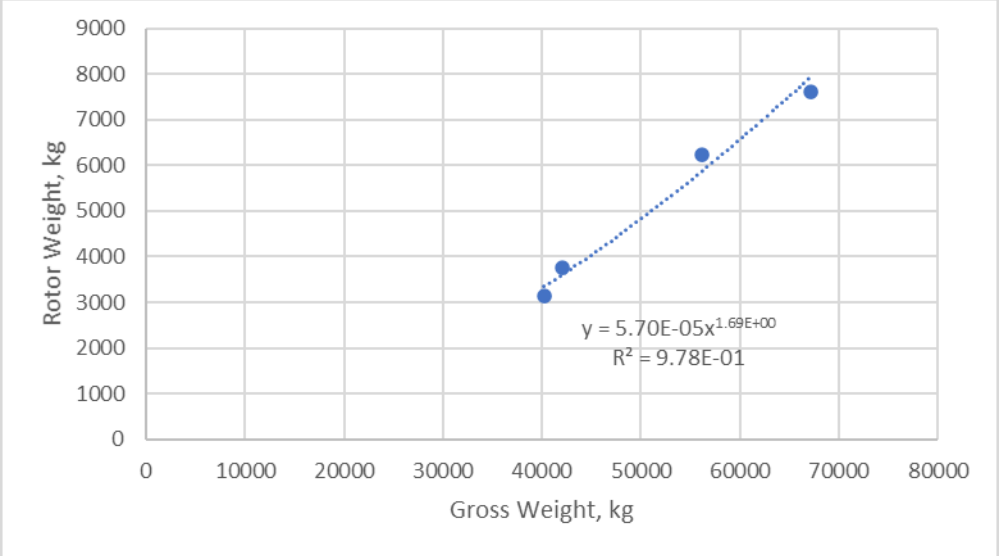

Figure 70. Tiltrotor (tube and wing fuselage) rotor group (total) weight as a function of gross weight

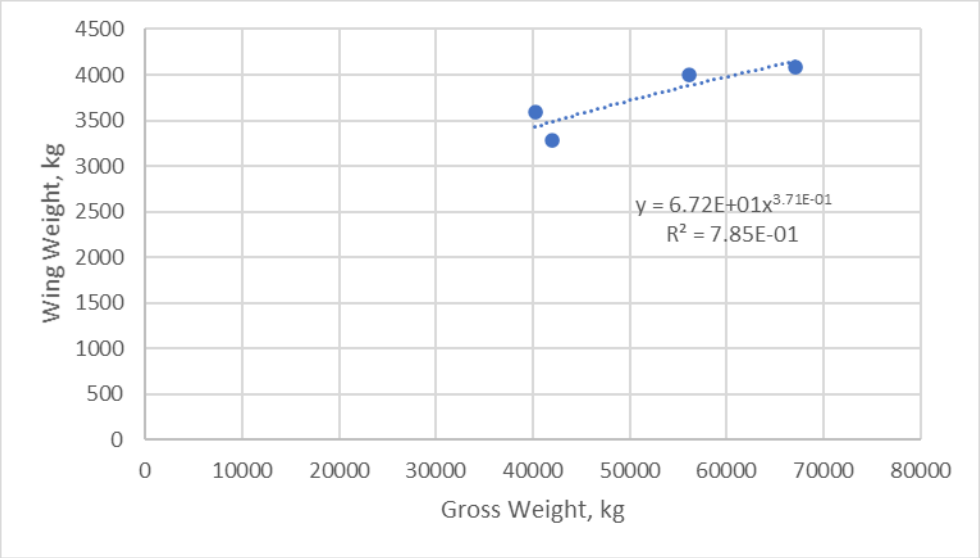

Figure 71. Tiltrotor (tube and wing fuselage) wing group weight as a function of gross weight

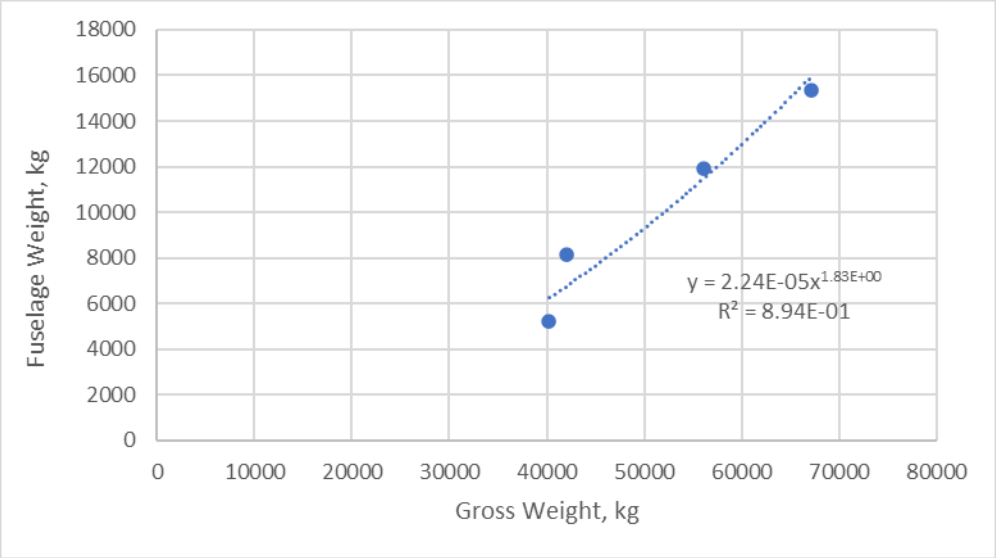

Figure 72. Tiltrotor (tube and wing fuselage) fuselage group weight as a function of gross weight

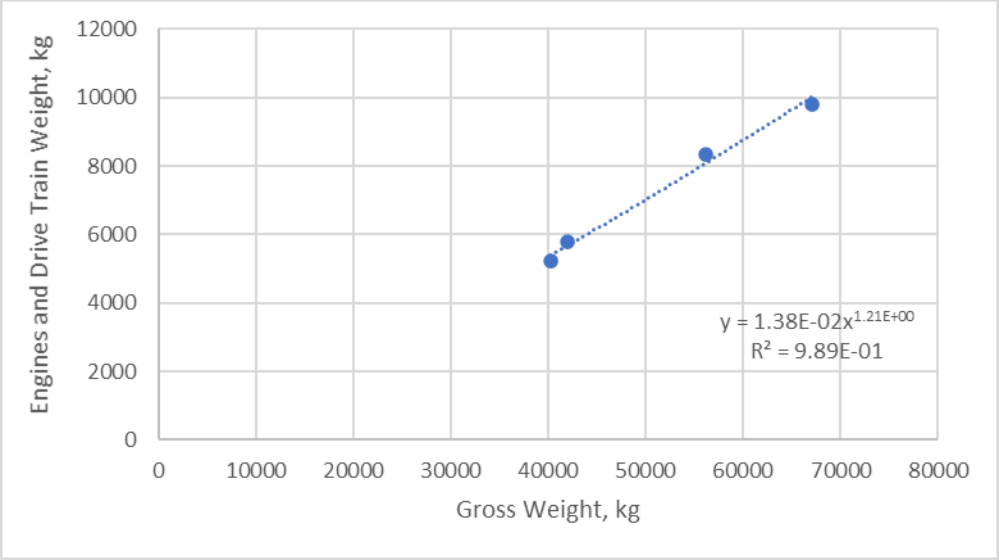

Figure 73. Tiltrotor (tube and wing fuselage) engines and drive train group weight as a function of gross weight

There was limited break out of fixed equipment weight estimates in Ref. 26. Therefore, only limited data is presented in Fig. 74 (assumes the linear curve fit goes through the zero intercept).

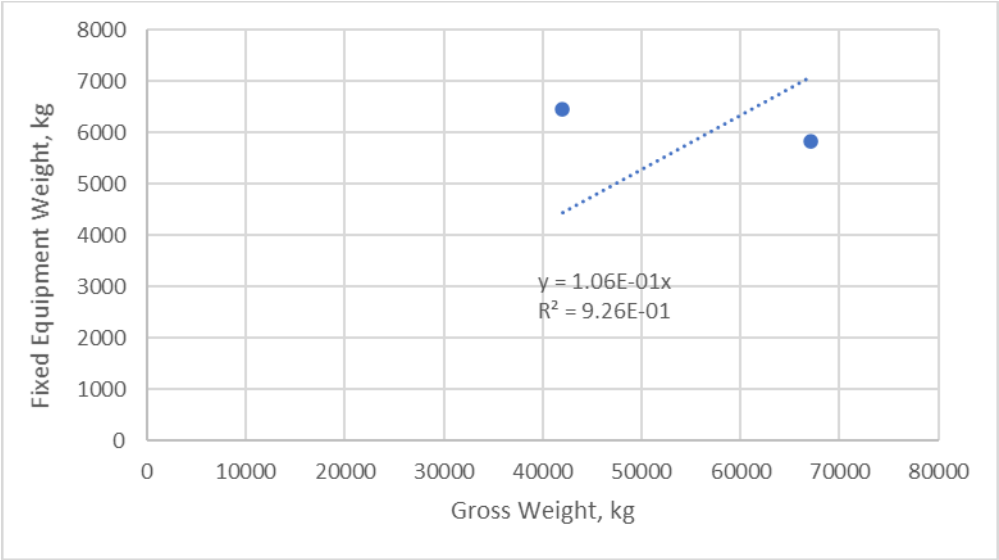

Figure 74. Tiltrotor (tube and wing fuselage) fixed equipment group weight as a function of gross weight

Figures 75-77 illustrated some general configurational sizing trends extracted from Refs. 26-29.

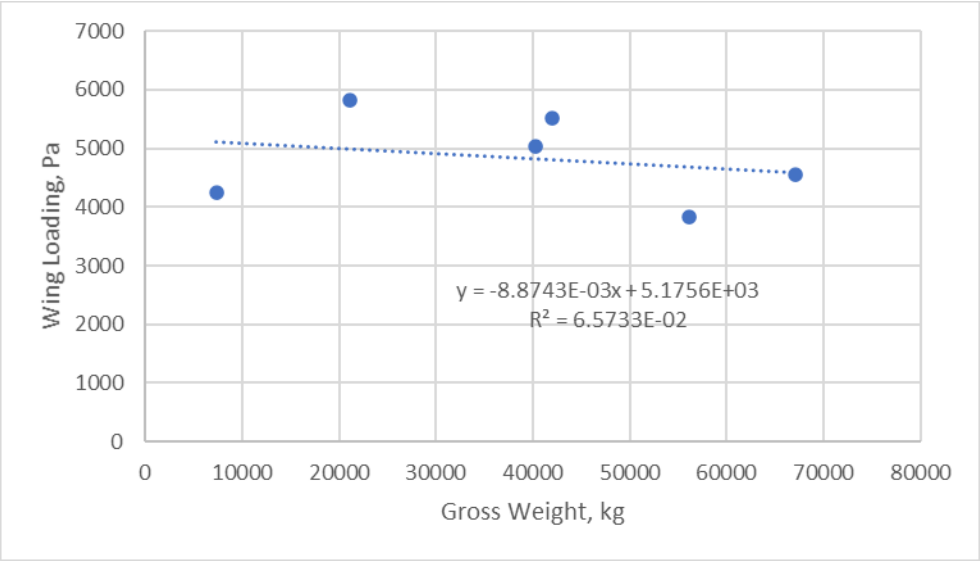

Figure 75. Tiltrotor (tube and wing fuselage) wing loading as a function of gross weight

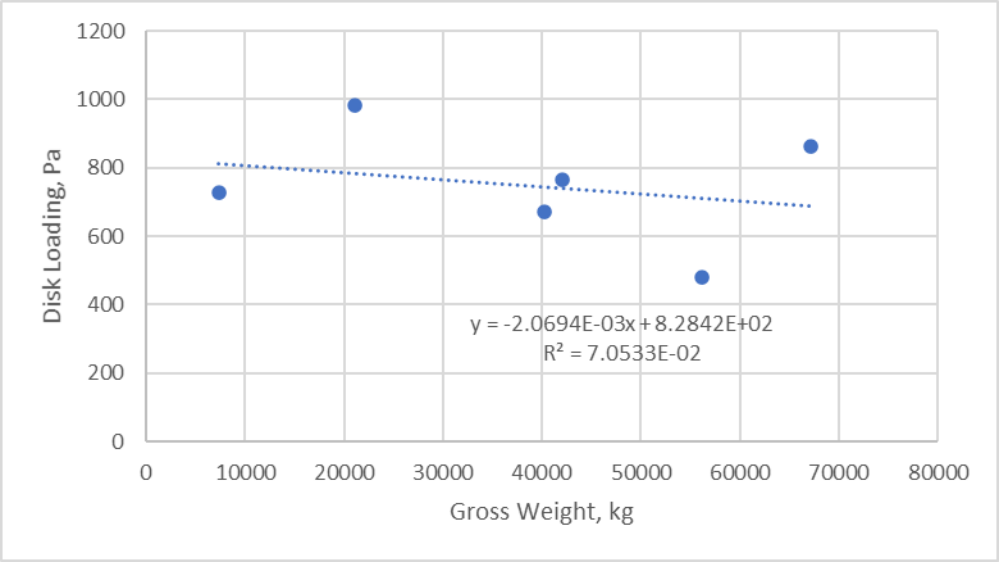

Figure 76. Tiltrotor (tube and wing fuselage) rotor disk loading as a function of gross weight

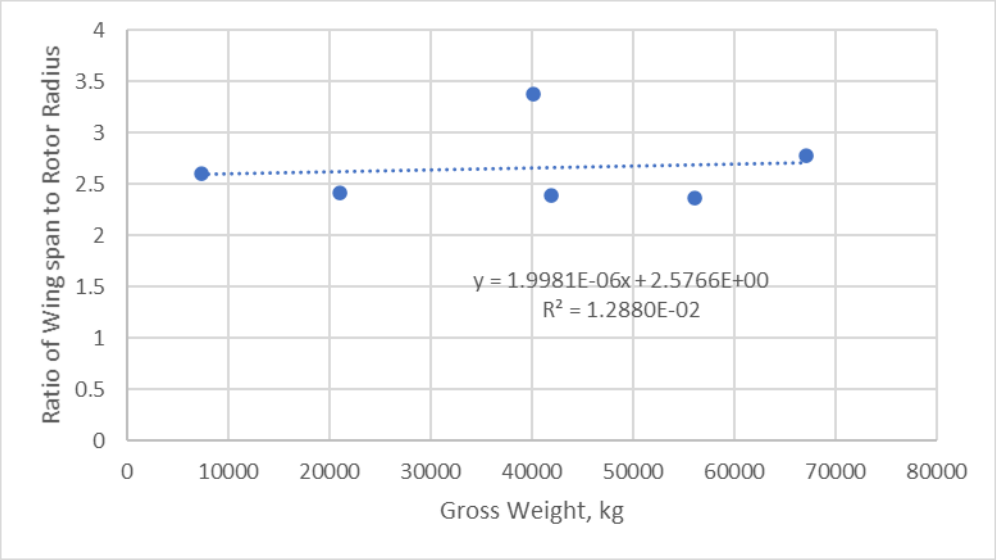

Figure 77. Tiltrotor (tube and wing fuselage) ratio of wing-span-to-rotor-radii as a function of gross weight

Figures 69-77 and their associated regression analysis results are derived from larger passenger carrying tiltrotor aircraft conceptual designs obtained from Refs. 19 and 26-29. To arrive at sizing estimates that are inclusive of not just larger aircraft but small to midsize vehicles as well, the following methodology was defined and used throughout the longer-range electric and hybrid-electric New Nomad BWB-tiltrotor aircraft discussion.

$$m_{EW} = 0.6579 m_{GW} \tag{1}$$

$$m_{RW}^{*} = \begin{cases} 5.7 \cdot 10^{-5} m_{GW}^{1.69} \\ or, alternatively, \\ (0.04 + 11 \cdot 10^{-7} m_{GW}) m_{GW} \end{cases} \tag{2}$$

$$m_{FW}^{*} = \begin{cases} 2.24 \cdot 10^{-5} m_{GW}^{1.83} \\ or, alternatively, \\ (0.0577 + 2.2 \cdot 10^{-6} m_{GW}) m_{GW} \end{cases} \tag{3}$$

$$m_{WW}^{*} = \begin{cases} 1.555 m_{GW}, & m_{GW} < 27300 \\ 147.38 m_{GW}^{0.371}, & m_{GW} \geq 27300 \end{cases} \tag{4}$$

$$m_{EDTW}^{*} = \begin{cases} 3.01 \cdot 10^{-2} m_{GW}^{1.21} \\ or, alternatively, \\ (0.117 + 4.71 \cdot 10^{-7} m_{GW}) m_{GW} \end{cases} \tag{5}$$

$$m_{FEW}^{*} = 0.106 m_{GW} \tag{6}$$

To arrive at small to midsize vehicle weight/mass estimates, the following simple linear scaling:

$$m_{SUM} = m_{RW}^{*} + m_{FW}^{*} + m_{WW}^{*} + m_{EDTW}^{*} + m_{FEW}^{*} \tag{7a}$$

$$\varphi_1 = \frac{1}{\left(1 + \frac{E_{Battery}}{E_{Total}}\right)} \left(\frac{m_{EW}}{m_{SUM}} - 1\right) + 1 \tag{7b}$$

$$m_{RW} = \varphi_1 m_{RW}^{*} \tag{8a-b}$$

$$m_{WW} = \varphi_1 m_{WW}^{*} \tag{9}$$

$$m_{FEW} = \varphi_1 m_{FEW}^{*} \tag{10}$$

$$m_{EDTW} = \varphi_1 m_{EDTW}^{*} \tag{11}$$

$$m_{FW} = \varphi_1 \varphi_2 m_{FW}^{*} \tag{12}$$

Note that the multiplier factor,φ_1, is intended to account for both the proportional nature of the vehicle's energy coming from a battery versus the total mission energy; the multiplier factor also accounts for the linear scaling from large to small and midsize tiltrotor aircraft. Admittedly, the multiplier factor, φ_1, is somewhat ad hoc in nature. Additionally, a second multiplier factor, φ_2, has been introduced (and herein assigned a value of $\varphi_2 = 1.2$) to account for non-tube-and-wing fuselage configurations, such as the blended-wing-body-type fuselage employed in the longer-range New Nomad tiltrotor aircraft examined in this paper.

Some limited validation has been performed comparing the estimates for the simple rotorcraft sizing analysis used in the paper and the results from Ref. 30. Reference 30 performed sizing analysis using the well-known and widely used NDARC (e.g., Ref. 31) to perform a design study for two tiltrotor aircraft variants (one employing turboshaft propulsion and one all-electric, i.e., batteries and electric motors) to meet a baseline NASA UAM mission profile (Ref. 20). This cross-sizing-tool validation is presented in Figs. 78-79.

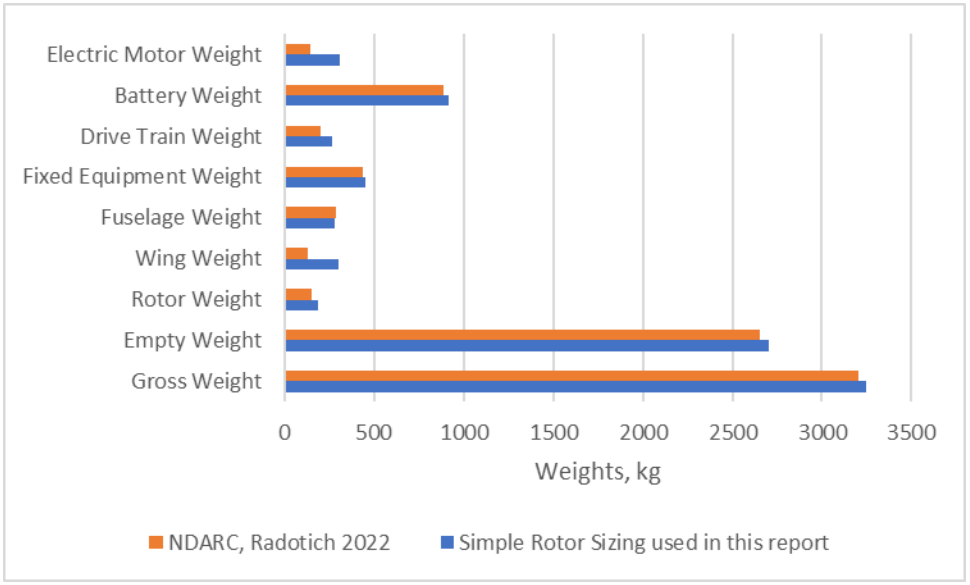

Figure 78. Validation of all-electric small tiltrotor sizing (simple sizing rotorcraft analysis used in this report as compared to Ref. 30 NDARC sizing)

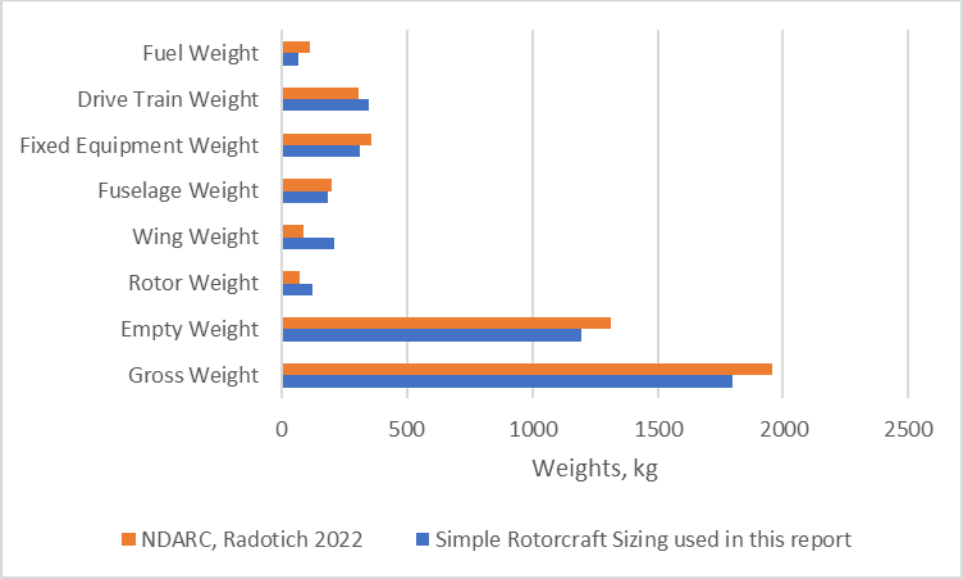

Figure 79. Validation of turboshaft-propulsion small tiltrotor sizing (simple sizing rotorcraft analysis used in this report as compared to Ref. 30 NDARC sizing)

Two key design decisions need to be made at the very beginning of the simple, first-order sizing analysis. First, to minimize the complexity of loading operations of multiple habitat modules on the long-range vehicle, a blended-wing-body-like fuselage with front and aft loading ramps and a telescoping accordion-like fuselage roof is adopted. This novel airframe configuration can be seen in the earlier presented Fig. 49. Second, the implementation of the hybrid turboelectric in the context of the mission profile, Fig. 80, a simple hybrid-electric power profile needs to also be defined (portion of power provided by batteries versus the turboshaft engines for cruise, hover, and edgewise forward flight and climb). Several hybrid turboelectric propulsion approaches for tiltwing and tiltrotor aircraft have been proposed and studied, e.g., Refs. 61-62. The approach taken in this study is that turboshaft engines provide most of the rotor power but are supplemented by in-parallel electric motors powered by batteries for partial power augmentation in hover and edgewise rotor forward flight and climb; all cruise power is provided solely by the turboshaft engines for most cases considered.

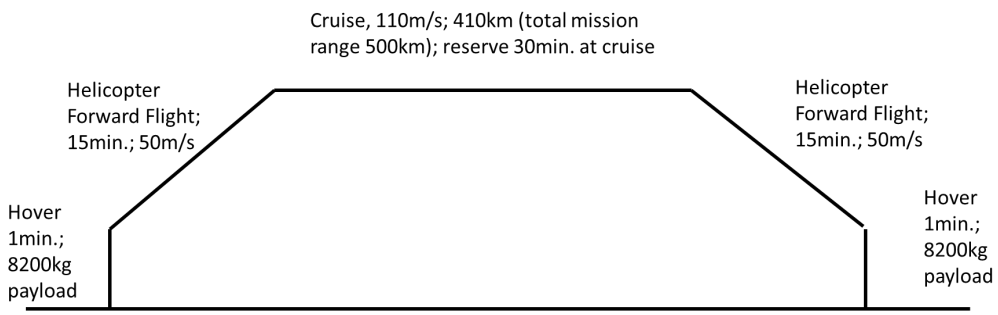

Figure 80. Generic Mission Profile for Long Range Mobility

Tables 30-36 are now presented to illustrate the impact on vehicle weight of the fraction of the mission energy provided by batteries versus the total mission energy expended. The sizing results in Tables 30-36 reflect the first opportunity to consider the novel blended-wing-body-tiltrotor configuration. Additionally, these sizing results demonstrate the increase in vehicle gross weight with increasing dependence on electric power from batteries for a given mission.

Table 30. First-Order Sizing Results for a Ratio of Electric Battery Energy to Total Mission Energy, $E_{Battery}/E_{Total}$, = 0

Main Rotor Disk Loading	973.2	N/m^2
Main Rotor Radius	5.9	m
Number of Blades	4	nondim.
Main Rotor Solidity	0.12	nondim.
Main Rotor Tip Speed	238.2	m/s
Nominal (Mean) Airplane-Mode Cruise Wing Loading	5000.1	N/m^2
Wing Span	15.4	m
Number of Electric Motors per Rotor	0	nondim.
Hover Power	2844.3	kW
Advance Ratio	0.21	nondim.
Nominal Helicopter-Mode Forward Flight Power	1656.6	kW
Vehicle Effective Lift over Drag in Airplane-Mode Cruise	10	nondim.
Nominal (Mean) Airplane-Mode Cruise Power	1069.0	kW
Energy from Battery over Total Mission Energy	0	nondim.
Prescribed Fraction of Power Delivered by Electric Motors in Hover versus Turboshaft Engines	0	nondim.
Prescribed Fraction of Power Delivered by Electric Motors in Helicopter-Mode Forward Flight versus Turboshaft Engines	0	nondim.
Prescribed Fraction of Power Delivered by Electric Motors in Airplane-Mode Cruise versus Turboshaft Engines	0	nondim.
Payload (Combined Passenger(s) and Habitat Modules)	8181.8	kg
Total Weight of Rotors	1039.7	kg
Fuselage Weight	1620.2	kg
Wing Weight	2628.2	kg
Total Turboshaft Engines and Drive Train Weight	2157.8	kg
Total Fuel Weight	433.0	kg
Total Battery Weight	0	kg
Total Electric Motor Weight	1223.4	kg
Total Fixed Equipment Weight	2093.5	kg
Total TOGW =	19378	kg

Table 31. First-Order Sizing Results for a Ratio of Electric Battery Energy to Total Mission Energy, $E_{Battery}/E_{Total}$, = 0.06

Main Rotor Disk Loading	973.2	N/m^2
Main Rotor Radius	6.12	m
Number of Blades	4	nondim.
Main Rotor Solidity	0.12	nondim.
Main Rotor Tip Speed	238.2	m/s
Nominal (Mean) Airplane-Mode Cruise Wing Loading	4986.8	N/m^2
Wing Span	16.0	m
Number of Electric Motors per Rotor	1	nondim.
Hover Power	3060.4	kW
Advance Ratio	0.21	nondim.
Nominal Helicopter-Mode Forward Flight Power	1782.4	kW
Vehicle Effective Lift over Drag in Airplane-Mode Cruise	10	nondim.
Nominal (Mean) Airplane-Mode Cruise Power	1150.2	kW
Energy from Battery over Total Mission Energy	0.06	nondim.
Prescribed Fraction of Power Delivered by Electric Motors in Hover versus Turboshaft Engines	0.125	nondim.
Prescribed Fraction of Power Delivered by Electric Motors in Helicopter-Mode Forward Flight versus Turboshaft Engines	0.125	nondim.
Prescribed Fraction of Power Delivered by Electric Motors in Airplane-Mode Cruise versus Turboshaft Engines	0	nondim.
Payload (Combined Passenger(s) and Habitat Modules)	8181.8	kg
Total Weight of Rotors	1176.6	kg
Fuselage Weight	1852.4	kg
Wing Weight	2700.6	kg
Total Turboshaft Engines and Drive Train Weight	2357.6	kg
Total Fuel Weight	442.7	kg
Total Battery Weight	571.0	kg
Total Electric Motor Weight	1306.7	kg
Total Fixed Equipment Weight	2252.5	kg
Total TOGW =	20841.9	kg

Table 32. First-Order Sizing Results for a Ratio of Electric Battery Energy to Total Mission Energy, $E_{Battery}/E_{Total}$, = 0.11

Main Rotor Disk Loading	973.2	N/m^2
Main Rotor Radius	6.37	m
Number of Blades	4	nondim.
Main Rotor Solidity	0.12	nondim.
Main Rotor Tip Speed	238.21	m/s
Nominal (Mean) Airplane-Mode Cruise Wing Loading	4971.2	N/m^2
Wing Span	16.7	m
Number of Electric Motors per Rotor	1	nondim.
Hover Power	3312.4	kW
Advance Ratio	0.21	nondim.
Nominal Helicopter-Mode Forward Flight Power	1929.2	kW
Vehicle Effective Lift over Drag in Airplane-Mode Cruise	10	nondim.
Nominal (Mean) Airplane-Mode Cruise Power	1244.9	kW
Energy from Battery over Total Mission Energy	0.11	nondim.
Prescribed Fraction of Power Delivered by Electric Motors in Hover versus Turboshaft Engines	0.25	nondim.
Prescribed Fraction of Power Delivered by Electric Motors in Helicopter-Mode Forward Flight versus Turboshaft Engines	0.25	nondim.
Prescribed Fraction of Power Delivered by Electric Motors in Airplane-Mode Cruise versus Turboshaft Engines	0	nondim.
Payload (Combined Passenger(s) and Habitat Modules)	8181.8	kg
Total Weight of Rotors	1345.0	kg
Fuselage Weight	2141.1	kg
Wing Weight	2781.1	kg
Total Turboshaft Engines and Drive Train Weight	2594.5	kg
Total Fuel Weight	453.9	kg
Total Battery Weight	1236.0	kg
Total Electric Motor Weight	1403.1	kg
Total Fixed Equipment Weight	2438	kg
Total TOGW =	22574.5	kg

Table 33. First-Order Sizing Results for a Ratio of Electric Battery Energy to Total Mission Energy, $E_{Battery}/E_{Total}$, = 0.23

Main Rotor Disk Loading	973.2	N/m^2
Main Rotor Radius	7.28	m
Number of Blades	4	nondim.
Main Rotor Solidity	0.12	nondim.
Main Rotor Tip Speed	238.2	m/s

Nominal (Mean) Airplane-Mode Cruise Wing Loading	4909.1	N/m^2
Wing Span	19.2	m
Number of Electric Motors per Rotor	1	nondim.
Hover Power	4320.5	kW
Advance Ratio	0.21	nondim.
Nominal Helicopter-Mode Forward Flight Power	2516.3	kW
Vehicle Effective Lift over Drag in Airplane-Mode Cruise	10	nondim.
Nominal (Mean) Airplane-Mode Cruise Power	1623.8	kW
Energy from Battery over Total Mission Energy	0.23	nondim.
Prescribed Fraction of Power Delivered by Electric Motors in Hover versus Turboshaft Engines	0.5	nondim.
Prescribed Fraction of Power Delivered by Electric Motors in Helicopter-Mode Forward Flight versus Turboshaft Engines	0.5	nondim.
Prescribed Fraction of Power Delivered by Electric Motors in Airplane-Mode Cruise versus Turboshaft Engines	0	nondim.
Payload (Combined Passenger(s) and Habitat Modules)	8181.8	kg
Total Weight of Rotors	2107.4	kg
Fuselage Weight	3481.8	kg
Wing Weight	3069.2	kg
Total Turboshaft Engines and Drive Train Weight	3578.4	kg
Total Fuel Weight	526.3	kg
Total Battery Weight	3224.3	kg
Total Electric Motor Weight	1782.0	kg
Total Fixed Equipment Weight	3180	kg
Total TOGW =	29131.1	kg

Table 34. First-Order Sizing Results for a Ratio of Electric Battery Energy to Total Mission Energy, $E_{Battery}/E_{Total}$, = 0.34

Main Rotor Disk Loading	973.2	N/m^2
Main Rotor Radius	9.11	m
Number of Blades	4	nondim.
Main Rotor Solidity	0.12	nondim.
Main Rotor Tip Speed	238.2	m/s
Nominal (Mean) Airplane-Mode Cruise Wing Loading	4758.3	N/m^2
Wing Span	24.3	m
Number of Electric Motors per Rotor	1	nondim.
Hover Power	6768.8	kW
Advance Ratio	0.21	nondim.
Nominal Helicopter-Mode Forward Flight Power	3942.2	kW
Vehicle Effective Lift over Drag in Airplane-Mode Cruise	10	nondim.

Nominal (Mean) Airplane-Mode Cruise Power	2544.0	kW
Energy from Battery over Total Mission Energy	0.34	nondim.
Prescribed Fraction of Power Delivered by Electric Motors in Hover versus Turboshaft Engines	0.75	nondim.
Prescribed Fraction of Power Delivered by Electric Motors in Helicopter-Mode Forward Flight versus Turboshaft Engines	0.75	nondim.
Prescribed Fraction of Power Delivered by Electric Motors in Airplane-Mode Cruise versus Turboshaft Engines	0	nondim.
Payload (Combined Passenger(s) and Habitat Modules)	8181.8	kg
Total Weight of Rotors	4500.4	kg
Fuselage Weight	7917.9	kg
Wing Weight	3625.4	kg
Total Turboshaft Engines and Drive Train Weight	6160.3	kg
Total Fuel Weight	680.2	kg
Total Battery Weight	7577.0	kg
Total Electric Motor Weight	2668.9	kg
Total Fixed Equipment Weight	4982	kg
Total TOGW =	46294.0	kg

Table 35. First-Order Sizing Results for a Ratio of Electric Battery Energy to Total Mission Energy, $E_{Battery}/E_{Total}$, = 0.4

Main Rotor Disk Loading	973.2	N/m^2
Main Rotor Radius	8.14	m
Number of Blades	4	nondim.
Main Rotor Solidity	0.12	nondim.
Main Rotor Tip Speed	238.2	m/s
Nominal (Mean) Airplane-Mode Cruise Wing Loading	4842.6	N/m^2
Wing Span	21.6	m
Number of Electric Motors per Rotor	1	nondim.
Hover Power	5400.6	kW
Advance Ratio	0.21	nondim.
Nominal Helicopter-Mode Forward Flight Power	3145.4	kW
Vehicle Effective Lift over Drag in Airplane-Mode Cruise	10	nondim.
Nominal (Mean) Airplane-Mode Cruise Power	2029.8	kW
Energy from Battery over Total Mission Energy	0.4	nondim.
Prescribed Fraction of Power Delivered by Electric Motors in Hover versus Turboshaft Engines	0.875	nondim.
Prescribed Fraction of Power Delivered by Electric Motors in Helicopter-Mode Forward Flight versus Turboshaft Engines	0.875	nondim.
Prescribed Fraction of Power Delivered by Electric Motors in Airplane-Mode Cruise versus Turboshaft Engines	0	nondim.
Payload (Combined Passenger(s) and Habitat Modules)	8181.8	kg

Total Weight of Rotors	3072.7	kg
Fuselage Weight	5237.8	kg
Wing Weight	3334.1	kg
Total Turboshaft Engines and Drive Train Weight	4687.5	kg
Total Fuel Weight	493.4	kg
Total Battery Weight	7053.1	kg
Total Electric Motor Weight	2178.2	kg
Total Fixed Equipment Weight	3975	kg
Total TOGW =	38213.6	kg

Table 36. First-Order Sizing Results for a Ratio of Electric Battery Energy to Total Mission Energy, $E_{Battery}/E_{Total}$, = 0.45

Main Rotor Disk Loading	973.2	N/m^2
Main Rotor Radius	9.01	m
Number of Blades	4	nondim.
Main Rotor Solidity	0.12	nondim.
Main Rotor Tip Speed	238.2	m/s
Nominal (Mean) Airplane-Mode Cruise Wing Loading	4767.1	N/m^2
Wing Span	24.0	m
Number of Electric Motors per Rotor	1	nondim.
Hover Power	6624.8	kW
Advance Ratio	0.21	nondim.
Nominal Helicopter-Mode Forward Flight Power	3858.3	kW
Vehicle Effective Lift over Drag in Airplane-Mode Cruise	10	nondim.
Nominal (Mean) Airplane-Mode Cruise Power	2489.9	kW
Energy from Battery over Total Mission Energy	0.45	nondim.
Prescribed Fraction of Power Delivered by Electric Motors in Hover versus Turboshaft Engines	1	nondim.
Prescribed Fraction of Power Delivered by Electric Motors in Helicopter-Mode Forward Flight versus Turboshaft Engines	1	nondim.
Prescribed Fraction of Power Delivered by Electric Motors in Airplane-Mode Cruise versus Turboshaft Engines	0	nondim.
Payload (Combined Passenger(s) and Habitat Modules)	8181.8	kg
Total Weight of Rotors	4339.8	kg
Fuselage Weight	7612.3	kg
Wing Weight	3596.6	kg
Total Turboshaft Engines and Drive Train Weight	6002.1	kg
Total Fuel Weight	585.0	kg
Total Battery Weight	9887.7	kg
Total Electric Motor Weight	2617.8	kg
Total Fixed Equipment Weight	4876	kg
Total TOGW =	47699.2	kg

Figure 81 summarizes some of the vehicle weight trends as a function of the ratio of the energy provided by batteries over the total mission energy. As this battery to total energy ratio increase the takeoff gross weight of the vehicle (and the battery weight) not surprisingly increases. Fuel weight (to run the turboshaft engines) is relatively constant for low- to mid-level values of battery to total energy ratios but, eventually, fuel weight also must increase to account for the heavier gross weight vehicles needed to fly the larger batteries.

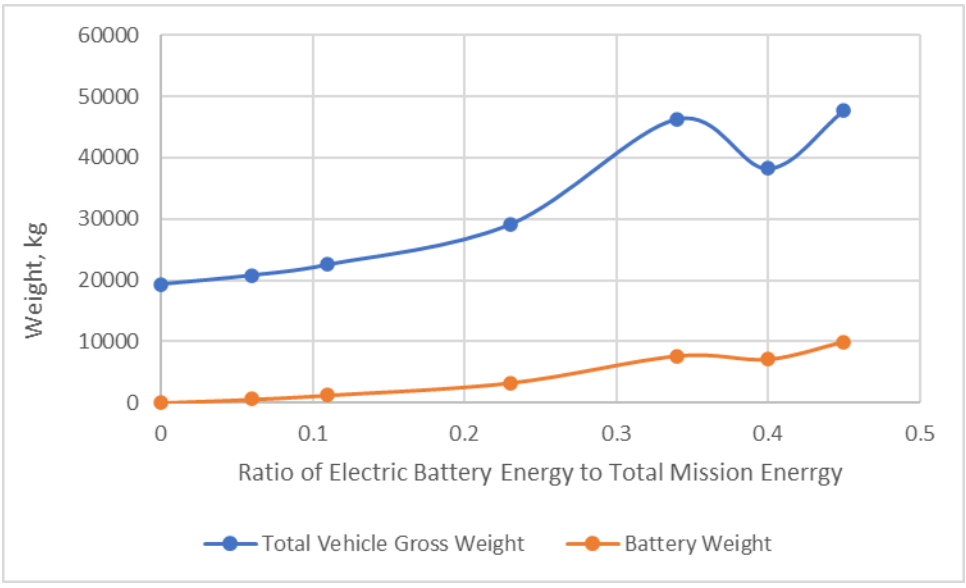

(a)

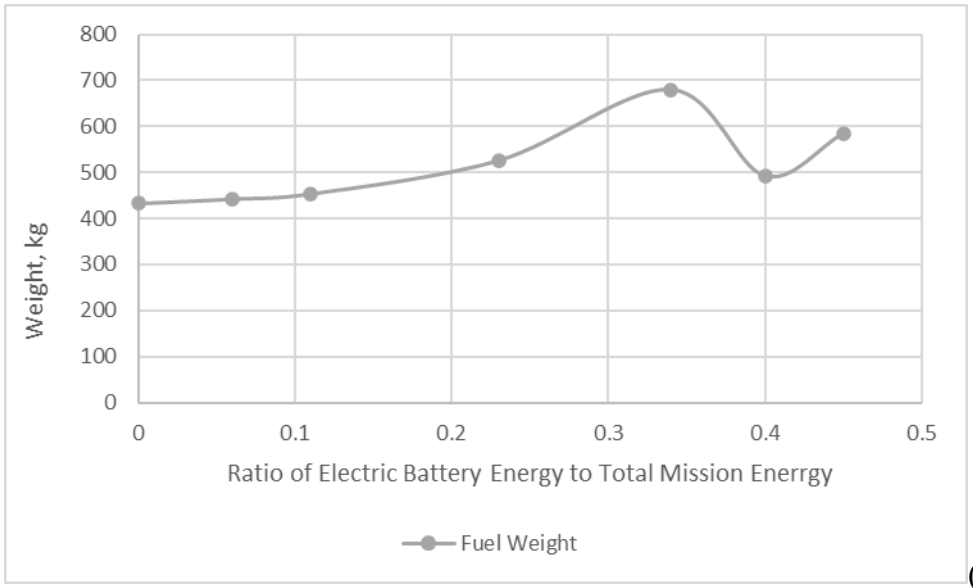

(b)

Figure 81. (a) Vehicle Gross Weight and Battery Weight and (b) Fuel Weight as a function of Ratio of Electric Battery Energy to Total Mission Energy, $E_{Battery}/E_{Total}$,

The above results (Tables 30-36 and Fig. 81a-b) suggest that a modest growth in vehicle gross weight for hybrid electric/turboshaft-engine vehicles can be expected for vehicles with ratios of electric battery energy to total mission energy on the order of 0.15 or less; ratios greater than that yield much larger vehicles that are not likely economically justifiable. More work needs to be performed, though, to examine this question of vehicle sizing for hybrid electric/turboshaft-engine tiltrotor aircraft. Additionally, the above results do not reflect any trade studies between payload requirements and total mission range.

Mobility and Habitability Systems Analysis Metrics

This notional NN transportation/habitation system architecture needs to be analyzed using new types of metrics and compared to transportation-only multi-modality systems. This section of the report attempts to define such metrics and provide initial discussion as to possible trends.

Single occupant/passenger daily cost savings, S_C, can be expressed as in Eq. 13. Where the following definitions hold: A_{Hab} is the nominal floor square footage of habitat; C_{Com} is the cost (rental or mortgage) of commercial property per unit square footage per day; C_{Hab} is the cost (rental or mortgage) of habitat module per unit square footage per day; C_{Resid} is the cost (rental or mortgage) of residential property per unit square footage per day; χ is the ratio of the share of cost savings for the occupant/passenger relative to the commercial/corporate entity, nondim.; ϕ is the ratio of the sum of residential and habitat daily costs (rental and mortgage) per unit square footage with respect to the cost of commercial property; $\phi = (C_{Resid} + C_{Hab})/C_{Com}$.

$$S_C = f(A_{Hab}, C_{Com}, C_{Hab}, C_{Resid}, \chi, \phi) \tag{13}$$

Equation 14 provides a proposed first order estimate of single occupant/passenger daily cost savings.

$$S_C \approx \frac{1}{2}\chi(1-\phi)C_{Com}A_{Hab} \tag{14}$$

Yearly total occupant/passenger cost savings, therefore, is simply given by Eq. 15.

$$S_{CY} = 365 S_c N_M, \tag{15}$$

As Fig. 82 illustrates, given Eq. 15, if the cost of residence and habitat costs (for a given square footage) is sufficiently small, then the cumulative yearly total occupancy cost savings are directly proportional to the number of habitat movements by NN aircraft. As the cost of residence and costs increases, then the yearly cost savings decrease to the point that there are no cost savings if the residence and habitat costs are roughly equal to the commercial property costs for that geographic location.

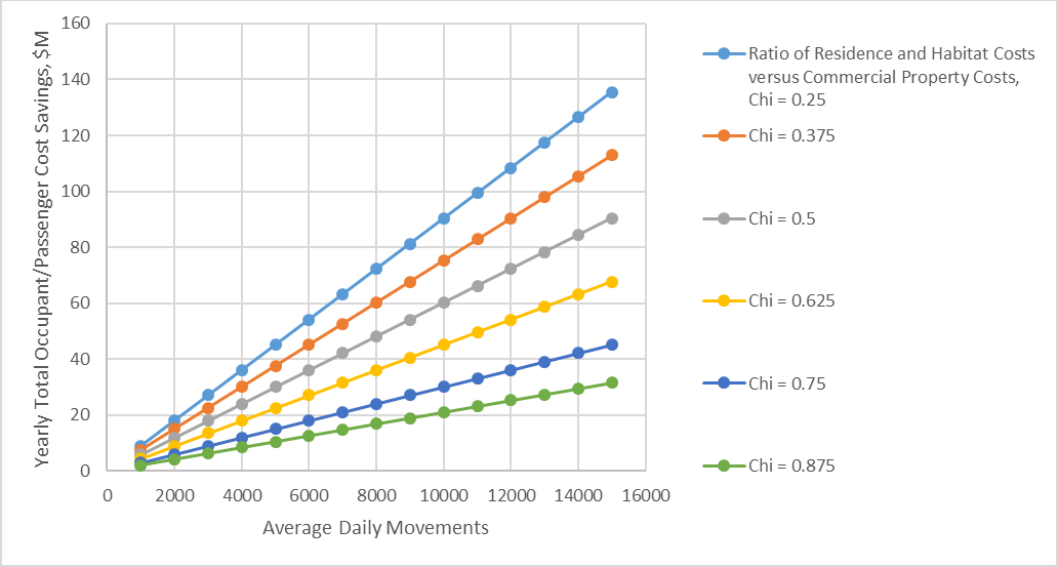

Figure 82. Yearly cost savings for all passengers/occupants (metric with greatest utility for passenger acceptance)

Equation 16 provides a proposed first order estimate of the commercial/corporate yearly cost savings. S_{CYC} is the yearly cost saving accrued by the corporate entities that own or rent the commercial property to which the use of habitats augment the office space available daily due to commuting and usage of habitats as temporary office space. (Ideally both the commuter and the corporation/employer can simultaneously derive cost saving benefits by the notional New Nomad transportation/habitation architecture.) Note, in Eq. 16, the introduction of the new parameter, N_M, which is the number of average daily habitat/transit movements for commute or work-related.

$$S_{CYC} = \frac{365}{2}(1-\chi)(1-\phi)C_{Com}A_{Hab}N_M \tag{16}$$

Functionally, daily occupant/passenger time savings can be expressed by Eq. 17. The parameter S_t is the daily time savings for single occupant/passenger (as compared to ground travel during prime commute hours), hours. The parameter d_A is the distance traveled by air during the aerial mobility phase of the trip, km. The parameter d_G is the distance traveled on the ground during the ground mobile phase of the trip, km. V_A is the nominal

aerial velocity, kilometers per hour. V_G is the nominal ground velocity from ground mobility option, kilometers per hour. V_{G0} is the nominal ground velocity from ground travel during prime commute hours, kilometers per hour.

$$S_t = g(d_G, d_A, V_A, V_G, V_{G0}) \tag{17}$$

Equation 18 provides a proposed first order estimate of the single movement time savings.

$$S_t \geq \left(\frac{1}{V_G} - \frac{1}{V_A}\right) d_A \tag{18}$$

Introducing a "circuity" correction, κ, to the aerial distance covered to arrive at a better estimate of the baseline ground distance (with no aerial transport) that needs to be covered.

$$S_t \approx \left(\frac{\kappa}{V_G} - \frac{1}{V_A}\right) d_A \tag{19}$$

Or, compared to ground mobility during non-prime/non-peak commute hours (potentially enabled by autonomous system control, i.e., sleeping in the habitat module while it is being driven to the work site, if that were allowed by regulations)

$$S_{t0} \geq \frac{(d_G + d_A)}{V_{G0}} - \frac{d_A}{V_A} \tag{20}$$

Or

$$S_{t0} \approx \frac{(d_G + \kappa d_A)}{V_{G0}} - \frac{d_A}{V_A} \tag{21}$$

Figure 83 illustrates, given Eq. 18 or Eq. 19, the anticipated trends of the daily time savings for single occupant/passenger (as compared to ground travel during prime commute hours), hours, as a function of the ratio of air speed to ground speed (as well as the secondary influence of the ratio of distance traveled by air versus ground) for habitat

movements. In general, the faster the portion of the habitat movement by air, versus by ground, the greater the time savings.

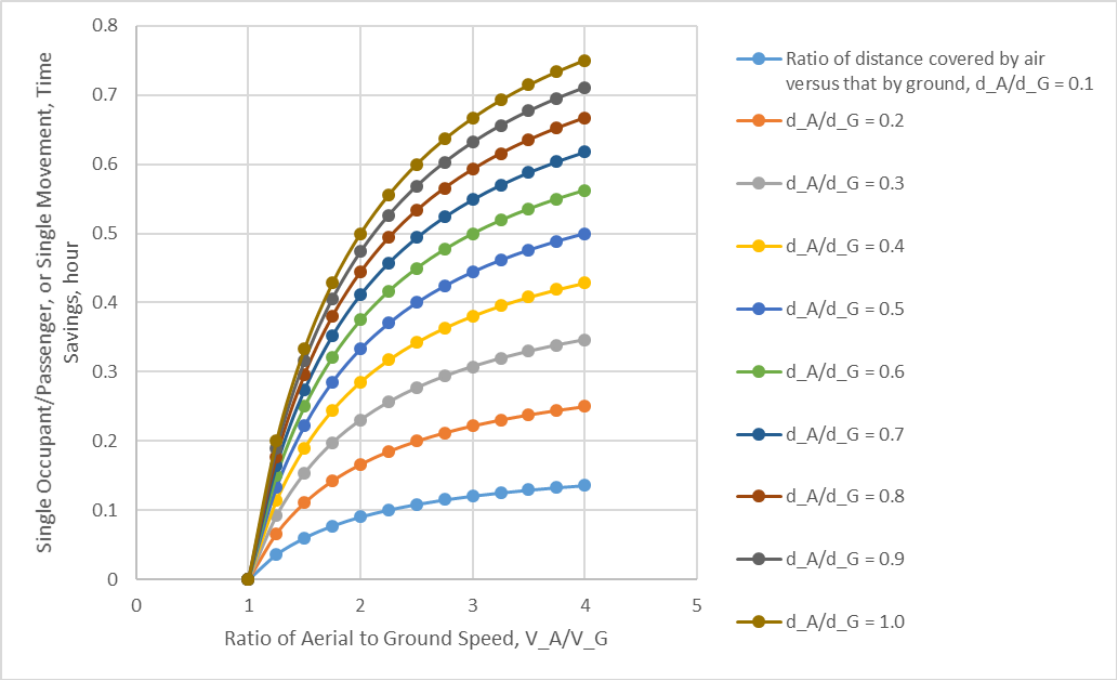

Figure 83. Time Savings for a single passenger/occupant – or, rather, a single habitat/transit movement (metric with the greatest utility for passenger acceptance)

Correspondingly, the total community yearly time savings, all movements for the whole year can be given by

$$S_{tY} \geq 365 S_t N_M \tag{22}$$

The above is perhaps potentially the metric with the greatest utility for urban planners. Figure 84 presents the anticipated trends of yearly cumulative time savings for all daily movements for a given urban/regional area, given Eq. 22.

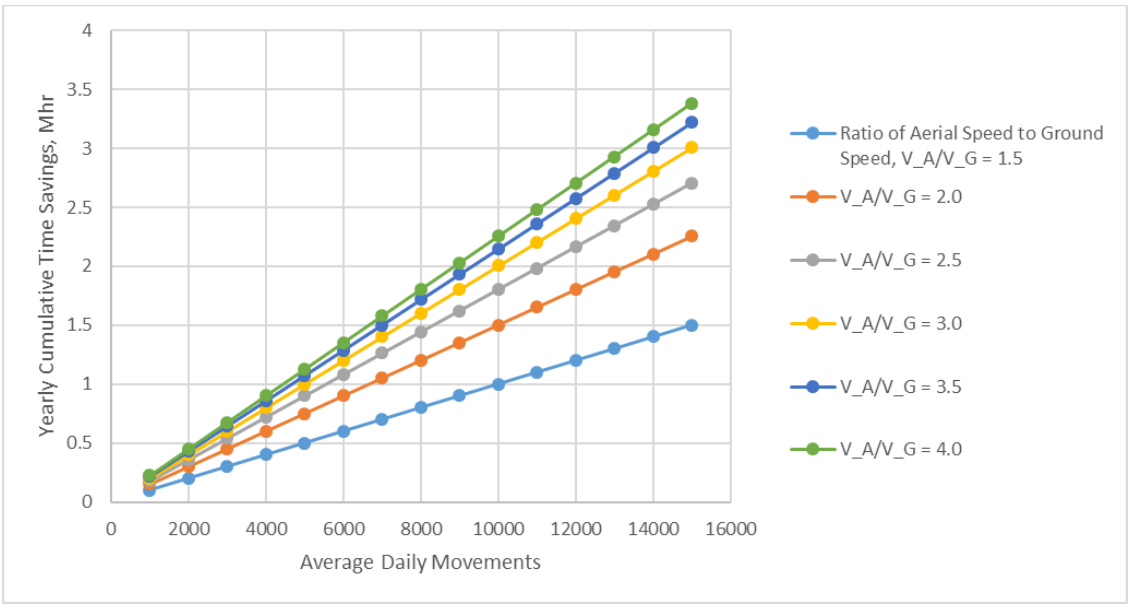

Figure 84. Yearly Cumulative Time Savings for all daily movements for a given urban/regional area (results for $d_A/d_G = 0.7$)

Functionally, a nondimensional "livability index" can be expressed by the expression.

$$L_I = h(S_C, S_t, N_{MR}, N_M, W) \tag{23}$$

There is not a standard definition of "livability" used by urban planners. But there are several factors that are typically considered when accessing the livability of various communities. The above functional relationship considers three such factors: daily cost of housing (and/or commercial properties) as represented by the parameter S_C; time (hours per day) required for commuting as represented by S_t; and the amount of cultural, entertainment, and recreational activity as represented by the newly introduced parameter N_{MR} . Note that W is the average yearly wage/salary for residents of urban/regional area, USD.

Equation 24 provides a proposed first order estimate of the proposed urban "livability index".

$$L_I = \frac{1}{W}\left(365 S_C + \frac{W}{8} S_t + C\frac{N_{MR}}{N_M}\right) \tag{24}$$

Figure 85 illustrates some representative results for the above livability index expression as a function of the air-to-ground-speed ratio. Figure 85 results are based on the following fixed parameters: $d_A/d_G = 0.7$; $\phi = 0.25$; $\kappa = 1$; C = 75,000 USD.

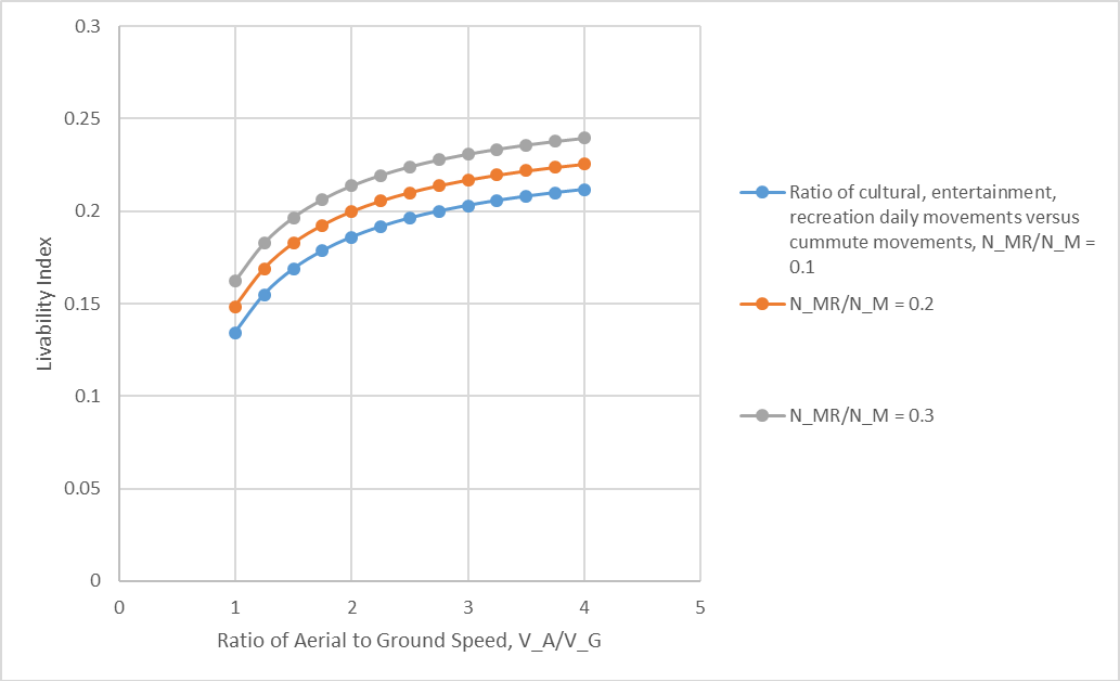

Figure 85. Livability Index trends with number of average daily occupant/passenger movements

Network Operational Modeling

References 9-10 used discrete event simulation tools to perform network operation modeling in support of earlier metropolitan/regional aerial transportation network analysis. Other network operational modeling work was performed for early on-demand air-taxis analysis, Ref. 20. The work of Refs. 9, 10, and 20 – i.e., for 'Hopper' networks – partly involved the use discrete event simulations to address questions as to vehicle fleet sizing (by assessing potential passenger supply and demand) and vertiport sizing and siting. In turn estimates of daily fleet energy expenditures as a function of daily passenger capacity was provided by the custom discrete simulations of the aerial fleet and traffic developed as a part of these earlier study efforts.

In the case of this work, more complex considerations need to be accounted for in the simulation modeling, if for no other reasons that integrated multimodal transportation is a foundational aspect of these New Nomad networks. Further, a multitude of transport origins and destinations need to account for where to pick up and drop off habitat modules for each transport movement. In many ways the network modeling required for New Nomad transportation is significantly more complex than the early "Hopper' network studies, Refs. 9-11. The fundamental questions that such network operational modeling would seek to answer are: (1) verify the validity and utility of the first-order metric estimates by means of simulation; (2) consider multi-modal (including air) transportation while considering the unique implications of NN networks on housing, commuting (behavior), and office space requirements both in the mid- to far-term future; (3) to perform trade studies by varying the aeroperformance and CONOPS characteristics of different notional NN aerial vehicles and demonstrating their impact on network operational performance.

Such New Nomad network work could be initiated by means of, for example, the Java-based Jaamsim open-source discrete event simulation (DES) tool, Ref. 25. A similar DES-based tool was used for the Refs. 9-11 "Hopper" network studies.

Figure 86 summarizes high-level simulation architecture/framework for performing New Nomad analysis with the goal of spanning across the spectrum of very fast (hour) multi-modal simulations (to establish passenger demand) to very slow (years/decades) of simulation (to estimate impacts on urban livability).

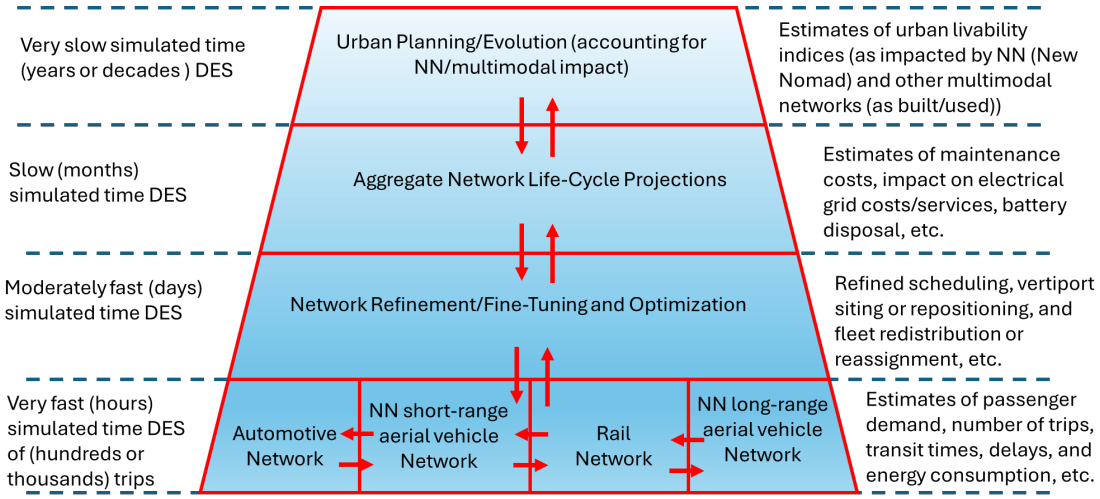

Figure 86. A Simulation Architecture/Framework for Future New Nomad Analysis

Figure 87 is a high-level simulation flow chart of the type of multi-modal very fast simulations required to make estimates of passenger demand, the number of trips per day, average transit time, delays, and daily total system energy consumption.

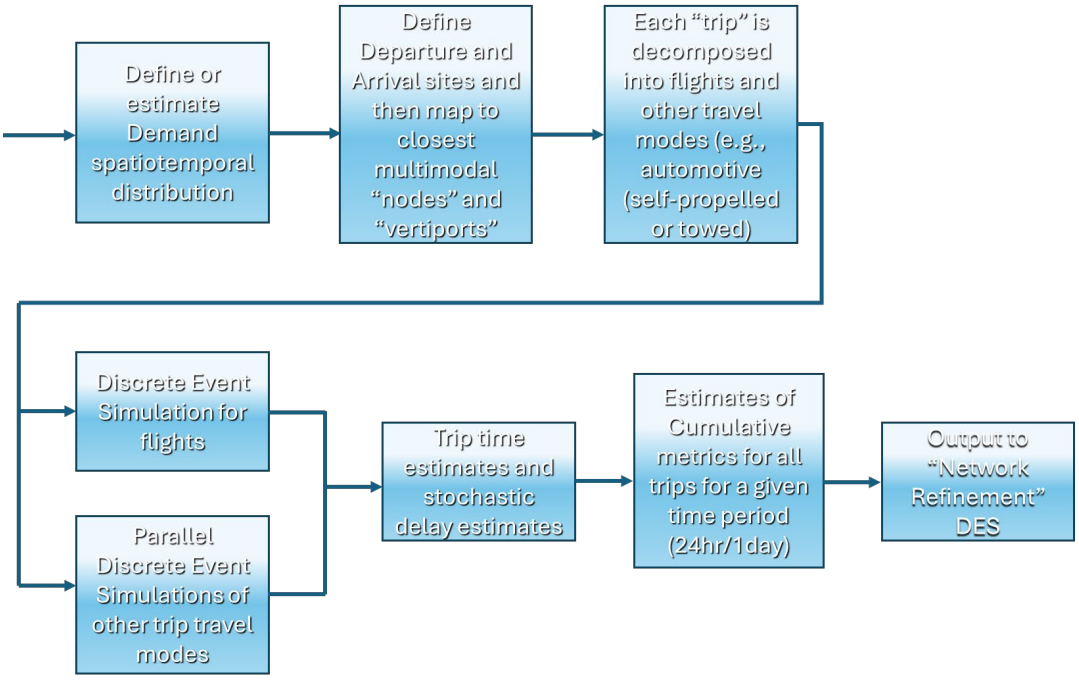

Figure 87. Very fast (hours) simulated time DES of (hundreds or thousands of trips (multi-modal in nature)

Figure 88 is a high-level moderately fast (days of simulated time) simulation of New Nomad aircraft/networks over multiple days of simulated times (with stochastic inputs as to passenger demand, delays, and other key parameters) to determine cumulative metrics that aid in the definition of 'best' aircraft fleet size and vertiport count and siting.

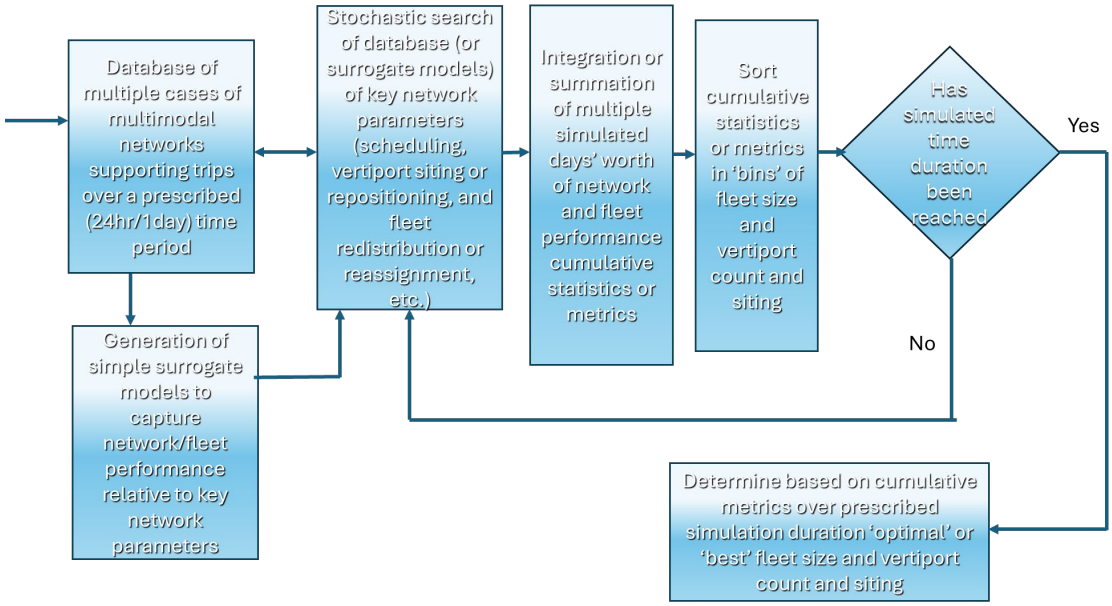

Figure 88. Moderately fast (days) simulated time DES

Figure 89 is a flow chart describing a slow (months of simulated time) DES simulation that seeks to estimate fleet maintenance costs, impact of electrical grid, and long-term solid-waste battery disposal.

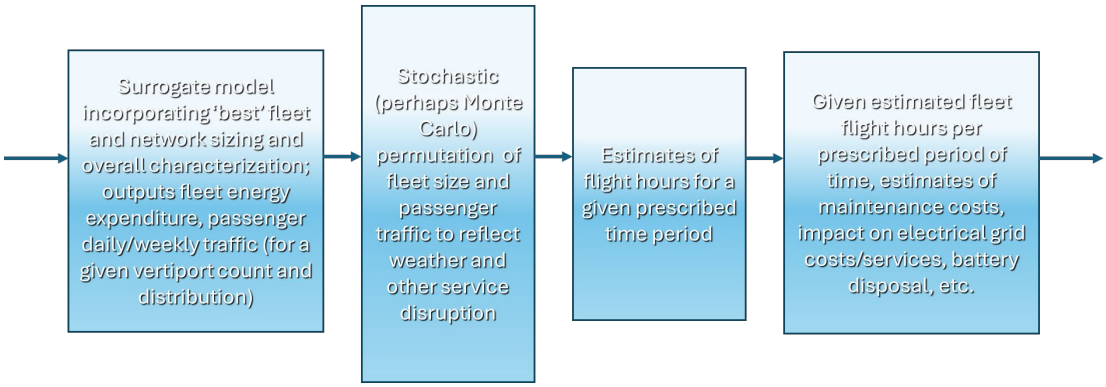

Figure 89. Slow (months) simulated time DES

Finally, Fig. 90 presents a high-level flow chart for the type of very slow (years or decades of simulated time) stochastic simulations required to make estimates of various urban livability indices that might be employed to assess the impact of New Nomad networks (and the overall habitat transport and, in parallel, habitation/transportation architecture) proposed in this study. This is fundamental system-of-systems assessment that can only be enabled by the broad range (and interdependent) of multi-time-scale simulations proposed in Figs. 86-90.

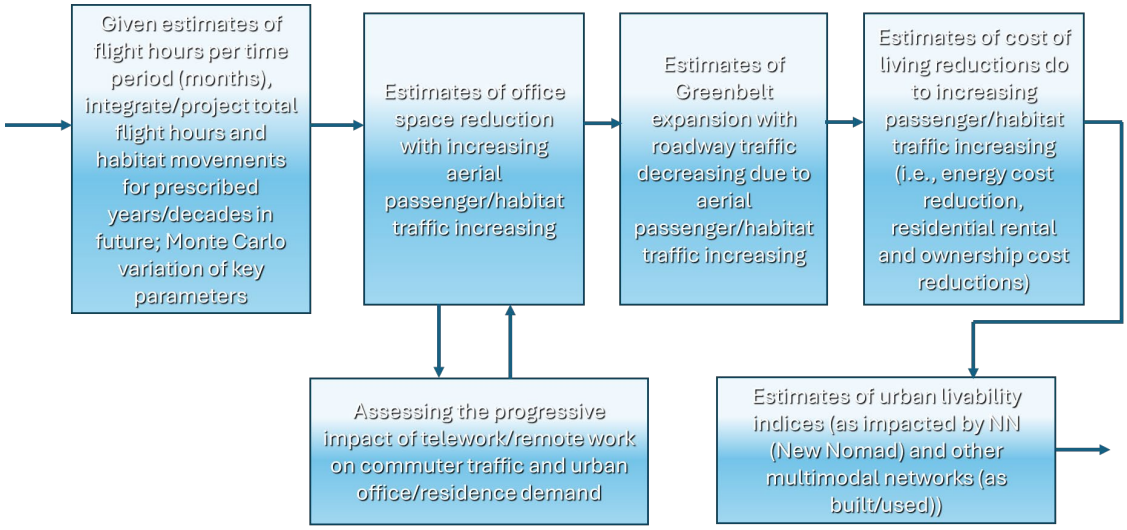

Figure 90. Very slow (years/decades) simulated time DES

The above introductory remarks as to New Nomad discrete event simulation is intended to kick-start a broadened discussion within the rotorcraft research community as to how to best model clean-sheet conceptual designs in a multi-modal and cross-functional (in a transport of passengers, goods, and services) sense, in either an urban or otherwise environment, for a wide-varying set of simulation time scales.

Future Work and Potential Technology Roadmap

From an aircraft design perspective, the unique aspects of the vehicles to be designed for short- and long-range aerial mobility in the context of the New Nomad paradigm is that the vehicles must be capable of carrying heavier cargo payloads than other all- or hybrid-electric propulsion aircraft being currently proposed. Further, the implied automated processes to load, stow, and unload "habitat module" cargo will also pose novel challenges as compared to the predominately very manual process of cargo loading employed for most current aircraft. This will require a revised interpretation of fuselage mold lines, cargo ramps, fuselage structures (and whether they are retractable or not) and general interior and external layout accommodations for ease and automation of loading/unloading. These novel fuselage mold lines and overall layouts may lead to new aerodynamic design configurations.

The New Nomad transportation/habitation system architecture paradigm opens a whole new suite of questions regarding multimodal transportation systems as well as new questions and options as to future urban planning.

Recent events (including the 2020-2022 COVID pandemic) have highlighted the desirability of a work-from-anywhere modality. This was largely due to the pervasiveness and effectiveness of telework tools and processes. Telework may at first seem to reduce the need for urban transportation concepts such as the New Nomad concept. But, on the other hand, this work-from-anywhere modality might even further expand the need for the adoption of new transportation systems and capabilities as discussed in this report. This is because of the heart of the New Nomad concept is much more than about urban public transportation – it is instead potentially more about a new concept of national mobility and work/home/recreation lifestyle balances – a potential new way of American living.

Accordingly, any technology roadmap for possible implementation of a New Nomad style transportation/habitation system architecture cannot be limited to just aviation technologies but must be much broader in nature. Further beyond the technology challenges of such a system architecture are many societal considerations/tradeoffs that would come into play if such an architecture was 'designed' and/or organically allowed to be developed.

Figures 91-92 detail some thoughts regarding technology road-mapping for New Nomad type transport and habitation architectures.

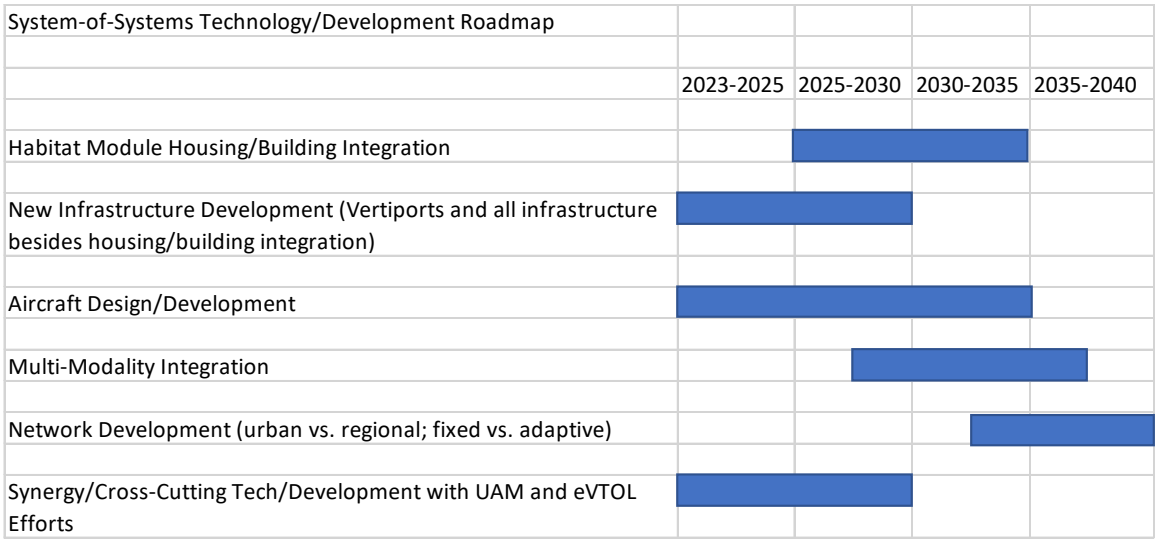

Figure 91. Potential System-of-Systems New Nomads Technology Roadmap

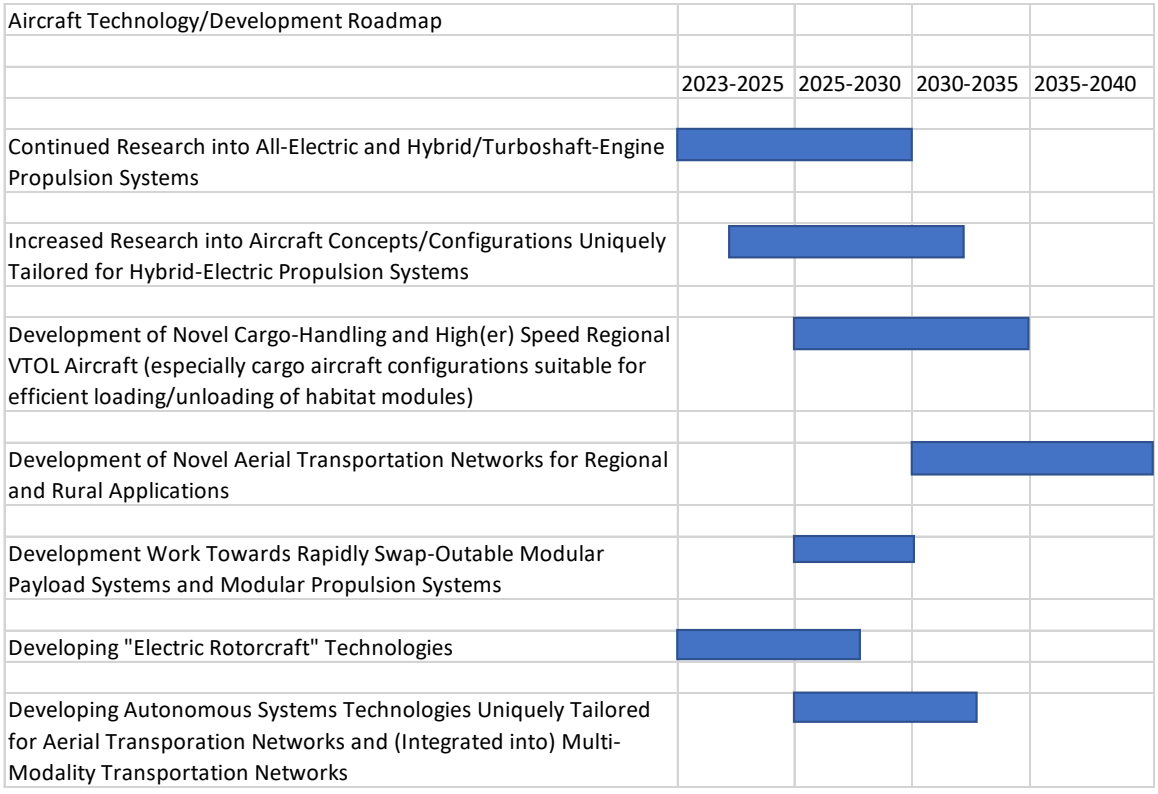

Figure 92. Potential Aircraft-Design-Centric New Nomads Technology Roadmap

This New Nomad work joins a growing body of research work into the emerging research area of metropolitan/regional aerial transportation systems (both small package delivery, cargo, and passenger-carrying vehicles), including, Refs. 9-13 and 20-22.

There is value in examining more than one system architecture of metropolitan/regional aerial transportation systems. The more variety in concepts, the greater likelihood for one day successful implementations of such transportation systems. Too narrow of a focus, or a laissez-faire attitude about implementation, could result in the failure of successfully adopting/implementing such transportation.

Noise and community acceptance will be a major consideration in the adoption or not of any novel metropolitan/regional aerial transportation system. Noise considerations were only discussed at a very high level in this report. Further, the baseline and alternate short-range aerial mobility reference designs in the report were not tailored for noise reduction – i.e., high disk loading and high tip speed rotors were incorporated in the designs to address gross weight considerations rather than noise considerations. Future work will have to begin to address noise and community acceptance. This will no doubt drive future reference designs to lower disk loading and lower tip speed rotors than that used in this study.

Another important consideration in any novel metropolitan/regional aerial transportation system is the significantly higher energy expenditure per distance covered for a vertical takeoff and landing aerial vehicle versus other ground-mobility options such as roadway and rail travel. The approach suggested in this report is twofold: first, it is important to compromise so as to ultimately reach an optimized choice/usage of the multimodal mobility modes to complete travel and, two, the introduction of the combined or integrated habitation and transit concept into discussion of future metropolitan/regional aerial transportation systems (so that one is not merely talking about passenger transport but, in addition, transportation of living/working spaces as well). Therefore, this second rationale is an attempt to justify the higher energy expenditure of aerial transport by showing a unique value-added to such transport through not only transporting people but living and/or working environments that are especially tailored to the needs of those passengers.

Concluding Remarks

With the rapid ongoing urbanization of the world, Americans risk losing the high-degree of freedom they've enjoyed for over a century to be able to travel on-demand and, further, relocate/adapt their living circumstances with relative ease. Future mobility and, further, habitation of Americans potentially could be greatly advanced if a multi-modality mobility and habitability system-of-systems architecture could be successfully devised. This work is intentionally very speculative to help begin a discussion within various

technical communities as to alternative directions for transportation and urban planning research.

In this regard, this study should be examined as a system-of-systems analysis study that touches upon not only rotorcraft design concepts and tools but also embraces urban planning and multimodal transportation concepts.

Three different "New Nomad" vehicles are defined: an all-electric single main rotor and tail rotor vehicle, an alternate ten-rotor all-electric multirotor vehicle configuration, and a long(er) range hybrid-electric/turboshaft blended-wing-body-type tiltrotor aircraft.

A significant amount of discussion is directed towards required design attributes of the aircraft payload "habitat modules" and their necessary integration into multi-modal transportations systems (in addition to their transport by the "New Nomad" aircraft as well as notional (on-demand) integration of these habitat modules into existing residential and commercial buildings.

Finally, new urban planning style "standard of living" metrics are discussed that are tailored towards the New Nomad transportation/habitation network concept. These metrics derived from potential full network operations simulations will help better outline the potential of the New Nomad paradigm.

References

1. Aiken, E.W., Ormiston, R.A., and Young, L.A., "Future Directions in Rotorcraft Technology at Ames Research Center," 56th Annual Forum of the American Helicopter Society, International, Virginia Beach, VA, May 2-4, 2000.

2. Young, L.A., Aiken, E.W., Johnson, J.L., Demblewski, R., Andrews, J., and Klem, J., "New Concepts and Perspectives on Micro-Rotorcraft and Small Autonomous Rotary-Wing Vehicles," AIAA 20th Applied Aerodynamics Conference, St Louis, MO, June 24-27, 2002.

3. Plice, L., Pisanich, G., Lau, B., and Young, L.A., "Biologically Inspired 'Behavioral' Strategies for Autonomous Aerial Explorers on Mars," IEEE Aerospace Conference, Big Sky, MT, March 2003.

4. Plice, L., "Robot Economy," Robosphere 2002: Workshop on Self-Sustaining Robot Ecologies, NASA Ames Research Center, Moffett Field, CA, November 2002.

5. Pisanich, G. and Young, L.A., "An Aerobot Ecology," Robosphere 2002: Workshop on Self-Sustaining Robot Ecologies, NASA Ames Research Center, Moffett Field, CA, November 2002.

6. Young, L.A., Aiken, E.W., and Briggs, G.A., "Smart Rotorcraft Field Assistants for Terrestrial and Planetary Science," 2004 IEEE Aerospace Conference, Big Sky, MT, March 2004.

7. Pisanich, G., Young, L.A., Ippolito, C., Plice. L., Lau, B., Roush, T., Lee, P., and Thakoor, S., "Initial Efforts towards Mission-Representative Imaging Surveys from Aerial Explorers," SPIE (International Society of Optical Engineers) Electronic Imaging Conference, San Jose, CA, January 2004.

8. Pisanich, G., Ippolito, C., Plice, L, Young, L., and Lau, B., "Actions, Observations, and Decision-Making: Biologically Inspired Strategies for Autonomous Aerial Vehicles," AIAA Aerospace Sciences Conference, Reno, NV, January 2004.

9. Alonso, J.J., Arneson, H.M., Melton, J.E., Vegh, J.M., Walker, C., and Young, L.A., "System-of-Systems Considerations in the Notional Development of a Metropolitan Aerial Transportation System: Implications as to the Identification of Enabling Technologies and Reference Designs for Extreme Short Haul VTOL Vehicles with Electric Propulsion," NASA TM 2017-218356, September 2017.

10. Melton, J., Kontinos, D., Grabbe, S., Alonso, J., Sinsay, J., and Tracey, B., "Combined Electric Aircraft and Airspace Management Design for Metro-Regional Public Transportation," NASA TM-2014-216626, October 2014.

11. Sinsay, J.D., Alonso, J.J., Kontinos, D.A., Melton, J.E., and Grabbe, S., "Air Vehicle Design and Technology Considerations for an Electric VTOL Metro-Regional Public Transportation System," 12th AIAA Aviation Technology, Integration, and Operations (ATIO) Conference and 14th AIAA/ISSMO Multidisciplinary Analysis and Optimization Conference, Indianapolis, IN, September 2012.

12. Young, L.A., "Accessibility Design and Operational Considerations for Urban Aerial Mobility Vehicles and Networks," Vertical Flight Society (VFS) Transformative Vertical Flight 2020: International Power Lift Conference (IPLC), San Jose, CA, January 21-23, 2020.

13. Young, L.A., "Urban Aerial Mobility Networks using Amphibious Vertical Takeoff and Landing Vehicles," 9th Biennial Autonomous VTOL Technical Meeting & 8th Annual Electric VTOL Symposium, Jan. 26–28, 2021.

14. Rayner, D.P., *Aircraft Design: A Conceptual Approach, 3rd Ed.*, AIAA Education Series, Reston, VA.

15. Rathod, V., "Design of a 4-seat, General Aviation, Electric Aircraft," Masters of Science in Aerospace Engineering Thesis, San Jose State University, May 2018.

16. Roskam, J. (Propeller Sizing Formula)

17. Whiteside, S, Pollard, B., Antcliff, K., Zawodny, N., Fei, X., Silva, C., Medina, G., "Design of a Tiltwing Concept Vehicle for Urban" NASA/TM–20210017971.

18. Johnson, W., Silva, C., "Observations from Exploration of VTOL Urban Air Mobility Designs" Presented at the 7th Asian/Australian Rotorcraft Forum, Jeju Island, Korea, October 30–November 1, 2018.

19. Harris, F.D., "Tiltrotor Conceptual Design," NASA/CR–2017–219474.

20. Patterson, M.D., Antcliff, K.R., and Kohlman, L.W., "A Proposed Approach to Studying Urban Air Mobility Missions Including an Initial Exploration of Mission Requirements," AHS International 74th Annual Forum & Technology Display, Phoenix, Arizona, USA, May 14-17, 2018.

21. Young, L.A., "Smart Precise Rotorcraft InTerconnected Emergency Services (SPRITES)," AIAA Science and Technology Forum and Exposition (SciTech 2018), Kissimmee, Florida, January 8-12, 2018.

22. Young, L.A., "A Multi-Modality Mobility Concept for a Small Package Delivery UAV," 7th AHS Technical Meeting on VTOL Unmanned Aircraft Systems, Mesa, AZ, January 24-26, 2017.

23. Airstream self-driving electric camper concept vehicle; https://www.airstream.com/air-lab/concepts/estream/; last accessed February 12, 2022.

24. Airbus and Italdesign "Pop Up" combined car and rotorcraft concept; https://www.airbus.com/en/newsroom/press-releases/2017-03-italdesign-and-airbus-unveil-popup; February 12, 2022.

25. JaamSim Development Team (2016). JaamSim: Discrete-Event Simulation Software. Version 2016-14. URL http://jaamsim.com. doi:10.5281/zenodo.57118.

26. Chung, W.W., Paris, A., Salvano, D., Linse, D., Trept, T., Wood, T., Young, R., Gao, H., Wright, K., Miller, D., Cheng, V. "Modeling High-Speed Civil Tiltrotor Transports in the Next Generation Airspace", Volume II, NASA CR-2011-215960.

27. Acree, C. and Snyder, C., "Influence of Alternative Engine Concepts on LCTR2 Sizing and Mission Profile", AHS Future Vertical Lift Aircraft Design Conference, January 18-20, 2012, San Francisco, CA.

28. Johnson, W., Yamauchi, G. K. and Watts, M. E., "Designs and Technology Requirements for Civil Heavy Lift Rotorcraft," Proceedings of the American Helicopter Vertical Lift Aircraft Design Conference, San Francisco, CA, January 18-20, 2006.

29. Wilkerson, J.B., and Smith, R.L., "Aircraft System Analysis of Technology Benefits to Civil Transport Rotorcraft," NASA/CR-2008-214594, 2008.

30. Radotich, M., “Conceptual Design of Tiltrotor Aircraft for Urban Air Mobility,” VFS Aeromechanics for Advanced Vertical Flight Technical Meeting, San Jose, CA, January 25-27, 2022.

31. Johnson, W., "NDARC: NASA Design and Analysis of Rotorcraft Theory," NASA/TP–20220000355/Vol 1-3.

32. Silva, C., Johnson, W., Antcliff, K.R., and Patterson, M.D., "VTOL Urban Air Mobility Concept Vehicles for Technology Development," 2018 Aviation Technology, Integration, and Operations Conference, AIAA Aviation Forum, AIAA 2018-3847, Dallas, TX, June 2018.

33. Johnson, W., "A Quiet Helicopter for Air Taxi Operations" Presented at the VFS Aeromechanics for Advanced Vertical Flight Technical Meeting, San Jose, CA, January 21–23, 2020.

34. Di Lello, E., Loutfi, A., Pecora, F., and Saffiotti, A., “Robotic Furniture in a Smart Environment: The PEIS Table,” Proceedings of the 5th International Conference on Intelligent Environments, Barcelona, Spain, 19th of July, 2009.

35. Zhang, Z., Chen, Z., and Li, W., “Automating Robotic Furniture with A Collaborative Vision-based Sensing Scheme,” 27th IEEE International Symposium on Robot and Human Interactive Communication, August 2018.

36. Mutluab, M., Léziarta, P.A., Khodra, H., Bernardino, A., and Ijspeerta, A.J., “Roombots extended: Challenges in the next generation of self-reconfigurable modular robots and their application in adaptive and assistive furniture,” Robotics and Autonomous Systems, Vol. 127, May 2020.
37. Stepniewski, W.Z., and Shinn, R.A., “A Comparative Study of Soviet vs. Western Helicopters,” NASA CR 3579, CR 3580, March 1983.
38. Tishchenko, M.N.; Nagaraj, V.T.; and Chopra, I. “Preliminary Design of Transport Helicopters.” Journal of the American Helicopter Society, Vol. 48, No. 2, April 2003.
39. Young, L.A., “Simulated Tiltrotor Aircraft Operation in Close Proximity to a Building in Wind and Ground-Effect Conditions,” AIAA Aviation 2015, Dallas, TX, June 22-26, 2015.
40. Young, L.A., Rajagopalan, G. and Yamauchi, G.K., “Simulated Rotor Wake Interactions Resulting from Civil Tiltrotor Aircraft Operations Near Vertiport Terminals,” 51st AIAA Aerospace Sciences Meeting, AIAA 2013-0801, Grapevine, TX, January 7-10, 2013.
41. Schenderlein, J. and Clayton, T., “Comparison of Helicopter Turboshaft Engines,” AIAA.
42. Young, L.A., Graham, D.R., and Stroub, R.H. “Experimental Investigation of Rotorcraft Hub and Shaft Fairing Drag Reduction,” AIAA Journal of Aircraft, Vol. 24, Dec. 1987, p. 861-867.
43. Martin, D.M., Mort, R.W., Young, L.A., Squires, P.K., “Experimental investigation of advanced hub and pylon fairing configurations to reduce helicopter drag,” NASA TM 4540, September 1993.

44. Martin, D.M., Mort, R.W., Squires, P.K., Young, L.A., "Hub and Pylon Fairing Integration for Helicopter Drag Reduction," 47th Annual Forum of American Helicopter Society, Phoenix, AZ, May 6-8, 1991.
45. Sung, D.Y., Lance, M.B., Young, L.A., Stroub, R.H., "An Experimental Investigation of Helicopter Rotor Hub Fairing Drag Characteristics," NASA TM 102182, September 1989.
46. Graham, D.R., Sung, D.Y., Young, L.A., Louie, A.W., Stroub, R.H., "Helicopter Hub Fairing and Pylon Interference Drag," NASA TM 101052, January 1989.
47. Stroub, R.H., Young, L.A., Louie, A.W. "Investigation of Generic Hub Faring and Pylon Shapes to Reduce Hub Drag," 13th European Rotorcraft Forum, Arles, France, September 8-11, 1987.
48. Stroub, R.H., Young, L.A., Louie, A.W. "Investigation of generic hub fairing and pylon shapes to reduce hub drag," NASA TM 100008, September 1987.
49. Young, L.A, Graham, D.R., Stroub, R.H., Louie, A.W., "Reduction of Hub- and Pylon-Fairing Drag," 43rd Annual Forum of the American Helicopter Society, Saint Louis, MO, May 18-20, 1987.
50. Boston, W. , "Self-Driving Cars Might Just Transform the Way We Work," The Wall Stree Journal; https://www.msn.com/en-us/autos/other/self-driving-cars-might-just-transform-the-way-we-work/ar-BB1ivXTF?ocid=msedgdhp&pc=U531&cvid=30c3abe167854c679fd35714ff408f64&ei=218; last accessed February 29, 2024.
51. Roberson, J.A, and Crowe, C.T., Engineering Fluid Mechanics, Houghton Mifflin Company, 1975.
52. Morrison, F.A., "Data Correlation for Drag Coefficient for Sphere," 2016; https://pages.mtu.edu/~fmorriso/DataCorrelationForSphereDrag2016.pdf; last accessed March 5, 2024.
53. Rajagopalan, G., Wadcock, A. J., Yamauchi, G. K. and Silva, M. J., "Experimental and Computational Study of the Interaction Between a Tandem-Rotor Helicopter and a Ship," Proceedings of the 61st Annual Forum of the American Helicopter Society, Grapevine, Texas, June 1-3, 2005.
54. PTC MathCAD commercial software tool; https://www.mathcad.com/en; last accessed March 15, 2024.
55. LuftCar VTOL hybrid air/ground mobility concept with detachable automobile; https://www.luftcar.com/; last accessed March 19, 2024.
56. Rajagopalan, R.G., Baskaran,V., Hollingsworth, A., Lestari, A., Garrick, D., Solis, E., Hagerty, B., "RotCFD - A Tool for Aerodynamic Interference of Rotors: Validation and Capabilities", AHS Future Vertical Lift Aircraft Design Conference, January 18-20, 2012 San Francisco.
57. Rajagopalan, G., Thistle, J., Polzin, W., "The Potential of GPU Computing for Design in RotCFD," AHS Technical Meeting on Aeromechanics Design for Vertical Lift, Holiday Inn at Fisherman's Wharf, San Francisco, CA, January 16-18, 2018.
58. Monaghan. B., "Overnight travel pod drives passengers while they sleep," *Indy 100*; https://www.msn.com/en-us/travel/news/overnight-travel-pod-drives-passengers-while-they-sleep/ar-BB1kKhd4?ocid=msedgdhp&pc=U531&cvid=aa5e8db92e5f439db239cb09a3ca1471&ei=106; last accessed April 15, 2024.

59. Young, L.A., "Performance, Inflow, and Tip Loss Characteristics of Rotors with Discontinuous Steps in Twist and Lift at their Blade-Tips," NASA/TM-2022-0017246, February 2023.
60. Young, L.A., "Novel Conceptual Designs for Stopped-Rotor Aerial Vehicles and Other High-Speed Rotorcraft," 6th Decennial VFS Aeromechanics Specialists' Conference, Santa Clara, CA, February 6-8, 2024.
61. Danis, R.A., Green, M.W., Freeman, J.L., and Hall, D.W., "Examining the Conceptual Design Process for Future Hybrid-Electric Rotorcraft," NASA/CR—2018–219897, May 2018.
62. Saias, C.A., et al, "Preliminary design of hybrid-electric propulsion systems for emerging UAM rotorcraft architectures," Journal of Engineering for Gas Turbines and Power, Volume 143, Issue 11, November 2021.
63. Patterson, M., et al, "A Proposed Approach to Studying Urban Air Mobility Missions Including an Initial Exploration of Mission Requirements," AHS International 74th Annual Forum & Technology Display, Phoenix, Arizona, USA, May 14-17, 2018.
64. Cicolani, L.S. and Ehlers, G.E., "Modeling and Simulation of a Helicopter Slung Load Stabilization Device," 58th Annual Forum of American Helicopter Society, Montreal, Canada, June 11-13, 2002.
65. Ranjana, S., et al, "A Methodology for Flight-Time Identification of Helicopter-Slung Load Frequency Response Characteristics Using CIFER," AIAA GNC Conference, Portland, OR, United States, August 1, 1999.
66. Johnson, W., *Helicopter Theory*, Princeton University Press, Princeton, New Jersey, 1980.

Appendix A – Bluff-Body/Fuselage Drag Prediction Correlation

Most low-speed rotorcraft generally have high drag because there are typically significant regions of the separated flow on their fuselages. One major source of this high drag is the parasite drag from the rotor shaft and pylon (fairing and/or hardware typically projecting above the fuselage cabin); refer to Refs. 42-49. It is arguably the case that low-speed rotorcraft aerodynamics is significantly comprised of bluff body flow. Accordingly, the first attempts to assess the accuracy of RotCFD, or any other CFD solver, should be focused on the bluff body flows. This appendix seeks to perform such initial assessments.

Figures A1-A6 are flow field (velocity vector and streamlines) predictions from RotCFD for different freestream velocities (and Reynolds numbers). The sphere has a one-meter radius; the density and viscosity values are all standard temperature and pressure (STP) in SI units. All lower Reynolds number cases needed to be run with double precision for the OpenCL GPU predictions; single precision was found to generate significantly inaccurate drag predictions for all lower Reynolds number cases. For higher Reynolds

number cases, single precision for the OpenCL GPU predictions appeared to be satisfactory. This is an open question for future work involving RotCFD predictions.

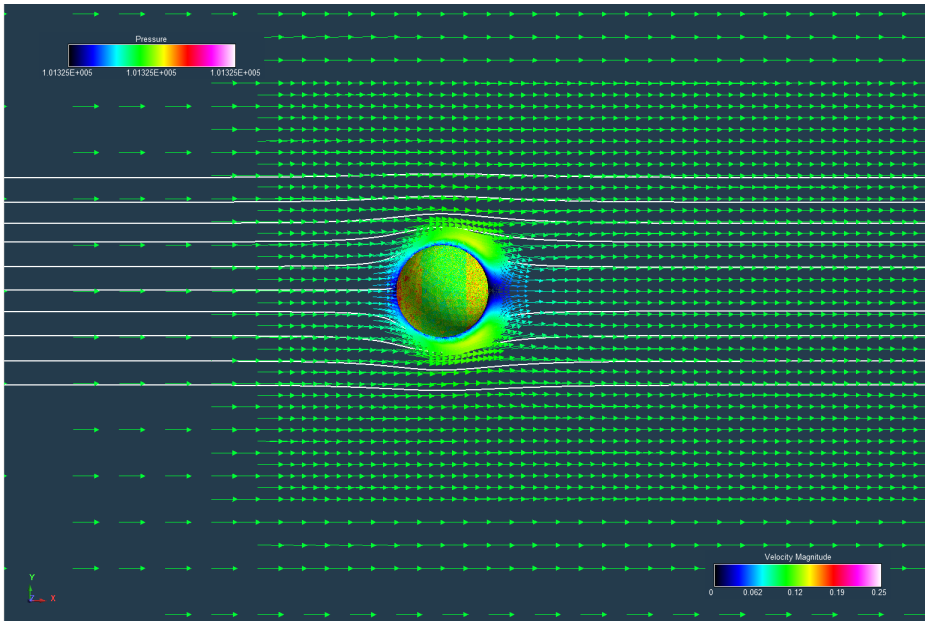

Figure A1. RotCFD flow field (side view with velocity vectors and streamlines) and surface pressure predictions as a function of Reynolds number for a sphere (laminar and V=0.1m/s)

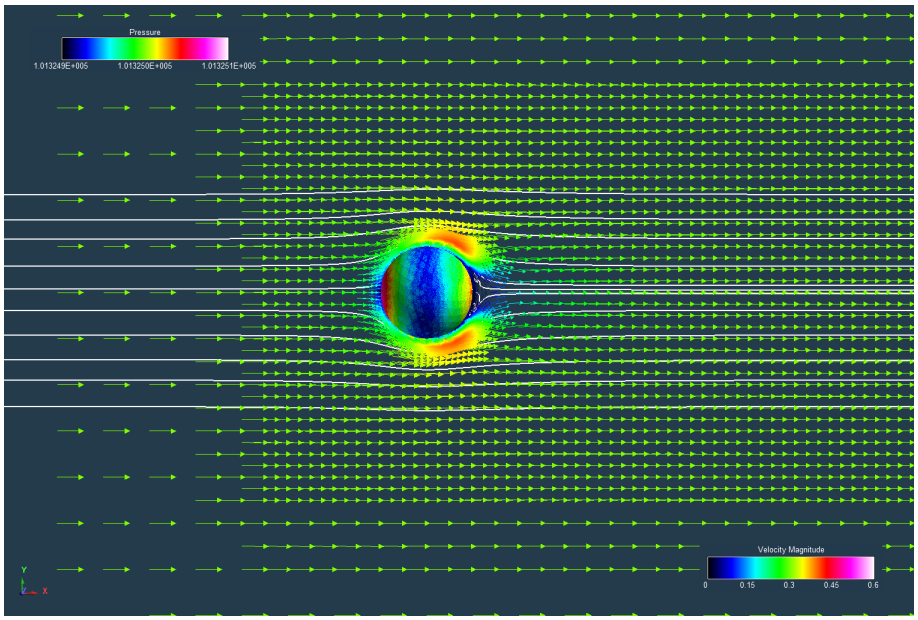

Figure A2. RotCFD flow field (side view with velocity vectors and streamlines) and surface pressure predictions as a function of Reynolds number for a sphere (laminar and V=0.3m/s)

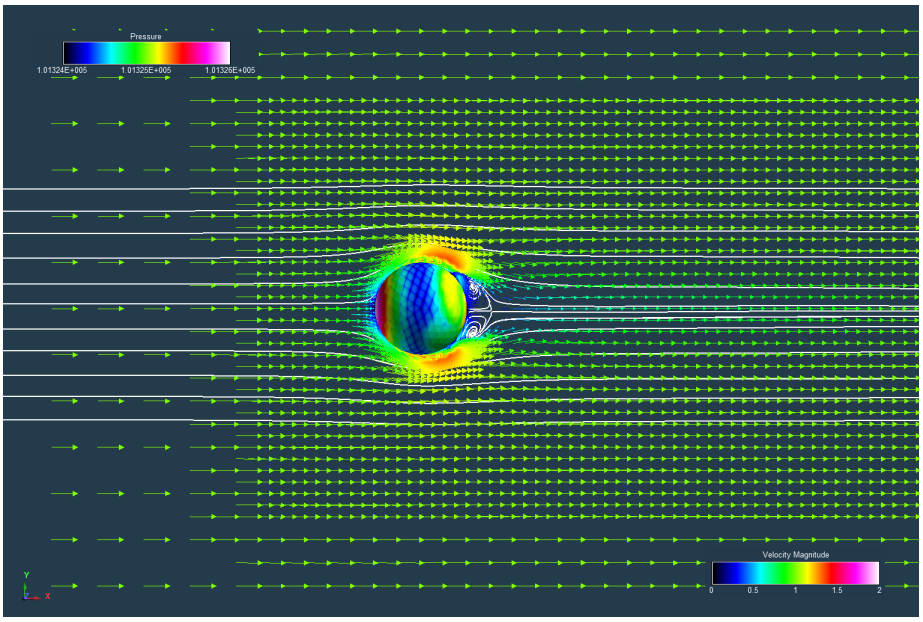

Figure A3. RotCFD flow field (side view with velocity vectors and streamlines) and surface pressure predictions as a function of Reynolds number for a sphere (laminar and V=1m/s)

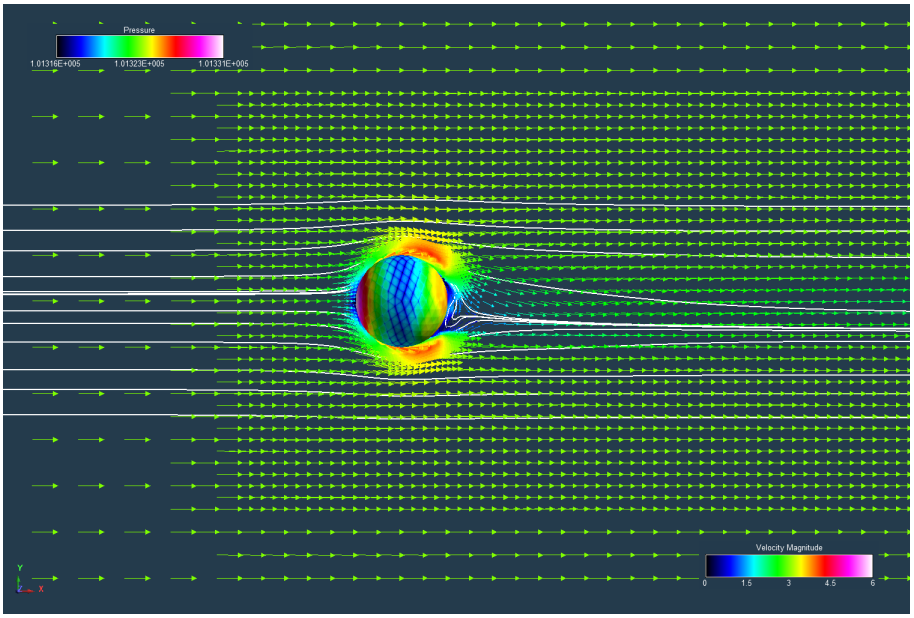

Figure A4. RotCFD flow field (side view with velocity vectors and streamlines) and surface pressure predictions as a function of Reynolds number for a sphere (turbulent and V=3m/s)

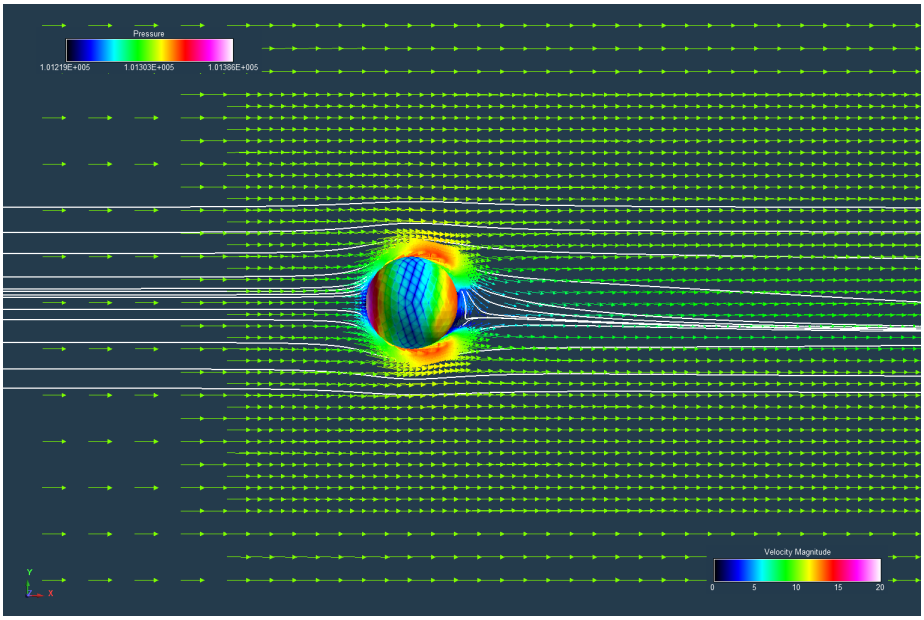

Figure A5. RotCFD flow field (side view with velocity vectors and streamlines) and surface pressure predictions as a function of Reynolds number for a sphere (turbulent and V=10m/s)

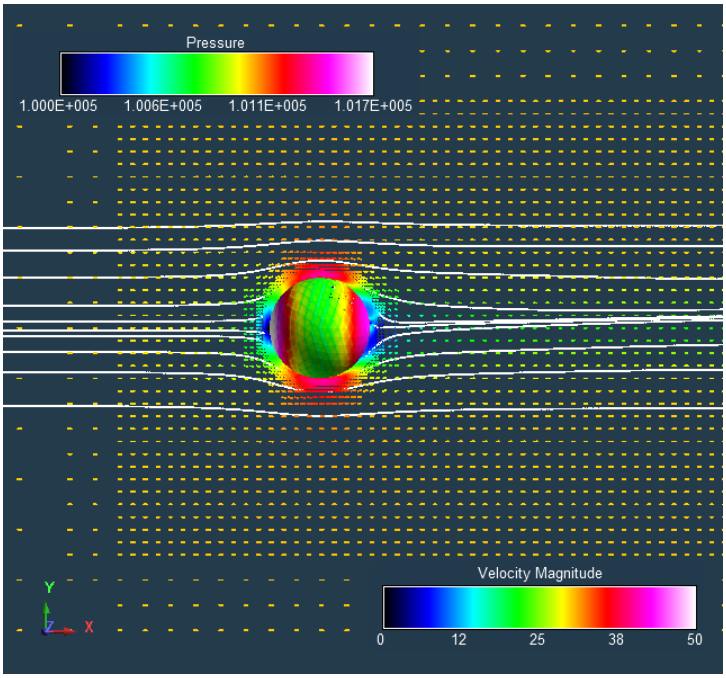

Figure A6. RotCFD flow field (side view with velocity vectors and streamlines) and surface pressure predictions as a function of Reynolds number for a sphere (V=30m/s)

Figure A7 presents the sphere drag coefficient as a function of Reynolds number. In Fig. A7 both a laminar-only and turbulent-only set of results are presented (RotCFD does not incorporate transition modeling). There are two sets of textbook/reference sets of sphere drag coefficient data to compare to the RotCFD results. RotCFD seems to be underpredicting the low-Reynolds number drag coefficients but seems to reasonably agree with the higher Reynolds number results. To get even this level of agreement, though, required the use of double precision for the OpenCL GPU runs for the lower Reynolds number cases.

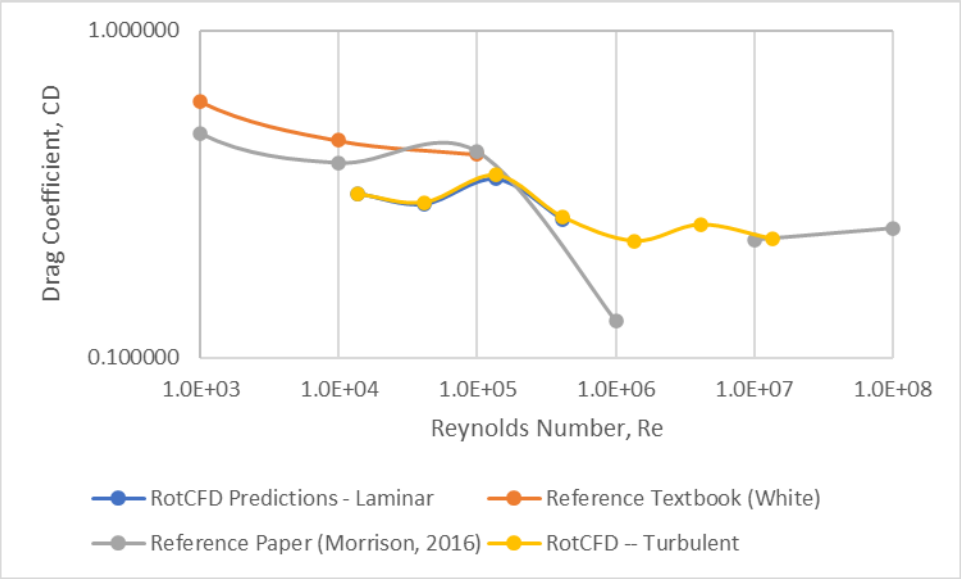

Figure A7. RotCFD drag coefficient predictions as a function of Reynolds number for a sphere versus reference textbook trends

The predicted drag coefficients approached experimental trend noted in fluid dynamics reference textbooks as Reynolds number increased to greater than 10^6. Some general sense of the sphere's "drag crisis" seems to be captured in the predictions, but as RotCFD does not have a transition model this predicted "drag crisis" is only suggested in a qualitative sense. At lower Reynolds numbers, the trend was qualitatively in agreement, but the drag was underpredicted by a considerable amount.

All RotCFD cases were run with body-fitting at a body grid refinement of 11 or 12 and a near-body refinement box refinement of 6 or 8. For cases at a freestream velocity of 100m/s, though, a non-body-fitted cartesian gridding for the bluff body had to be employed to allow for converged solutions. All cases were run with the 'realizable kappa-epsilon" turbulence model (unless otherwise noted) with zero surface roughness and a freestream turbulence intensity of 1%. For those regions of the flow that exceeded a local Mach number of 0.2, the solver switched from an incompressible unsteady Reynolds-averaged Navier-Stokes solver to a compressible mass-weighted Favre Averaged Navier-Stokes

solver. For the higher Reynolds number cases, the OpenCL GPU's were run in single precision mode; for lower Reynolds number cases, the GPU's were run in double precision mode.

Figure A8-A14 present velocity vectors, streamlines, and surface pressures for a cube at different freestream velocities (and Reynolds numbers). The velocity vector plane is at the midsection of the cube face.

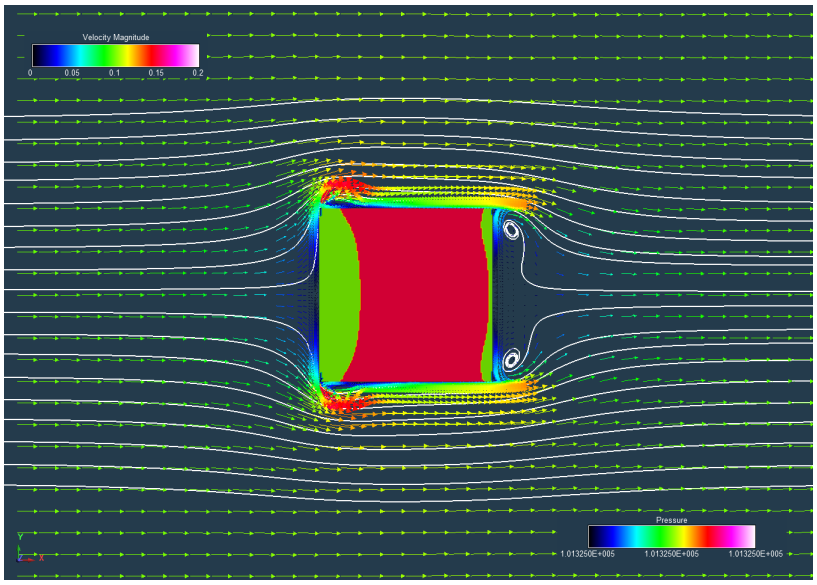

(a)

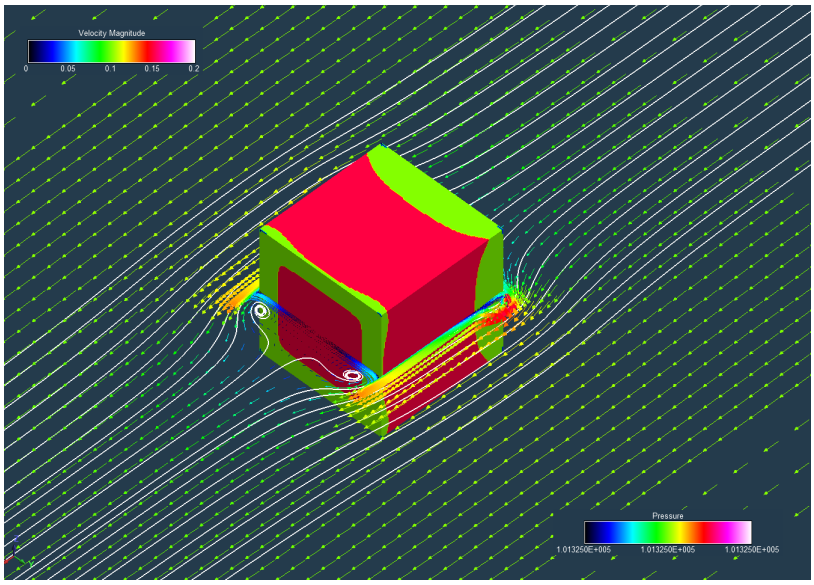

(b)

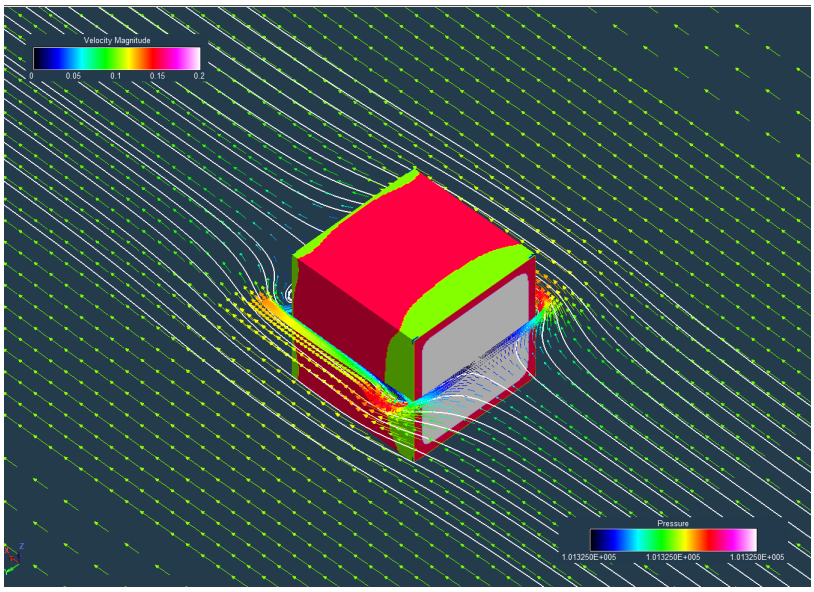

(c)

Figure A8. RotCFD flow field and surface pressure predictions as a function of Reynolds number for a cube (V=0.1m/s): (a) side view, (b) isometric rear view, and (c) isometric forward view

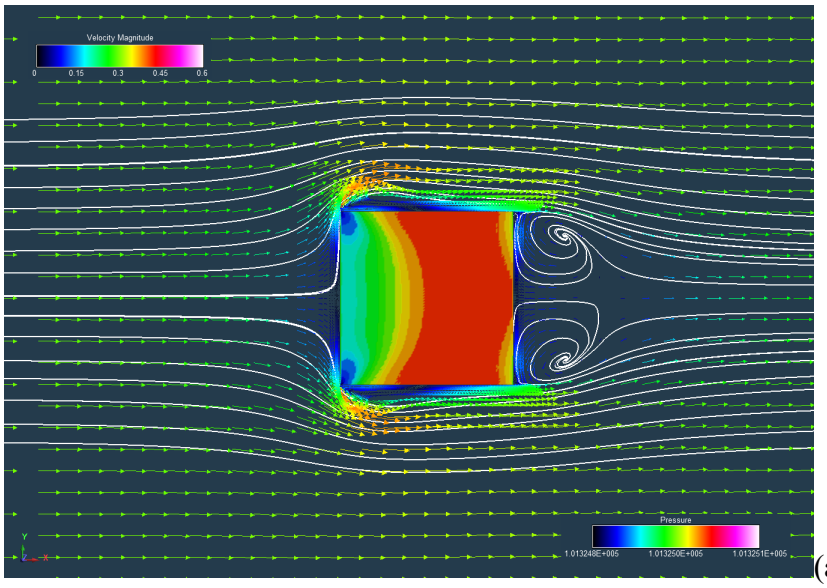

(a)

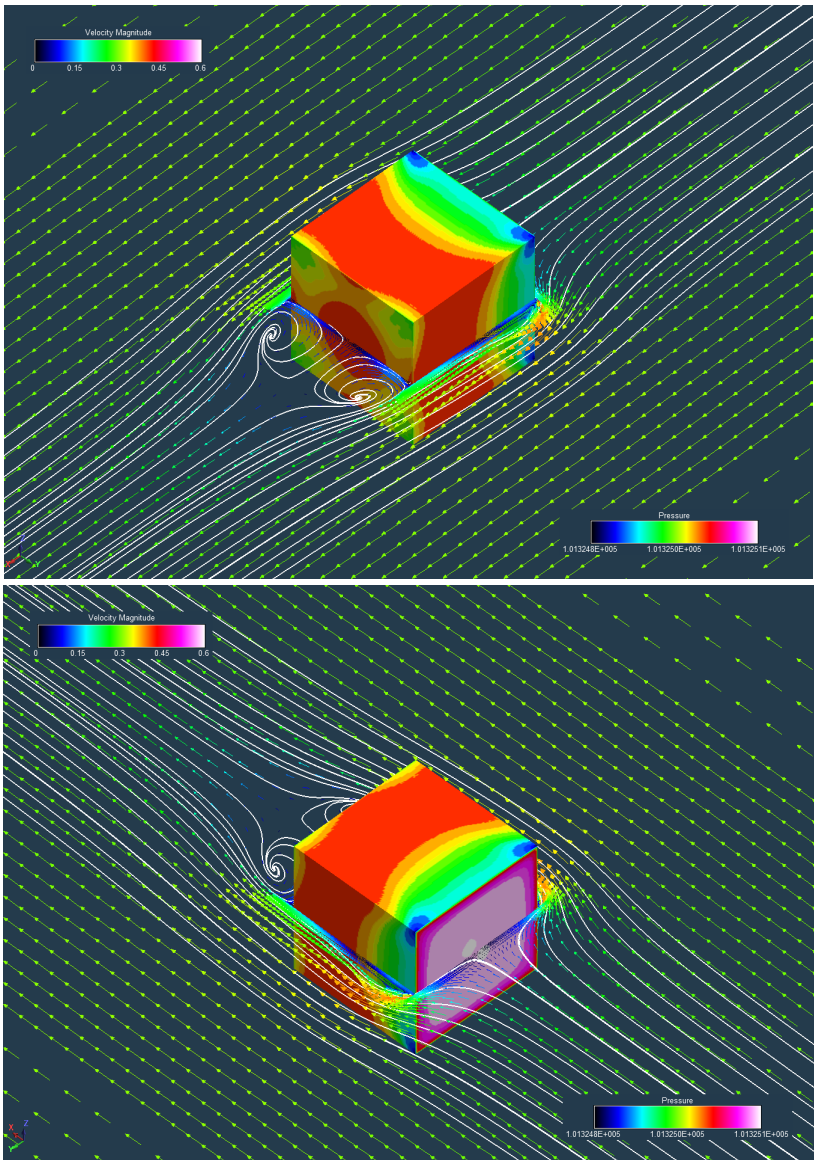

Figure A9. RotCFD flow field and surface pressure predictions as a function of Reynolds number for a cube (V=0.3m/s): (a) side view, (b) isometric rear view, and (c) isometric forward view

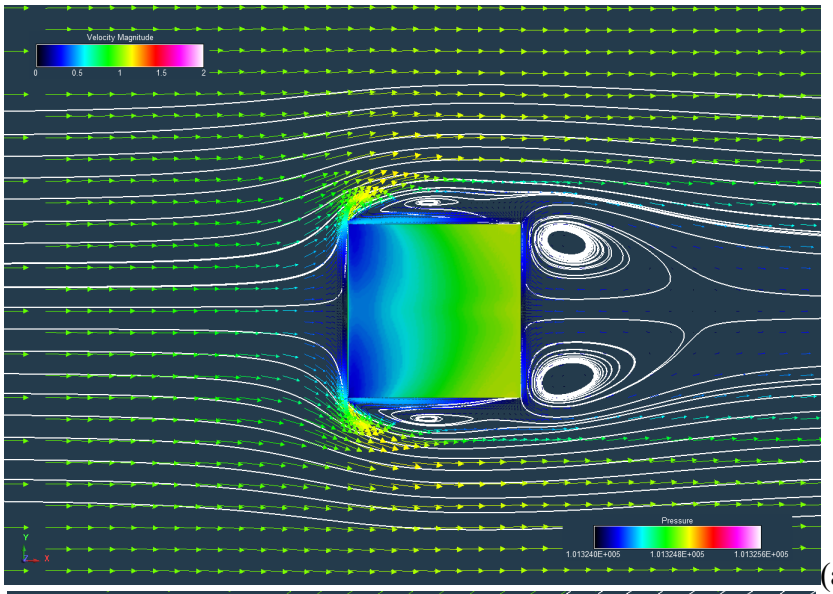
Velocity Magnitude
0
0.5
1
1.5
2
Pressure
1.013240E+005
1.013248E+005
1.013256E+005

(a)

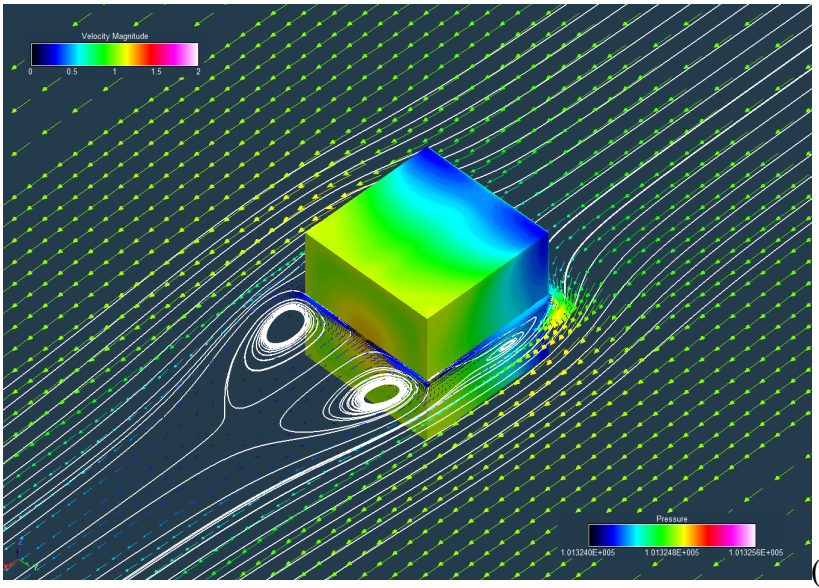
Velocity Magnitude
0
0.5
1
1.5
2
Pressure
1.013240E+005
1.013248E+005
1.013256E+005

(b)

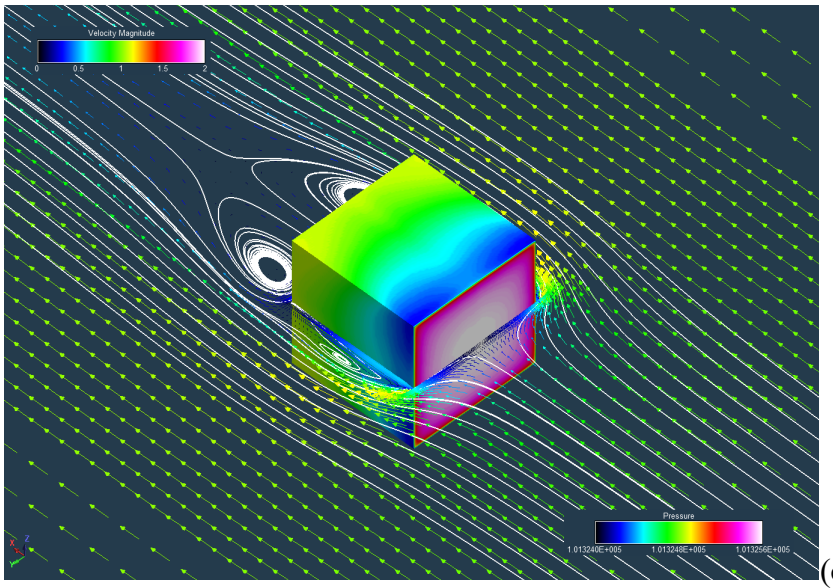

(c)

Figure A10. RotCFD flow field and surface pressure predictions as a function of Reynolds number for a cube (V=1m/s): (a) side view, (b) isometric rear view, and (c) isometric forward view

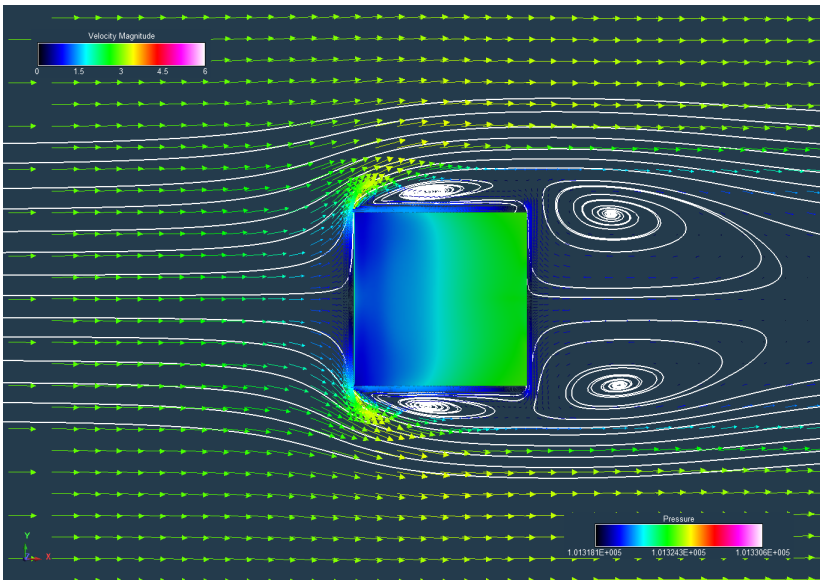

(a)

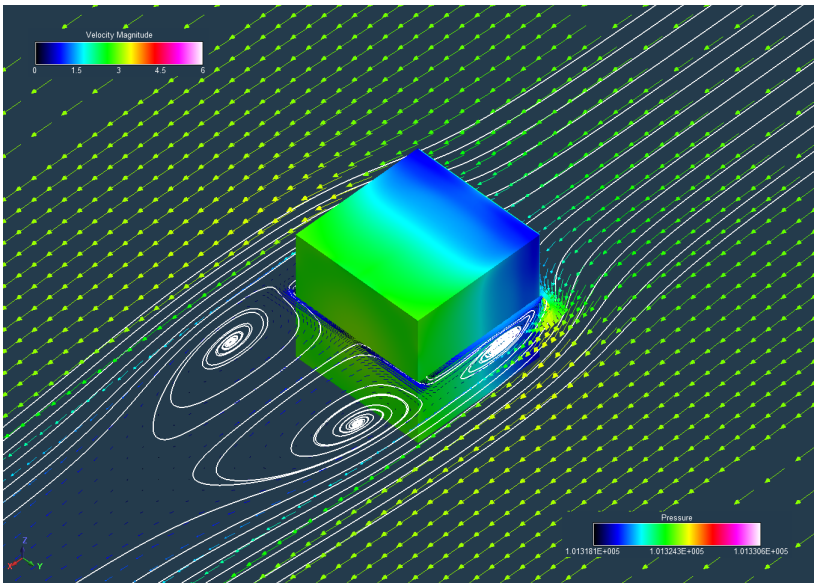

(b)

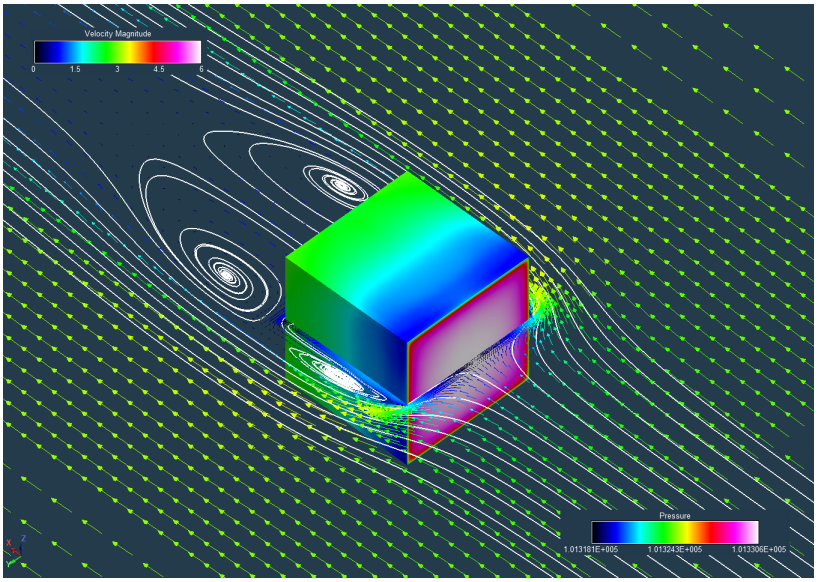

(c)

Figure A11. RotCFD flow field and surface pressure predictions as a function of Reynolds number for a cube (V=3m/s): (a) side view, (b) isometric rear view, and (c) isometric forward view

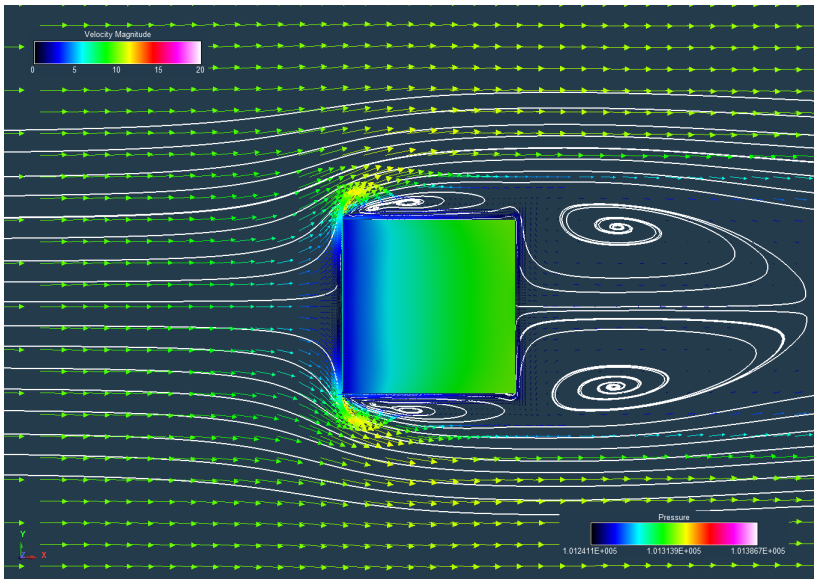
Velocity Magnitude
0
5
10
15
20
Pressure
1.012411E+005
1.013139E+005
1.013867E+005

(a)

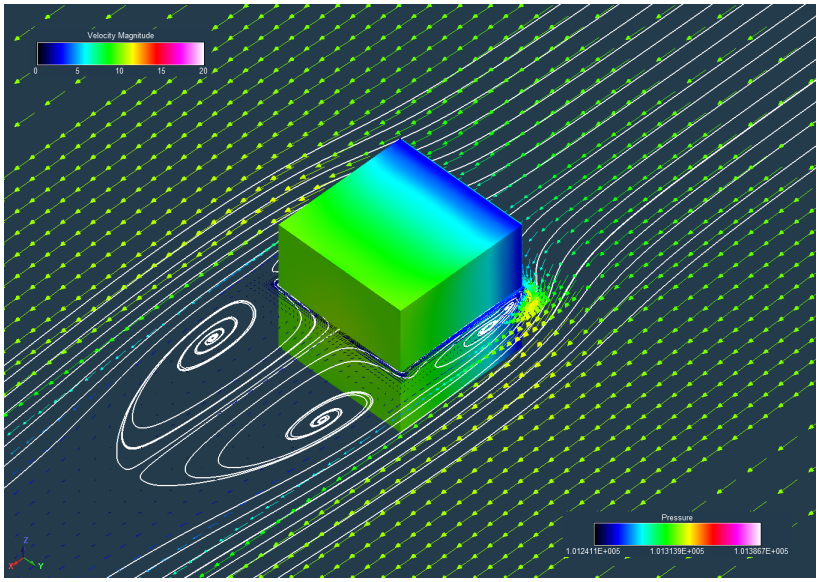
Velocity Magnitude
0
5
10
15
20
Pressure
1.012411E+005
1.013139E+005
1.013867E+005

(b)

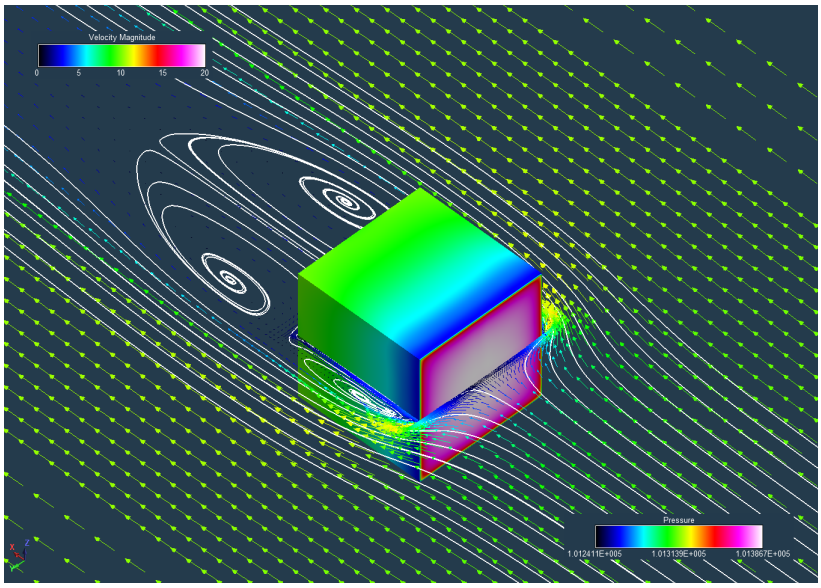

(c)

Figure A12. RotCFD flow field and surface pressure predictions as a function of Reynolds number for a cube (V=10m/s): (a) side view, (b) isometric rear view, and (c) isometric forward view

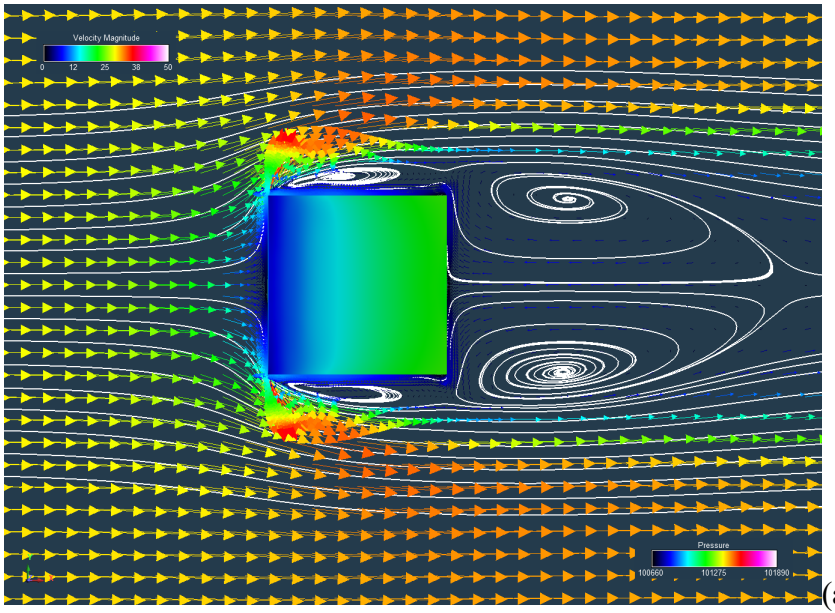

(a)

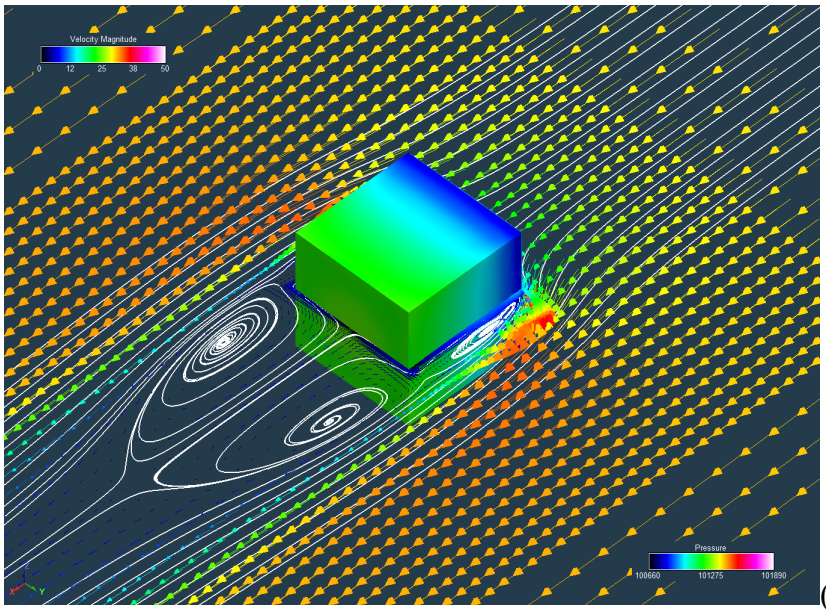

(b)

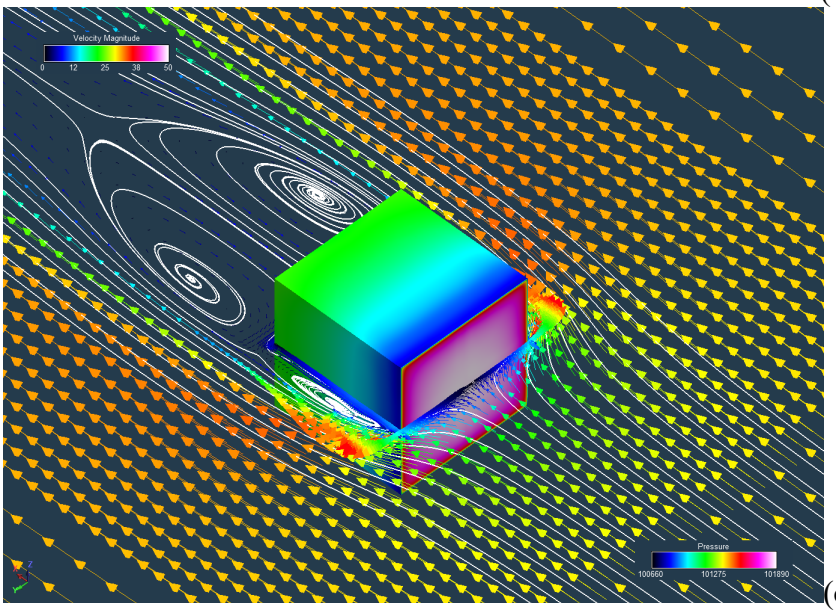

(c)

Figure A13. RotCFD flow field and surface pressure predictions as a function of Reynolds number for a cube (V=30m/s): (a) side view, (b) isometric rear view, and (c) isometric forward view

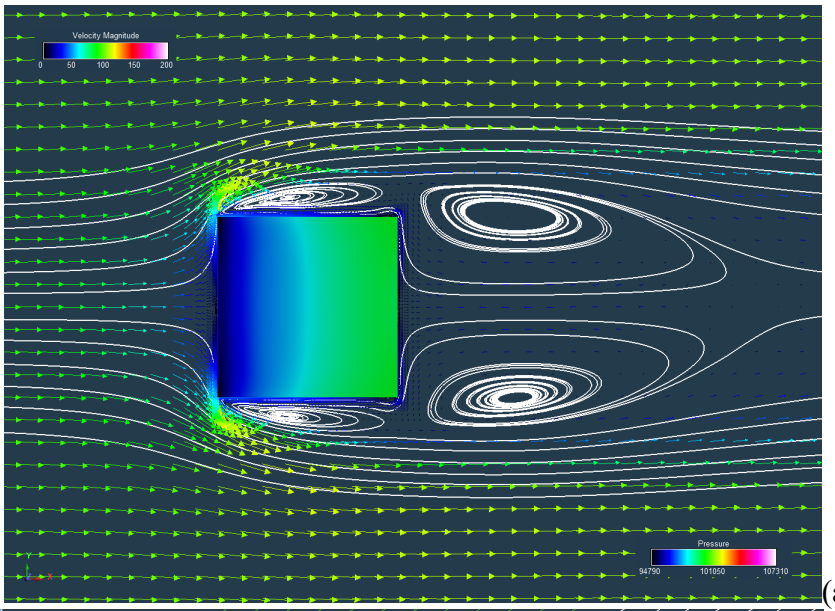
Velocity Magnitude
0 50 100 150 200
Pressure
94790 101050 107310
(a)

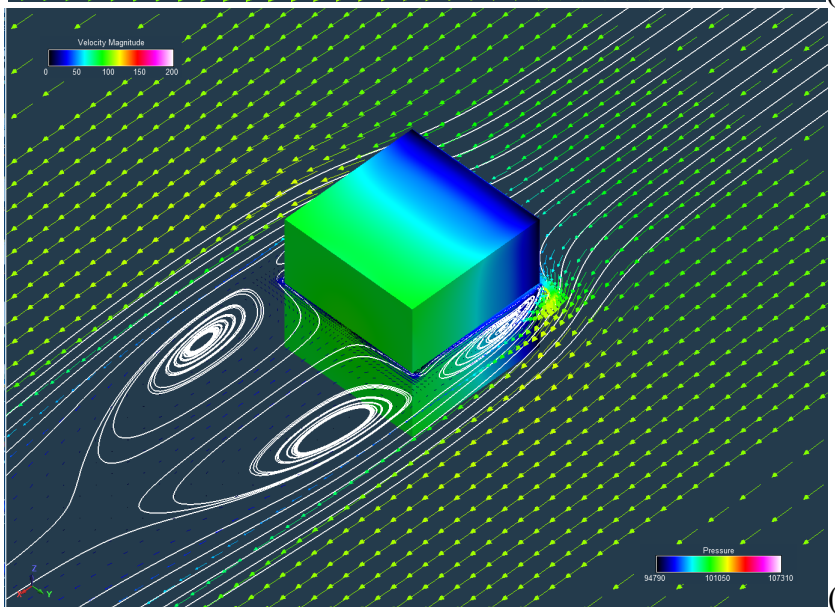
Velocity Magnitude
0 50 100 150 200
Pressure
94790 101050 107310
(b)

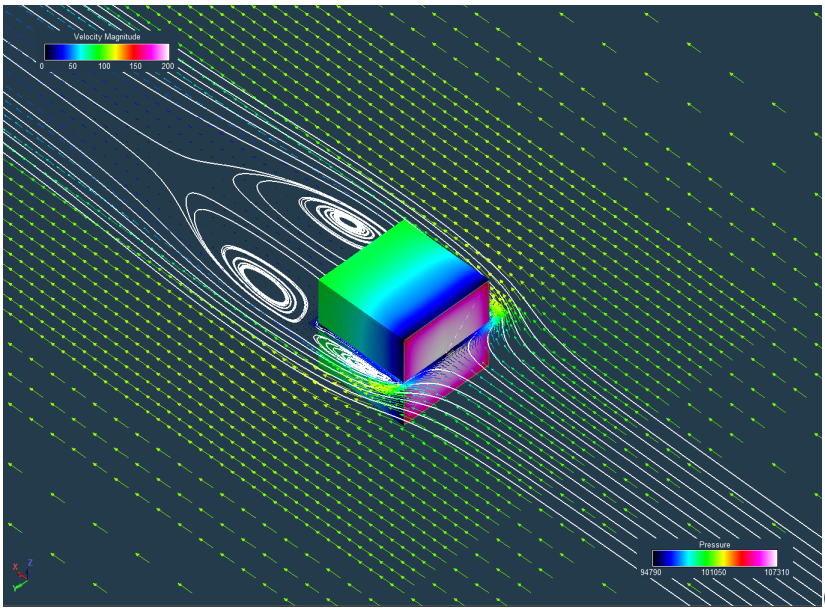

(c)

Figure A14. RotCFD flow field and surface pressure predictions as a function of Reynolds number for a cube (V=100m/s): (a) side view, (b) isometric rear view, and (c) isometric forward view

Figure A15 presents RotCFD predictions of the cube drag coefficient with Reynolds number. Reference textbooks typically indicate that the cube drag coefficient is a constant value for all but the lowest Reynolds numbers. This can be observed as well in the RotCFD predictions (with turbulent modeling). To achieve this agreement, it was necessary to run RotCFD with OpenCL GPU with double precision; only at the highest Reynolds numbers was single precision satisfactorily accurate. The observed agreement with reference textbook drag coefficient values is likely primarily obtainable because of the sharp corners of the modeled cubes which, in turn, resulted in more predictable lines of separated flow.

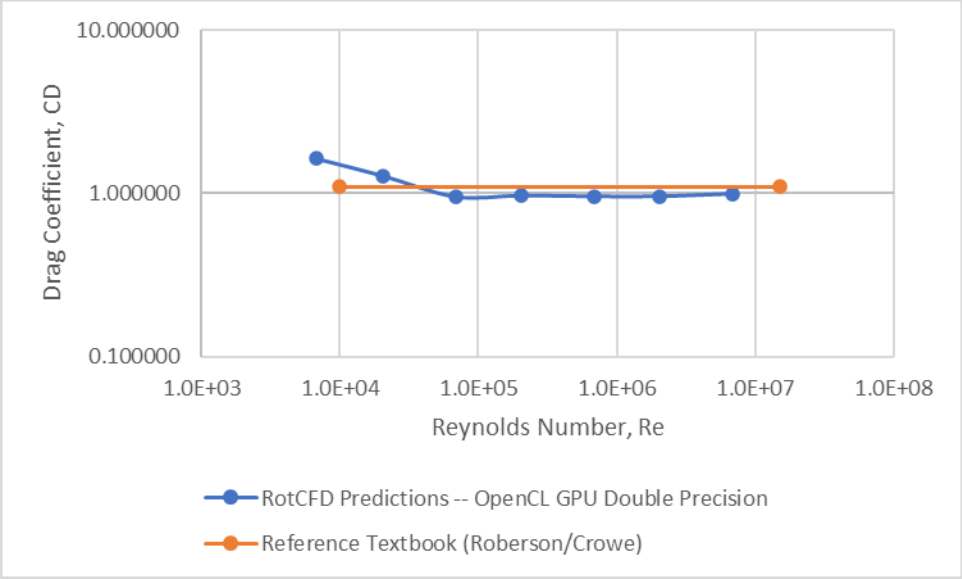

Figure A15. RotCFD drag coefficient predictions as a function of Reynolds number for a cube as compared reference textbook trends

Figures A16-21 are RotCFD predicted flow fields and streamlines for a cube at a forty-five incline with respect to the freestream velocity.

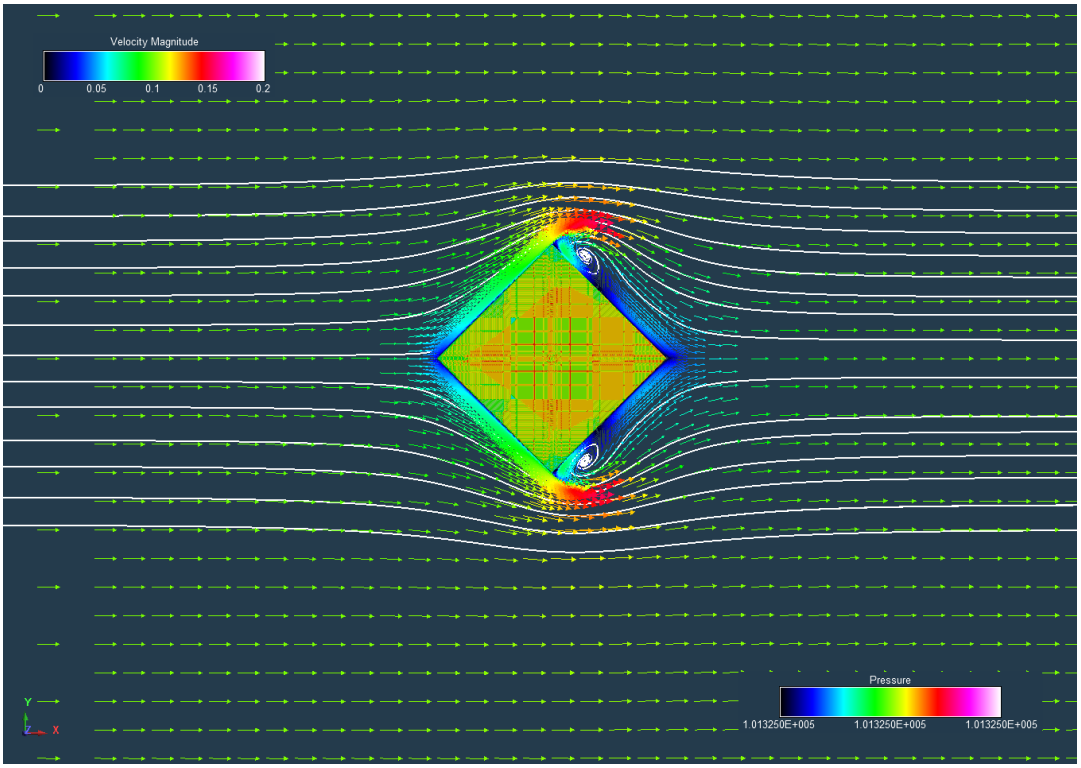

Figure A16. RotCFD (side view velocity vector and streamlines) predictions as a function of Reynolds number for a cube at a 45Deg. inclination (V=0.1m/s)

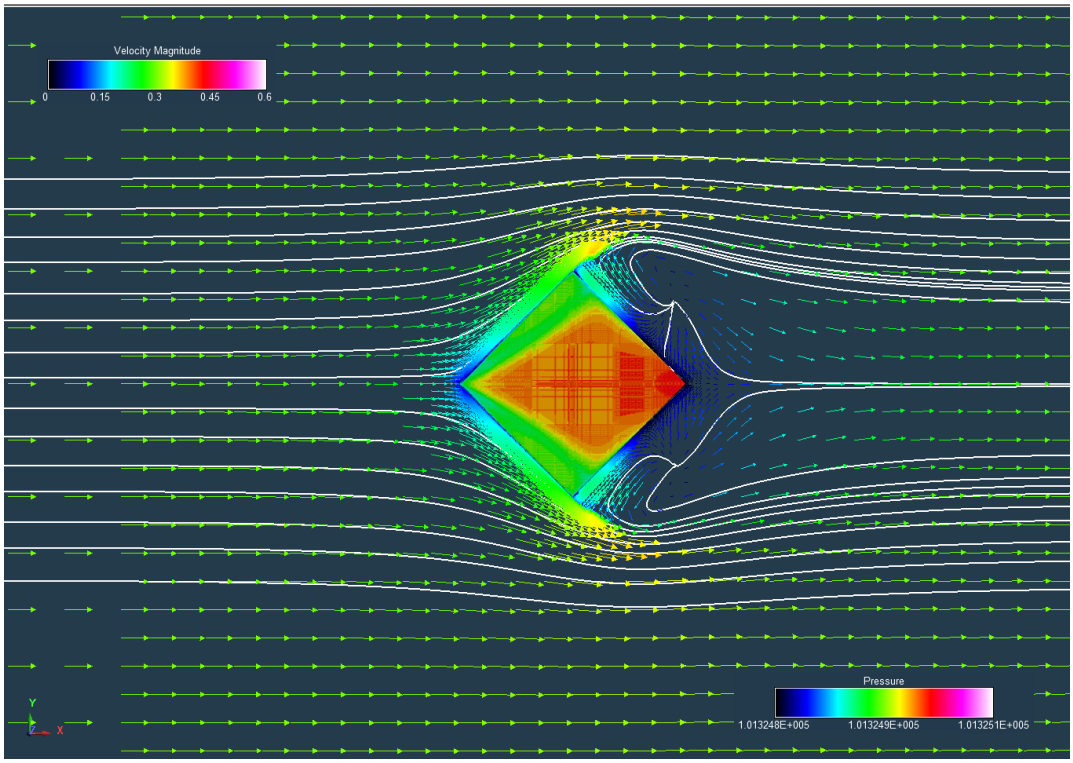

Figure A17. RotCFD (side view velocity vector and streamlines) predictions as a function of Reynolds number for a cube at a 45Deg. inclination (V=0.3m/s)

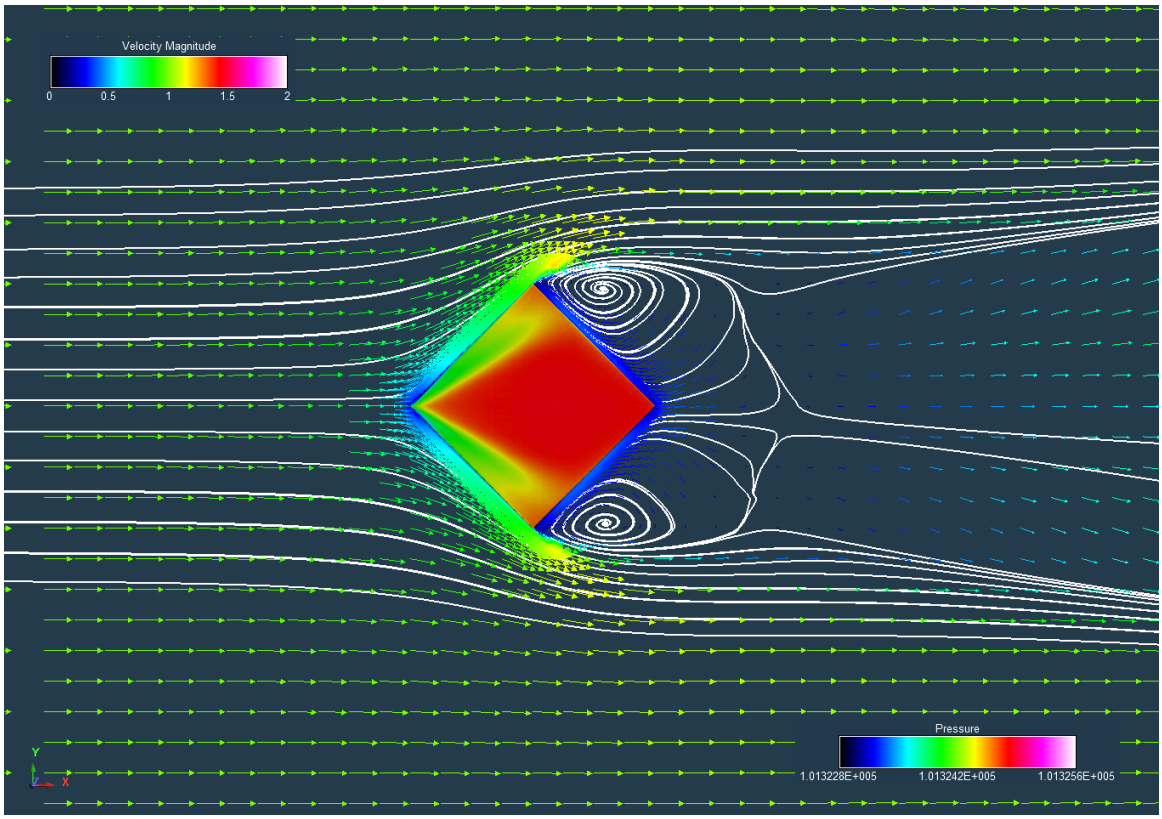

Figure A18. RotCFD (side view velocity vector and streamlines) predictions as a function of Reynolds number for a cube at a 45Deg. inclination (V=1m/s)

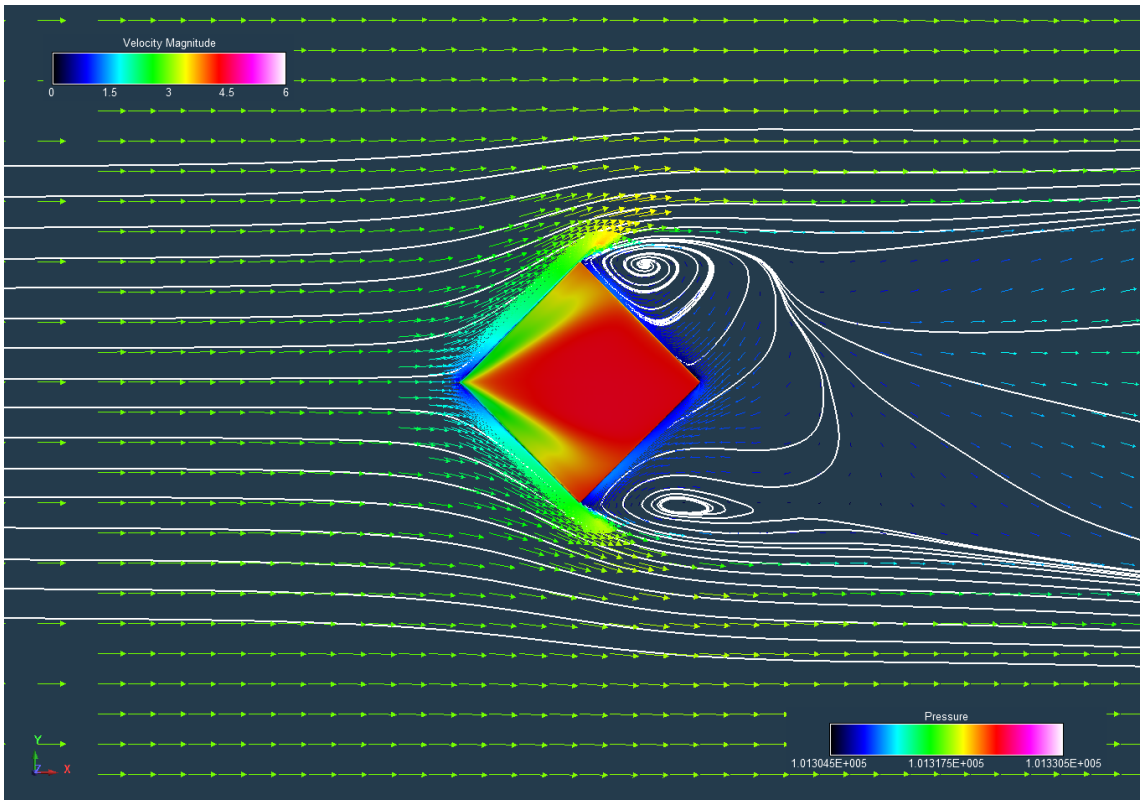

Figure A19. RotCFD (side view velocity vector and streamlines) predictions as a function of Reynolds number for a cube at a 45Deg. inclination (V=3m/s)

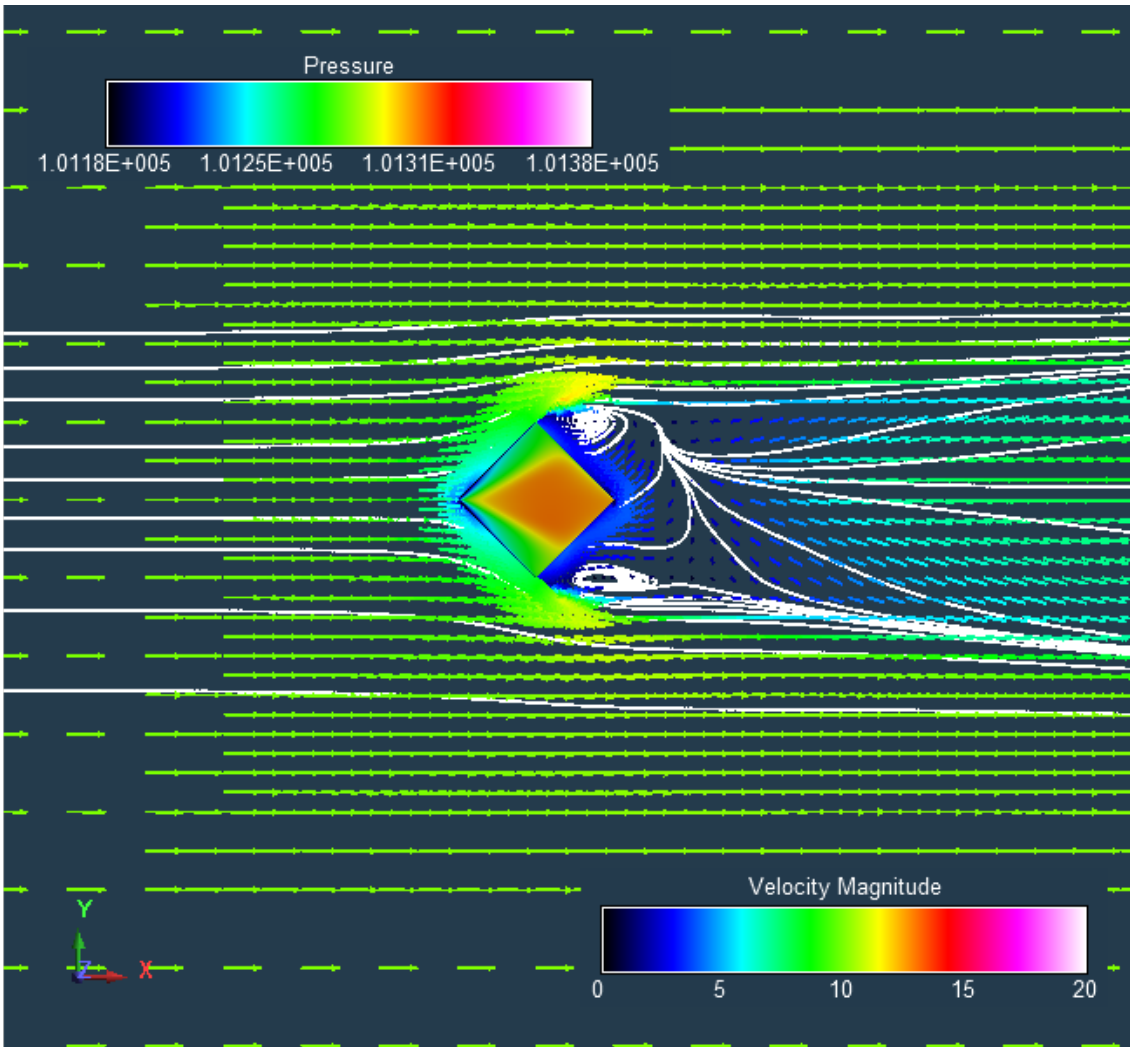

Figure A20. RotCFD (side view velocity vector and streamlines) predictions as a function of Reynolds number for a cube at a 45Deg. inclination (V=10m/s)

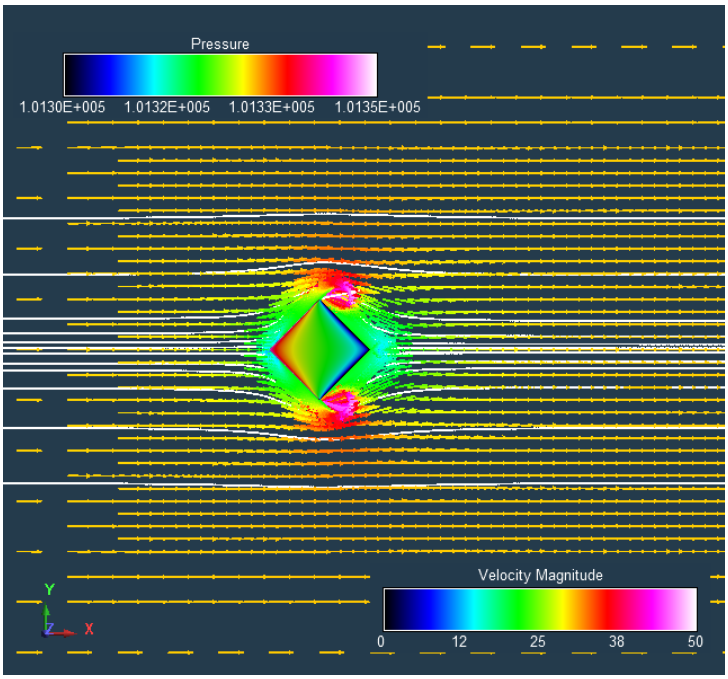

Figure A21. RotCFD (side view velocity vector and streamlines) predictions as a function of Reynolds number for a cube at a 45Deg. inclination (V=30m/s)

Figure A22 presents RotCFD predictions of the drag coefficient of a cube with a forty-five-degree incline with respect to the freestream velocity. Reference textbooks typically indicate that the forty-five-degree inclined cube drag coefficient is a constant value for all but the lowest Reynolds numbers. This can be observed as well in the RotCFD predictions (with turbulent modeling). To achieve this agreement, it was necessary to run RotCFD with OpenCL GPU with double precision; only at the highest Reynolds numbers was single precision satisfactorily accurate. The observed agreement with reference textbook drag coefficient values is likely primarily obtainable because of the sharp corners of the modeled cubes which, in turn, resulted in more predictable lines of separated flow.

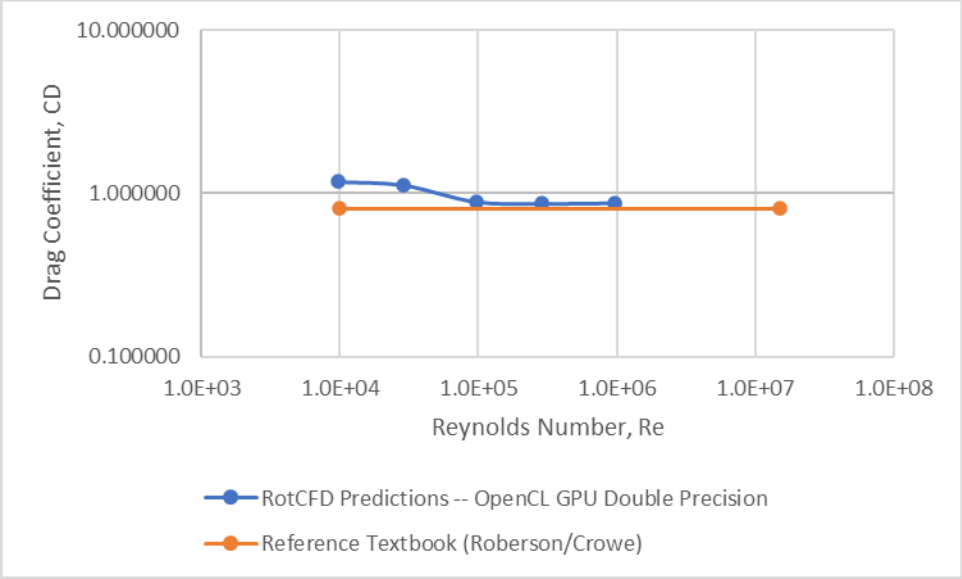

Figure A22. RotCFD drag coefficient predictions as a function of Reynolds number for a cube at a 45Deg. inclination as compared to reference textbook trends

Figures A23-27 present flow field and streamline predictions of a forward-facing hemispherical shell. This flow problem is another well-known simple three-dimensional bluff body that is cited in almost every introductory fluid dynamics reference textbook.

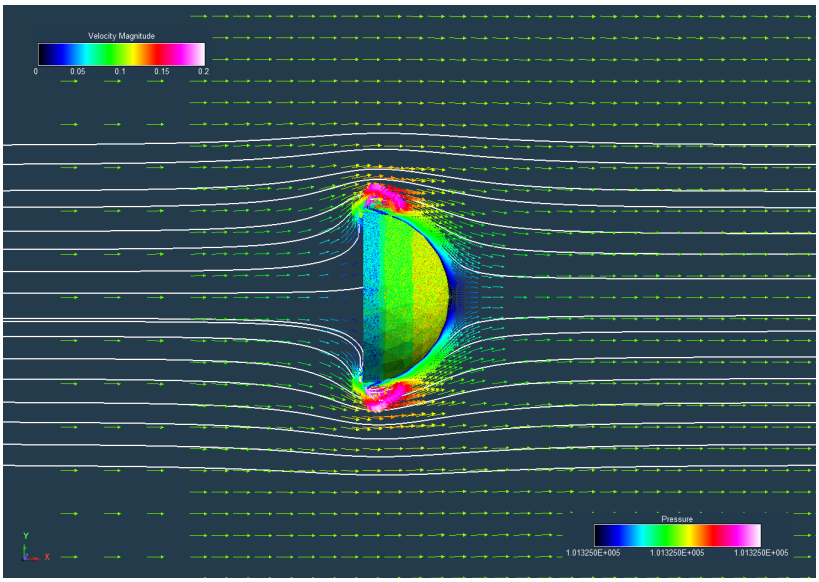

(a)

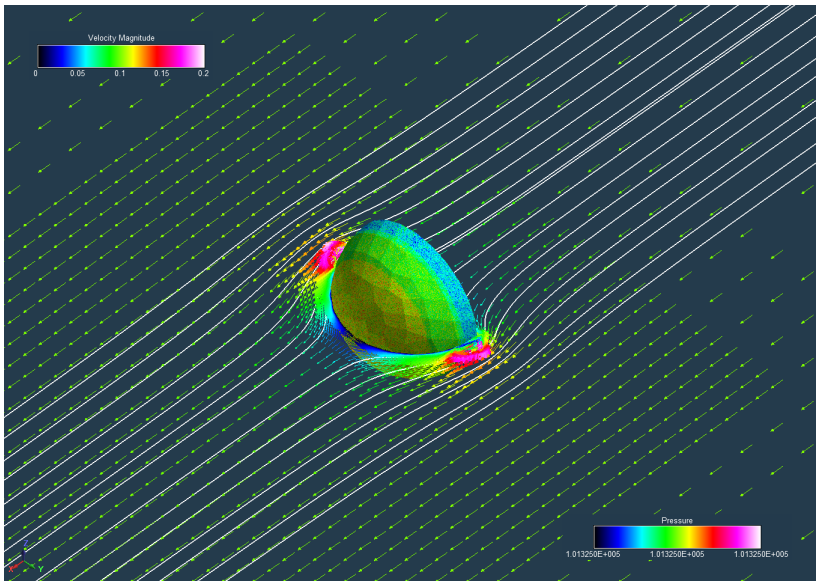

(b)

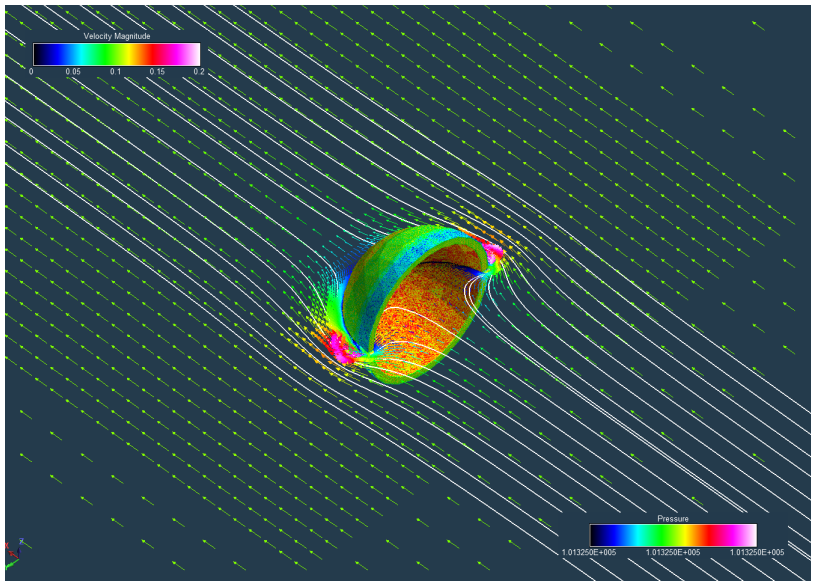

(c)

Figure A23. RotCFD flow field and surface pressure predictions as a function of Reynolds number for a forward-facing hemispherical shell (V=0.1m/s): (a) side view, (b) isometric rear view, and (c) isometric forward view

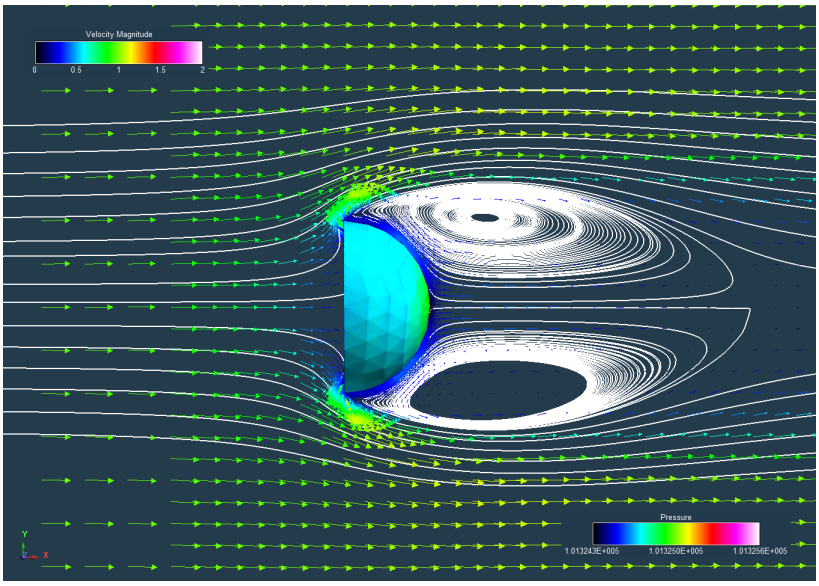
Velocity Magnitude
0
0.5
1
1.5
2
Pressure
1.013243E+005
1.013250E+005
1.013256E+005

(a)

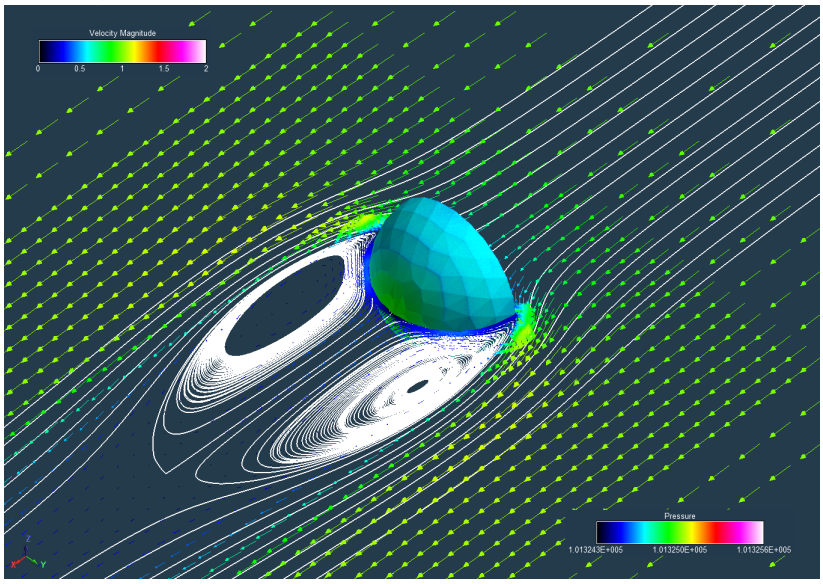
Velocity Magnitude
0
0.5
1
1.5
2
Pressure
1.013243E+005
1.013250E+005
1.013256E+005

(b)

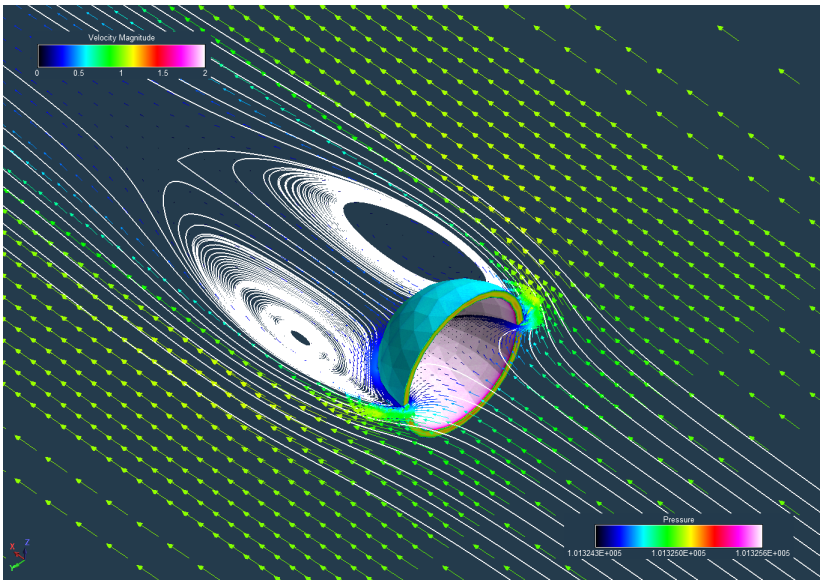

(c)

Figure A24. RotCFD flow field and surface pressure predictions as a function of Reynolds number for a forward-facing hemispherical shell (V=1m/s): (a) side view, (b) isometric rear view, and (c) isometric forward view

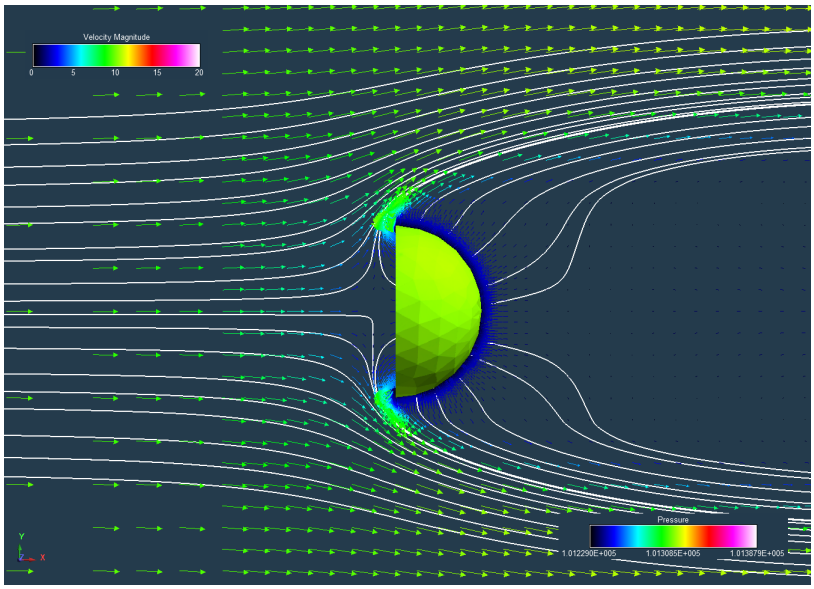

(a)

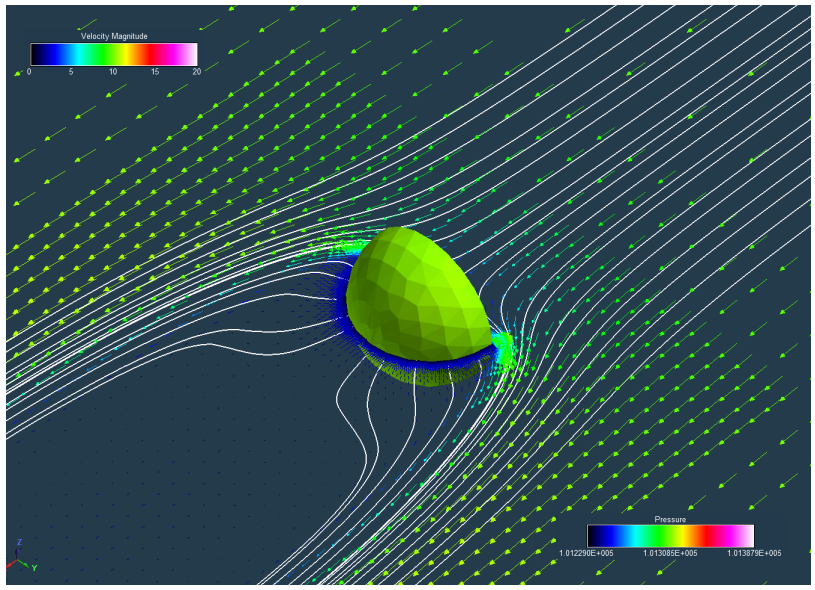

(b)

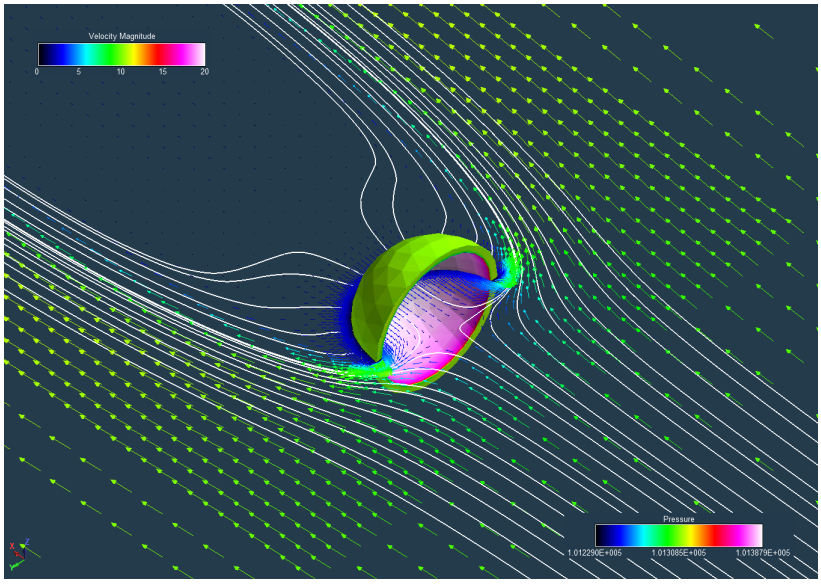

(c)

Figure A25. RotCFD flow field and surface pressure predictions as a function of Reynolds number for a forward-facing hemispherical shell (V=10m/s): (a) side view, (b) isometric rear view, and (c) isometric forward view

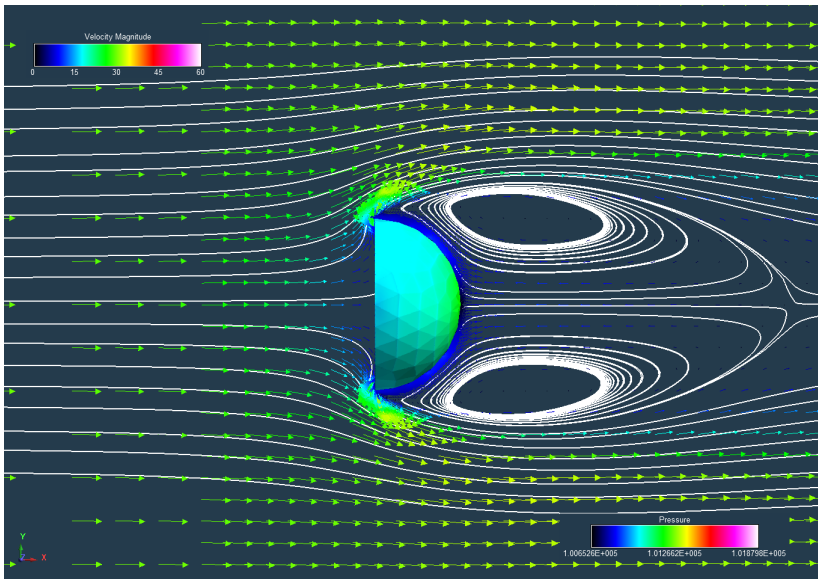
Velocity Magnitude
0
15
30
45
60
Pressure
1.006526E+005
1.012662E+005
1.018798E+005

(a)

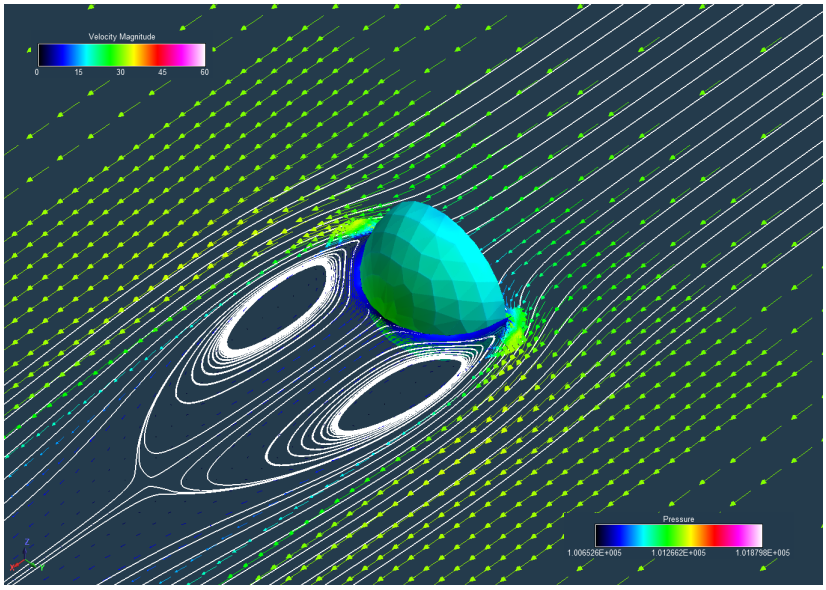
Velocity Magnitude
0
15
30
45
60
Pressure
1.006526E+005
1.012662E+005
1.018798E+005

(b)

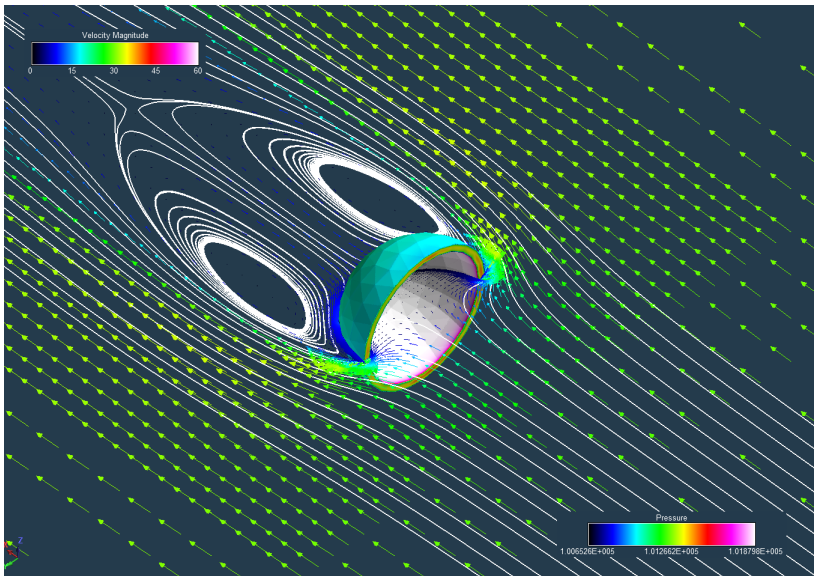

(c)

Figure A26. RotCFD flow field and surface pressure predictions as a function of Reynolds number for a forward-facing hemispherical shell (V=30m/s): (a) side view, (b) isometric rear view, and (c) isometric forward view

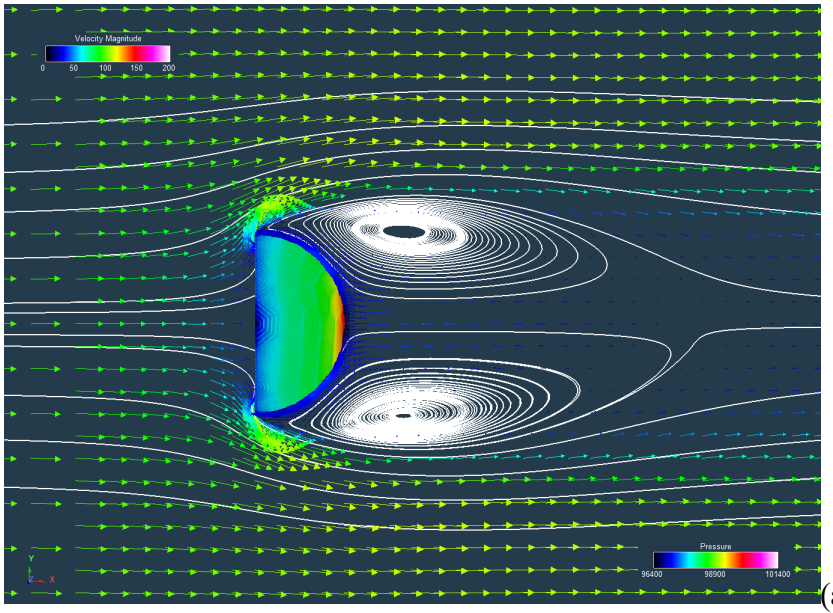

(a)

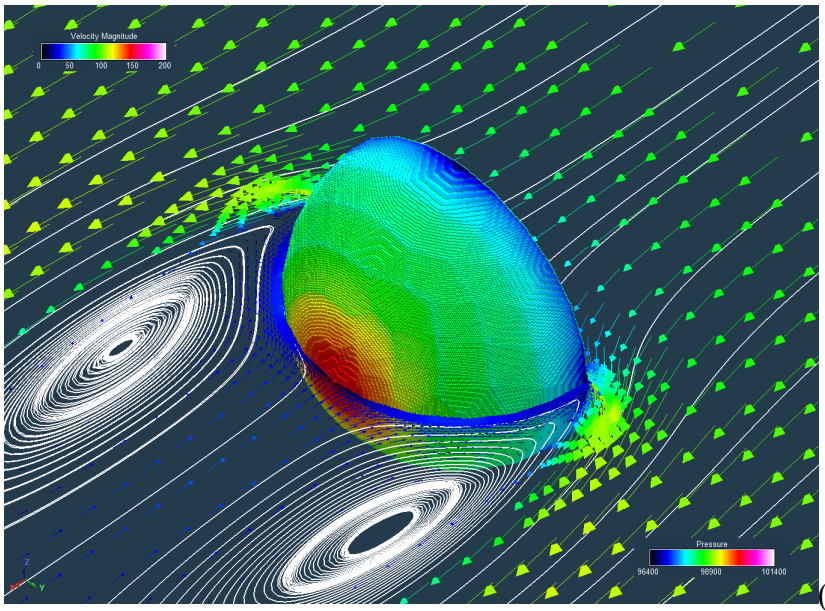

(b)

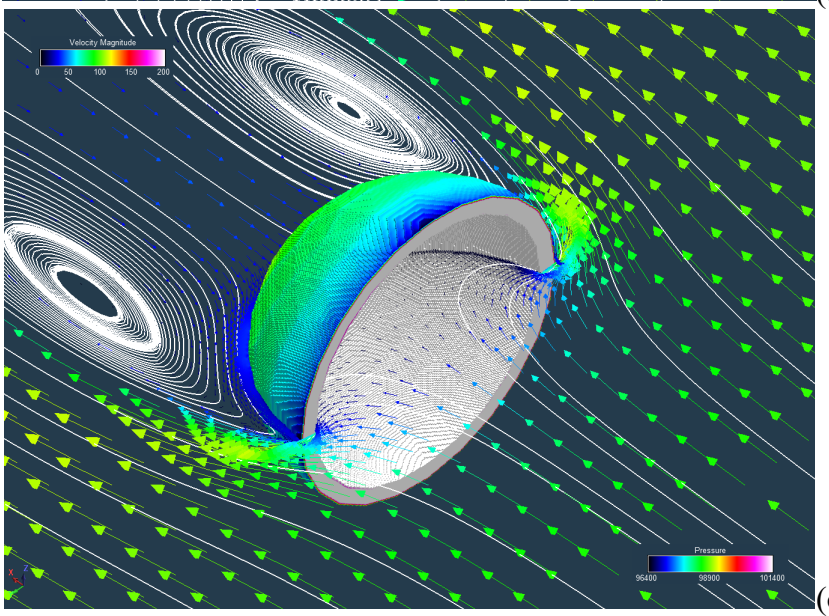

(c)

Figure A27. RotCFD flow field and surface pressure predictions as a function of Reynolds number for a forward-facing hemispherical shell (V=100m/s): (a) side view, (b) isometric rear view, and (c) isometric forward view

Figure 28 presents the RotCFD drag coefficient predictions for the forward-facing hemispherical shell as a function of Reynolds number. The RotCFD predictions are again in good agreement (slightly underpredicted) as compared to the often-cited reference textbook value.

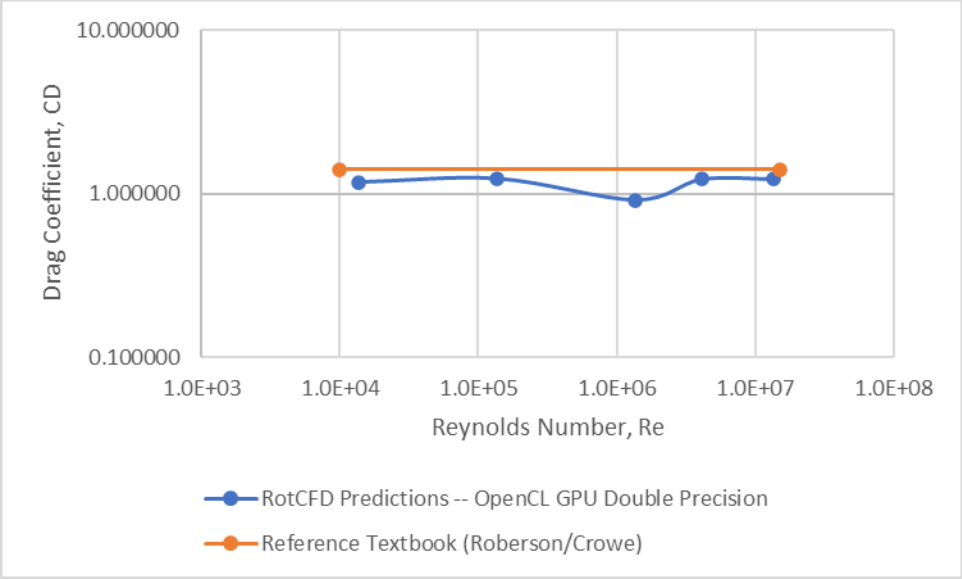

Figure A28. RotCFD drag coefficient predictions as a function of Reynolds number for a forward-facing hemispherical shell as compared to reference textbook trends

Figures 29-34 are RotCFD prediction surface pressures and flow fields for backward-facing hemispherical shells.

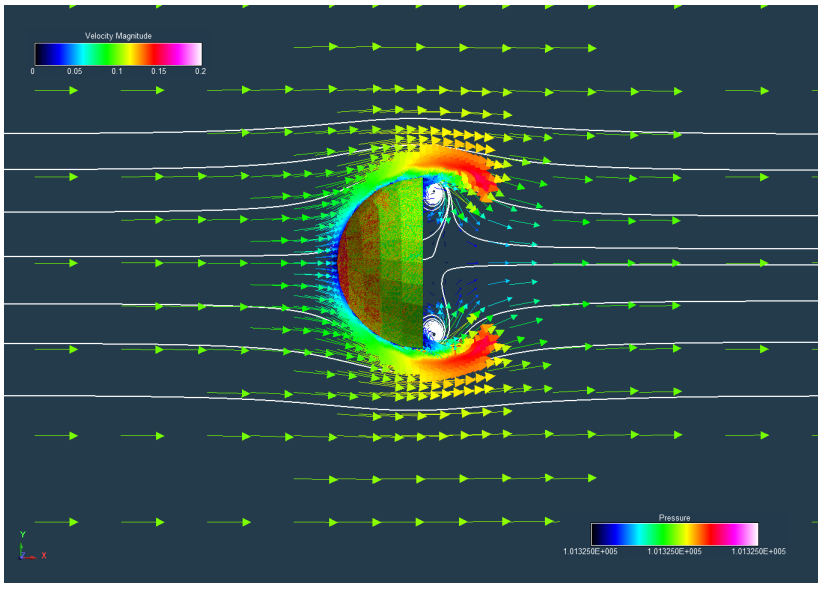

(a)

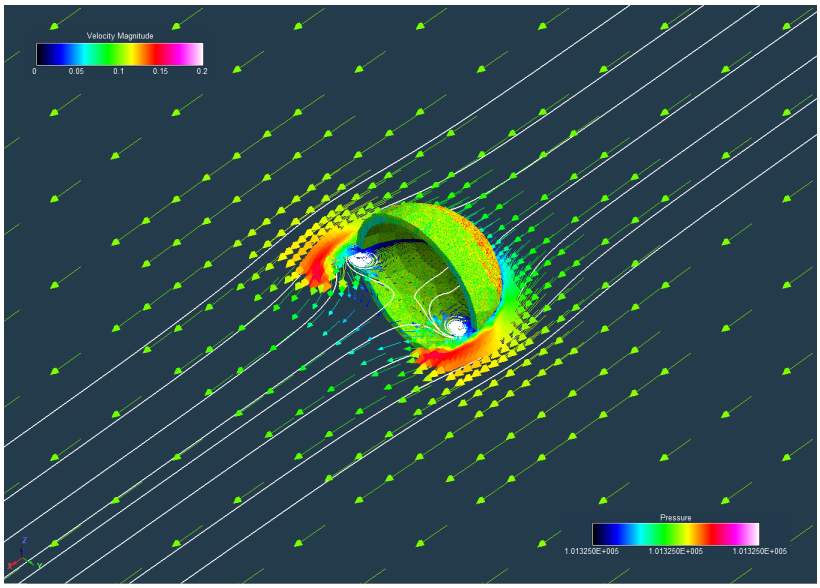

(b)

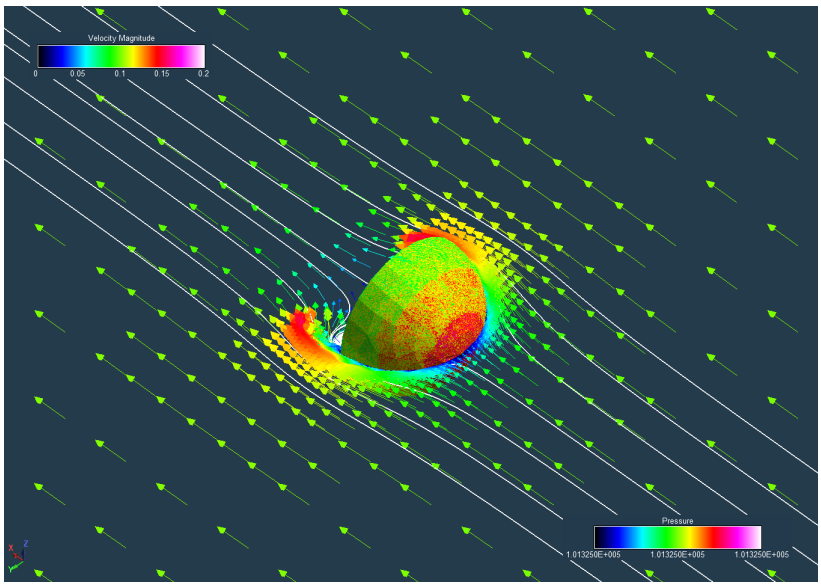

(c)

Figure A29. RotCFD flow field and surface pressure predictions as a function of Reynolds number of (V=0.1m/s) for a backward-facing hemispherical shell: (a) side view, (b) isometric rear view, and (c) isometric forward view

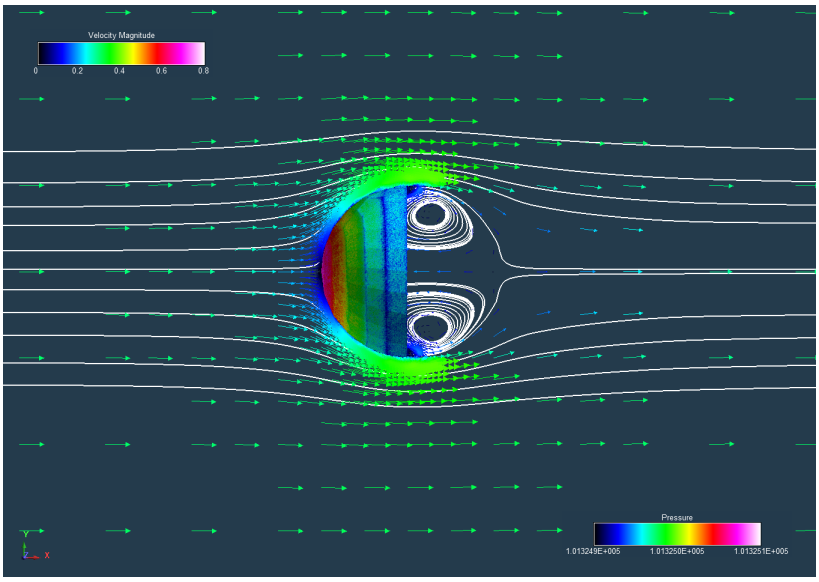
Velocity Magnitude
0
0.2
0.4
0.6
0.8
Pressure
1.013249E+005
1.013250E+005
1.013251E+005

(a)

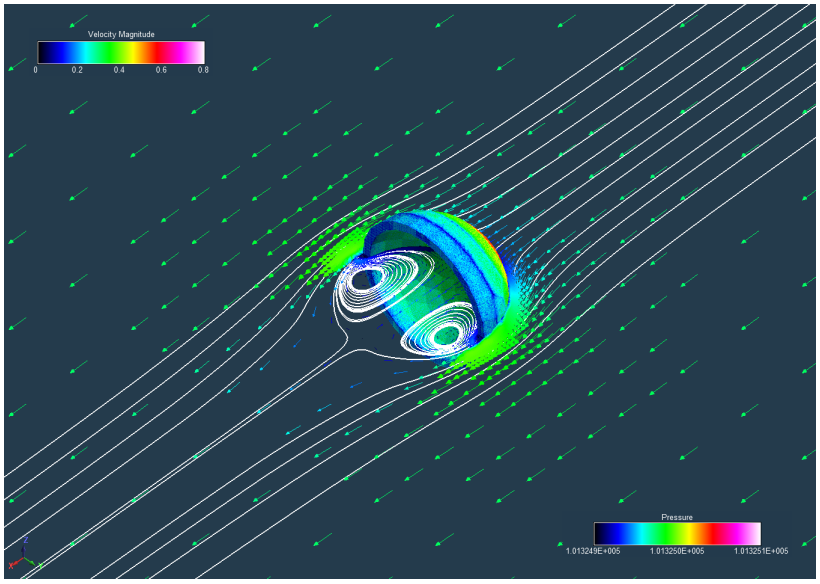
Velocity Magnitude
0
0.2
0.4
0.6
0.8
Pressure
1.013249E+005
1.013250E+005
1.013251E+005

(b)

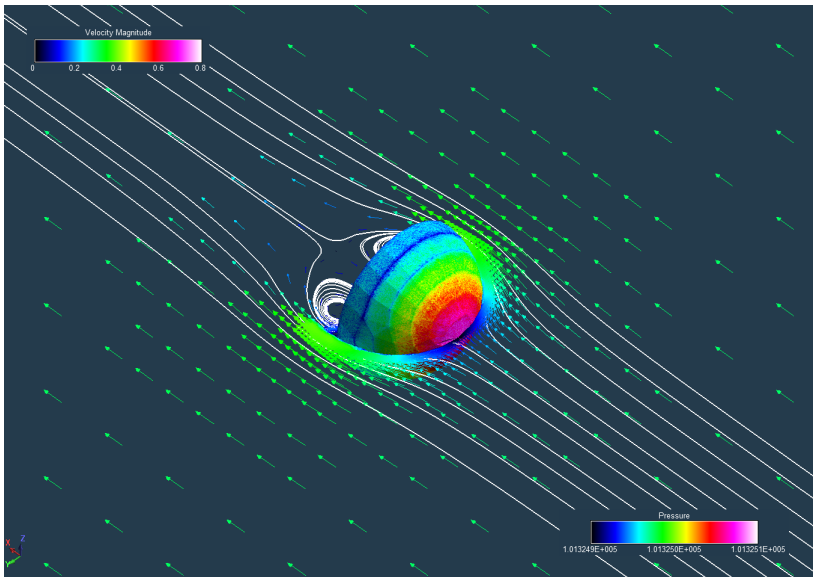

(c)

Figure A30. RotCFD flow field and surface pressure predictions as a function of Reynolds number of (V=0.3m/s) for a backward-facing hemispherical shell: (a) side view, (b) isometric rear view, and (c) isometric forward view

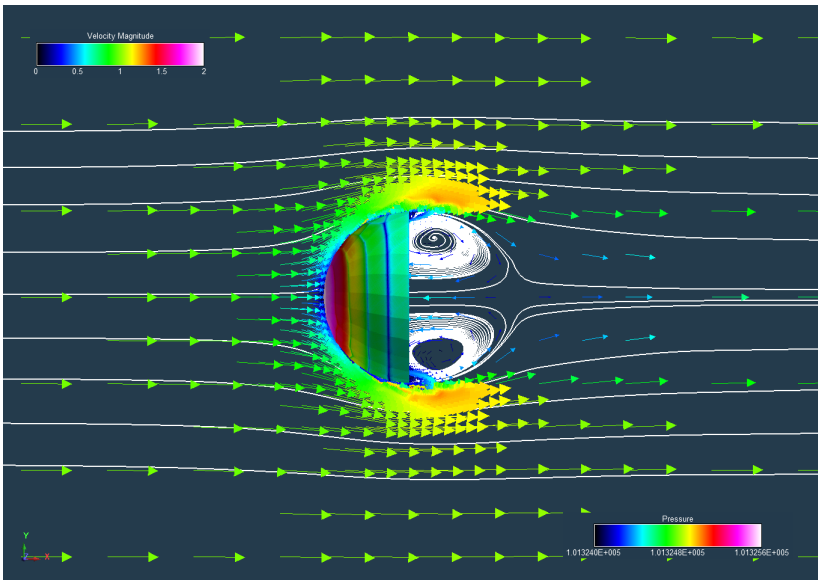

(a)

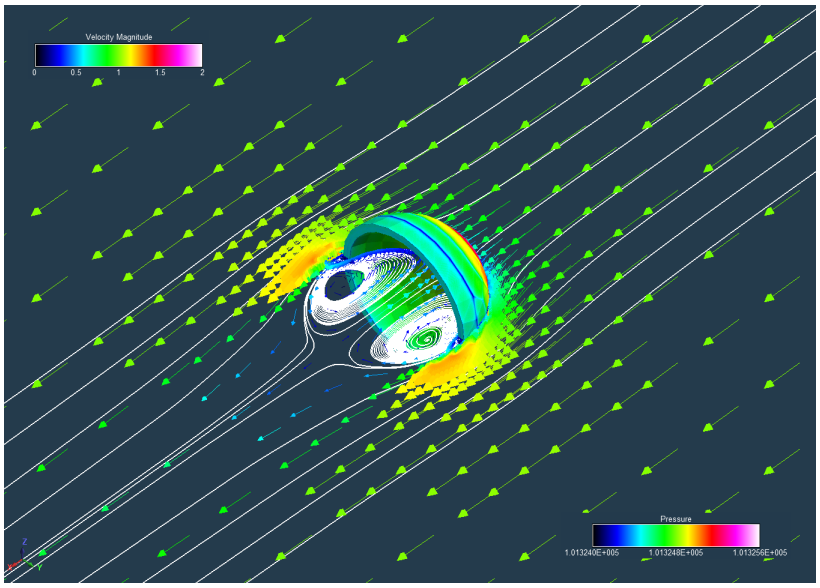

(b)

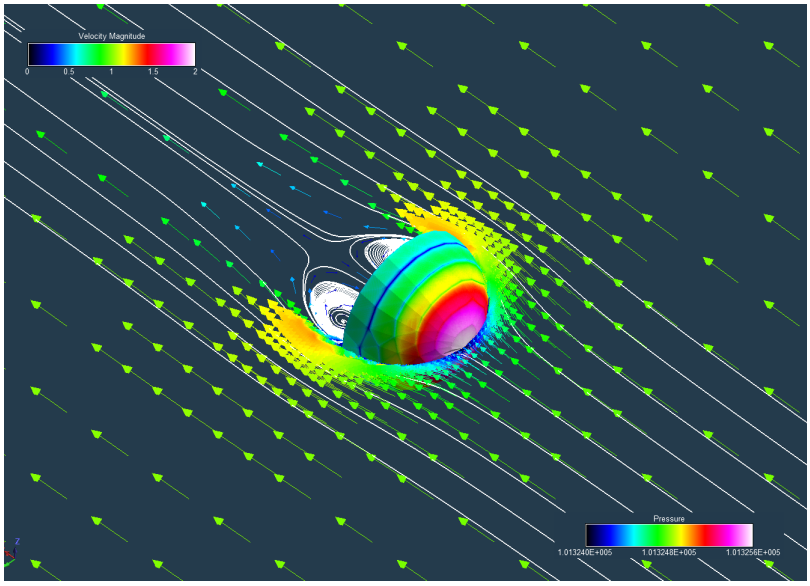

(c)

Figure A31. RotCFD flow field and surface pressure predictions as a function of Reynolds number of (V=1m/s) for a backward-facing hemispherical shell: (a) side view, (b) isometric rear view, and (c) isometric forward view

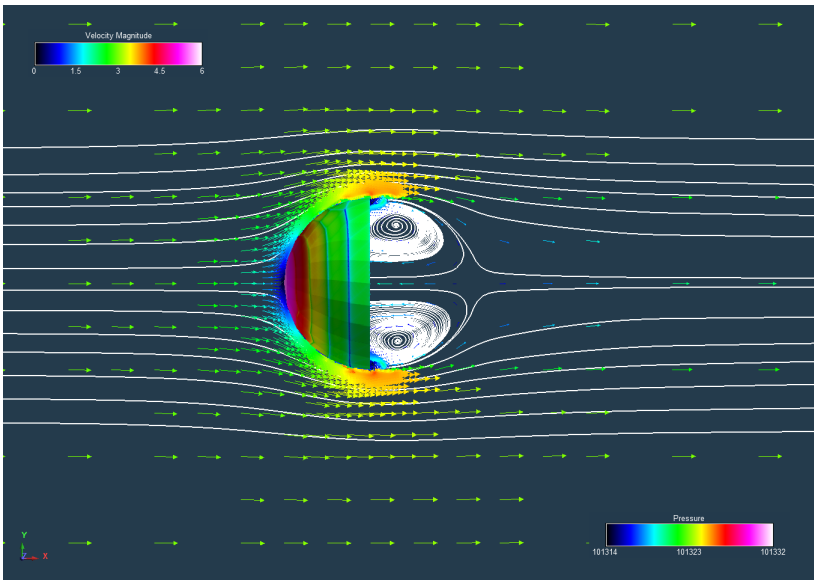
Velocity Magnitude
0
1.5
3
4.5
6
Pressure
101314
101323
101332

(a)

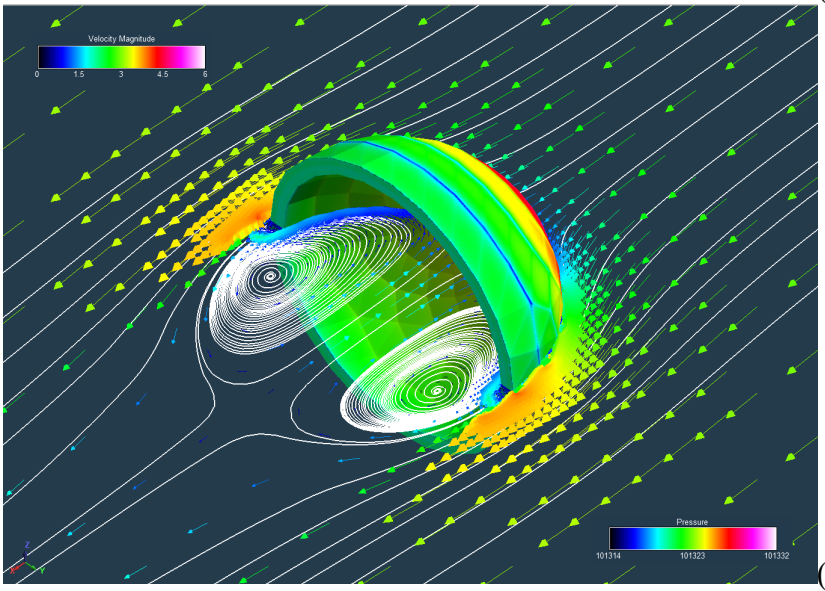
Velocity Magnitude
0
1.5
3
4.5
6
Pressure
101314
101323
101332

(b)

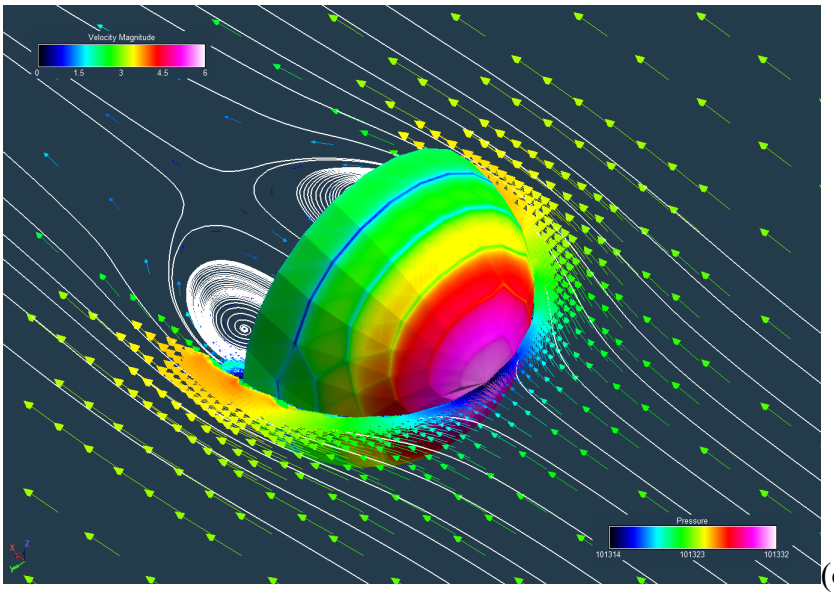

(c)

Figure A32. RotCFD flow field and surface pressure predictions as a function of Reynolds number of (V=3m/s) for a backward-facing hemispherical shell: (a) side view, (b) isometric rear view, and (c) isometric forward view

Figure A33 presents RotCFD predicted drag coefficients for the backward-facing hemispherical shells. Reference textbook drag coefficient values are presented as well. RotCFD modestly overpredicts the drag coefficients. Even with OpenCL GPU double precision, the predicted drag coefficients at the lowest Reynolds numbers are still high. This may be because the spherical 'nose' of the hemispherical shell makes the flow harder to predict, even though the body is still considered to be a three-dimensional bluff body.

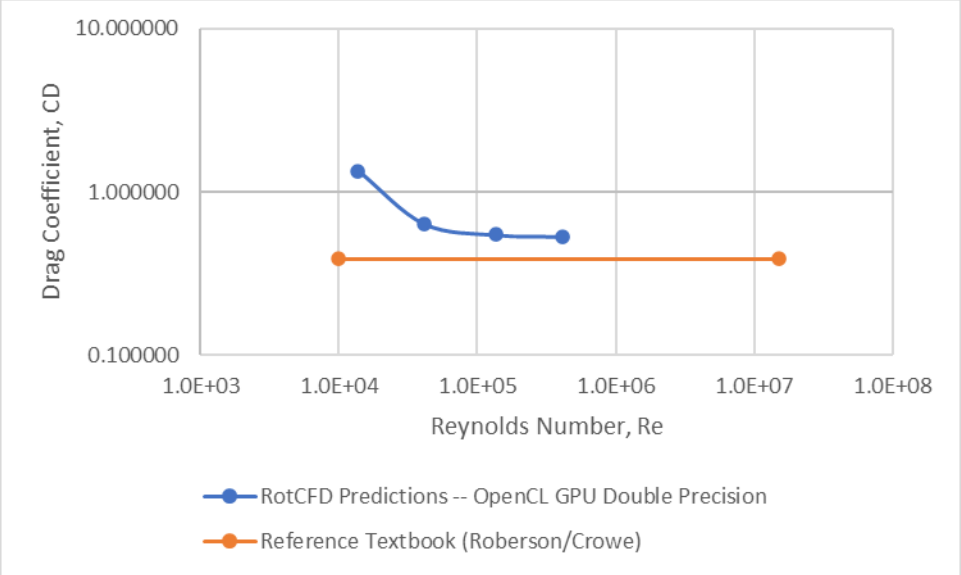

Figure A33. RotCFD drag coefficient predictions as a function of Reynolds number for a backward-facing hemispherical shell versus reference textbook trends

All the bodies in Appendix A were generated by the RotCFD supplemental tool called ShapeGen. These bodies were generated with default settings for the CAD-generation of these bodies. In some cases, discernable faceting of the simple bodies can be observed prior to their CFD-gridding. This faceting is generally an undesirable geometric artifact. Future work should consider performing a sensitivity analysis of the CFD-gridding fineness/refinement but should also more carefully consider the CAD-generated geometric fidelity with the idealized body being generated.

Appendix B – Finite Span Wing Drag Prediction Correlation

Even a highly refined cartesian-grid for a wing surface is inadequate for accurate wing aerodynamic predictions. The automated body-fitted gridding provided by RotCFD is required. The automated body-fitted gridding feature for RotCFD, though, can have trouble with the sharp trailing edges of the wings. Refer to Fig. B1 for some initial planform views of the wing flow field (q-criterion isosurfaces) and upper surface pressures.

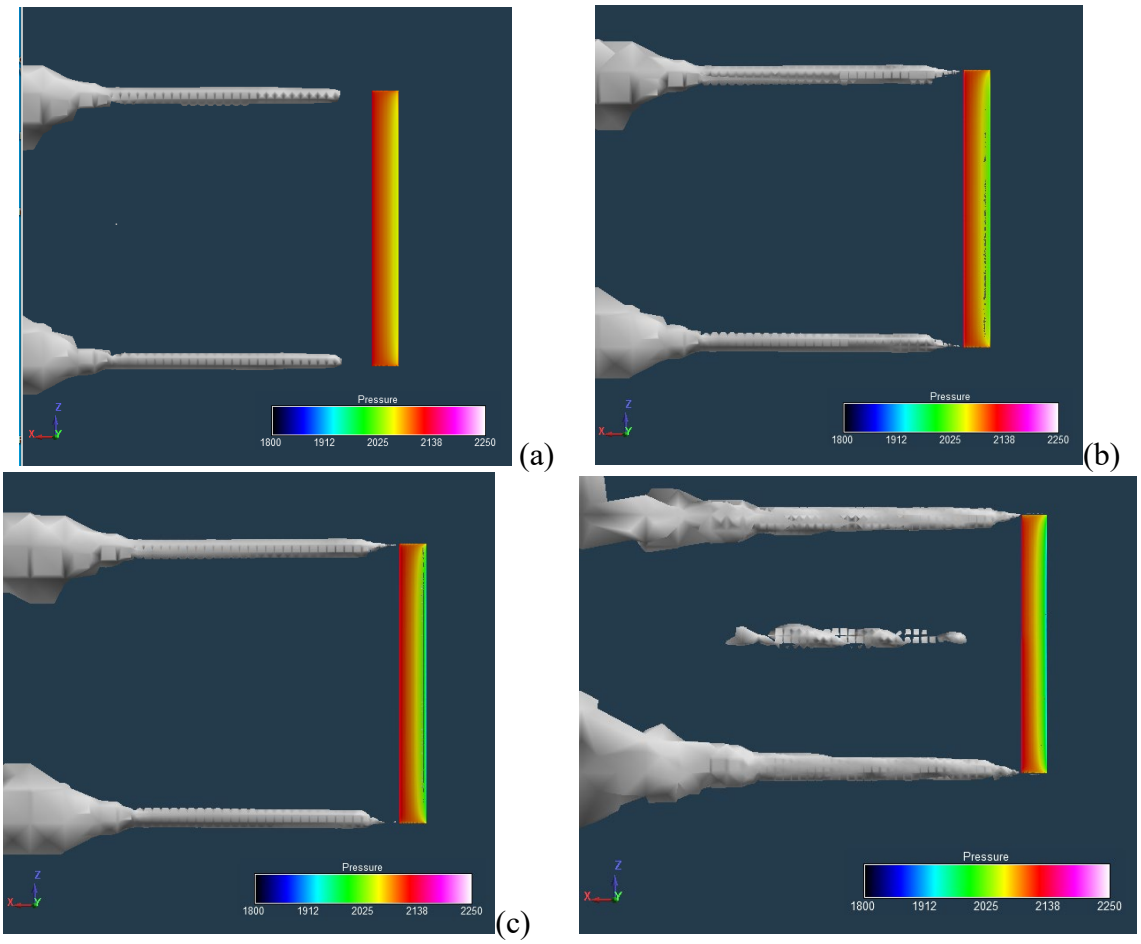

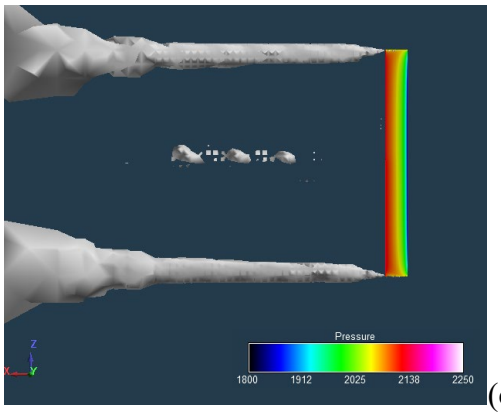

(e)

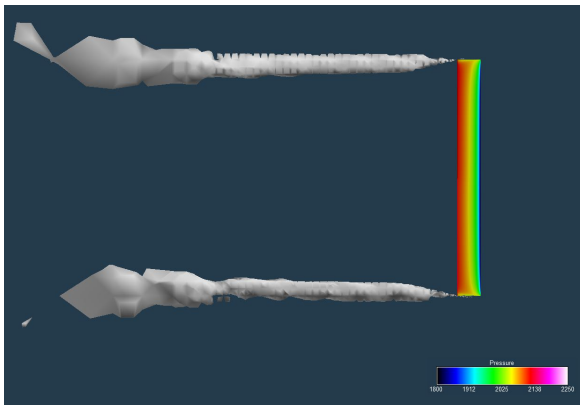

(f)

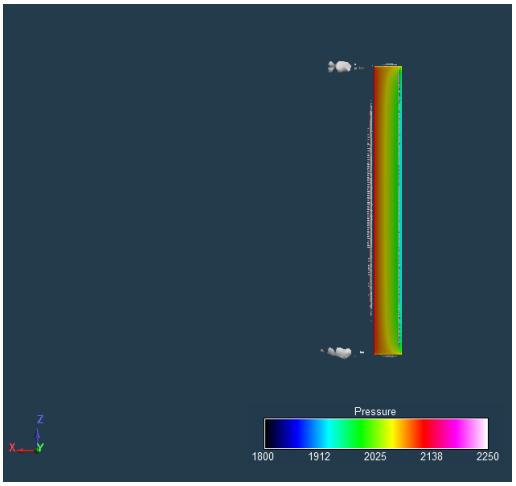

(g)

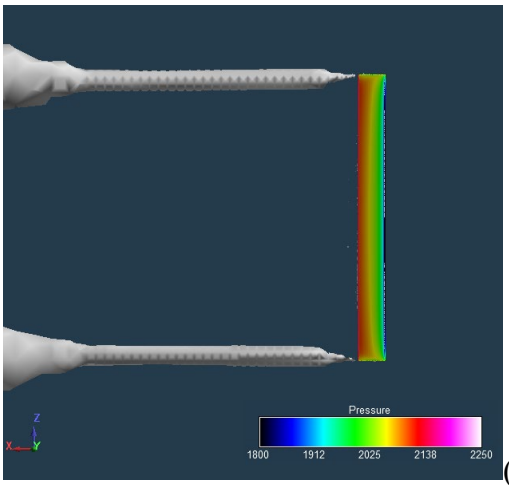

(h)

Figure B1. RotCFD predictions of a finite span (unswept, constant chord) wing: (a) AOA=2Deg.; (b) AOA=4Deg.; (c) AOA=6Deg.; (d) AOA=8Deg.; (e) AOA=10Deg.; (f) AOA=12Deg.; (g) AOA=14Deg.; (h) AOA=16Deg.

The original finite-span (rectangular planform) wing body was also generated by the RotCFD supplemental CAD tool, ShapeGen. The wing cross-section uniformly used the NACA0012 airfoil. ShapeGen default value settings for the three-dimensional wing generation were used. This yielded some faceting of the aft-portion (from mid-chord to trailing edge) of the wing surface as the default CAD settings seemed to be, in hindsight, inadequate; refer to Fig. B2. This CAD geometric fidelity for finite-span wings in the context of ShapeGen settings needs to be further explored in the future.

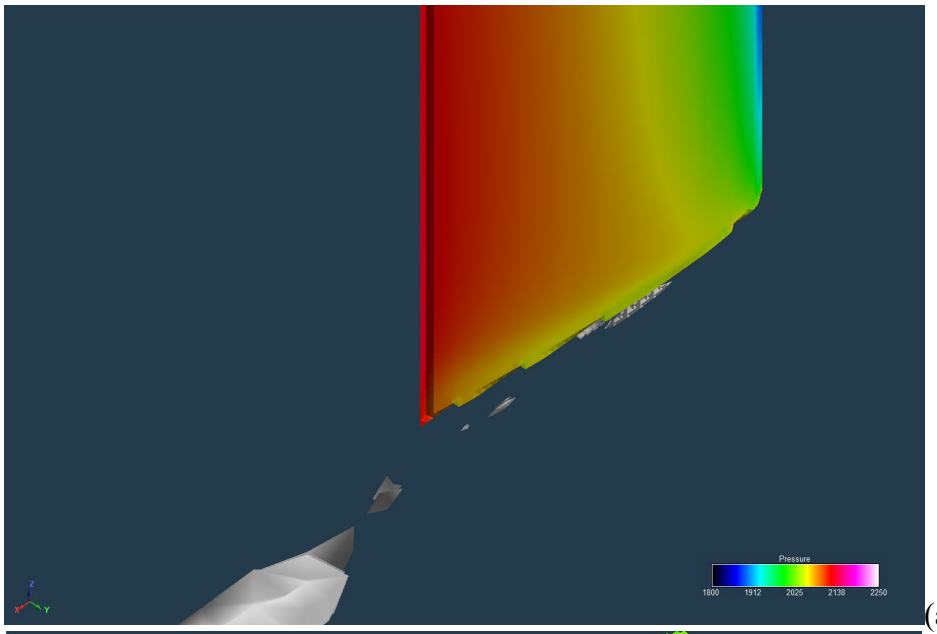
Pressure
1800
1912
2025
2138
2250

(a)

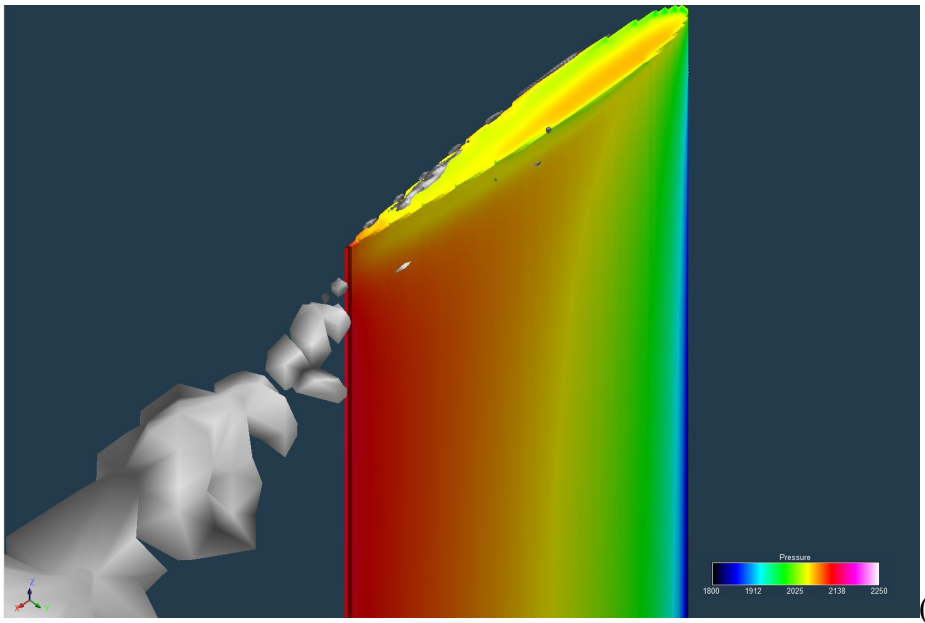
Pressure
1800
1912
2025
2138
2250

(b)

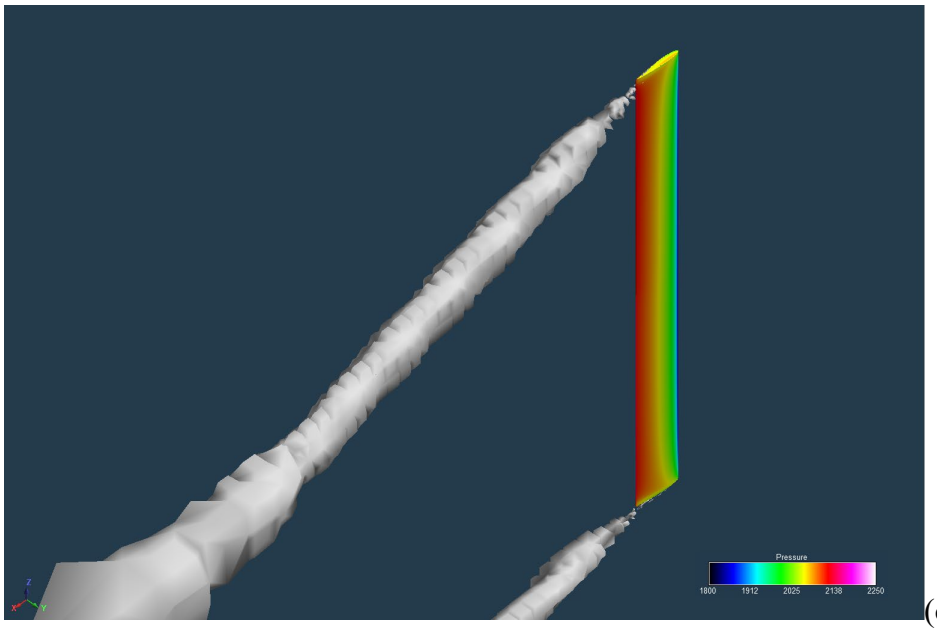

(c)

Figure B2. RotCFD automated body-fitted gridding and challenges with sharp trailing-edges for wings: (a) close-up starboard wingtip (with gridding artifact/defect), (b) close-up of port wingtip (gridding acceptable), and (c) isometric view of complete wing

Figure B3a-b presents RotCFD-predicted lift-curves and drag polars for the finite-span wing. Also shown in Fig. B3a-b is an effective 'strip theory' result (again from RotCFD by assuming 'nonrotating blades' (modeled by setting the rotor rpms to near-zero values) being equivalent to wings when running RotCFD's actuator line representations of the rotor blades. RotCFD tends to overpredict the lift-curve for the finite-span wing considered, especially between $8 \leq AOA \leq 12$Deg. This overprediction seems to be a consequence of the original ShapeGen CAD-geometry generation (yielding the above noted faceting on the aft portion of the wing cross-sections). Attempting to compensate for these original faceting artifacts by going to higher grid-fineness/refinement and/or use of OpenCL GPU double versus single precision did not significantly change the predicted lift and drag estimates.

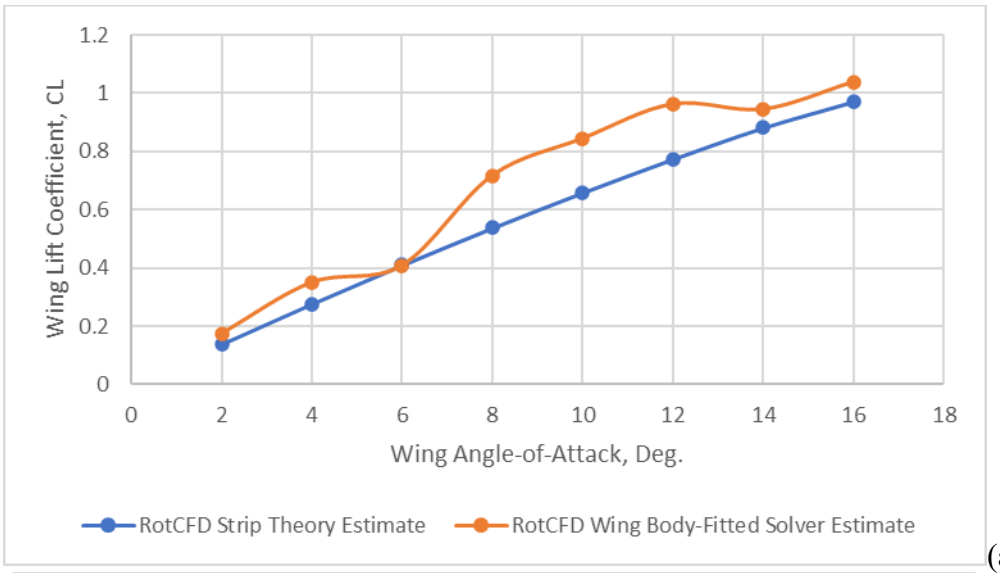

(a)

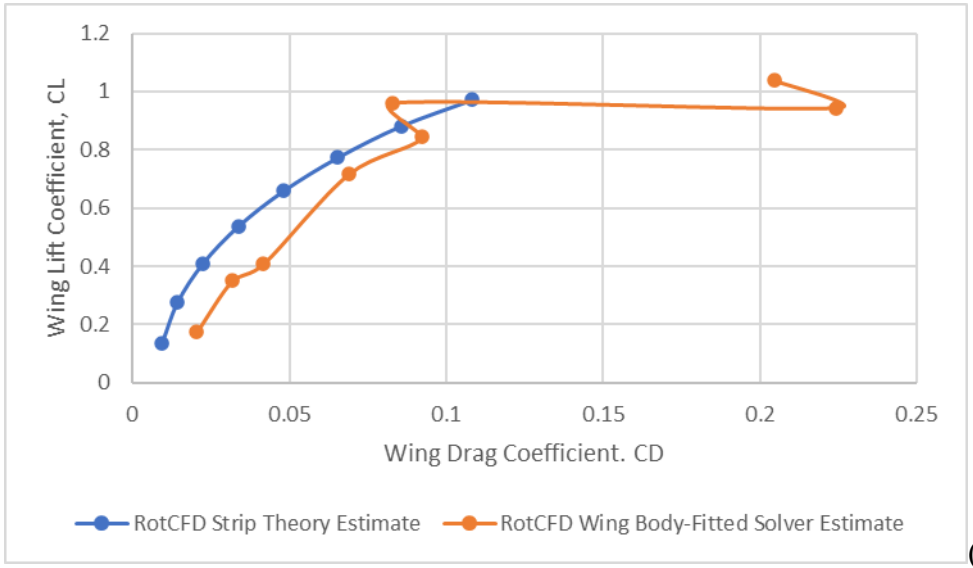

(b)

Figure B3. RotCFD predicted finite-span wing aerodynamic characteristics (presented with 'strip theory' predictions (also predicted by RotCFD): (a) lift curve slope; (b) drag polar curve

RotCFD body-resolved finite-span wing profile drag predictions were also overpredicted relative to the 'strip theory' results. The induced drag predictions seemed to be in closer agreement with 'strip theory,' as can be seen in Fig. B3b.

"Strip theory" is a classic wing theory technique that estimates the lift of a finite-span wing in 'strips', i.e., small spanwise increments and assuming the flow is two-dimensional in each strip. This alternate, but equivalent, approach through to generate "strip theory" lift and drag estimates for finite-span wings within RotCFD is a powerful ability. As a minimum, it is computationally faster than a body-resolved CFD prediction of a finite-span wing. This ad hoc "strip theory" capability was first explored in Ref. 59, with additional exploration of the technique in Ref. 60.

Figure B4a-c presents some flow field results for the mid-span of the body-resolved finite-span wing. These flow field results are for wing angle-of-attacks of 8, 10, and 12Deg.

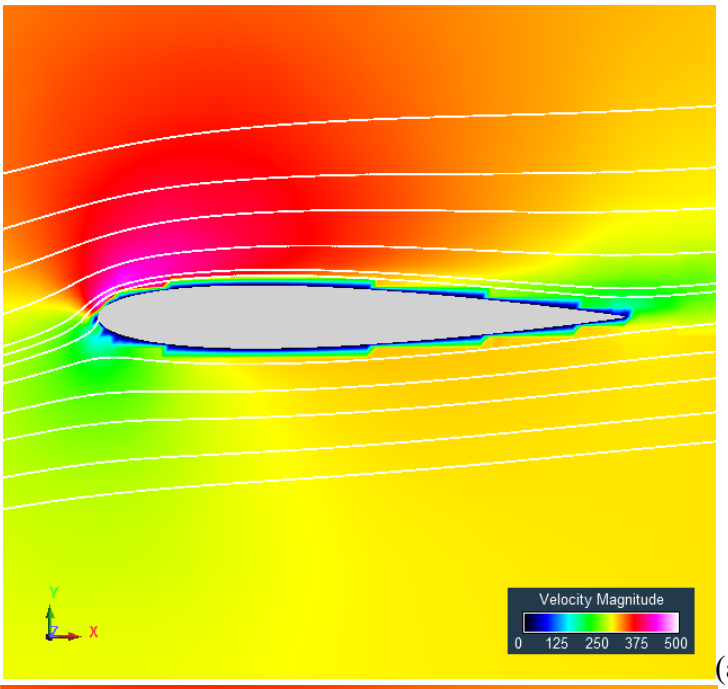

(a)

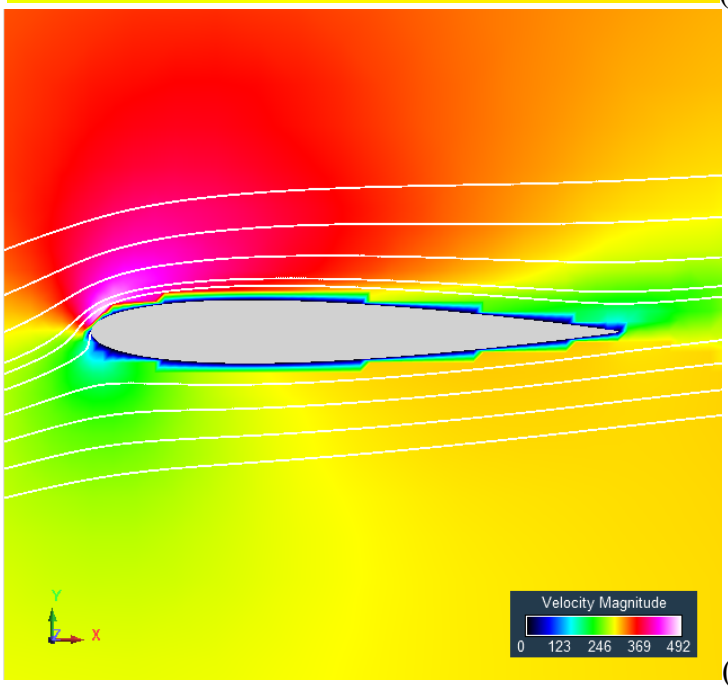

(b)

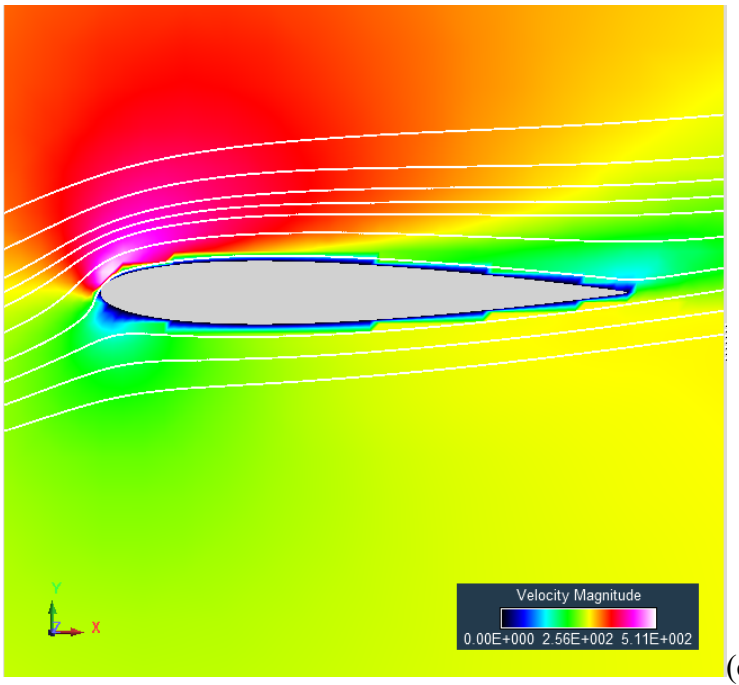

(c)

Figure B4. RotCFD predicted velocity magnitude contours and streamlines at mid-span of the finite-span wing (V=300ft/s): (a) AOA=8Deg.; (b) AOA=10Deg.; (c) AOA=12Deg.